

Molecular Mechanics and Ab Initio Simulations
of Silicon (111) Surface Reconstructions,
Semiconductors and Semiconductor Superlattices,
H Abstraction for Nanotechnology, Polysilane,
and Growth of CVD Diamond

Thesis by
Charles Bruce Musgrave

In Partial Fulfillment of the Requirements
for the Degree of
Doctor of Philosophy

California Institute of Technology

Pasadena, California

1995

Defended September 29, 1994

© Charles B. Musgrave 1995

All Rights Reserved

Table of Contents

Chapters	Page
Acknowledgements	v
Abstract	vi
Introduction	1
Chapter 1 Review of Methods	8
Chapter 2 SR-SOR Step for Growth of CVD Diamond	30
Chapter 3 Ab initio Study of H Abstraction in Nanotechnology	64
Chapter 4 The Hessian Biased Force Field for Polysilane Polymers	93
Chapter 5 Force Fields for Semiconductors and Their Superlattices	149
Chapter 6 Silicon (111) Surface Reconstructions	232
Chapter 7 Generalized London Potential for Hydrocarbon Reactions	269

To my parents

Acknowledgements

I have benefited from the help and support of many people during my stay at Caltech. My advisor, Bill Goddard acted as a wise mentor, and inspiring example of unquenched enthusiasm for science. I thank him for his support and friendship. K. T. Lim, Rick Muller, and Terry Coley were always helpful in answering my computer questions. I also want to thank Jim Gerdy, Erik Bierwagen, Yue Jin Guo, Mario Blanco, Ersan Demiralp, Jamil Tahir-Kheli, Naoki Karasawa, Xiaojie Chen and Jean-Marc Langlois for sharing their expertise with me. The entire Goddard group has contributed greatly to my research here at Caltech and without them this work would have proven much more difficult.

I have also benefited from many collaborators both in and out of the Goddard group. These scientists not only provided scientific insight, mentorship, and fulfilling interaction, but also friendship. I am grateful to each of them; Ralph Merkle of Xerox, Steve Harris of General Motors, Eric Drexler of the Foresight Institute, Jenna Zinck of Hughes, and Jason Perry, Siddharth Dasgupta, Jinsong Hu, and Bob Donnelly of the Goddard group.

I'd also like to thank my friends who never quite knew what I was working on, but supported me anyway. Jessica and Jean were especially good to me. I especially appreciate Luanne Tseng for her patience, and friendship. My brother Richard and sisters Adriana and Gabriela have each given me their support. Without the support and efforts of my parents none of this would be possible. To them I am ever thankful.

Abstract

This thesis describes the application of *ab initio* and molecular mechanics quantum chemical methods to several problems in the materials and surface sciences. Chapter 1 reviews these methods. Chapter 2 details the application of these methods to study the reaction rate of a proposed mechanism for growth of CVD diamond. Chapter 3 uses high level *ab initio* methods to study the feasibility of a hydrogen abstraction tool for nanotechnology. Chapter 4 uses *ab initio* methods together with experimental data to develop a force field potential to model polysilane polymers. Chapter 5 is comprised of the development of atomistic potentials to describe semiconductors and their superlattices and interfaces. The approach of Chapter 5 is extended in Chapter 6 by combining the bulk force field with force field parameters developed from the Biased Hessian Method applied to unique clusters to model the reconstructions of the Si (111) surface. Chapter 7 concludes this thesis with a description of the Generalized London Potential which was developed to accurately model chemical reactions at the accuracy of high level configuration interaction methods, but with the practicality of molecular mechanics.

1.0 Introduction

Advances in quantum chemistry and molecular dynamics have progressed to the point where materials behavior predictions from computational atomistic simulations are being realized. Much progress has also been made in solving the more challenging problems involved in simulating materials processing. Advances in computer hardware together with advances in theory have lead to application of computational materials science to numerous important industrial and scientific problems, however many issues remain.

Our goal was to develop and apply molecular mechanics and quantum chemistry methods to simulate and predict the materials properties. We have chosen to simulate several challenging materials problems, which required the development and extension of techniques and which illustrate the success of our approach; (i) Si (111)¹⁻³ surface reconstruction, (ii) chemical vapor deposition (CVD) growth of diamond, (iii) properties of bulk semiconductors and their (iv) interfaces and superlattices, (v) H abstraction for nanotechnology, and (vi) polysilane polymers.

In the case of surface reconstruction, the primary goals are to determine the atomic structure of the surface and its stability. For the various Si(111) surface reconstructions the differences in stability are very small and therefore only methods that are highly accurate should be employed in order to correctly resolve the energetic differences between the various structures. This is the case in many other systems as well. Advanced *ab initio* methods with high accuracy are the natural choices for studying systems where slight differences in geometry or energy need to be resolved.⁴ However, except in the few cases of surfaces with small unit cells, *ab initio* quantum chemical methods are not practical since they scale as N^s where N is the number of electrons and s is at least 4, and depends on the method employed. Furthermore, few of the most accurate methods that have been developed for molecules and clusters have been extended to crystalline systems. One quantum based method that shows promise in simulating large systems, such as the recon-

struction of surfaces is density functional theory (DFT),^{5,6} especially if the method includes the local density approximation, the gradient correction and algorithms to reduce the scaling factor. Currently there is insufficient experience with these methods and their accuracy for such systems is yet to be determined, however, preliminary results are promising. These methods can be applied to relatively large unit cells for single point energy calculations. However, these calculations are computationally intensive, particularly optimization of geometries, and computation of Hessians for frequency predictions.

Quantum chemical methods are not practical for (i) or other large systems because they include the electrons in the simulations.⁷ Molecular mechanics methods were developed to overcome this problem. In molecular mechanics, the atoms of the system are treated as classical particles that interact with each other via two, three, four,..., n-body interactions. The series of interactions is usually truncated at a small n, like 4 or 5. The potentials that model these interactions take on various forms. In the method⁸ we employ these are represented by spring-like *valence* terms for atoms connected by a series of bonds. Including bond terms, bond angle terms, dihedral torsion terms, coupling terms and *nonbond* terms. For atoms not connected by a string of bonds, there are Coulombic and van der Waals terms.

Each type of specific interaction has its own spring constant. In bulk silicon Si-Si bonds are modelled by the same potential. Bonds between a Si with three-fold coordination and a four-fold coordinated Si would have a different spring constant. Since molecular mechanics includes only interactions between the atoms as classical particles in a system, the effects of the electrons are averaged out. The number of interactions is therefore relatively small leading to a relatively simple algebraic expression for the energy of the system, in contrast to the much more complicated Schrödinger equation.

The molecular mechanics total energy can be calculated by summing the individual energy terms. The properties of the system can be calculated from the

expression for the total energy. For example, forces are first derivatives of the energy with respect to the atomic coordinates, and vibrational frequencies are the square roots of the diagonalized second derivative matrix. Consequently, the energy of the system, and thus the system properties, are functions of the spring constants. This set of spring constants, called the force field or potential, can be optimized so as to reproduce the system properties. Often this procedure is empirical and involves varying the force constants to reproduce the experimental properties of the system. This is often very involved and can consume a major portion of the research activity.

Once an accurate force field is available, it can be used to study arbitrary systems containing the interactions modelled by the force field. For moderately sized systems, less than a few thousand atoms, simulations of geometry optimization, phonon dispersion curves, vibrational frequencies, elastic constants, and thermodynamic properties are all carried out on inexpensive work stations over periods of less than several days. The development of Cell-Multipole Methods⁹ has enabled simulations of systems with up to 1 to 10 million atoms at present.

The advantages of molecular mechanics are (a), it can handle large systems relatively quickly and (b), the classical nature of the energy and other properties make it easy to understand, especially if valence-like terms are used to model the interactions. On the other hand, there are several drawbacks. One arises from the same feature that gives it its advantage; since electrons are not included in the simulation, quantum effects are neglected. The most important quantum effect is that of bond dissociation and formation. During a chemical reaction major changes to the electronic configuration of the system occur as what were once bonding interactions become antibonding or nonbonding interactions. So as a system nears a transition state, neglect of the Pauli principle leads to unphysical results, for example excess covalent bonds. This problem will make simulation of (ii), CVD diamond film growth and (v), H abstraction reactions unreliable. One way to circumvent this disadvantage is to (a), combine molecular mechanics and *ab initio* methods for a simulation in such a way that *ab initio* methods are applied to the portion of the

system undergoing reaction, and molecular mechanics is applied to large numbers of atoms in the nonreacting portion of the system which usually affect the energy through strain effects. Another way to circumvent this drawback is to (b) develop for force field expressions that take into account the Pauli Principle. One such approach is the Generalized London Potential method developed by Donnelly¹⁰ and applied to hydrocarbon reactions in collaboration with Musgrave.¹¹ In chapter 2 we report the results of approach (a) to study the CVD growth of diamond and in chapter 7 we report the efforts of approach (b). The reactions involved in the mechanisms to grow diamond are similar to the reactions envisioned to make diamond using nanotechnology. In chapter 3 we describe the simulations of hydrogen abstraction and carbon addition for making diamond using nanotechnology concepts.

Another disadvantage with the molecular mechanics approach is that the approximate method entirely depends on (c) the availability of a force field. Assuming the force field has been developed, (d) it may not be transferable to the system under study. That is, although the force field may model experimental properties of one system well, it may break down when transferred to a similar system. Additionally, (e) there may not be sufficient experimental properties to determine an accurate potential through an empirical fit. We use the Biased Hessian Method of Dasgupta and Goddard¹² for developing force fields for molecules to overcome (c) and (d). The Biased Hessian Method increases the number of constraints on a force field by requiring it to fit the vibrational frequencies, *and* also the normal modes which are the *ab initio* vibrational eigenvectors. The force field is obtained by minimizing an error function which depends on the fit to the normal modes, the experimental frequencies and the *ab initio* normal modes.

In the simulation of (i), Si surface reconstructions and (vi), polysilane polymers we are faced with systems for which insufficient experimental information exists to apply the Biased Hessian method in the standard way. In the case of Si (111) surface reconstruction, clusters needed to model the surface have not been experimentally detected. In the case of developing force fields for polysilane polymers,

the experimental vibrational frequencies are incomplete for some of the oligomers needed to develop the atomic potentials. Therefore in these cases the biased Hessian method cannot be used to develop a force field that reproduces the experimental information, since the experimental information currently does not exist. In chapter 6 we describe a method based on developing scales that describe the ratio of the force constants fit to experimental frequencies to force constants that were fit to the *ab initio* frequencies. We then describe how we apply these scales to the force field for the experimentally unobserved cluster by applying the scales to the FF fit to *ab initio* frequencies. We then apply this scaled force field to study the reconstructions of the Si (111) surface. Chapter 4 describes how (e), the lack of experimental information was over come to simulate (vi), polysilane polymers. Crystalline polysilane is not experimentally studied, because no crystalline samples have been prepared. We developed force fields for the $\text{Si}_n\text{H}_{2n+2}$ oligomers which can then be used on the extended, periodic system. However, the set of experimental frequencies is incomplete for Si_3H_8 and $n\text{-Si}_4\text{H}_{10}$. Consequently, we develop a scaling method which uses scales between experimental *frequencies* and *ab initio frequencies*. The scales are averages of these ratios for a particular class of vibrations within each molecule. If one of the modes within that class is not experimentally known, then we apply the scale from that class and molecule to the *ab initio* frequency of that mode. These scaling methods are thought to be accurate since the standard deviation of the ratios within each molecule is very small. We test the method by applying the force field to larger oligomers of polysilane and comparing to the scaled *ab initio* frequencies. The $n\text{-Si}_4\text{H}_{10}$ potential is then applied to the polysilane crystal.

Polymers are simple molecular extensions of oligomers and application of a force field from an oligomer to the extended system is expected to include the important physics that determines the material's properties. On the other hand, crystalline systems that are not molecular crystals, for example the diamond and zinc-blende crystals cannot be treated this way. To simulate the semiconductor (iv), materials we need to develop force fields directly for periodic systems. Our

molecular mechanics simulations of (i), Si (111) surface reconstructions (ii), growth of CVD diamond and (iv), semiconductor interfaces and superlattices involves combining bulk potentials with atomic interactions that either model the surface configurations, the interface configurations, or a surface chemical reaction. We develop potentials to model periodic systems, specifically (iii), the semiconductor crystals using a method similar to the Biased Hessian approach. In the periodic case, we do not use a normal mode description (although this will soon be possible). We fit to the special points in the Δ direction of the phonon dispersion curve and to the elastic constants. To complete the force field to simulate (iv) we use an extrapolation scheme to extend the potentials from the group IV, III/V or II/VI crystals to include terms necessary to describe the interfaces between various combinations of the materials. We describe our work on semiconductor force fields, interfaces and superlattices (iii and iv), in chapter 5.

2.0 References

1. K. E. Khor and S. Das Sarma, Phys. Rev. B **40**, 1319 (1989).
2. D. Vanderbilt, Phys. Rev. B **36**, 6209 (1987).
3. H.-X. Wang and R. P. Messmer, Phys. Rev. B, **41**, 9241 (1990).
4. Bauschlicher, C. W. and Langhoff, S. R., Chem. Phys. Lett., 135, 67, (1987); Taylor, P. R. and Partridge, H., J. Phys. Chem., 91, 6148, (1987). For an excellent review see Bauschlicher, C. W., Langhoff, S. R., and Taylor, P. R., Adv. Chem. Phys., 77, 103, (1990).
5. W. Pickett, H. Krakauer and P. Allen, Phys. Rev. B**38**, 2721 (1988).
6. J. Ihm and M. Cohen, Phys. Rev. B**21**, 3754 (1980).
7. C. B. Musgrave, J. K. Perry, R. C. Merkle, and W. A. Goddard III, Nanotechnology **2**, 187 (1991).
8. S. L. Mayo, B. D. Olafson and W. A. Goddard III, J. Phys. Chem. **92**, 7488 (1990).
9. H. Q. Ding, N. Karasawa, and W. A. Goddard, J. Chem. Phys., **97**, 4309 (1992).
10. R. E. Donnelly, C. B. Musgrave, and W. A. Goddard III, to be submitted.
11. C. B. Musgrave, R. E. Donnelly, and W. A. Goddard III, to be submitted.
12. S. Dasgupta and W. A. Goddard III, J. Chem. Phys. **90**, 7207 (1989).

Chapter 1

Review of Methods

1.0 Review of Methods

This chapter gives a brief review of the methods used in this thesis, including *ab initio* methods, molecular mechanics, and the Biased Hessian method.

1.1 Review of *Ab Initio* Quantum Chemistry Methods

Ab initio quantum chemistry theory is used to find approximate solutions to the electronic Schrödinger equation

$$\mathcal{H}\Psi = E\Psi \quad (1)$$

for the *electronic wave function* Ψ , where the Hamiltonian of the system is given by

$$\mathcal{H} = \frac{-\hbar^2}{2m} \sum_{i=1}^n \nabla_i^2 - \sum_{A=1}^M \sum_{i=1}^n \frac{Z_A e^2}{r_{iA}} + \sum_{i=1}^n \sum_{j>i} \frac{e^2}{r_{ij}}. \quad (2)$$

Here the first sum includes the kinetic energy of the electrons, the second sum includes the Coulombic interaction between the electrons and nuclei and the third sum includes the Coulombic interactions of the electrons with each other. Z_A are the nuclear charges, n the number of electrons and M the number of atoms in the molecule. In (2) we have ignored the nuclear kinetic energy since the nuclei are assumed to be at rest relative to the motion of the electrons. This approximation works well in practice and is called the Born-Oppenheimer approximation. The Coulombic interactions between the nuclei themselves are also not included since they remain constant with the assumption of fixed nuclei. The wave function will then be a function of the electron coordinates and only parametrically dependent on the nuclear coordinates. To generate a potential energy surface one calculates the wave function energy at various input nuclear coordinates. To calculate the forces on the molecule, one takes derivatives with respect to the nuclear coordinates. To calculate a Hessian, one computes the matrix of second derivatives and to extract the vibrational frequencies and eigenvectors one diagonalizes the Hessian.

The solution to the many-electron Schrödinger equation will be an antisymmetrized n -fold product of spin orbitals. Since electrons are Fermions they must

satisfy the Pauli principle which states that no two electrons can occupy the same spin orbital. This constraint on the solution is imposed by antisymmetrizing the wave function by making Ψ a Slater determinant or sum of Slater determinants. Constructing wave functions from Slater determinants also insures that the electrons are indistinguishable.

1.2 The Hartree-Fock Wave Function

The simplest wave function which obeys the Pauli Principle and can describe the ground state of the electronic Hamiltonian is, of course the single determinant Ψ . The single determinant Ψ that best approximates a solution to (1) is called the Hartree-Fock wave function. Now

$$\Psi^{HF} = \mathcal{A} [\psi_a(1)\psi_b(2) \cdots \psi_z(N)] \quad (3)$$

can be varied until it solves (1), the HF solution. This is done by applying the variation principle which states that the best description of the wave function is the one that minimizes the energy. To apply this in practice involves introducing parameters which vary the shape of the spin orbitals. The most common way of doing this is by using a set of atomic orbitals ϕ_μ on each of the atoms as a basis for describing the spatial portion of the spin orbitals. Each basis function, in this case a fixed atomic orbital, is mixed into the spin orbital by an amount determined by its orbital coefficient, $C_{\mu i}$:

$$\psi_i(\mathbf{r}) = \sum_{\mu=1}^K C_{\mu i} \phi_\mu(\mathbf{r}). \quad (4)$$

Increasing the size of the basis set allows us to better describe the electronic orbitals, however at a greatly increased computational cost. It is best then to be judicious in the basis set expansion, including sufficient functions so as to accurately describe the wave function, but not so many terms as to make the calculation too costly. Usually these types of calculations follow the law of diminishing returns as each additional basis function of a wisely chosen basis set improves the description of Ψ less than the preceding function.

Applying the variational principle by minimizing the expectation value of the energy

$$E = \langle \Psi^{HF} | \mathcal{H} | \Psi^{HF} \rangle \quad (5)$$

with respect to the set of coefficients $C_{\mu i}$ leads to a pseudo-one particle equation

$$H^{HF} \psi_i = E_i \psi_i \quad (6)$$

where

$$H^{HF} = h + \sum_j (2\hat{J}_j - \hat{K}_j) \quad (7)$$

includes a sum over the Coulomb (J_j) and exchange (K_j) interactions with the other particles. The one electron operator \hat{h} is a function of the coordinates of only one electron. It therefore includes the electronic kinetic energy and the Coulombic interactions between the electrons and the nuclei. Equation (6), known as the Hartree-Fock equation is in eigenvalue form. The operator H^{HF} is known as the Fock operator. The spin orbitals are the eigenfunctions and the energies of the spin orbitals are the eigenvalues. The spin functions ψ_i are expansions of the basis functions, so the HF equation can be transformed into a matrix equation by multiplying (6) on the left by $\phi_\mu(1)$ and the appropriate spin function, substituting in (4), and integrating. This leaves

$$\sum_\nu^K C_{\nu i} \langle \phi_\mu(1) | H^{HF}(1) | \phi_\nu(1) \rangle = E_i \langle \phi_\mu(1) | \phi_\nu(1) \rangle. \quad (8)$$

The matrix

$$S_{\mu\nu} = \langle \phi_\mu(1) | \phi_\nu(1) \rangle \quad (9)$$

is defined as the overlap matrix and the matrix

$$F = \langle \phi_\mu(1) | H^{HF}(1) | \phi_\nu(1) \rangle \quad (10)$$

is called the Fock matrix. We also define the matrix of expansion coefficients \mathbf{C} and the diagonal matrix \mathcal{E} of eigenvalues E_i which are the orbital energies. So

integrating the HF equations and using the above definitions allows us to write the equation

$$\mathbf{FC} = \mathbf{SC}\mathcal{E}. \quad (11)$$

This matrix equation is known as the Roothaan equation. The matrices are of size $K \times K$, where K is the number of basis functions so the time required to solve such an equation grows rapidly with K . Since the Fock operator of the HF and Roothaan equations depends on the eigenfunctions through the Coulomb and exchange operators, the equations are nonlinear. This makes it necessary to use an iterative procedure to find solutions to (6) or (11).

1.3 The SCF Procedure

The iterative procedure used for solving these equations is known as the self consistent field (SCF) procedure. First to minimize the energy we require that the first order variation of the energy with respect to orbital variation be zero. We expand the energy to second order in changes to the orbitals and derive

$$\sum_i \langle \delta\phi_i | F_i | \phi_i \rangle = 0 \quad (12)$$

where variations in the orbitals are restricted to be orthogonal to the orbital being varied. The SCF procedure involves setting the shape of all the spin orbitals at a starting guess value by estimating \mathbf{C} . This defines the Hartree-Fock potential for this starting guess wave function and we can obtain the new expansion coefficients and orbital energies by diagonalizing the Fock matrix. If the new expansion coefficients are the same as the original ones, then the wave function is converged. If they are significantly different then we use the orbitals described by this intermediate \mathbf{C} to start the procedure over again and repeat until self-consistent. The n lowest energy spin orbitals are occupied and the $2k-n$ remaining orbitals are unoccupied and referred to as virtual orbitals. The Hartree-Fock method does not allow the electrons to dynamically correlate their motions because they interact with each other only in an average way. This approximation makes HF very fast

and still capable of describing many processes reasonably well. On the other hand, many physical properties will be poorly described, for example the dissociation of bonds. Because the electrons do not correlate their motions dynamically, as a bond breaks upon atom separation, the electrons continue to doubly occupy the bonding orbital, which becomes nonbonding as the bond breaks. What is required is that the doubly occupied orbital that describes the bond of the molecule become two singly occupied nonoverlapping orbitals of the fragments. So near equilibrium HF describes the ground state relatively well, but it poorly describes strains, bond dissociation, excited states, chemical reactions, etc. Furthermore, this deficiency leads to overestimates in the HF vibrational frequencies, typically 10 to 20% too large.

Much of quantum chemistry research has been devoted to improving upon HF by including additional electron correlation. The inclusion of additional correlation leads to a series of improved theories, all using HF as their starting point. These include the Generalized Valence Bond¹ (GVB), Complete Active Space SCF² (CASSCF), Configuration Interaction (CI), Multi Reference CI (MRCI), Multiconfiguration SCF (MCSCF), and second order Møller-Plesset perturbation theory³ (MP2) wave functions.

1.4 Configuration Interaction Wave Functions

The HF wave function, and all wave functions that use it as a starting point explicitly include all of the electron-electron interactions in \mathcal{H} ,

$$\sum_{i>j=1}^N \frac{e^2}{r_{ij}} \tag{13}$$

but solve for the wave function in terms of a hierarchy of increasingly accurate solutions. The Hartree-Fock wave function was limited to a single determinant. Although HF satisfied the Pauli principle, there is no reason additional Slater determinants (electronic configurations) cannot be allowed to be included in the wave function. The configurations are obtained by replacing one or more of the occupied HF spin orbitals with unoccupied virtual orbitals. The resulting Slater determinant

is called an excited determinant. If one orbital is replaced, then the excitation is referred to as a single excitation, two orbitals replaced leads to a double excitation, etc. At this point we can do a series expansion for the ground state wave function in the Slater determinants to make what is known as the CI wave function

$$\Psi = C_0 \Psi_0 + \sum_{single} C_1 \Psi_1 + \sum_{double} C_2 \Psi_2 + \dots + \sum_{n-tuple} C_n \Psi_{n-tuple}. \quad (14)$$

As we include additional configurations, we can improve upon the description of the wave function, however the computational costs of determining the coefficients of the Slater determinants increases with the length of the series. Therefore, this series is usually truncated very early, for example at the double excitations in many cases, and even this leads to very large calculations for moderately sized molecules. The coefficients are solved for by applying the variational principle to the CI wave function and optimizing the configuration coefficients to minimize the energy of the system. The HF*SD CI wave function is an example of CI method that is truncated at the level of double excitations. Here all single and double excitations of the valence electrons are allowed into the virtual orbitals with reference to only the HF configuration.

1.5 MRCI Wave Functions

The MRCI wave function is similar to the CI wave function just described, except that rather than just including excitations of the valence electrons into the virtual orbitals from the HF determinant, we include valence excitations to the virtual orbitals with reference to other important configurations (references). If the CI wave function is not truncated, then the MRCI and CI wave functions are degenerate. However, since we truncate the CI series at doubles in most cases, the excitations from the references, which are excited Slater configurations themselves can contribute significantly to lowering the energy of the wave function. Allowing these extra references from which we can excite from greatly improves the CI description of transition states where several electronic states mix into the transition state wave function. For example, in the case of H transfer between methyls the

important configurations are the HF configuration, the antibond configuration with one node and the antibond configuration with two nodes. The GVB*SD CI wave function is a multireference CI that includes up to double excitations. This MRCI wave function is a high accuracy approximation to complete CI. The improvement over the HF*SD CI wave function for the description of transition states is shown in chapter 3. As the MRCI wave function is calculated on larger and larger systems a drawback is encountered in that the correlation energy included in the calculation decreases as the size of the system increases. For example, the MRCI energy of two infinitely separated molecules will be greater than the sum of the MRCI energies of the component molecules. This is because a greater fraction of the valence space is allowed to be excited in the smaller calculation where the larger calculation is restricted to a larger fraction by the truncation in the series. As the series of excitations is extended this effect becomes less important, but the expense of the calculation becomes prohibitively large.

Because MRCI calculations, from only a few references and truncated at the doubles level, can still be prohibitively expensive we have in some cases used smaller CI calculations which do a good job of approximating the results of GVB*SD CI.^{4,5} These wave functions restrict the orbitals from which excitations can be made. For example, in the correlation consistent CI (CCCI)⁶ wave function all single and double excitations of the active electrons (active electrons are those in orbitals that undergo significant change during a reaction, for example the electrons in a breaking bond) and all single excitations of the other valence electrons into the virtual space relative to the three GVB configurations are allowed (thus double excitations from the valence space is not allowed). Since double excitations from the valence space are so numerous and do not contribute to the correlation as significantly as the allowed excitations, the essential physics of a reaction is retained while greatly improving the cost of the calculation. An equivalent way of writing the CCCI wave function would be $\text{GVB}^*(\text{SD}_{\text{active}} + \text{S}_{\text{valence}})$.

A similar wave function, called the dissociation consistent CI (DCCI)⁷ wave

function can be constructed which allows double excitations which are the product of single excitations from the valence space with single excitations from the active space. When higher order excitations are allowed an even larger hierarchy of wave functions can be made. Often, the set of wave functions in this hierarchy are tested on a small system analogous to the one under study by comparing to experiment. We can then determine which of them best describes the phenomena of interest without being computationally expensive. In some cases a method may seem to give accurate results, although the quality of the results are fortuitous. Therefore care must be taken when using such a method. It is therefore often useful to apply the method to small model systems that are well understood or experimentally measured.

1.6 MCSCF Wave Functions

In addition to optimizing the configuration coefficients it is possible to re-optimize the orbital coefficients (therefore the orbitals from which you build the configurations are no longer confined to be the HF orbitals). This type of solution is referred to as a MCSCF wave function. Once the orbital's coefficients are reoptimized, then the configuration coefficients can be reoptimized until self consistency is obtained. This procedure allows one to obtain much of the correlation energy with far fewer configurations than a MRCI or CI. The CASSCF or GVBCI-SCF² wave function is an example of an MCSCF wave functions.

In the CASSCF wave function an active space is picked. This space consists of orbitals that vary significantly during the process being studied. For example, in the case of H transfer between methyls the active space would include the C-H-C orbitals along the symmetry axis with zero, one and two nodes. The electrons are the radical of the reactant, the radical of the product and the H electron. All symmetry and spin allowed configurations of these three active electrons in the three orbitals are generated. Thus a CASSCF makes no restrictions on the excitations the active electrons can make within the active space.

1.7 The Generalized Valence Bond Wave Function

Probably the simplest and most economical way of improving the HF wave function is the generalized valence bond wave function developed by Goddard and coworkers. A brief summary of the GVB approach as described by Bobrowicz¹ is given here to illustrate the method. The main aim of the GVB wave function is to describe bond dissociation properly. To remove the HF deficiency GVB allows bonds to be described by two singly occupied, overlapping orbitals which make up a GVB pair. This removes the condition HF imposes on the bonding orbital; that it remain doubly occupied during the dissociation process. The GVB pair can then be written as

$$\Psi_{pair} = \mathcal{A} [(\phi_1\phi_2 + \phi_2\phi_1) \alpha\beta] \quad (15)$$

where \mathcal{A} is the antisymmetrizer and where the overlap, S_{12} between the two orbitals describing the bond is not zero

$$S_{12} = \langle \phi_1 | \phi_2 \rangle \neq 0. \quad (16)$$

Each orbital is associated with one of the atoms participating in the bond. For example, ϕ_1 is localized on atom 1 and ϕ_2 on atom 2. As these orbitals are optimized to describe the bond properly their shape changes to describe the polarization of charge. For simplicity we focus here on the perfect pairing form of the wave function GVB-PP which has the form

$$\Psi = \mathcal{A} [\Psi_{core} \Psi_{open} \Psi_{pair}], \quad (17)$$

where

$$\Psi_{core} = \prod_{i=1}^{n_{core}/2} (\phi_i\alpha) (\phi_i\beta) \quad (18)$$

contains all doubly occupied orbitals in the core space of the molecule however, not the doubly occupied bonding orbitals. The function

$$\Psi_{open} = \prod_{i=1}^{n_{open}/2} (\phi_i\alpha) \quad (19)$$

is the product of all the singly occupied orbitals. To maximize the exchange interaction (Hund's Rule) the singly occupied orbitals will have the same spin. The core and open shell electrons are treated exactly as they are for the wavefunction.

$$\Psi_{pair} = \prod_{i=1}^{n_{pair}} (C_{gi}\phi_{ig}\phi_{ig} - C_{ui}\phi_{iu}\phi_{iu}) (\alpha\beta - \beta\alpha), \quad (20)$$

describes all GVB pairs. Here we have rewritten Ψ_{pair} so that the two orbitals which make up the spatial part of the bond are a linear combination of the symmetric bonding HF-like orbital and antisymmetric antibonding HF-like orbital. The symmetric orbital ϕ_{ig} of pair i is just the sum of $\phi_1 + \phi_2$, while the antisymmetric orbital ϕ_{iu} is the difference $\phi_1 - \phi_2$ and therefore has a node through the bond.

The general energy expression for GVB-PP wave functions is

$$E = \sum_i^{occ} 2f_i h_{ii} + \sum_{i,j}^{occ} (a_{ij} J_{ij} + b_{ij} K_{ij}) \quad (21)$$

where h , J , and K are the standard one-electron, Coulomb, and exchange energies. This expression for the energy is similar to the HF expression except that the coefficients of the Fock, Coulomb and Exchange energies are now functions of the pair coefficients C_{gi} and C_{ui} .

The coefficient of the Fock energy is called the orbital occupation coefficient f_i and given by

$$\begin{aligned} f_i &= 1 & i \text{ is a core orbital} \\ f_i &= \frac{1}{2} & i \text{ is an open orbital} \\ f_i &= (C_i)^2 & i \text{ is a pair orbital with pair coefficient } C_i. \end{aligned} \quad (22)$$

The coefficients for the two-electron Coulomb and exchange operators can be written as

$$a_{ij} = 2f_i f_j$$

$$b_{ij} = -f_i f_j$$

except that

$$\begin{aligned}
 b_{ij} &= -\frac{1}{2} && \text{if } i \text{ and } j \text{ are both open orbitals} \\
 a_{ii} &= f_i && \text{if } i \text{ is a pair orbital} \\
 b_{ii} &= 0 && \text{if } i \text{ is a pair orbital} \\
 a_{ij} &= 0 && \text{if } i \text{ and } j \text{ are in the same pair} \\
 b_{ij} &= C_i C_j && \text{if } i \text{ and } j \text{ are in the same pair.}
 \end{aligned}$$

With the energy expression (21), the general condition for convergence is that the first-order change in the energy due to orbital changes be zero, leading to

$$\sum_i \langle \delta\phi_i | F_i | \phi_i \rangle = 0, \quad (12)$$

where F_i is the generalized Fock operator for orbital ϕ_i ,

$$F_i = f_i \mathbf{h} + \sum_j^{occ} a_{ij} \mathbf{J}^j + b_{ij} \mathbf{K}^j, \quad (23)$$

Since F_i depends on the orbitals, this equation is nonlinear and we solve for (12) iteratively until self-consistency is achieved.

1.8 Summary

The preceding review of *ab initio* quantum chemistry methods illustrates the type of calculations that are done on small molecules. Many other methods have been developed to be more accurate or faster. Often however, these methods have deficiencies which make them inappropriate for application to certain classes of problems. The various semi-empirical methods for example are very fast, and work well for unstrained molecules. However, in the case of transition states or strained systems the method gives highly inaccurate results. The pseudospectral methods were also developed to be much faster than standard QC methods. These methods however have so far proven very accurate for the systems studied. An exhaustive review of the methods available today would span many large volumes and because

this review is only meant to cover some introductory material we stop our review of *ab initio* methods here.

2.0 Review of Molecular Mechanics

A molecular mechanics calculation begins by defining the coordinate information of a given list of atoms. The form of the atomic potential used in this thesis also requires that a list of the bonds in the system be specified. Given the coordinate and coordination information the program (MSI/Polygraf)⁸ makes a list of all bond, angle, dihedral torsions, cross, and non-bond interactions. Each interaction is classified by the atom types involved and an energy term is assigned for that interaction. The molecular mechanics energy can then be calculated by summing this series of energy terms and the properties of the system can be calculated from the energy function. The energy of the system and thus the system properties are functions of the spring constants in each valence term of the energy expression.

2.1 Form of the Force Field

In some molecular mechanics methods the potential is only dependent on the atom type, and geometry. Thus the coordination must be determined implicitly from the geometry. In the valence form of the potential the valence interactions are determined based on the connectivity input, thus atoms with equivalent nuclei, but with different coordination numbers have different force constants and thus different functions describing their interactions with other atoms, while in the nonvalence form they have the same force constants. The advantage to the valence method is that it greatly simplifies the functional form of the potential and facilitates physical understanding of the calculation. The general form of the force field⁹ we use is

$$E = E^{val} + E^Q + E^{vdw}, \quad (1)$$

where E^{val} includes all terms involving bonds and angles where E^Q describes electrostatic interactions, and E^{vdw} describes the van der Waals nonbond interactions.

The valence term is taken as

$$E^{val} = E^{bond} + E^{angle} + E^{cross} + E^{torsion} \quad (2)$$

which includes all terms involving bonds between atoms and the coupling of these bonds. When the notation MSXX is used to label the force field it indicates that both one-center and two-center cross terms are included, the MS stands for materials simulations.

2.2 Electrostatics

The electrostatic term is written as

$$E^Q = C_{coul} \sum'_{i>j} \frac{q_i q_j}{R_{ij}} \quad (3)$$

involving partial charges q_i (in units of the electron charge, $|e|$) on the various atoms. [Here $C_{coul} = 332.0637$ ensures that energies are in kcal/mol with distances in Å.]

2.3 van der Waals

The van der Waals (vdW) potential represents the long-range attraction (London dispersion) and short-range repulsion (Pauli orthogonalization of non-bonded electrons). Such terms are often ignored in force fields (their effects being embedded in valence terms).

The vdW interactions are described with the Lennard-Jones 12-6 form

$$E^{vdw} = \sum'_{i>j} D_{ij}^{vdw} [\rho_{ij}^{-12} - 2\rho_{ij}^{-6}], \quad (4a)$$

where

$$\rho_{ij} = \frac{R_{ij}}{R_{ij}^{vdw}}. \quad (4b)$$

In addition we assumed the standard combination rule

$$R_{ij}^{vdw} = \sqrt{R_{ii}^{vdw} R_{jj}^{vdw}} \quad (5a)$$

$$D_{ij}^{vdw} = \sqrt{D_{ii}^{vdw} D_{jj}^{vdw}}. \quad (5b)$$

2.4 Nonbond Exclusions

The summation over i and j in (3) and (4) *excludes* bonded atoms [1-2 cases] and next-nearest neighbors [1-3 cases]. It is assumed that these interactions (which would be partially shielded) are included in the valence interaction terms for bonds and angles, respectively. We found that the next-next-nearest neighbors [1-4 cases] are very important in determining the lattice constant and include them plus all longer interactions.

2.5 Bond Terms

We take E^{bond} as a sum over all bond pairs where each has the form of a Morse function,⁹

$$E^{Morse}(R) = D_e [\chi^2 - 2\chi] \quad (6)$$

with

$$\chi = e^{-\alpha(R - R_e)} \quad (7)$$

and

$$\alpha = \sqrt{\frac{k_R}{2D_R}}. \quad (8)$$

This describes anharmonicity and allows a proper description of bond dissociation. There are three independent parameters R_e , k_R , and D_R ; however D_R is not sensitive to the data used in the fits.

2.6 Angle Terms

For each atom J there are six angle terms $I - J - K$. The functional form for the diagonal angle term is taken as⁹

$$E^{cosine}(\theta) = \frac{C}{2} [\cos \theta - \cos \theta_e]^2, \quad (9)$$

where the force constant is

$$k_\theta = \left(\frac{\partial^2 E}{\partial \theta^2} \right)_{\theta_e} = C \sin^2 \theta_e. \quad (10)$$

This form (9) leads correctly to $dE/d\theta = 0$ for $\theta = 0, 180^\circ$ and has a barrier of

$$E_\theta^{barrier} = \frac{C}{2} [1 + \cos \theta_e]^2. \quad (11)$$

2.7 Angle Cross Terms (1-Center)

For each angle term $I - J - K$, we include in E^{cross} the couplings between the bonds ($IJ - JK$) and the coupling between each bond and the angle (IJ with IJK and JK with IJK). These have the form of⁹

$$E_{RR} = K_{RR} (R_1 - R_{1e}) (R_2 - R_{2e}), \quad (12)$$

where R_1 is the $I - J$ distance and R_2 is the $J - K$ distance and

$$E_{R\theta} = D_{R\theta} (R - R_e) (\cos \theta - \cos \theta_e), \quad (13)$$

where there are two terms, one for $R = R_{IJ}$ and the other for $R = R_{JK}$. $D_{R\theta}$ is related to the force constant as

$$k_{R\theta} = \left(\frac{\partial^2 E_{R\theta}}{\partial R \partial \theta} \right)_{R_e, \theta_e} = -D_{R\theta} \sin \theta_e. \quad (14)$$

2.8 Torsion Terms

Consider the bond $J - K$. The dihedrals involving various atoms I bonded to J and L bonded to K are given the energy dependence described by⁹

$$E^{tor} = \frac{1}{2} V_{tor} [1 + \cos m\phi], \quad (15)$$

where ϕ is the dihedral angles ϕ_{IJKL} . This has minima (with zero energy) for $m\phi = 180^\circ$, and maxima (with energy V_{tor}) for 0° (cis), and $m\phi = 360^\circ$. We sum (16) over all $D_{IJ} = (C_I - 1) \times (C_J - 1)$ dihedral terms, where C_i is the coordination number of atom i , and divide by D_{IJ} so that V_{tor} is the total barrier.

2.9 Additional Cross Terms

For two angles sharing a common bond and apex, the one-center angle-angle cross terms has the form⁹

$$E_{\theta\theta 1} = F_{\theta\theta} (\cos \theta_1 - \cos \theta_{1e}) (\cos \theta_2 - \cos \theta_{2e}). \quad (16)$$

The two-center angle-angle cross term involves the coupling between two angles sharing a common bond, but not a common apex,⁹

$$E_{\theta\theta 2} = G_{\theta\theta} (\cos \theta_1 - \cos \theta_{1e}) (\cos \theta_2 - \cos \theta_{2e}) f(\phi), \quad (17a)$$

where the force constant is

$$k_{\theta\theta 2} = \left(\frac{\partial^2 E_{\theta\theta 2}}{\partial \theta_1 \partial \theta_2} \right)_{\theta_{1e}, \theta_{2e}} = G_{\theta\theta} \sin \theta_{1e} \sin \theta_{2e} f(\phi_e). \quad (17b)$$

Thus for a sequence of four bonds, $I - J - K - L$, $\theta_1 = \theta_{IJK}$, and $\theta_2 = \theta_{JKL}$. For a given $J - K$ there are D_{IJ} possibilities.

2.10 Vibrational States Periodic Systems (Phonons)

Using the above force constants to build an energy expression allows us to manipulate the energy to calculate system properties. This section describes the general concepts necessary to compute phonon dispersion curves. The detailed substitutions of the derivatives of the energy etc. are straightforward, although often tedious.

Consider the energy expanded near equilibrium, these calculations expand

$$R_i - R_i^e + \delta R_i \quad (18)$$

$$E(R_i) = E(R_i^e) + \sum_i (E'_i)_e \delta R_i + \frac{1}{2} \sum_{i,j} (E''_{ij})_e \delta R_i \delta R_j. \quad (19)$$

Here the force at equilibrium is zero

$$F_i = - (E'_i)_e = - \left(\frac{\partial E}{\partial R_i} \right)_e = 0 \quad (20)$$

and

$$(E''_{ij})_e = \left(\frac{\partial^2 E}{\partial R_i \partial R_j} \right)_e = \Phi_{ij} \quad (21)$$

is the Hessian.

Newton's equation of motion becomes

$$M_I \frac{d^2 [\delta R_{\alpha I}(t)]}{dt^2} = - \sum_{\beta J=1}^{3N} \Phi_{\alpha I, \beta J} [\delta R_{\beta J}(t)], \quad (22)$$

where α and β are the x, y, z components of the atomic coordinates and $I, j = 1, \dots, N$. Assuming periodic motion with frequency ω ,

$$\delta R_{\alpha I}(t) = \delta R_{\alpha I}^0 e^{i(\mathbf{k} \cdot \mathbf{R} - \omega t - \phi)} \quad (23)$$

leads to the eigenvalue equation

$$\omega^2 M_I (\delta R_{\alpha I}^0) = \sum_{\beta J} \Phi_{\alpha I, \beta J} (\delta R_{\beta J}^0) e^{i \mathbf{k} \cdot (\mathbf{R}_{\beta J} - \mathbf{R}_{\alpha I})}. \quad (24)$$

For the Γ point this leads to the eigenvalue equation

$$\bar{\Phi} \bar{\mathbf{U}} = \bar{\mathbf{U}} \lambda, \quad (25)$$

where

$$\bar{\Phi}_{\alpha I, \beta J} = \frac{\Phi_{\alpha I, \beta J}}{\sqrt{M_I M_J}} \quad (26)$$

$$\lambda_{ij} = \delta_{ij} C_{freq}^2 \omega_i^2 \quad (27)$$

(with ω in cm^{-1} , mass in atomic mass units, R in \AA , and energy in kcal/mol, then $C_{freq} = 108.5913$) and

$$\bar{U}_{\alpha I, j} = \sqrt{M_I} (\delta R_{\alpha I, j}^0) \quad (28)$$

describes the j^{th} vibrational mode.

3.0 The Biased Hessian Method

The calculation of properties using molecular mechanics methods depends on the quality and availability of a force field. Often a force field is applied to a

system only to find that it is inadequate for the phenomena of interest. At this point it is necessary to acquire an improved force field. One way to do this is to use the Biased Hessian method of Dasgupta and Goddard.¹⁰

The energy expression of a molecule can be expanded as:

$$E(X_1 \dots Z_N) = E_0 + \sum_{i=1}^{3N} \left(\frac{\partial E}{\partial R_i} \right)_0 (\delta R_i) + \frac{1}{2} \sum_{i, j=1}^{3N} \left(\frac{\partial^2 E}{\partial R_i \partial R_j} \right)_0 (\delta R_i)(\delta R_j) + \dots \quad (29)$$

where the force on the i^{th} component is:

$$F_i = - \frac{\partial E}{\partial R_i}, \quad (30)$$

and

$$H_{ij} = \frac{\partial^2 E}{\partial R_i \partial R_j} \quad (31)$$

is the Hessian. From *ab initio* HF wave functions we calculate¹¹ a full Hessian

$$H_{\alpha i, \beta j}^{HF} = \frac{\partial^2 E^{HF}}{\partial R_{\alpha i} \partial R_{\beta j}}, \quad (32)$$

where $R_{\alpha i}$ is the α component (x, y, z) of the coordinates of atom i . After mass weighting,

$$\bar{H}_{\alpha i, \beta j}^{HF} = \frac{1}{\sqrt{M_i M_j}} H_{\alpha i, \beta j}^{HF}, \quad (33)$$

the vibrational modes $\{\mathbf{U}_i^{HF}\}$ and vibrational frequencies $\{\nu_i^{HF}\}$ are obtained by solving

$$\bar{\mathbf{H}}^{HF} \mathbf{U}_i^{HF} = \mathbf{U}_i^{HF} \lambda_i^{HF}, \quad (34)$$

where

$$\lambda_i^{HF} = (C_{freq} \nu_i^{HF})^2 \quad (35)$$

and $C_{freq} = 108.5913$ converts units so that energies are in kcal/mol, distances are in Å, frequencies are in cm^{-1} , and masses are in atomic mass units (C^{12} has mass = 12.0000 amu). This Hessian provides an enormous number of constraints

useful in determining the force field. Thus there are $g(g + 1)/2$ independent pieces of information [for example, 666 for Si_4H_{10}], where $g = 3N - 6$ is the number of degrees of freedom. In contrast, fitting just the frequencies leads to only g conditions [36 for n- Si_4H_{10}]. However, at the HF level the calculated frequencies, ν_i^{HF} , are 10-20% too high. This led to the development of the Hessian Biased method⁶ for FF parameterization in which the force field is fit to the biased Hessian

$$H^{HB} = U^{HF} \lambda^{exp} \tilde{U}^{HF}, \quad (36)$$

where \tilde{U} is the transpose and λ^{exp} is the diagonal matrix based on experimental frequencies

$$\lambda_i^{exp} = (C_{freq} \nu_i^{exp})^2. \quad (37)$$

This Hessian has the property that, $H^{HB} U^{HF} = U^{HF} \lambda^{exp}$, that is, the eigenvalues match experiment (or a combination of experimental frequencies and scaled *ab initio* frequencies) while the eigenfunctions match HF theory. Thus, H^{HB} has the best available information on the vibrational modes. The method does require accurate mode assignments.

To optimize the force field we minimize the error function

$$ERR = W_{geom} \sum_{i=1}^{3N} (\delta E'_i)^2 + W_{hess} \sum_{i \leq j=1}^{3N} (\delta E''_{ij})^2 + W_{strs} \sum_{i=1}^6 (\delta \Sigma_i)^2 + W_{cij} \sum_{i < j=1}^6 (\delta C_{ij})^2, \quad (38)$$

where δ denotes the difference between the quantities calculated from the force field and the reference values from experiment (N is the number of atoms). Here E'_i is the energy gradient (negative force, which should be zero for each atom), and E''_{ij} is the second derivative of the energy (Hessian). For periodic cases we ignore the Hessian and include Σ_i , which is the lattice stress (6 independent values of which should be zero), and C_{ij} , the elastic constants (3 independent values for cubic crystals).

The Hessian term is transformed to the eigenvalue form and replaced by

$$W_{freq} \sum_{i=1}^{3N} (\delta\nu_i)^2 + W_{offdiag} \sum_{i < j=1}^{3N} (\delta H_{ij})^2. \quad (39)$$

In general the optimum geometry at the HF level differs slightly from experiment, raising the question as to which structure is used in (10). We use the structures optimized at the Hartree-Fock level of theory. Previously¹² we advocated the use of the experimental structure for determining force constants from the *ab initio* calculations primarily because the internuclear separations (which strongly affect the Hessian) reflect the experimental system. However, in molecules with low frequency torsions, a slight difference in structure can cause a noticeable rotational contamination of the torsional modes. Since we want to use frequency scaling parameters to compare various molecules, it is better to derive the frequencies for all molecules at the *ab initio* minima (rather than at the experimental minimum for molecules where experimental geometries are available and the *ab initio* minimum for those where experimental geometries are not available). Fortunately, the differences between the *ab initio* and experimental geometries are small.

4.0 References

1. Bobrowicz, F. W. and Goddard, W. A. in Methods of Electronic Structure Theory (Ed. Schaefer, H. F.), 79, 1977.
2. Smith, D. and Goddard III, W. A., *J. Am. Chem. Soc.* **109**, 5580 (1987).
3. C. Møller and M. S. Plesset, *Physical Review*, **46**, 618 (1934).
4. C. B. Musgrave, J. K. Perry, R. C. Merkle and W. A. Goddard, III, *Nanotechnology* **2**, 187 (1991).
5. C. B. Musgrave, S. J. Harris and W. A. Goddard, III, to be submitted.
6. Carter, E. A. and Goddard, W. A., *J. Chem. Phys.*, **88**, 1752, (1988).
7. Carter, E. A. and Goddard, W. A., *J. Chem. Phys.*, **88**, 3132, (1988).
8. These calculations used POLYGRAF from Molecular Simulations Inc. (Burlington Mass).
9. S. L. Mayo, B. D. Olafson and W. A. Goddard III, *J. Phys. Chem.* **92**, 7488 (1990).
10. S. Dasgupta and W. A. Goddard III, *J. Chem. Phys.* **90**, 7207 (1989).
11. Gaussian86: M. J. Frisch, J. S. Binkley, H. B. Schlegel, K. Raghavachari, C. F. Melius, R. L. Martin, J. J. P. Stewart, F. W. Bobrowicz, C. M. Rohlfing, L. R. Kahn, D. J. Defrees, R. Seeger, R. A. Whiteside, D. J. Fox, E. M. Fleuder, and J. A. Pople, Carnegie-Mellon Quantum Chemistry publishing Unit, Pittsburgh,PA, 1984.
12. N. Karasawa, S. Dasgupta, and W. A. Goddard III, *J. Phys. Chem.* **95**, 3358 (1991).

Chapter 2

SR-SOR Step for Growth of CVD Diamond

Abstract

Recombination of a Surface-Radical with a Surface-Olefin (SR-SOR) to form a six-membered ring is a critical step in the current mechanism for chemical vapor deposition (CVD) growth of the diamond (100) surface. We compare the potential energy surfaces (PES) and activation barriers (E_{act}) calculated with various *ab initio* methods for the SR-SOR recombination step. The PES of SR-SOR- C_3H_7 is calculated at various levels of correlation to compare the resultant geometries of the reactant and transition states and to compare the topology of the PES. The *ab initio* calculations of the C_3H_7 PES include Hartree-Fock (HF), second order Møller-Plesset (MP2), Generalized Valence Bond-Configuration Interaction (GVB-CI or CASSCF) and GVB times singles and doubles CI (GVB*SD CI). We estimate the rate constant for SR-SOR by combining quantum chemistry calculations, molecular mechanics calculations, and transition state theory. The cluster models were corrected for steric interactions of the cluster with the rest of the surface and for strain effects on the lattice. We also compare the barrier and geometries obtained when using two different clusters; (i) C_3H_7 , and (ii) $C_{10}H_{15}$ to model the surface. HF and MP2 were used to model the reactants, and saddle point of the larger cluster modeling the surface. Our results show that the barrier calculated for the larger cluster was slightly lower than the barrier of the small cluster. The *ab initio* Hessian matrix was diagonalized to find the vibrational frequencies, which were used to construct a partition function for calculating the entropy. Transition state theory was used to obtain the rate constant, $k = 2 \times 10^{13} e^{-8800/RT} \text{ sec}^{-1}$. This implies that under normal growth conditions SR-SOR is fast compared with competing gas-surface reactions.

1.0 Introduction

Because of strong industrial interest in developing low pressure technologies for synthesizing diamond, there has been considerable effort in elucidating the fundamental mechanisms of diamond film growth.¹⁻³ The understanding of the kinetics and thermochemistry of carbon-hydrogen systems is so developed that it has been expected that chemical vapor deposition (CVD) of diamond could be understood at a level of detail far greater than that of most other CVD processes. The assumption usually made is that the gas phase reactions are a good analogue to reactions on a diamond surface. The assumption depends on whether the electronic rearrangement that occurs during reaction is local and to what extent the surface constrains the reaction. To calculate a rate constant for SR-SOR on this surface we combine several methods. The strategy is to use *ab initio* methods on small clusters where they are less expensive and where the accuracy in modelling the local electronic structure of the system is critical. Furthermore, molecular mechanics techniques were employed where they were most accurate and cost effective; in estimating the strain energies of the reaction on a lattice of approximately 500 atoms. This hybrid technique gives an alternative, more accurate method to semi-empirical methods when studying the energies of large systems where only a small portion is undergoing significant electronic structure rearrangement.

For tetrahedral electronic materials (Si, GaAs, ...) the (100) surface has generally been the surface of interest for commercial growth of thin films by CVD and MBE technology. Hence the mechanisms for diamond growth on this surface is of interest. Both AFM and STM measurements have established that the stable surface is hydrogen terminated with a 2×1 reconstruction as indicated in Figure 1a. A close-up of the 5-membered rings (denoted as C_5) is shown in Figure 1b. This C_5 ring must be opened and converted to a 6-membered ring (C_5 to C_6) during growth. Such a process is potentially rate determining, and hence an understanding of the mechanism is relevant. In this chapter we use *ab initio* quantum chemistry theory, molecular mechanics, and transition state theory to analyze the critical Surface

Radical-Surface Olefin Recombination (SR-SOR) step in the proposed mechanism, and we estimate its rate constant on the diamond surface.

A number of experiments have shown that methyl radicals are generally the dominant gas phase precursor species reacting with the surface to grow diamond,^{4–8} and several detailed chemical kinetics mechanisms have been proposed to analyze growth on various idealized diamond surfaces.^{9–16} For the most part, these models have relied on the assumption that a growing diamond surface behaves like an alkane and that the chemistry on diamond surfaces is controlled by the local electronic environment, as in alkanes. In addition to assuming behavior similar to that of alkanes, often rate constants for gas phase reactions have been used to predict the reaction rates of analogous reactions taking place on the growing CVD diamond surface. This assumption holds in most instances, however dynamical constraints imposed by the diamond surface restrict nuclear motions such that transition states can only be reached by straining the surrounding structure. Furthermore, several of these mechanisms rely on the ability of semi-empirical methods to predict transition state barriers.

Recently, Garrison et al.¹⁶ proposed dimer opening reactions for the (100)–(2×1):H diamond surface based on molecular dynamics simulations using Brenner’s hydrocarbon potential.¹⁷ These reactions form part of a complete chemical kinetics mechanism which can make quantitative predictions for the growth rates in hot filament, microwave plasma, flame and plasma jet CVD systems. The virtue of the Garrison mechanism is that it consists entirely of reactions which have well-known analogs in hydrocarbon chemistry, immediately making the mechanism plausible.

2.0 The Mechanism

- i.* The Garrison mechanism (Figure 2) commences with addition of a CH_3 radical to a surface radical site (Figure 2b to Figure 2c), forming the structure denoted as C_5M .
- ii.* The next step (Figure 2c to Figure 2d) is abstraction of a hydrogen atom

from the CH_3 group to make the radical denoted as C_5M^* .

- iii.* Through the β -scission electronic rearrangement (Figure 2d to Figure 2e), this structure isomerizes to another radical, denoted as C_{5d}^* . Here the dimer bond breaks and a double bond forms between the carbon atom (C_β) of the original structure and the carbon atom (C_α) that started as an adsorbed methyl (now the α -carbon of the olefin). Such unimolecular reactions are generally fast compared with bimolecular reactions.
- iv.* The final SR-SOR step in the mechanism (Figure 2e to Figure 2f) is intramolecular attack of the radical carbon (C_r) of C_{5d}^* with the C_α of the double bond. This leads to a 6-membered ring denoted as C_6^* , containing a radical site (C_β). It is this step that we examine herein.

Gas phase reactions involving radical attack at a doubly bonded carbon, such as



are typically very fast and proceed with almost no barrier. However, on the surface two factors considerably decrease the rate:

- i.* the initial equilibrium distance between the radical carbon, C_r , and the α -carbon, C_α , is 2.85 Å, almost twice the normal CC bond distance, and
- ii.* C_r is tightly constrained by the lattice from moving toward C_α , while C_α cannot move toward C_r without straining the $C_\alpha-C_\beta$ π -bond.

Although all the steps in the mechanism have analogous gas phase reactions, some of the reactions are modified by the strains introduced when putting these reactions on a surface. Thus, on the growing diamond surface the SR-SOR reaction step



could have a significant barrier. The question is whether the constrained SR-SOR reaction (6), is sufficiently slow on the diamond surface as to limit the rate of di-

amond formation. We concentrate on examining the critical step in the Garrison mechanism: the attack of the radical carbon of C_d^* at the CH_2 end of the double bond, leading to a 6-membered ring containing a radical. We refer to the radical carbon as C_1 , the α -carbon as C_2 and the β -carbon of the olefin as C_3 , as shown in Figure 3. We refer to the final step as the Surface Radical-Surface Olefin Recombination Step (SR-SOR).

In the gas phase the analogue of the SR-SOR ring closing step is the attack of an olefin by a methyl. Reactions involving radical attack at a doubly bonded carbon, such as



typically have almost no barrier. This reaction in particular proceeds with a very small barrier in the gas phase as the methyl is free to approach the olefin and the resulting σ -bond more than compensates for the breaking of the π -bond throughout the reaction. However, on the surface two factors may considerably increase the barrier. (i) The equilibrium distance between the radical carbon, C_1 and the α -carbon, C_2 is 2.85 Å, almost twice the normal CC bond distance; (ii) C_1 is tightly constrained by the lattice from moving toward C_2 , while C_2 , being the tail of the olefin cannot move toward the radical carbon without moving out of the plane defined by the double bond and the two sub-surface carbons below C_3 , straining or perhaps breaking the π -bond. Thus, on the surface the constraints imposed by the lattice force the reaction to proceed over a significant activation barrier. The surface does not allow the radical to freely engage the olefin and for the reaction to proceed the tail of the olefin must bend towards the radical. This process involves the straining of the π -bond without any significant contribution from the σ bond as it is too far away to stabilize the transition state. Barriers are the result of bonds dissociating while new bonds are only partially formed and thus unable to contribute enough to the stability of the system to make up for the energy to break the original bond. Because it is the bond dissociation process that is poorly described by more

approximate methods, the transition state is also poorly described. Because transition states are not well described by simple wave functions or by semiempirical wave functions that are parameterized to describe unstrained systems and thus do not adequately include the effects necessary to describe transition states it is important to determine what is the minimum level of correlation necessary to adequately describe various transition states to make quantitative predictions of reaction rates. In this chapter we compare the results of various *ab initio* quantum chemistry methods in predicting the barriers and PES of the critical Surface Radical-Surface Olefin Recombination (SR-SOR) step in the proposed mechanism. The questions we ask are; (i) what is the appropriate level of correlation necessary to accurately predict the PES and reaction barriers, (ii) what size cluster is needed to model the relevant parts of the surface and (iii) what are the characteristics of various methods that lead to the variation in reaction barriers.

3.0 Calculational Details

3.1.1 Ab Initio Quantum Chemistry

The simplest wave function used is the wave function in which each molecular orbital is doubly occupied (except the radical orbital). HF should give a qualitative picture of the SR-SOR reaction under study. HF will tend to over estimate reaction barriers since it generally over estimates stretching frequencies of bonds due to its poor description of the bond breaking process (a doubly occupied orbital of the molecule must become two singly occupied orbitals for the fragments). We can remedy this problem by removing the HF constraint that a bond be described with a single doubly occupied orbital. Additionally, wave functions needed to describe transition states can be significantly more complex than those needed to describe minima. HF, being a single determinant wave function precludes the contributions of important configurations along the reaction path. At the transition state, the electronic structure includes a resonance between the reactant and product states, which requires a multi-configuration wave function for proper description of the

partially broken bonds and partially formed bonds. Thus, to obtain more accurate potential energy surfaces for reactions such as (1) or (2) than HF, it is essential to include all important electron correlation effects that change during the reaction. For this purpose we use the GVB-CI method. GVB^{18,19} is the simplest wave function which describes bond dissociation properly, by allowing each bond to be described with two singly occupied, overlapping orbitals leading to a proper description of dissociation. In the GVB-CI method all electrons involved in bonds that change during the reaction are correlated, and all other pairs of electrons are calculated self consistently. For Reactions (1) and (2) there are three such electrons. For the reactant these correspond to the π -bond electrons and the radical electron of the α -carbon. In the product they correspond to the new $C - C$ σ -bond electrons and the radical electron on the C_3 . There are two ways to spin pair these three electrons (one corresponding to reactant and the other to the product) and the GVB-CI method calculates all orbitals self consistently (these three plus all other electrons) while optimizing the spin coupling. Simply, all symmetry- and spin-allowed configurations of three active electrons in three orbitals are generated. Although this wave function is an improvement on the description of the reaction by HF, it will still tend to over estimate the reaction barriers. After calculating the GVB-CI wave function, we then allow all single and double excitations from the three GVB-CI configurations to all possible virtual orbitals, which is called a GVB*SD CI. This calculation is rather computationally intensive and was not attempted for the larger $C_{10}H_{15}$ cluster. GVB*SD CI has been shown to accurately approximate the results of very complete CI calculations.²⁰

To describe the reaction path we considered 40 positions of the critical carbon, C_2 in the cluster shown in Figure 3. These points were selected to describe the reactant and saddle points (the exit channel was not examined, although the geometry and energy of the product, C_6^* was calculated). Calculations were carried out at the points (R_{12} , R_{23}) shown in Figure 4. R_{12} corresponds to the distance parallel to the surface from the initial position of C_2 , while R_{23} refers to the dis-

tance from the original position of C_2 perpendicular to the surface. We fixed C_1 , C_3 and the two hydrogens on C_1 and on C_3 representing the bulk atoms. Then for each value for R_{12} and R_{23} , we optimized the position of the other three hydrogens. This optimization was carried out at the MP2 level of Møller-Plesset perturbation theory.²¹ MP2 is based on the Hartree-Fock wave function and although through perturbations it can include additional electron correlation not included in HF, it may not include all the important electron correlation needed to describe transition states well. Hence, the energies and forces on C_1 , C_2 and C_3 may not be accurate in the transition region. However the $C - H$ bonds should be well described with MP2 and hence the H positions are expected to be accurate. For each such geometry (R_{12} and R_{23}) from MP2 we calculated the GVB-CI and GVB*SD CI energies, denoted GVB-CI_{MP2} and GVB*SD CI_{MP2} .

In addition to the calculations performed on the C_3H_7 cluster, we perform *ab initio* calculations on a larger cluster to estimate the effects of cluster size on the reaction barriers. The cluster consists of 10 carbon atoms and 15 hydrogens (as shown in Figure 1b), where the product is bicyclononane with a radical at one of the tertiary carbons. We consider only two geometries. (i) The reactant geometry and; (ii) The transition state geometry. In these calculations, the positions of C_1 , C_2 and C_3 and the hydrogen atoms bonded to these three carbon atoms were all optimized, which gives a better model of the relaxation on the surface than the smaller cluster. The remaining 7 carbon atoms and 12 hydrogen atoms were held fixed to model the lattice. This optimization was carried out at the MP2 level of Møller-Plesset perturbation theory.²¹ Using the MP2 optimized geometries we calculate the GVB-CI_{MP2} reactant and saddle point energies to obtain MP2 and GVB-CI_{MP2} barriers.

For all GVB calculations on the 3-carbon cluster we use the Dunning²² and Huzinaga²³ double ζ basis set plus diffuse s and p functions ($\zeta^s = 0.0474$, $\zeta^p = 0.0365$) plus one set of d polarization functions ($\zeta = 0.75$). The triple zeta contraction of the 6s set was used for hydrogens. The 6-31G** basis set was used for the

MP2 optimizations on the 3-carbon cluster while 6-31G* was used for the MP2 optimizations on the 10-carbon cluster. MP2 was performed using GAUSSIAN 92²⁴ on Hewlett Packard 730s. The HF, GVB-CI, and GVB*SD CI calculations on FPS 522 and CRAY YMP computers used the GVB²⁵ and MOLECULE SWEDEN Suites of programs.²⁶

3.1.2 Potential Energy Surface

Using the HF, GVB-CI_{MP2}, MP2 and GVB*SD CI_{MP2} energies versus the reaction coordinates we calculate the potential energy surfaces shown respectively in Figures 5a-d, with the reaction paths shown by the dashed curves. The reaction energy versus distance along the reaction paths are shown in Figures 6a-d. The barriers and transition state geometries are shown in Table 1. The calculated reaction barrier generally falls with increasing levels of correlation. Hartree-Fock (HF) leads to a barrier about a factor of two too high and to a poor location of the transition state geometry. The $E_{act} = 9.3$ kcal/mol from the GVB*SD CI is expected to be about 1 kcal/mol too high from residual errors due to incompleteness of the basis set and the CI expansion. Thus for the SR-SOR process, we obtain a corrected GVB*SD CI activation barrier of

$$E_{act}^{exact} \approx 8.3 \text{ kcal/mol.} \quad (3)$$

We calculated the zero point energy contribution to the vibrational adiabatic barrier by computing the MP2 vibrational frequencies at the transition and initial states. This adds 0.13 kcal/mol to the activation barrier, leading to

$$E_{cluster}^{act} \approx 8.4 \text{ kcal/mol.} \quad (4)$$

Table 2 lists the contributions to the energy barrier for the SR-SOR step.

3.2 Discussion and Results of Ab Initio Calculations

Table 1 lists the reaction barriers and geometries for the transition state from various levels of calculation on the C₃H₇ cluster. The calculated reaction barrier

falls with increasing levels of correlation, except for the MP2 case. Thus, $E_{act}^{HF} = 18.1$ kcal/mol, $E_{act}^{MP2} = 10.0$ kcal/mol, $E_{act}^{GVB-CI} = 10.5$ kcal/mol and $E_{act}^{GVB*SDCI} = 9.3$ kcal/mol. As expected, HF leads to a barrier much too high (by almost 10 kcals/mol) and to a poor location of the transition state geometry. This error is exponentiated in calculating the reaction rate and can lead to errors in the rate constant on the order of 100 at CVD diamond growth temperatures.

We find that the MP2 level of correlation leads to a good value for the barrier (higher than the GVB*SD CI by only 0.5 kcal/mol) and transition state geometry, but favors a shorter π -bond and a larger $C_1 - C_2$ distance in the initial state than the GVB-CI and GVB*SD CI levels by about 0.02 Å and 0.05 Å, respectively. Since for the GVB-CI_{MP2} and GVB*SD CI_{MP2} PES we use the positions of the three movable hydrogens calculated from the constrained MP2 geometry optimizations, the bias of MP2 towards a shorter π -bond in the initial state may leave moderate amounts of strain in these three hydrogen's positions. To determine the size of this effect and to further refine the transition state barriers, several single point energies were calculated for each of the three H degrees of freedom and fit to a quadratic at the transition and initial states. For each degree of freedom, we find that the MP2 geometry accurately describes the H angles for GVB-CI and GVB*SD CI at the the transition and initial states, despite its inaccuracy in predicting the position of C_2 for the initial state. The refined GVB*SD CI geometries, for example lead to a barrier only 0.1 kcal/mol less than the GVB*SD CI_{MP2} barrier. With the exception of HF, the transition state geometries change relatively little despite the changes in the reaction barriers. The transition state geometries predicted by all four methods keep the $C_2 - C_3$ π -bond and the plane of the adsorbed CH_2 group coplanar up through the transition state. This positions the tail of the olefin for attack by the radical while maintaining the π -bond and therefore leads to a rather gently sloping entrance channel. The accuracy of the MP2 barrier is considered fortuitous, and its ability to accurately approximate the GVB*SD CI barrier in general remains

undetermined.

The effects of cluster size were determined from *ab initio* calculations on a $C_{10}H_{15}$ cluster. We consider only two states. (i) The reactant geometry and; (ii) The transition state geometry. The two carbon atoms, C_1 and C_3 are allowed to optimize their positions, in contrast to C_3H_7 . Because these two carbon atoms change hybridization during the reaction they are expected to relax towards the surface from their positions in C_5 . However, the amount of relaxation is reduced because although the change in hybridization causes the relaxation, the constraint that each of the subsurface atoms already have 4 bonds reduces the increase in the order of the bonds of C_1 and C_3 with the sub-surface carbon atoms, thus reducing the strain imposed on the surrounding lattice. For the initial state of SR-SOR for example, the radical carbon would generally like to relax into the surface, increasing its bond order with the sub-surface carbons. However, orthogonality constraints between the p -orbital of the radical electron and bonds between the two sub-surface carbons and the surrounding lattice reduce relaxation into the surface. The MP2 geometry optimization results in moderate relaxation of C_1 and C_3 towards the surface, and increases in the distances between C_1 and C_3 and C_1 and C_2 from their positions in $C_d^*-C_3H_7$. The effect is larger for geometries where C_1 and C_3 have sp^2 character, and is reduced as these atoms change hybridization to sp^3 during the reaction. Thus, the relaxation towards the surface is largest for the reactant geometry and smaller for the transition state, although because the transition state maintains a large amount of sp^2 character on the surface carbons the effect is only slightly smaller for the transition state. The remaining 7 carbon atoms and 12 hydrogen atoms were held fixed, thus providing some estimate of the constraints of the lattice on the reaction barrier. The optimization results in an MP2 barrier for the reaction on this cluster of 11.2 kcal/mol. The approximately 1 kcal/mol increase in the barrier results in a reduction of the reaction rate by approximately 40 percent at 1200k, since rates depend exponentially on the barriers. The differences are attributed to the additional relaxation of the strains near the reacting part of

the cluster where hybridization changes are significant. In addition, portions of the surface which do not directly participate in the reaction, but which have significant changes in their electronic structure during the reactions, including a portion of the strain effects which were included in the molecular mechanics calculations on the smaller cluster are better estimated. The improvement in the model when $C - C - C$ bond angles of the surface are modeled by $C - C - C$ bond angles in the cluster, rather than $H - C - H$ bond angles, as in C_3H_7 allows for the improved description of the hybridization changes and also better models the strains in these bond angles.

Our results show that HF provides a poor description of the transition state. This is similar to the results seen with HF on other transition states. Previous work, for example showed that for hydrogen exchange reactions, HF greatly over estimates the experimental reaction barrier and barriers predicted by other more sophisticated techniques.²⁷ Their results show that HF over estimates the experimental results by approximately 250 percent (this includes some error due to the incompleteness of the basis set). Not only does HF greatly over estimate the barrier, but it also predicts a poor transition geometry. The over estimate of the barrier is reduced by including correlation with MP2, GVB, GVB-CI, and GVB*SD CI. Although the MP2 perturbation wave function is based on the HF wave function, it predicts a barrier and transition state very similar to that of GVB-CI and GVB*SD CI with the largest error being in the description of the initial state. Although its high-accuracy here is most likely fortuitous, the MP2 description of the reaction is much superior to HF and should generally be considered as the minimum level calculation necessary for quantitative prediction of reaction barriers. Even sophisticated, computationally expensive calculations like GVB*SD CI wave functions over estimate the barriers. Musgrave et al. showed the over estimate of GVB*SD CI in the hydrogen exchange reactions were still 10 to 20 percent too large (after taking into account the difference in zero point energy).²⁷ The effect is partially due to the incompleteness of the basis set and partially due to the incompleteness of the configuration expansion. The over estimate due to the truncation of the CI becomes more prominent as the

clusters studied become larger due to the size consistency problems of CI methods. We estimate that at the cluster size studied and the level of basis set used we over estimate the barrier by approximately 1 kcal/mol based on comparisons of GVB*SD CI results with experimental results on other systems.²⁷

Semi-empirical methods (e.g. MNDO) that are parameterized to describe stable molecules may also provide poor descriptions of transition states and reaction barriers. For example, Valone showed that these methods produced large errors in the reaction barrier for *H* transfer between two methyls.²⁸ Although semi-empirical methods are capable of modeling large systems, it is not recommended that they be used for modelling transition states where the approximations used for the methods become less valid. The most frequent hypothesis used in modeling CVD diamond growth kinetics has been that the chemistry of diamond is similar to that of analogous hydrocarbon molecules. For example, gas-surface rate constants for diamond growth have been taken more or less directly from gas phase data.^{11,12} This hypothesis has been verified experimentally for the *H* abstraction reaction from a diamond surface. In this work we examined a reaction between a radical and a π -bond. In the gas phase this reaction has hardly any barrier. However, in our case the reaction is subject to severe dynamical constraints introduced by putting it on the surface of the very rigid diamond lattice. Our results show that there is a significant difference in activation barriers between the reaction on the diamond surface and the analogous reaction in the gas phase. Thus, the analogy between diamond and the alkane hydrocarbons may in general be a better approximation for gas-surface reactions than for some surface-surface reactions, like SR-SOR. On the other hand, SR-SOR-like sites are present on the (111) surface, the reconstructed (110) surface and at steps. We can thus extend the results of the (100)-(2×1):*H* SR-SOR to approximate the nature of the transition states of other SR-SOR reactions. We conclude that the analogy is potentially very useful, but it must be used with considerable care.

3.3 Molecular Mechanics Calculations

Strain imposed on the lattice by the reacting surface species as calculated with molecular mechanics using the MSXX many-body force field fit to the diamond phonon dispersion curves and elastic constants.²⁹ To model the reaction we increased the cubic unit cell by a factor of 4 in the z direction and by factors of 5 in the x and y directions (leading to 800 atoms in the unit cell). We then cleaved the (001) surface,²⁹ leading to a slab which was then hydrogenated. The cluster atoms optimized in the quantum chemistry calculations were held fixed at the initial, final, and transition state geometries, while the remaining atoms of the slab were optimized.²⁹ Strains and steric interactions included in the *ab initio* cluster calculations were not included in the molecular mechanics energy to avoid double counting of this portion of the energy. The lattice strain energy (not including van der Waals interactions) and the van der Waals energy were calculated for the transition state and the reactant state. These energies do not include the interactions already included in the *ab initio* calculations on the cluster. The steric interaction with the surrounding lattice *decreases* in the transition state relative to the initial state. The strain imposed on the lattice at the transition state relative to the reactant state is calculated to add 0.73 kcal/mol to the barrier while the van der Waals interactions subtract 0.34 kcal/mol from the barrier. Thus the van der Waals and strain effects are small. The total of 0.39 kcal/mol adds to the net electronic structure barrier to yield a net

$$E_{act}^{surface} = 8.8 \text{ kcal/mol.} \quad (5)$$

Cell structure and atomic coordinates were updated at each optimization cycle. The atomic coordinates were optimized³⁰ using conjugate gradient techniques until the RMS force per degree of freedom was less than 0.01 (kcal/mol)/Å.

3.4 Transition State Theory

We determined the entropy change ΔS^\ddagger between reactants and the transition state from vibrational mode analyses that included the effects of the constraints on

the vibrational levels during the reaction. First, the Hessian (second derivative matrix) was calculated using MP2 theory at each geometry of the C_3H_4 cluster.²⁴ Next, the $3N - 6$ vibrational levels were calculated by diagonalizing the (mass-weighted) Hessian.³⁰ Finally, these energy levels were used to construct a partition function from which the entropy was calculated.³⁰ For the transition state the imaginary vibrational frequency was ignored.

The TST pre-exponential factor is given by

$$A = \left(\frac{ek_B T}{h} \right) e^{\Delta S^\ddagger / R}, \quad (6)$$

where $\ln e = 1$, k_B is the Boltzmann constant, T is the temperature, h is the Planck constant, R is the gas constant, and ΔS^\ddagger is the change in entropy between C_d^* and the transition state. We estimated the entropies for the initial, transition, and final states of reaction (6), leading to $\Delta S^\ddagger = -2.6$ cal/mol-K and

$$A = 5.6 \times 10^{12} \quad (7)$$

from equation (9).

Combining (4) with (8) leads to a total rate constant for SR-SOR of

$$k_{SR-SOR} = 5.6 \times 10^{12} e^{-8800/RT} \text{ sec}^{-1}. \quad (8)$$

The unimolecular reaction (6) on the diamond surface competes primarily with abstraction and addition reactions involving gas phase H atoms. To examine the relative importance of these competing gas phase reactions, we compare reaction (6) with reaction (12)



in which the radical site recombines with a gas phase H atom. At 1200K the characteristic time scale for (6) is $1/k_{SR-SOR} = 7 \times 10^{-12}$ sec. In contrast, assuming k_{12} is in the range³¹ 10^{13} to 10^{14} cm³/mole-sec with a H atom concentration³¹ of 10^6 to 10^{10} atoms/cm³, leads to characteristic time scales of 10^{-3} to 10^{-8} sec.

Thus the SR-SOR reaction is 10^4 to 10^9 times faster than other steps in the growth process, indicating that it does not affect the rate of diamond growth in the Garrison mechanism.

4.0 Conclusion

Different levels of correlation predict reaction barriers and potential energy surfaces with some variation. The largest errors were those produced by the HF method which was expected, considering that it describes the bond dissociation process poorly. We conclude that HF is a poor method for predicting quantitative aspects of transition states. Although HF greatly over estimates the barriers, it does so consistently. Semi-empirical methods, on the other hand give highly inconsistent results⁷ and are not recommended for the prediction of transition states or other highly strained systems. MP2, was not expected to estimate the results of higher level methods so well. We attribute much of this improvement over HF to fortuitous cancellation of errors, however even in the general case, MP2 is a major improvement over HF. Furthermore, MP2 did not reproduce the initial state geometries of GVB-CI and GVB*SD CI. This inaccuracy in the geometry leads us to believe that the result for the activation barrier at the MP2 level was fortuitous. Although the accuracy of MP2 is fortuitous, we recommend it as the minimum level of correlation needed to calculate transition barriers with reasonable accuracy. The GVB-CI result shows that as expected, the inclusion of all correlation within the active space greatly improves the description of the transition state over HF and provides a greatly improved activation energy. Although the activation energy is higher than that predicted by MP2, we contend that in general, GVB-CI provides a more robust method for predicting transition states than MP2. GVB-CI, however, requires moderately CPU intensive calculations that in all but the smallest systems would be impractical for computing the PES. GVB*SD CI is an even more computationally intensive method that is well established at predicting the results of complete CI calculations. It describes additional dispersion and gives better approximations to

the potential energy surface. For quantitative accuracy GVB*SD CI is the method of choice. This becomes even more true when reaction rates are to be calculated from activation barriers.

We make our best estimate of the rate for the SR-SOR step by combining the barrier from GVB*SD CI *ab initio* calculations with strain energies from molecular mechanics and entropic contributions from transition state theory. The rate equation we predict of $k_{SR-SOR} = 5.6 \times 10^{12} e^{-8800/RT} \text{ sec}^{-1}$ predicts that the SR-SOR recombination step does not limit diamond growth under the range of conditions for which diamond is grown, rather the activation of surface sites by H abstraction will be the limiting step. The methods of combining quantum chemical calculations with classical molecular mechanics calculations is useful in that it concentrates the power of accurate *ab initio* methods on the structure undergoing reaction while adding in strain effects of the surrounding surface using inexpensive molecular mechanics. Methods that treat a large enough portion of the surface to include strain effects are necessarily approximate to avoid large computational costs, often leading to misleading results, especially for reaction barriers.

6.0 References

*To whom correspondence should be addressed.

1. J. C. Angus and C. C. Hayman, *Science* **241**, 913 (1988).
2. K. E. Spear, *J. Am. Ceram. Soc.* **72**, 171 (1989).
3. W. A. Yarbrough and R. Messier, *Science* **247**, 688 (1990).
4. C. J. Chu, M. P. D'Evelyn, R. H. Hauge, and J. L. Margrave, *J. Appl. Phys.* **70**, 1695 (1991).
5. C. E. Johnson, W. A. Weimer, and F. M. Cerio, *J. Mat. Res.* **7**, 1427 (1992).
6. S. J. Harris and A. M. Weiner, *Thin Solid Films* **212**, 201 (1992).
7. S. J. Harris, A. M. Weiner, T. A. Perry, *J. Appl. Phys.* **70**, 1385 (1991).
8. W. A. Yarbrough, K. Tankala, T. J. Debroy, *Mat. Res.* **7**, 379 (1992).
9. S. J. Harris, *Appl. Phys. Lett.* **56**, 2298 (1990).
10. S. J. Harris and D. N. Belton, *Thin Solid Films* **212**, 193 (1992).
11. D. N. Belton and S. J. Harris, *J. Chem. Phys.* **96**, 2371 (1992).
12. M. Frenklach and H. Wang, *Phys. Rev. B* **43**, 1520 (1991).
13. M. E. Coltrin and D. S. Dandy, *J. Appl. Phys.* **74**, 5803 (1993).
14. W. A. Yarbrough, in *Diamond Optics IV*, A. Feldman and S. Holly Editors (SPIE, Bellingham, Washington, 1991), p. 1534.
15. S. J. Harris and D. G. Goodwin, *J. Phys. Chem.* **97**, 23 (1993).
16. B. J. Garrison, E. J. Dawnkaski, D. Srivastova, and D. W. Brenner, *Science* **255**, 835 (1992).
17. D. W. Brenner, *Phys. Rev. B* **42**, 9458, (1990).
18. F. W. Bobrowicz and W. A. Goddard, III, *Methods of Electronic Structure Theory* ed. HF Schaefer (New York: Plenum) p. 79.
19. W. J. Hunt, P. J. Hay and W. A. Goddard, III, *J. Chem. Phys.* **57**, 738 (1972).
20. C. W. Bauschlicher and S. R. Langhoff, *Chem. Phys. Lett.* **135**, 67 (1987).
21. C. Møller and M. S. Plesset, *Physical Review*, **46**, 618 (1934).
22. T. H. Dunning, *J. Chem. Phys.* **53**, 2823 (1970).

23. S. J. Huzinaga, *Chem. Phys.* **42**, 1293, (1965).
24. M. J. Frisch, G. W. Trucks, M. Head-Gordon, P. M. W. Gill, M. W. Wong, J. B. Foresman, B. G. Johnson, H. B. Schlegel, M. A. Robb, E. S. Replogle, R. Gomperts, J. L. Andres, K. Raghavachari, J. S. Binkley, C. Gonzalez, R. L. Martin, D. K. Fox, D. J. Defrees, J. Baker, J. J. P. Stewart, and J. A. Pople, *Gaussian 92 Revision*, Gaussian, Inc. Pittsburgh, PA, (1992).
25. W. A. Goddard, III, unpublished.
26. J. Almlöf, C. W. Bauschlicher, M. R. A. Blomberg, D. P. Chong, A. Heiberg, S. R. Langhoff, P-Å Malmqvist, A. P. Rendell, B. O. Roos, P. E. M. Siegbahn and P. R. Taylor *MOLECULE SWEEDEN (PROGRAM)*, unpublished.
27. C. B. Musgrave, J. K. Perry, R. C. Merkle and W. A. Goddard, III, *Nanotechnology* **2**, 187 (1991).
28. S. M. Valone, in *Proc. 1990 NATO Adv. Study Inst. on Diamond and Diamond-Like Films and Coatings*, (1990).
29. C. B. Musgrave, J. Hu, W. A. Goddard, III, to be submitted.
30. These calculations used POLYGRAF from Molecular Simulations Inc. (Burlington Mass.).
31. D. G. Goodwin, *J. Appl. Phys.* **74**, 6895 (1993).

Table 1. Transition state geometries and barriers at various levels of correlation.

Level	Barrier (kcal/mol)	R ₁ (Å)	R ₂ (Å)
HF	18.1	-0.58	-0.075
MP2	10.0	-0.54	-0.042
CASSCF	10.5	-0.50	-0.023
GVB*SD CI	9.3	-0.51	-0.025

Table 2. Contributions to the activation energy for the SR-SOR step.

Calculation	Energy (kcal/mol)
a. Quantum Chemical Calculations	
GVB*SD CI	9.30
Corrections (Basis set and Correlation)	-1.0
Differential Zero Point Energy	0.13
Net Electronic Structure Barrier	8.43
b. Force Field Calculations	
Strain from Balance of Surface	0.73
van der Waals Interactions	-0.34
c. Total E_{act}	8.82

Figure Captions

Figure 1. (a) Dimer paired structure of the H stabilized C(100) surface; (b) Enlargement of (a). Unshaded = H, shaded = Bulk C, hatched = bulk terminating C.

Figure 2. The Brenner-Garrison mechanism for dimer ring opening during CVD growth of C(100).

Figure 3. The C_3H_7 cluster used to generate the PES surfaces.

Figure 4. The points R_{12} and R_{23} used to generate the PES surfaces of the SR-SOR step on the C_3H_7 cluster.

Figure 5a. The energy surface for the SR-SOR reaction from CASSCF calculations. The reactant site is denoted as 0.0. The saddle point for the reaction is denoted as 10.5. The product is far to left and top of the figure. The contour spacing is 1.15 kcal/mol.

Figure 5b. The energy surface for the SR-SOR reaction from MP2 calculations. The reactant site is denoted as 0.0. The saddle point for the reaction is denoted as 10.0. The product is far to the left and top of the figure. The contour spacing is 1.15 kcal/mol.

Figure 5c. The energy surface for the SR-SOR reaction from GVB-SD CI calculations. The reactant site is denoted as 0.0. The saddle point for the reaction is denoted as 9.3. The product is far to the left and top of the figure. The contour spacing is 1.15 kcal/mol.

Figures 6a-c The energy along the reaction paths for the CASSCF, MP2 and GVB*SD CI reaction surfaces, respectively.

Figure 1

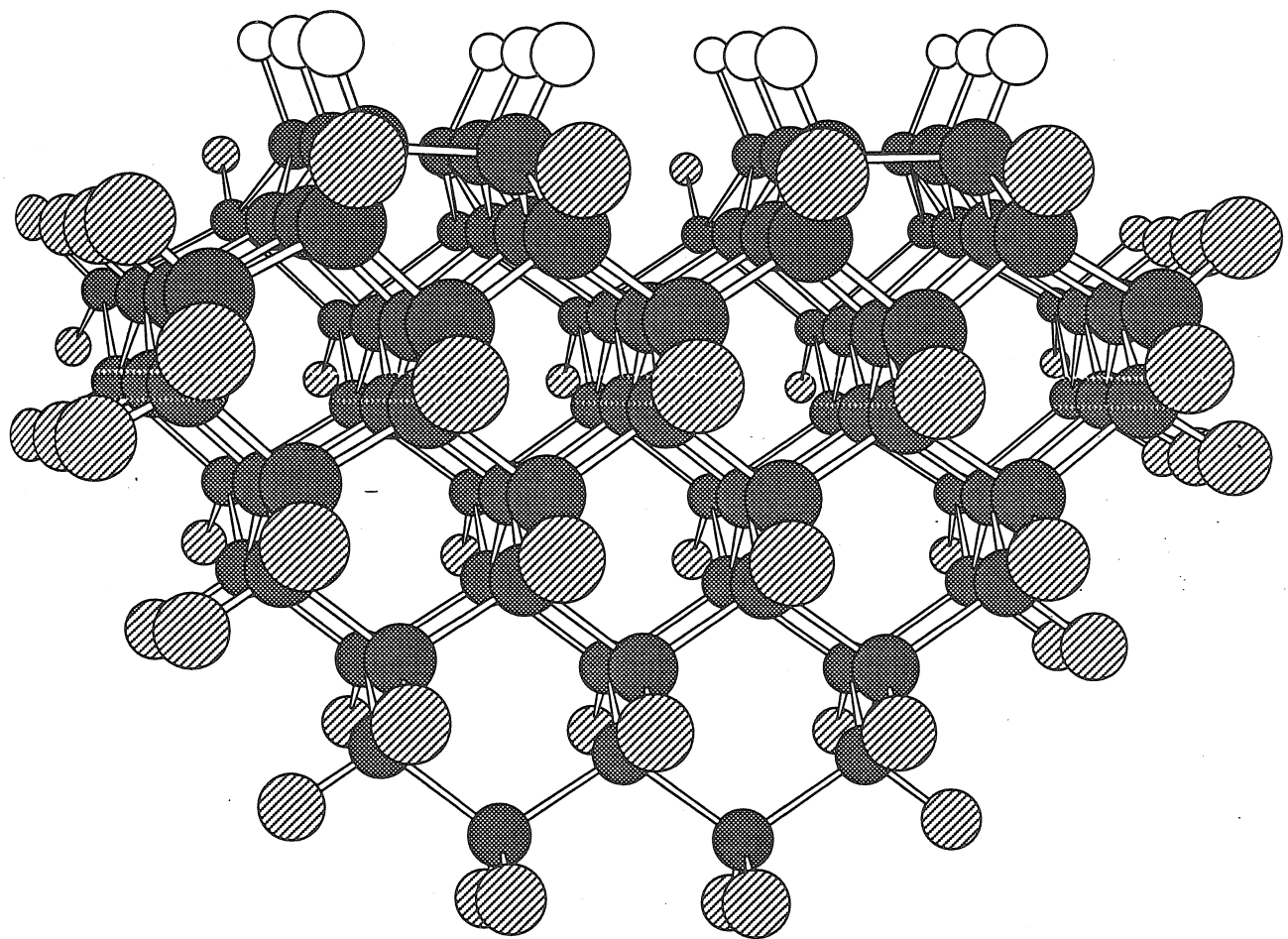


Figure 1

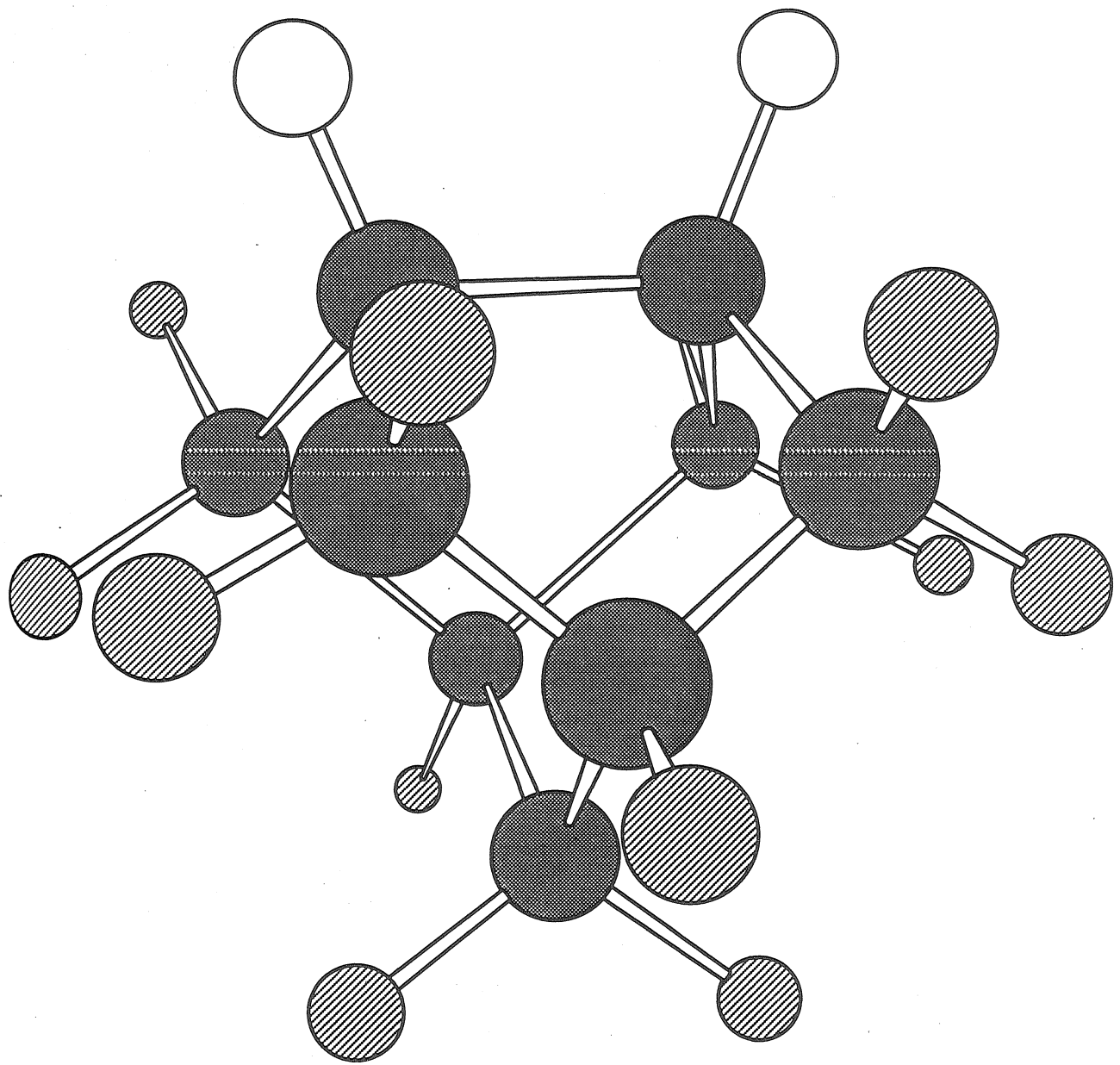


Figure 2

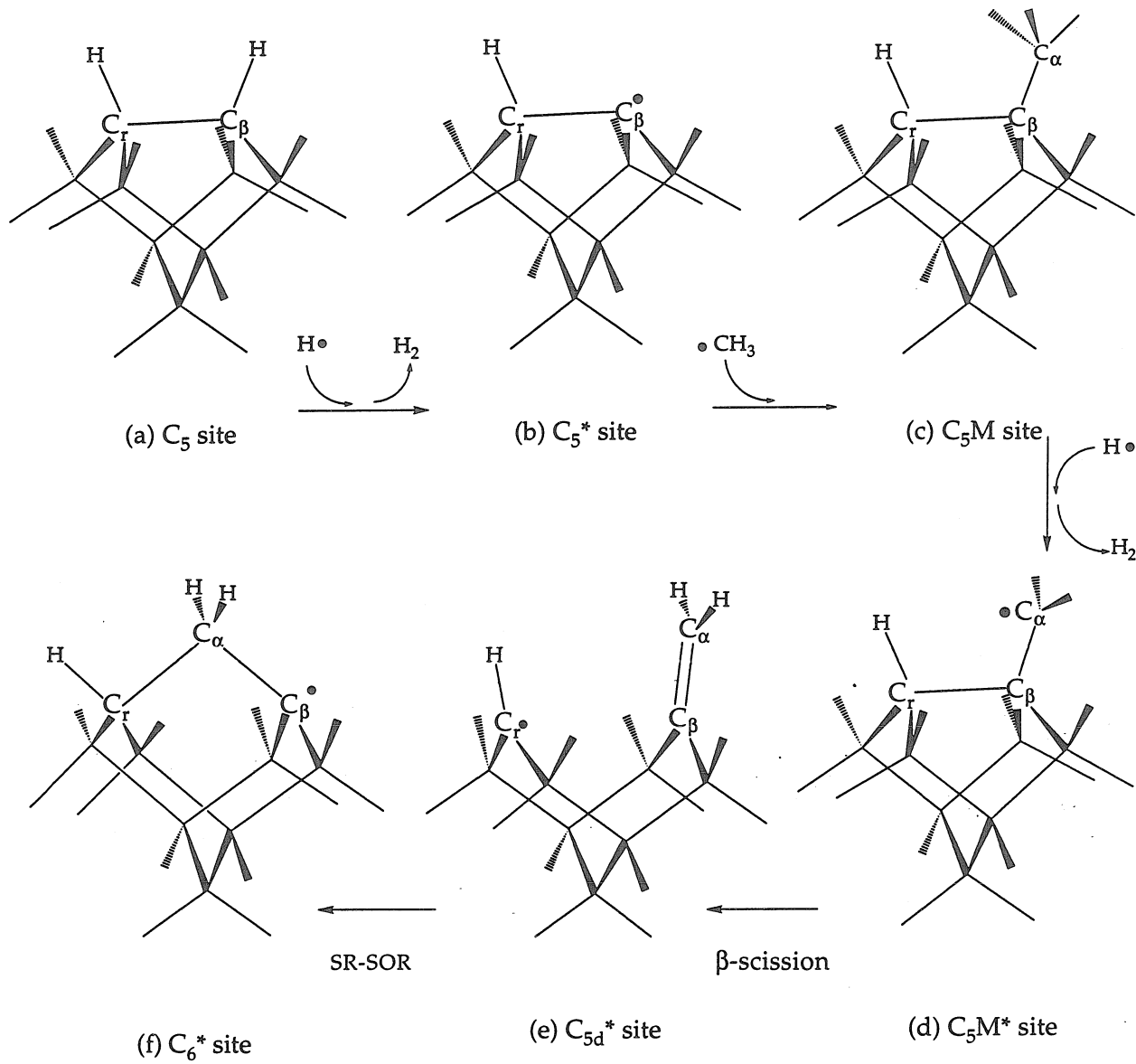


Figure 3

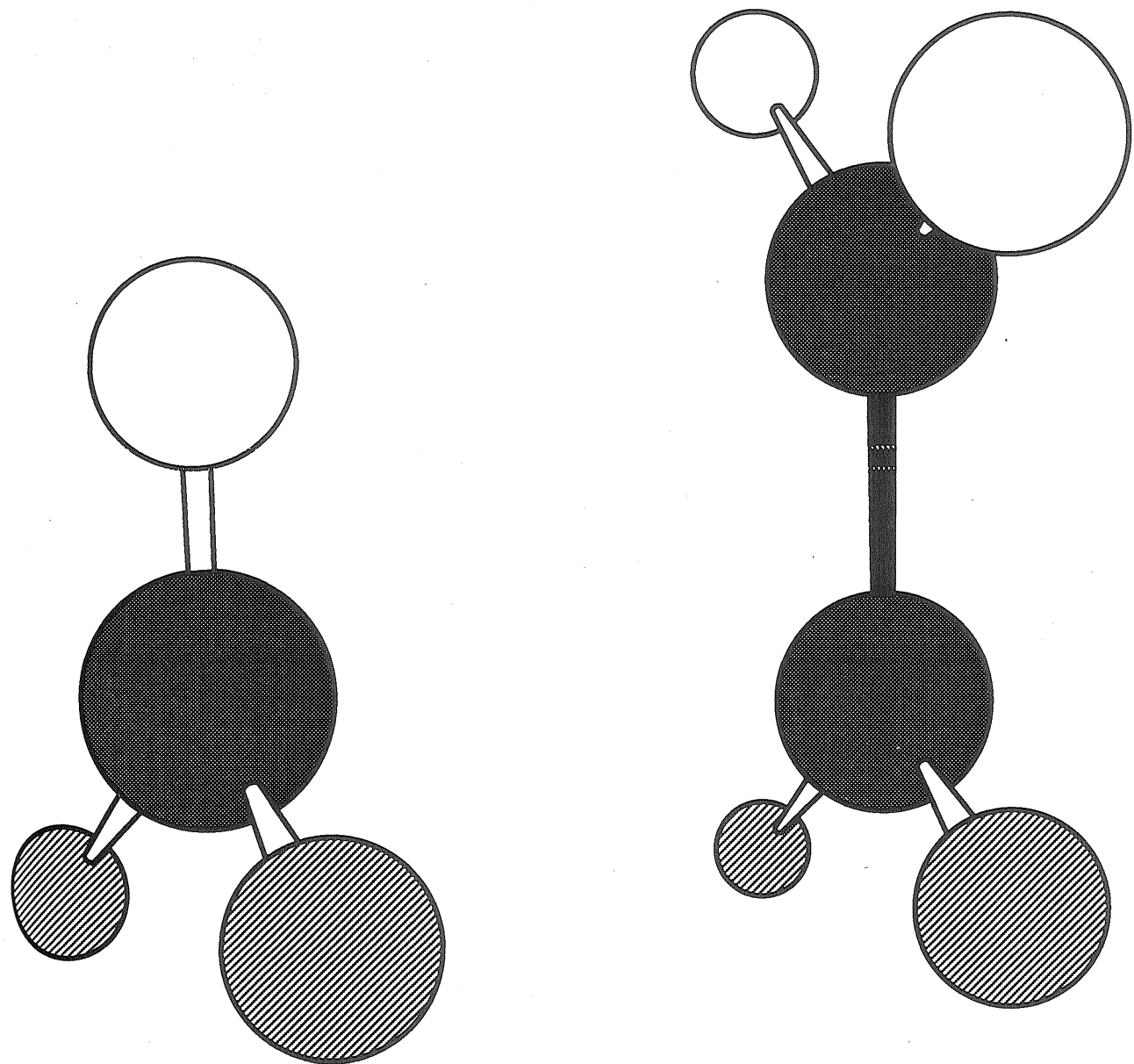


Figure 4 Pairs of R_1 and R_2 used for *ab initio* calculations.

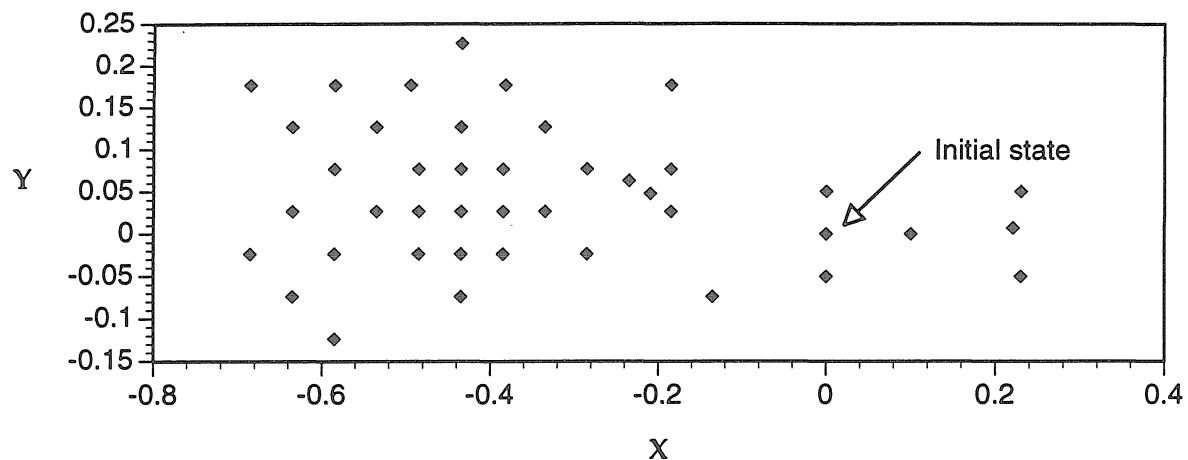


Figure 5

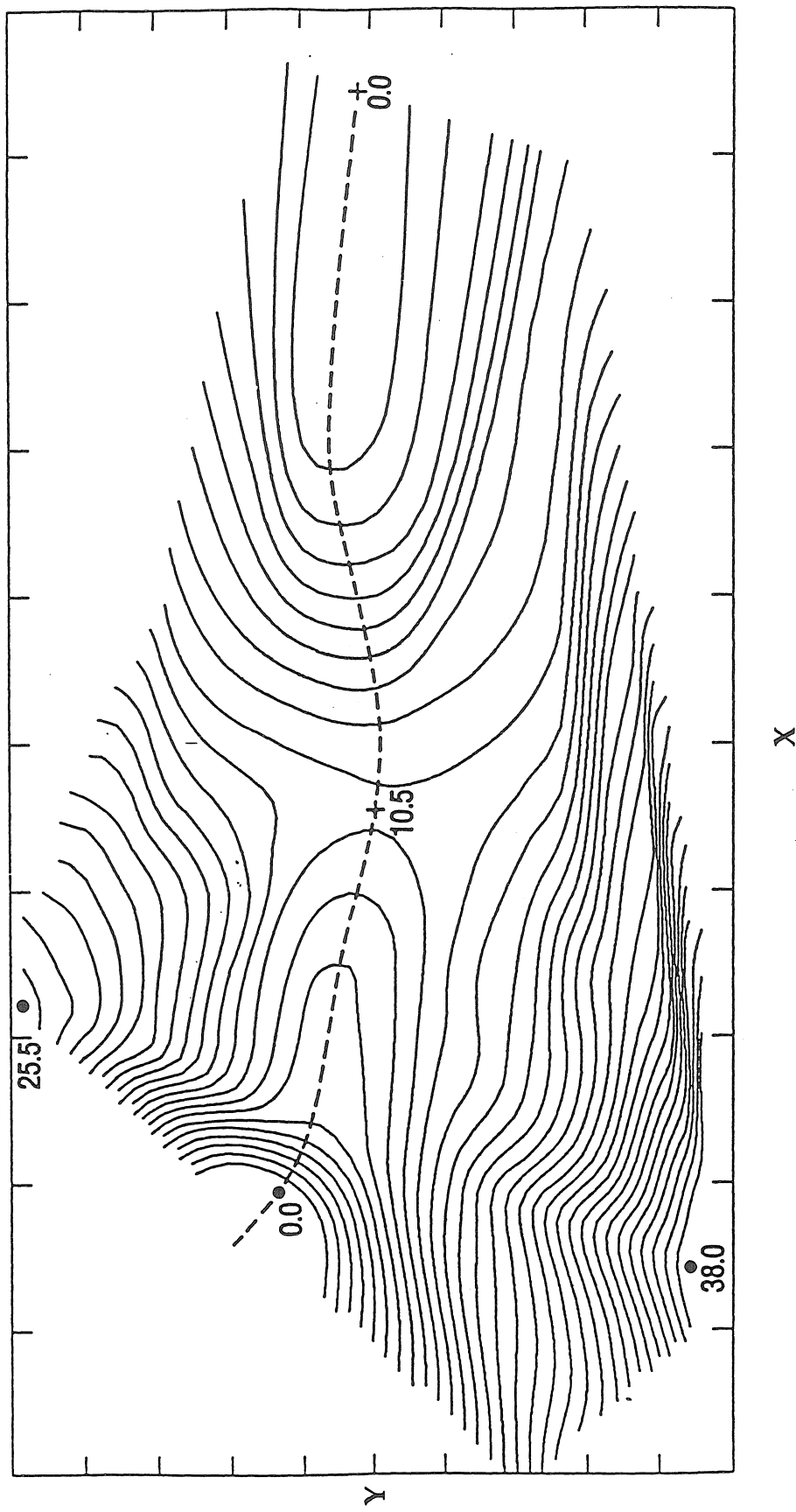


Figure 5

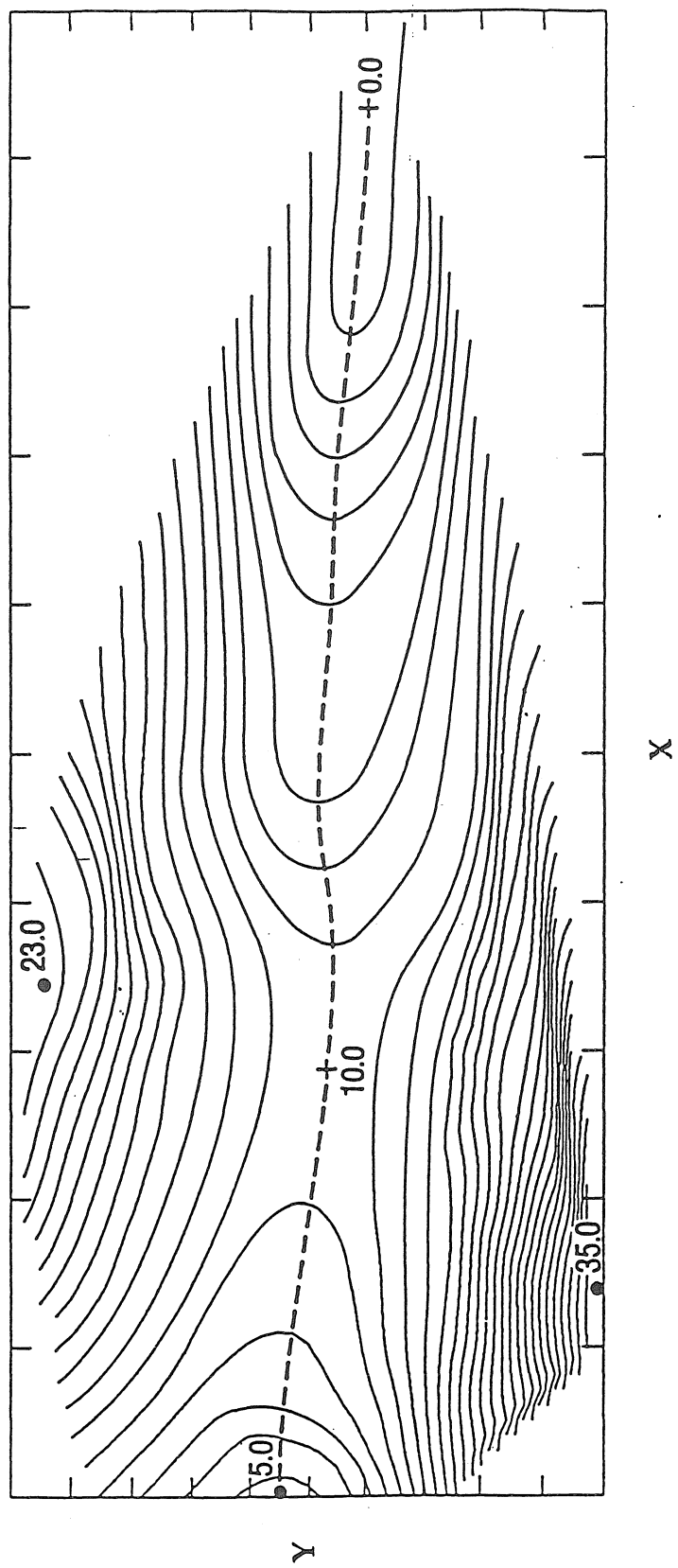


Figure 5

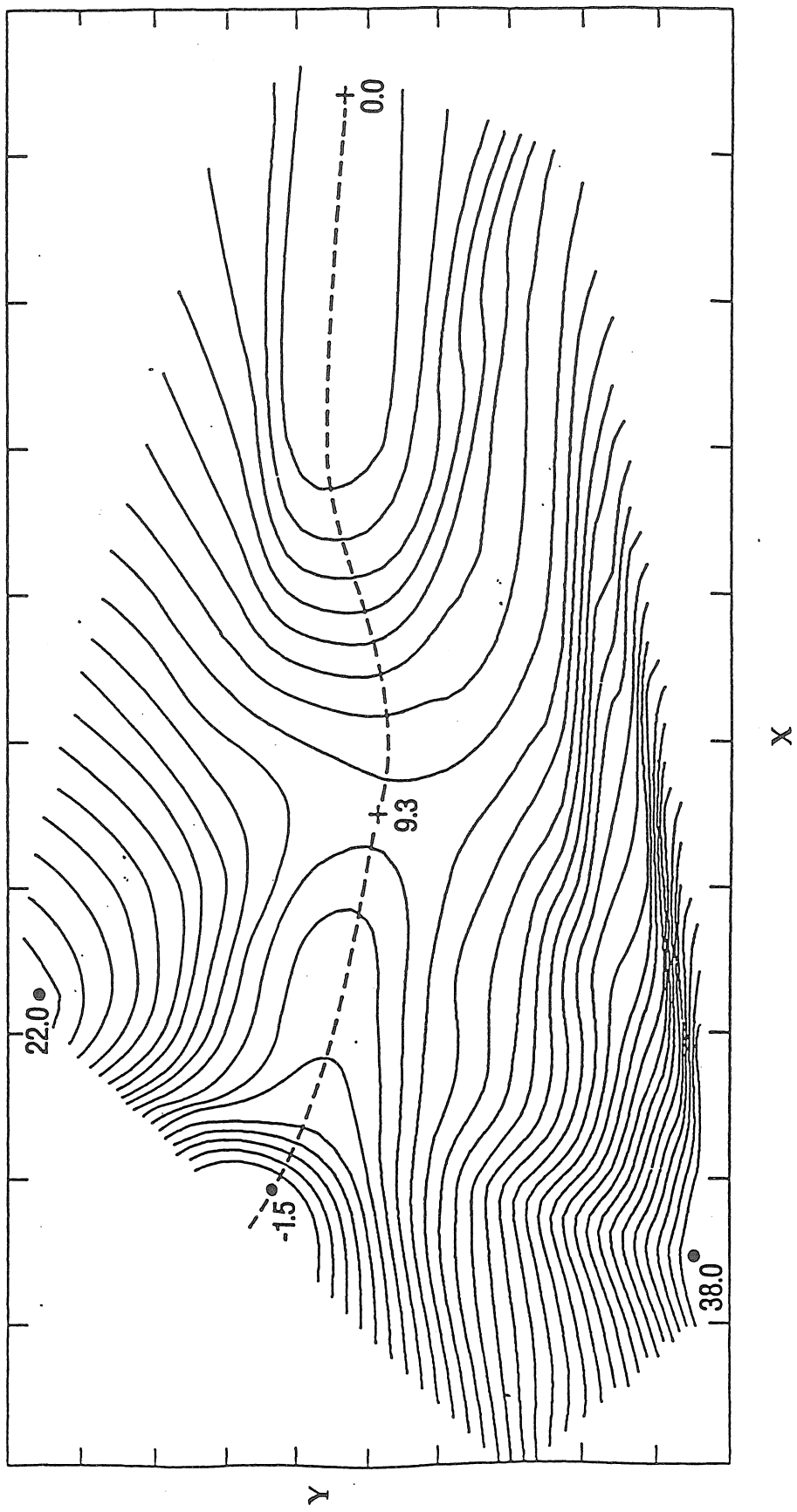


Figure 6 Energy Along Reaction Path

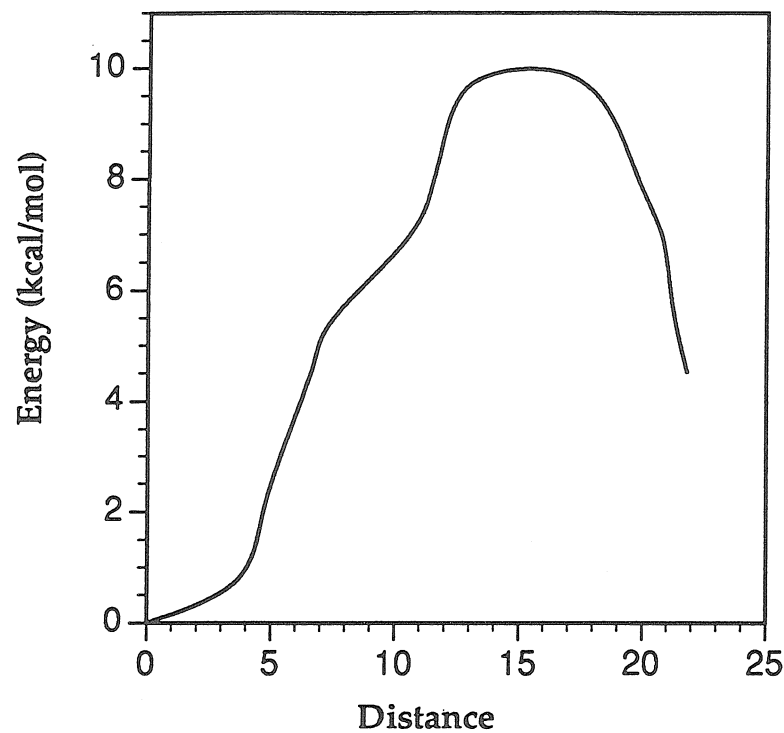


Figure 6 . Energy along Reaction Path

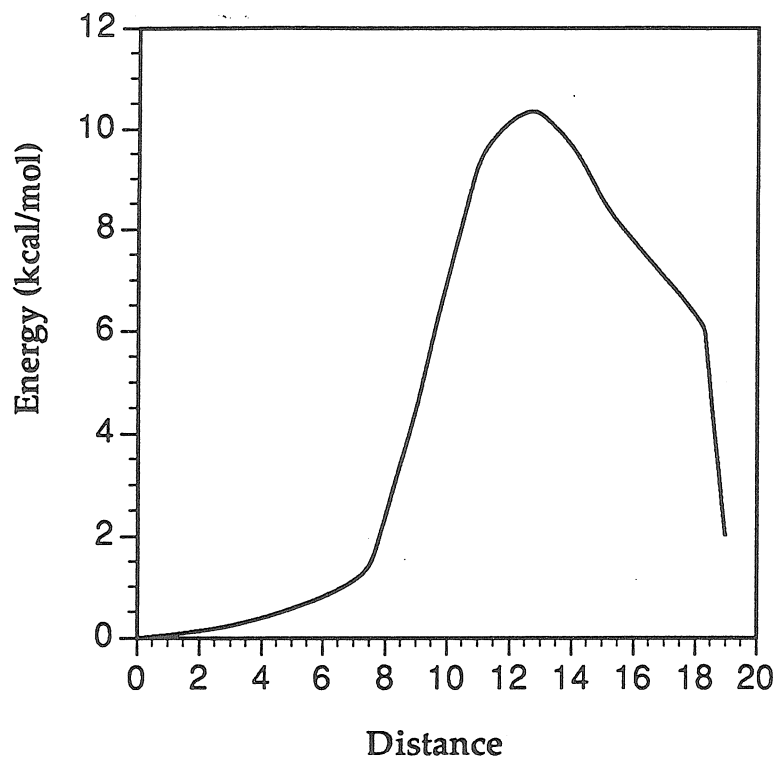
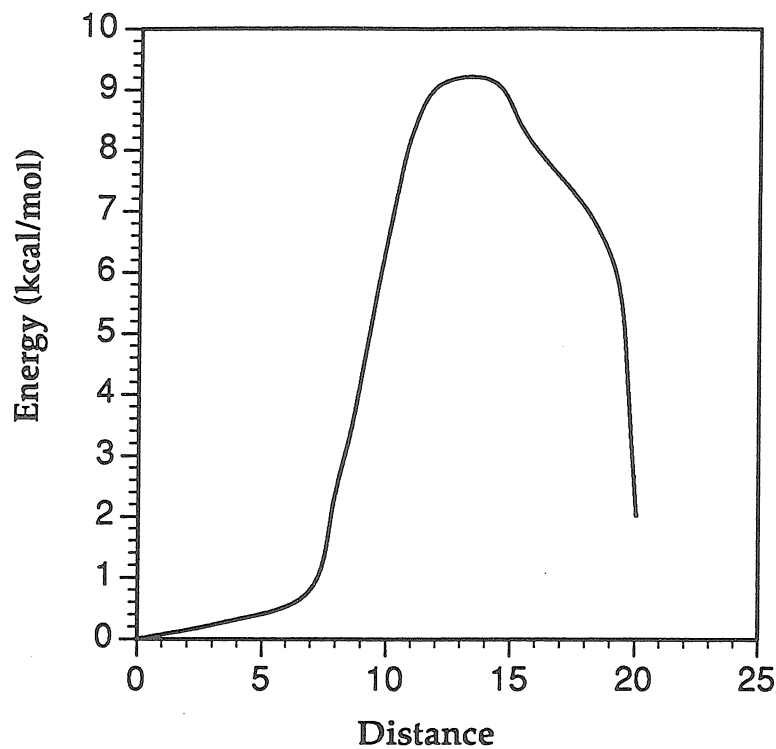


Figure 6 Energy Along Reaction Path



Chapter 3

Ab initio Study of H Abstraction in Nanotechnology

Abstract

Processes which use mechanical positioning of reactive species to control chemical reactions by either providing activation energy or selecting between alternative reaction pathways will allow us to construct a wide range of complex molecular structures. An example of such a process is the abstraction of hydrogen from diamond surfaces by a radical species attached to a mechanical positioning device for synthesis of atomically precise diamond-like structures. In the design of a nanoscale, site specific hydrogen abstraction tool, we suggest the use of an alkynyl radical tip. Using ab initio quantum chemistry techniques including electron correlation we model the abstraction of hydrogen from dihydrogen, methane, acetylene, benzene and isobutane by the acetylene radical. Of these systems, isobutane serves as a good model of the diamond (111) surface. By conservative estimates, the abstraction barrier is small (less than 7.7kcal/mol) in all cases except for acetylene and zero in the case of isobutane. Thermal vibrations at room temperature should be sufficient to supply the small activation energy. Several methods of creating the radical in a controlled vacuum setting should be feasible. Thermal, mechanical, optical and chemical energy sources could all be used either to activate a pre-cursor, which could be used once and thrown away, or alternatively to remove the hydrogen from the tip, thus refreshing the abstraction tool for a second use. We show how nanofabrication processes can be accurately, and inexpensively designed in a computational framework.

1.0 Introduction

Mechanical positioning of reactive species can be used to convert mechanical energy to chemical energy to select between alternative reactions, or to provide activation energy. Mechanosynthesis is the employment of these mechanochemical processes to synthesize molecular structures.¹ Atomically precise mechanosynthesis promises to let us manufacture complex systems of molecular machinery. Examples include: self-replicating assemblers,² molecular scale surgical systems,² computers made with molecular logic elements,³ and macroscopic machines made of diamond-like materials.¹ Construction of such systems will require the ability to precisely manipulate structure on an atomic level. The great specificity of the chemical reactions required to synthesize designs with specific atomic structures should be achievable with mechanochemical tools capable of positioning the reactive moieties with sub-angstrom accuracy. Mechanochemistry allows alternative reaction transition states to be selected by maneuvering the reactive species in to a position where the chosen reaction has the smallest barriers. Such positional control requires that the tool exert forces and torques on the reactive molecule to move it over the potential energy surface of interaction with the workpiece.

Feynman in a talk entitled “*There is Plenty of Room at the Bottom*,” 1960 is credited with first pointing out that the laws of physics said nothing about the impossibility of using mechanical means to direct chemical reactions to synthesize molecules and materials. Applying positional control to reactions will require that the tool have certain properties to make synthesis reliable, feasible, and practical. The tool must (a) have the proper chemical properties (b) be relatively small to reduce steric interactions with the workpiece (c) be capable of remaining chemically and mechanically stable under thermal motions and strains induced during positioning (d) be bound to a system which can transfer forces and torques to the

reactive portion of the tool (e) be selective between alternative reactions and (f) be easily made. Molecular tips attached to atomic force microscope (AFM) tips, scanning tunneling microscope (STM) tips, or molecular robotic arms have been suggested.⁴ Because construction of atomically precise machinery might require about as many unit operations as there are atoms in the system, it is important that reactions be fast. To increase the speed of reactions with moderate barriers, forces can be exerted between the work piece and reactive species to effectively increase the pressure on the system, reducing the barrier height. Moderate reductions in the barrier heights lead to substantial increases in the reaction rate because thermal vibrations have an exponential Boltzman probability of overcoming the reaction barrier. Mechanochemistry not only reduces the barriers by converting mechanical energy to chemical energy, but also maximizes the effective reactive concentration by positioning the reactive moieties to best advantage. These speed enhancing steps together with multiple mechanochemical machines working simultaneously can compensate for the loss of parallelism when compared against solution based reactions. Mechanochemical synthesis also increases the range of synthetic steps that can be used to build novel structures by the use of applied torques; a moiety attached to both the tool and the workpiece can be twisted, for example, to break π -bonds.¹

Nanomachines made of complex specific arrangements of diamond-like material offer several advantages. First, diamond is light, and stiff. Macroscopic machines could be made stronger and simultaneously much lighter, making such activities as air and space travel substantially more practical. Moving parts of such machines would be lighter and therefore, faster. Furthermore, hydrocarbons are abundant, making raw materials readily available and inexpensive. Stiffness is not only a desirable property of finished machines it is also useful during construction since the material surrounding the reactive site on the workpiece must be stiff. This

allows it to withstand the compressive forces that might be needed to reduce reaction barriers, to withstand the tensile forces during moiety abstraction, and to withstand torques applied to break π -bonds. Building machines of diamond will include maneuvering hydrocarbons into reactive sites, torsion of structures, insertions into bonds, and preparation of reactive sites by removing unwanted moieties to create radical sites. Abstraction of hydrogen is likely to be the most repeated step and common to building a wide range of molecular structures, including diamond-like structures. Highly reactive species are commonly thought to play a crucial role in the chemical vapor deposition (CVD) synthesis of diamond.⁵⁻⁷ The abstraction of hydrogen via any of several radicals is one of the central mechanisms involved in the growth of diamond. It is not unreasonable, therefore, to expect that the atomically precise synthesis of diamond-like materials will utilize site-specific hydrogen abstraction via a radical as one of the main steps. Drexler has proposed using a molecular tip made of an ethynyl radical¹ bound to a mechanical base on the tool (Figure 1).

While many radicals exist, the desire for a simple, general, positionally accurate and sterically undemanding hydrogen abstraction tool can be used to narrow the search to a structure which (a) has a very high affinity for hydrogen (b) is not encumbered by surrounding groups (c) can be made part of an extended structure which can be used as a “handle” for positioning and can be attached to an STM or AFM tip (d) is mechanically and chemically stable during positioning (e) is selective between alternative reactions such as abstraction of a neighboring hydrogen or bonding to a nearby carbon atom and (f) is easily made or regenerated. Perhaps the most natural structure in this regard is the ethynyl radical. The C-H bond in acetylene is one of the strongest bonds to hydrogen; thus, the ethynyl radical formed by removing this hydrogen is likely to have a higher affinity for hydrogen

than almost any other chemical structure. Further, the ethynyl radical can easily be incorporated into structures which provide a high degree of steric exposure. A structure resembling the propynyl radical, but with the carbon furthest from the radical site embedded in an extended diamond-like structure (Figure I) provides both excellent steric exposure to the radical and a “handle” for positioning the radical for the desired abstraction. Attachment of the tool to an STM or AFM tip may develop from technology designed for attachment of proteins to surfaces.⁴ Drexler showed that the bending stiffness of an ethynyl- like tip attached to an adamantyl group is ~ 6 N/m and can be increased to ~ 65 N/m by building up a surrounding collar.¹ If the reaction requires application of mechanical force to supplement thermal energy, then bending stiffness may need to be increased. Stiffness also is desirable to achieve selectivity. STM and AFM positng is stable to more than sub- \AA ngstrom accuracy. However, bending modes of the ethynyl tip will be active at moderate temperatures. If during positioning of the tip, the bending of the radical and displacement of the AFM or STM relative to the workpiece positions the reactive portion of the tip near a branched transition state, for example (one pathway leading to abstracting the neighboring hydrogen), then selectivity is reduced. Drexler has shown that at worst at room temperature with a bending stiffness of 20 N/m and transition states separated by 1.2 \AA the unwanted reaction rate is less than 10-12 times the rate of the target reaction.¹ Transition states between neighboring hydrogens on the (111) surface of diamond are separated by 2.5 \AA , and transition states for other possible reactions in diamond-like structures also generally exceed 1.2 \AA , making mechanochemical reactions highly selective. The strong C-H bond of alkynes (127-132 kcal/mol)⁸⁻¹² should give large exothermicities and small barriers (rapid reactions) for alkynyl radical abstraction of hydrogen from weaker sp² and sp³ hybridized C-H bonds (see Table 1). The large exothermicity would also give

a small reverse reaction rate constant. Compressive mechanical forces could be applied to supplement thermal energy in cases where the barriers are large; however, care must be taken so that the alkynyl radical tip does not bend away from the transition state. In the cases we study, the barriers are such that this is not an issue. Several methods of creating the radical should be feasible. The process of creating the radical should take place in an inert environment: vacuum, helium, or some other extremely non-reactive system would be appropriate. The activation energy required to create the abstraction tool could be provided from thermal, mechanical, optical, or chemical sources. There are two obvious approaches. In the first, a pre-cursor compound is activated to create the abstraction tool. The tool is then used once and discarded. A second pre-cursor would then be activated to abstract a second hydrogen. Thus, in a functioning system using this approach, a steady supply of the pre-cursor would be required as well as a method for disposing of the used abstraction tools. In the second approach, the abstraction tool would be refreshed by the removal of the hydrogen after each use. Of course, the ethynyl radical was selected on the basis of its strong C-H bond, so removal of the hydrogen might at first seem paradoxical. However, there are several methods of solving this problem. One would be to first weaken the C-H bond, and then abstract the hydrogen from the abstraction tool using a weaker radical. Drexler¹ proposed that the C-H bond could be weakened by positioning a weak radical near the carbon atom. A second weak radical could then abstract the hydrogen from the tip. An alternative to the attack by two weak radicals strategy would be photo exciting the acetylene to obtain the $\pi\pi^*$ state which would rearrange to the structure with a weak C-H bond and thereby allow removal of the hydrogen. Our primary concern is to analyze the energy barriers associated with hydrogen abstraction using alkynyl radicals to determine the feasibility of such a tool, rather than to analyze

the methods of creating such a tool. We model the chemically active site of the tool by the acetylene radical and determine the transition state geometry and activation energy for transferring the hydrogen from several species: H₂, CH₄, C₂H₂, C₆H₆, and CH(CH₃)₃. The geometry of the various transition states can be used to position a working hydrogen abstraction tool for fast reaction and without bending the tip. The barrier height itself can be used to calculate an abstraction rate at a given temperature and thus, how long the abstraction tool must remain at the transition state until the probability that abstraction has occurred reaches a given value. Various levels of generalized valence bond (GVB) and configuration interaction (CI) ab initio calculations are used. To calibrate the accuracy of these calculations, we consider the abstraction barriers and transition states for hydrogen transfer between methyl and methane and for hydrogen transfer between H and H₂ as compared to other theoretical and experimental results.¹³⁻¹⁵

2.0 Results

The barrier to the acetylene radical abstraction of hydrogen from isobutane (sp³ carbon) is conservatively estimated to be less than 0.45 kcals/mol (Figure II). Reaction barriers calculated at various levels of correlation are shown in Table 2. The barrier to abstraction of hydrogen by the acetylene radical from benzene (sp² carbon) is estimated to be less than 7.7 kcals/mol. The Hartree-Fock times Singles and Doubles Configuration Interaction (HF*SD CI) consistently overestimates the Generalized Valence Bond times Singles and Doubles Configuration Interaction (GVB*SD CI) barriers while the Dissociation Consistent Configuration Interaction (DCCI) consistently underestimates the GVB*SD CI barriers. The GVB*SD CI barriers will be conservatively high due to a lack of a third diffuse p function, zero point corrections, and lack of more correlation of the valence electrons. Transition states were optimized at the Correlation Consistent Configuration Interaction

(CCCI) level (Table 3). Although CCCI does not accurately predict activation barriers, it does accurately describe the transition state geometries. For the largest cases, the number of spin eigenfunctions in the Configuration Interaction (CI) calculation grows beyond our computational capabilities (Table 4). This makes calculation of abstraction from benzene and isobutane at the GVB*SD CI level impractical; however, the overestimated, yet small barriers at the HF*SD CI level shows that the acetylene radical hydrogen abstraction is feasible; thermal vibrations at room temperature providing sufficient energy to overcome the barriers. Table 5 shows the exothermicities for the various abstractions. There is little difference in the accuracy of the methods in predicting the exothermicities because all the methods describe bound states rather well. Note that the exothermicities are for reactions where the product radical species are not allowed to relax. This describes abstraction from surfaces where relaxation is constrained. Exothermicities for gas phase reactions will be higher. The transition state is poorly described by many semi-empirical methods and by ab initio methods with insufficient electron correlation and small basis sets and large variation of the predicted barriers can be seen in Table 2.

3.0 Calculational Details

Standard ab initio quantum chemistry methods are employed and results are given for several levels of calculation. The simplest wave function used is the wave function in which each molecular orbital is doubly occupied. This single configuration (one determinant) Hartree-Fock (HF) wave function is the lowest energy antisymmetrized n-fold product of molecular orbitals and should give a qualitative picture of the hydrogen abstraction reactions studied. HF will tend to overestimate the abstraction barrier since the radical-hydrogen stretching frequency is too high due to the poor description by HF of the bond breaking process (a doubly occupied orbital of the molecule must become two singly occupied orbitals for the

fragments). This problem is remedied by using a GVB (Generalized Valence Bond) wave function,¹⁶ which allows each bond to be described with two singly occupied, overlapping orbitals leading to a proper description of dissociation. When solved for self-consistently, this calculation is termed a Generalized Valence Bond Configuration Interaction Self Consistent Field (GVBCI-SCF) or equivalently a Complete Active Space Self Consistent Field (CASSCF). Simply, all symmetry and spin allowed configurations of three active electrons in three orbitals are generated. These electrons are the radical of the reactant, the hydrogen and the radical of the product. All other orbitals (considered inactive) are doubly occupied as in Hartree-Fock. It is found that three configurations are all that is necessary to adequately describe the transition state. These are the dominant configuration (with the Hartree-Fock occupations of the orbitals) and the single and double excitations of the electrons in the doubly occupied R_1 -H- R_2 bonding orbital to the empty R_1 -H- R_2 antibonding orbital. The R_1 - R_2 antibonding orbital (with a node at the hydrogen center) is singly occupied in all three configurations. While this level of calculation includes the most important correlation, it will still tend to overestimate the abstraction barrier and, thus, will only serve as a zeroth order wave function for large CI (Configuration Interaction) expansions which will account for additional dispersion.

Ideally, we would like to do a CI calculation in which all single and double excitations of the valence electrons are made into the virtual orbitals with reference to the three most important configurations describing the abstraction. This type of multi-reference CI (called a GVB*SD CI) has been well established at approximating proximating results of complete CI calculations.¹⁷ However, this CI has not been carried out for the largest cases, abstraction of hydrogen from isobutane and benzene by the acetylene radical. Thus we have considered some smaller CI calculations which will do a good job in approximating the barriers for the larger CI.

The first of these is the CCCI wave function.^{18,19} It involves making all single and double excitations of the active electrons and all single excitations of the other valence electrons into the virtual space relative to the three GVB references, or simply $\text{GVB}^*(\text{SD}_{\text{active}} + \text{S}_{\text{valence}})$. The second CI, called a DCCI (Dissociation Consistent Configuration Interaction), will add the double excitations which are the product of a single excitation of an active electron and a single excitation of a valence electron, or $\text{GVB}^*(\text{SD}_{\text{active}} * \text{S}_{\text{valence}} + \text{S}_{\text{valence}})$. The third CI does all single and double excitations of the valence electrons (active and inactive) relative to only one reference, a calculation called HF*SD CI (or equivalently 1 reference SDCI). Table 4 shows the sizes of the CI expansions in terms of the number of spin eigenfunctions (SEFUs) for each of the systems studied. The HF*SD CI already approaches the limits of our programs (2 million SEF's) in the cases of isobutane and benzene, for which the GVB*SD CI is not possible. In all other cases, however, the GVB*SD CI's are of small to medium size and will serve as benchmarks to calibrate the accuracy of the smaller CI's. The standard basis sets of Dunning/Huzinaga are used.^{20,21} Their double zeta contraction of the 9s5p set is used on all carbons, with the addition of one set of d polarization functions ($\zeta_d=0.75$). On the active carbons, diffuse s and p functions ($\zeta_s=0.0474$ and $\zeta_p=0.0365$) are also added. For active hydrogens or hydrogens bound to active carbons (in the case of methane), the triple zeta contraction of the 6s set is used, supplemented with a p polarization function ($\zeta_p=0.60$). For all other hydrogens, the double zeta contraction of the 4s set is used, scaled by a factor of 1.2. The basic geometries of the various systems studied are illustrated schematically in Figure III. The geometries will be optimized at the CCCI level. The orbital optimization at the GVBCI-SCF level is the most time consuming step, so this CI will be a simple correction to that wave function. It would be impractical to do a full geometry optimization, so certain constraints are assumed. Namely,

only the relevant parameters to the description of the hydrogen abstraction (R_{1H} and R_{2H} or combinations thereof) will be optimized. In the case of abstraction on from methane (by the methyl radical or by the acetylene radical), the $H-C-H_{abs}$ bond angle is also optimized since this angle changes from 109.5° for methane to 90° for the methyl radical. For isobutane, we would expect a small relaxation from a tetrahedral $C-C-H_{abs}$ bond angle to something more planar at the transition state and in the radical species. But Page and Brenner,²² in their work on abstraction of hydrogen from isobutane by atomic hydrogen, found that full relaxation of the t-butyl species reduced the abstraction barrier by only 1.7 kcal/mol at the GVBCI-SCF level. However, since the goal of this work is to show the feasibility of using an alkynyl radical tip as a hydrogen abstraction tool, a conservative overestimate of the abstraction barriers is acceptable. So the $C-C-H_{abs}$ bond angle is fixed to 109.5° in these calculations. All other radicals are expected to show little or no relaxation and are fixed to the experimental values of their hydrogen bound counterparts. All calculations are run with the GVB²³ and MOLECULE/SWEDEN²⁴ suites of programs on the Caltech group's Alliant FX/80 and FPS 500.

4.0 Discussion

4.1 H-H-H:

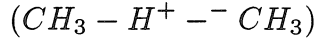
A great deal of theoretical work has been done on this system,¹⁵ and, due to its simplicity, it provides a good test of our hydrogen basis set and, to a lesser extent, our methods. While the calculated equilibrium bond distance in H_2 compares favorably to experiment (0.74\AA vs. 0.74144\AA ²⁵), the calculated dissociation energy for H_2 (D_e) is 105.4 kcal/mol as compared to the experimental number of 108.6 kcal/mol.²⁵ This discrepancy of 3 kcal/mol is chiefly due to the lack of a second p polarization function. In contrast, the transition state is well described by the GVB*SD CI (in this case only, the CCCI, DCCI and GVB*SD CI are equiva-

lent since there are no valence electrons in addition to the three active electrons). The optimized geometry has a H-H distance of 0.94Å (compared to Liu's value of 0.930Å¹⁵) and a barrier of 10.3 kcal/mol (compared to Bauschlicher's value of 9.56 kcal/mol using a large ANO basis set¹⁵). The geometries for all the systems studied are listed in Table 3 and the abstraction barriers are listed in Table 2. An error of less than 1 kcal in the barrier is adequate for the calculations at hand, particularly since the barrier is overestimated. It should be noted, however, that the Hartree-Fock barrier is well off the mark at 24.3 kcal/mol and that the apparently good result at the GVBCI-SCF level (9.9 kcal/mol) is primarily due to the weak H-H bond strength (87.5 kcal/mol) at this level. The HF*SD CI number including the Davidson correction is in fortuitous agreement with the reference barrier height of 9.56 kcal/mol. This is rather symptomatic of the Davidson correction, which can often overestimate the contributions from additional correlation.

4.2 CH₃-H-CH₃:

The methyl-methane hydrogen transfer reaction is perhaps more representative as a test case of the systems in which we are most interested. There has been less theoretical work done on this system¹⁴ but a reliable experimental number for the abstraction barrier of 14.2 kcal/mol¹³ gives a good benchmark for us to work with. Theoretical investigations into this reaction have not been successful in obtaining quantitative accuracy in the barrier height. The best calculations overestimate the barrier by 5-6 kcal/mol. Part of this is due to some assumptions made in the calculations, namely the neglect of zero-point corrections, the Born-Oppenheimer approximation and temperature effects. However, the sum of these effects should only lower the theoretical activation energy by 1-2 kcal/mol (see Sana, et.al.¹⁴). Our results agree well with previous theoretical work. The optimized transition state geometry is virtually identical to the full gradient optimized structure of

Wunsch, et al.,¹⁴ which was done at the Hartree-Fock level. The calculated barrier is 20.4 kcal/mol, higher than experiment by 6.2 kcal/mol. Test calculations with a large ANO basis set²⁶ only lowered the barrier to 19.2 kcal/mol, indicating that the discrepancy between theory and experiment is likely a correlation problem rather than a basis set problem. The importance of ionic terms such as



are probably underestimated in the CI calculations due to biases against anionic states and would require additional correlation of the non-active valence electrons. This could be a formidable task even for such a small system and would not be possible with our current code for the larger cases we wish to study. However, again, since these factors all tend to lead to an overestimate of the barrier height the results for abstraction of hydrogen by the acetylene radical can be considered a conservative upper limit to the actual barrier height. These calculations on the methyl-methane system also offer a comparison of the smaller CI's to the GVB*SD standard. We find the CCCI result (29.8 kcal/mol) to be comparable to the GVBCI-SCF number (27.8 kcal/mol), being slightly higher due to the stronger C-H bond at the CCCI level (113.2 kcal/mol vs. 97.6 kcal/mol at the GVBCI-SCF level and 107.2 kcal/mol at the GVB*SD CI level). This indicates that correlation of the non-active electrons is important in obtaining quantitative accuracy for the hydrogen abstraction barriers. The DCCI, which includes only limited correlation of the inactive electrons, underestimates the GVB*SD CI barrier by 2.9 kcal/mol. Alternatively, the HF*SD CI, which sacrifices some of the active electron correlation, overestimates this barrier by 2.1 kcal/mol. The combination of these two CI calculations should offer an upper and lower limit to the GVB*SD CI for those large cases where that CI is not feasible.

4.2 H-H-CCH, CH₃-H-CCH, C₆H₅-H-CCH and HCC-H-CCH

Results of calculations on these systems underscore the results of methyl-methane. In particular, Hartree-Fock greatly overestimates the activation energies, GVBCI-SCF and CCCI offer some improvement but still overestimate these barriers, and DCCI and HF*SD CI bracket the results of the GVB*SD CI. In the case of abstraction from methane and benzene, we found the geometries were most conveniently optimized by using the coordinate system R_{1H} + R_{2H} and R_{1H} - R_{2H}. In the case of abstraction from H₂, it was easier to optimize the transition state in terms of the coordinates R_{1H} and R_{2H}. This was likely due to the fact that the barrier was small at the CCCI level and that it occurred quite early, with only an 8% increase in the H-H bond length. To a large degree the barrier height and the position of the barrier is determined by the exothermicity of the reaction. Other properties, such as the polarizability of the bonds, play a role as well. The largest barrier (and latest transition state) was for abstraction from acetylene, with an activation energy of 14.6 kcal/mol. This is as expected, since this particular reaction is thermoneutral. The calculated exothermicities of the other reactions are listed in Table 5 (see also Table 1, for the experimental bond dissociation energies). H₂ and CH₄ are the most exothermic and have the smallest barriers. These barriers maybe considered negligible as the calculations on H + H₂ and methyl-methane showed the numbers to be overestimated. Abstraction from benzene is less exothermic and shows a small but non-negligible barrier. In addition, the phenyl-H bond is stretched 14% at the transition state in comparison to an 11% stretch of the methyl-H bond. All of these results correlate with the exothermicities of the reactions.

1.3.2 (CH₃)₃C-H-CCH:

Finding the transition state for abstraction from isobutane proved to be quite difficult. The potential energy surface has many of the same features as that of H-H-

CCH, in particular, a small, early barrier which leads to non-quadratic behavior in the region of the saddle point. Due to the computational costs of these calculations, it was necessary to sacrifice some accuracy in order to find the transition state. In the end, the values of $R_{1H}=1.2\text{\AA}$ and $R_{2H}=1.5\text{\AA}$ are in agreement with results for abstraction from methane and benzene by the acetylene radical. The large CI calculations strongly indicate that there is no barrier for abstraction of hydrogen, the more conservative number giving a barrier of only 0.45 kcal/mol. This again correlates with the large exothermicity of this reaction, which is calculated from snap bond energies. If one considers that the t-butyl group should relax somewhat at the CCCI transition state and, thus, lower the energy of the barrier still, the argument for the absence of a barrier becomes even more persuasive. Since this system is a good model for the hydrogenated diamond (111) surface C-H bond, we conclude that no barrier exists to abstraction of hydrogen from this surface by acetylene. Barriers on other surfaces of diamond are likely nonexistent or negligibly small.

4.4 Abstraction from Acetylene:

Now that it has been established that an alkynyl tipped hydrogen abstraction tool would be able to abstract hydrogen from diamond surfaces with little or no thermodynamic hindrances, it would be desirable to find a method for removing the hydrogen from the tip. A simple alternative, but less elegant strategy, is to make a new tip for each abstraction and dispose of the tool after use. What makes the acetylene good at abstracting hydrogen is the strength of its C-H bond. However, this bond is quite weak in the $3B_u$ excited state (see Table 6). We calculate a bond strength of 41.7 kcal/mol doing a GVBCI-SCF in which all 10 valence electrons are active in 10 orbitals, followed by a Multi-Reference times Singles and Doubles Configuration Interaction (MR*SD CI) in which all configurations in the GVBCI

with coefficients > 0.05 are chosen as references. In the case of the triplet excited state, there are 4 references and, in the case of dissociated $\text{H} + \text{CCH}$, there are 6 references. The geometry for the excited state is optimized at the $\text{MR}^*\text{SD CI}$ level. The molecule is not linear in this state, having a C-C-H bond angle of 132.0° . The C-C bond length also increases to 1.38\AA from 1.20\AA for the ground state, reflecting the double bond character of this bond. The weakening of the C-C bond in the excited state leads directly to the weakening of the C-H bonds, as the triple bond character can be restored upon dissociation of one of the C-H bonds. The weakening of the C-H bond leaves the acetylene prone to abstraction, making it easy to remove the hydrogen and refresh the tip. So photoexcitation of the alkynyl tip from its ground state to the 1B_u excited state, followed by relaxation to the triplet would facilitate the breaking of the tip-hydrogen bond. Drexler also made an alternative proposal for removing the hydrogen from the tip by destabilizing the H-tip bond with a second tip and disposing of the H into a H sink.¹

5.0 Conclusion

We model the abstraction of hydrogen from H_2 , CH_4 , C_2H_2 , C_6H_6 , and $\text{CH}(\text{CH}_3)_3$ by the acetylene radical using accurate CI ab initio quantum chemistry techniques. From our results, conservative estimates show that the reaction barriers for abstraction from sp^3 hybridized carbons are negligible, or zero for the case of isobutane. The barriers are small for sp^2 hybridized carbons and slightly larger for sp hybridized carbons. Therefore, abstraction tools based on ethynyl radical molecular tips should reliably and rapidly abstract hydrogen from most carbon structures at moderate temperatures. We also find that the hydrogen bond to the $\pi\pi^*$ excited ethynyl tip is relatively weak, and therefore can be broken to refresh the tip. We also wish to show how nanofabrication processes can be accurately and inexpensively designed in a computational framework.

6.0 References

1. Drexler, K. E., *Nanosystems: Molecular Machinery, Manufacturing, and Computation*, John Wiley & Sons, scheduled for publication in 1992.
2. Drexler, K. E., *Engines of Creation*, Anchor Press/Doubleday, (New York), 1986.
3. Drexler, K. E., *Molecular Electronic Devices*, Elsevier Science Publishers B.V. North-Holland (Amsterdam) , 1988.
4. Drexler, K. E., *J. Vac. Sci. Technol.*, B9 (2), 1394, (1991).
5. Celii, F. G., Pehrsson, P. E., Wang, H. and Butler, J. E., *Appl. Phys. Lett.*, 52, 2043, (1988).
6. Harris, S. J., Weiner, A. M. and Perry, T. A., *Appl. Phys. Lett.*, 53, 1605, (1988); Harris, S. J. and Weiner, A. M., *J. Appl. Phys.*, 67, 6520, (1990).
7. Goodwin, D. G. and Gavillet, G. G., *J. Appl. Phys.*, 68, 6393, (1989).
8. Wodtke, A. M. and Lee, Y. T., *J. Phys. Chem.*, 89, 4744, (1985).
9. Ervin, K. M., Gronert, S., Barlow, S. E., Gilles, M. K., Harrison, A. G., Bierbaum, V. M., Depuy, C. H., Lineberger, W. C. and Ellison, G. B., *J. Am. Chem. Soc.*, 112, 5750, (1990).
10. Segal, J., Wen, Y., Lavi, R., Singer, R. and Wittig, C.J., *J. Phys. Chem.*, 95, 8078, (1991).
11. Green, P. G., Kinsey, J. L. and Field, R. W., *J. Chem. Phys.*, 91, 5160, (1989).
12. Segal, J., Lavi, R., Wen, Y. and Wittig, C.J., *J. Phys. Chem.*, 93, 7287, (1989).
13. Tedder, J. M., *Angew. Chem. Int. Ed. Engl.*, 21, 401, (1982).
14. Wunsch, E., Lluch, J. M., Oliva, A. and Bertran, J., *J. Chem. Soc. Perkin Trans. II*, 211, (1987); Sana, M., Leroy, G. and Villaveces, J. L., *Theor.*

Chim. Acta., 65, 109, (1984); Rayez-Meaume, M. T., Dannenberg, J. J. and Whitten, J. L., J. Am. Chem. Soc., 100, 747, (1978).

15. Liu, B. J., Chem. Phys., 58, 1925, (1973); Bauschlicher, C. W., Langhoff, S. R. and Partridge, H., Chem. Phys. Lett., 170, 345, (1990) and references therein; Siegbahn, P. and Liu, B. J., Chem. Phys., 68, 2457, (1978).
16. Bobrowicz, F. W. and Goddard, W. A. in Methods of Electronic Structure Theory (Ed. Schaefer, H. F.), 79, 1977.
17. Bauschlicher, C. W. and Langhoff, S. R., Chem. Phys. Lett., 135, 67, (1987); Taylor, P. R. and Partridge, H., J. Phys. Chem., 91, 6148, (1987). For an excellent review see Bauschlicher, C. W., Langhoff, S. R., and Taylor, P. R., Adv. Chem. Phys., 77, 103, (1990).
18. Carter, E. A. and Goddard, W. A., J. Chem. Phys., 88, 1752, (1988).
19. Carter, E. A. and Goddard, W. A., J. Chem. Phys., 88, 3132, (1988).
20. Dunning, T. H., J. Chem. Phys., 53, 2823, (1970).
21. Huzinaga, S. J., Chem. Phys. 42, 1293, (1965).
22. Page, M. and Brenner, D. W., J. Am. Chem. Soc., 113, 3270, (1991).
23. Goddard III, W. A., et al., Caltech, unpublished.
24. MOLECULE-SWEDEN is an electronic structure program system written by Almlöf, J., Bauschlicher, C. W., Blomberg, M. R. A., Chong, D. P., Heiberg, A., Langhoff, S. R., Malmqvist, P-Å; Rendell, A. P., Roos, B. O., Siegbahn, P. E. M. and Taylor, P. R.
25. Huber, K. P. and Herzberg, G., Molecular Structure IV: Constants of Diatomic Molecules, Van Nostrand Reinhold Company (New York), 1979.
26. Almlöf, J. and Taylor, P. R., J. Chem. Phys., 86, 4070, (1987).
27. McMillen, D. F. and Golden, D. M., Ann. Rev. Phys. Chem., 33, 493, (1982).

Table 1. Experimental bond dissociation energies (kcal/mol).

R-H	D_0 [reference]
$H - H$	102.3 [25]
$CH_3 - H$	105.1 [27]
$(CH_3)_3 - H$	93.2 [27]
$C_6H_5 - H$	110.9 [27]
$HCC - H$	126.6 [11], 131.3 [9]

Table 2. Barriers for the hydrogen abstraction reaction, $R_1\text{-H} + R_2 \rightarrow R_1\text{+H-}R_2$, calculated at the CCCI optimized geometry (kcal/mol). Negative energies indicate that the CCCI transition state geometry is lower in energy than the reactants. Numbers in parentheses are the barriers when the Davidson correction is included.

$R_1 - H - R_2$	HF	GVBCI-SCF	CCCI
$H - H - H$	24.3	9.9	10.3
$CH_3 - H - CH_3$	34.9	27.8	29.8
$H - H - CCH$	11.6	8.0	5.4
$CH_3 - H - CCH$	14.6	8.6	10.2
$(CH_3)_3 - H - CCH$	11.0	5.9	8.0
$C_6H_5 - H - CCH$	18.3	12.0	14.3
$HCC - H - CCH$	30.0	22.9	24.1
$R_1 - H - R_2$	DCCI	HF*SD CI	GVB*SD CI
$H - H - H$	10.3	10.5 (9.6) ^c	10.3 (10.3)
$CH_3 - H - CH_3$	17.5	22.5 (19.5)	20.4 (18.8)
$H - H - CCH$	0.8	4.5 (3.2)	3.3 (2.7)
$CH_3 - H - CCH$	-2.9	4.2 (2.0)	2.2 (1.3)
$(CH_3)_3 - H - CCH$	-7.0	0.45 (-2.78)	
$C_6H_5 - H - CCH$	-0.7	7.7 (4.1)	
$HCC - H - CCH$	11.6	17.0 (13.7)	14.6 (12.9)

Table 3. Transition state geometries optimized at the CCCI level. See text for constraints on these geometries.

$R_1 - H - R_2$	R_{1H}	R_{2H}	H-C-C angle
$H - H - H$	0.94	0.94	
$CH_3 - H - CH_3$	1.36	1.36	105.2
$H - H - CCH$	0.80	1.61	
$CH_3 - H - CCH$	1.22	1.48	105.5
$(CH_3)_3 - H - CCH$	1.20	1.50	
$C_6H_5 - H - CCH$	1.24	1.42	
$HCC - H - CCH$	1.28	1.28	

Table 4. Number of spin eigenfunctions in each of the CI calculations for the transition state. If the transition state has higher symmetry, then the number of SEF is doubled for the product or reactant state.

$R_1 - H - R_2$	CCCI	DCCI	HF*SD CI	GVB*SD CI
$H - H - H$	191	191	139	191
$CH_3 - H - CH_3$	4914	71666	79428	310778
$H - H - CCH$	2160	18234	15189	53048
$CH_3 - H - CCH$	9477	150557		
$(CH_3)_3 - H - CCH$	21676	695842	1675566	
$C_6H_5 - H - CCH$	17265	587343	587343	1514151
$HCC - H - CCH$	2697	42201	55211	221805

Table 5. Calculated exothermicities (kcal/mol). Numbers in parentheses include the Davidson correction.

$R_1 - H - R_2$	HF	GVBCI-SCF	CCCI
$H - H - CCH$	33.9	31.6	31.8
$CH_3 - H - CCH$	28.9	28.4	27.0
$(CH_3)_3 - H - CCH$	28.5	27.9	24.2
$C_6H_5 - H - CCH$	18.7	18.2	15.4
$R_1 - H - R_2$	DCCI	HF*SD CI	GVB*SD CI
$H - H - CCH$	30.1	30.0 (27.5)	29.9 (28.1)
$CH_3 - H - CCH$	29.2	26.9 (25.5)	26.8 (25.4)
$(CH_3)_3 - H - CCH$	27.4	26.8 (25.9)	
$C_6H_5 - H - CCH$	18.9	18.3 (18.0)	

Table 6. Calculated relevant energetics of ground-state acetylene and the excited-state triplet (kcal/mol).

$R_1 - H - R_2$	R_{1H}	R_{2H}	H-C-C angle
$T_e(^3B_u \leftarrow ^1\sum_g^+)$	72.3	92.0	90.2
$D_e(^1\sum_g^+ HCC - H)$	116.5	122.3	131.9
$D_e(^3B_u HCC - H)$	44.2	30.3	41.7

Figure Captions

Figure 1. Acetylene radical hydrogen abstraction molecular tip attached to diamond-like material.

Figure 2. Schematic diagram showing the transition barrier and exothermicity of the acetylene radical abstraction of hydrogen from isobutane.

Figure 3. Geometries for the transition states.

Figure 1: Acetylene radical hydrogen abstraction
molecular tip attached to diamond-like material.

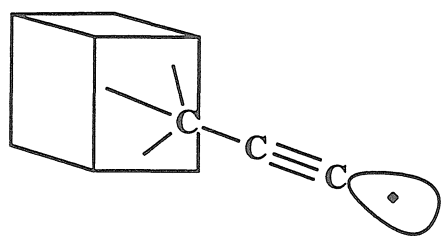


Figure 2: Schematic diagram showing the transition barrier and exothermicity of the acetylene radical abstraction of hydrogen from isobutane.

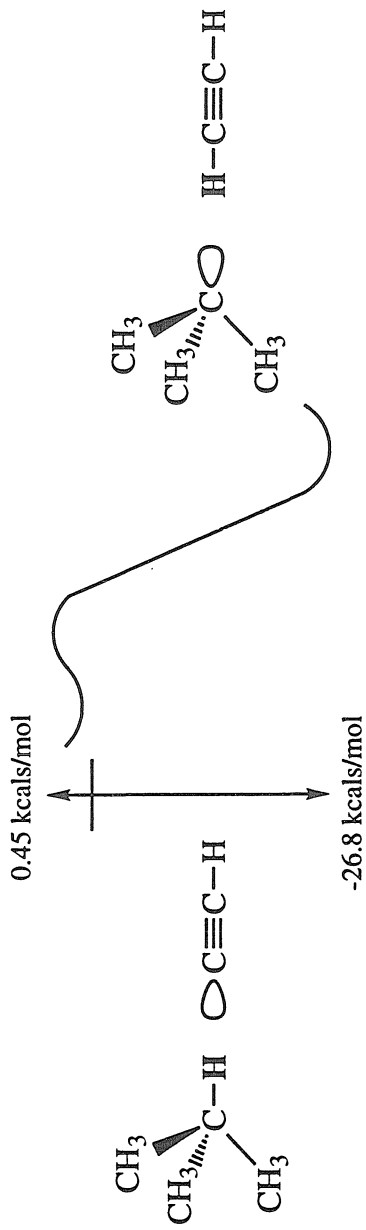


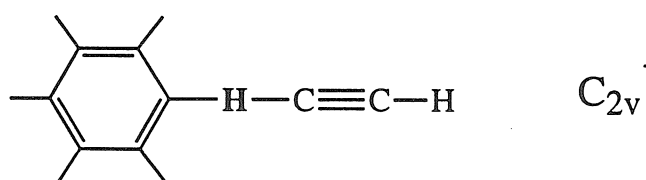
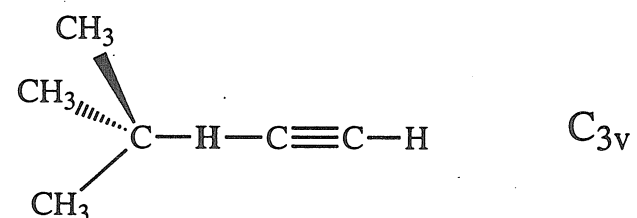
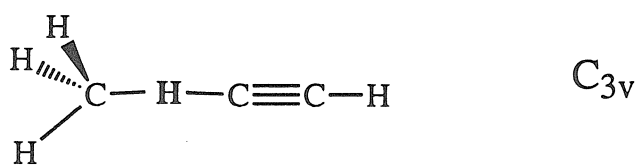
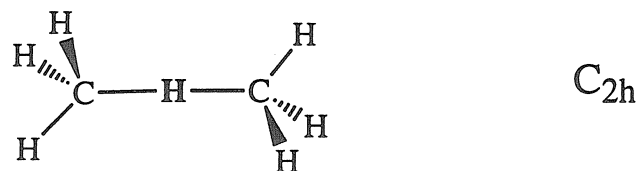
Figure 3: Geometries for the transition states

<u>System</u>	<u>Symmetry</u>
---------------	-----------------

$\text{H}-\text{H}-\text{H}$	$D_{\infty h}$
------------------------------	----------------

$\text{H}-\text{H}-\text{C}\equiv\text{C}-\text{H}$	$C_{\infty v}$
-----------------------------------------------------	----------------

$\text{H}-\text{C}\equiv\text{C}-\text{H}-\text{C}\equiv\text{C}-\text{H}$	$D_{\infty h}$
----------------------------------------------------------------------------	----------------



Chapter 4

The Hessian Biased Force Field for Polysilane Polymers

Abstract

We report a force field (FF) suitable for molecular dynamics simulations of polysilane polymers. This FF, denoted MSXX, was developed using the Hessian biased method to describe accurately the vibrational states, the *ab initio* torsional potential energy surface, and the *ab initio* electrostatic charges of polysilane oligomers. This MSXX FF was used to calculate various spectroscopic and mechanical properties of the polysilane crystal. Stress-strain curves and surface energies are reported. Gibbs molecular dynamics calculations (Nosè, Rahman-Parrinello) were used to predict various materials properties at higher temperatures. Phonon dispersion curves and elastic constants were calculated at various temperatures. Although this polymer is of increasing industrial interest we could find no experimental data with which to compare these predictions.

I. Introduction

Polysilane polymers, $-[-SiH_2-]_n-$ denoted herein as P(SiH), have become of significant interest. The substituted derivatives of P(SiH) can be used as precursors to SiC ceramics, as nonlinear optical materials, as semiconducting polymers, and as photoresists.¹ The polysilane polymers are amorphous and their structural, physical, and electronic properties are not well characterized.²⁻⁵ In order to predict such properties, we have developed a force field expected to be accurate for predicting structural, mechanical, vibrational, and thermodynamic properties.

Section II develops the force field and Section III applies this force field to the prediction of various properties for P(SiH) oligomers. The properties of P(SiH) crystals are predicted in Section IV.

II. Development of the MSXX Force Field

II.A Introduction

The general form of the force field is taken as

$$E = E^{val} + E^Q + E^{vdw}. \quad (1)$$

Here

$$E^Q = C_{coul} \sum_{i>j} \frac{q_i q_j}{R_{ij}} \quad (2)$$

represents the Coulombic interactions between partial charges on the various atoms ($C_{coul} = 332.0637$ converts units so that the R is in Å and E^Q is in kcal/mol),

$$E^{vdw} = \sum_{i>j} E_{ij}^{vdw}(R_{ij}) \quad (3)$$

represents the long-range attraction (London dispersion) and short-range repulsion (Pauli orthogonalization of nonbonded electrons), and

$$E^{val} = E^{bond} + E^{angle} + E^{cross} + E^{torsion} \quad (4)$$

represents all terms involving bonds between atoms and coupling behavior of these bonds.

Our general approach to developing force fields is to emphasize the use of accurate quantum chemical calculations on model systems. Thus the atomic charges [for E_Q] and the torsional potentials about single bonds [for $E_{torsion}$] are taken directly from Hartree-Fock (HF) calculations using good basis sets. The force constant parameters important in describing valence interactions (E_{bond} , E_{angle} , E_{cross}) are taken from the Hessian (second derivative of energy with respect to atomic coordinates) calculated from HF wavefunctions. However the eigenvalues of this Hessian are modified [the Hessian Biased⁶ FF, HBFF] since HF vibrational frequencies are too high. Herein we derive the HBFF for P(SiH) using the model systems: SiH_4 , Si_2H_6 , Si_3H_8 , $n-Si_4H_{10}$. Only the vdW terms, (3), are not based on HF calculations. The vdW parameters for Si and H were obtained from the Dreiding force field⁷ which were based on fits to experimental structural data for simple solids and on extrapolations.

II.B Calculations

For each model system we carried out HF calculations using the 6-31G** basis set. The geometry was optimized at the HF level (using Gaussian 92⁸ and PS-GVB1⁹) and this geometry was used in determining the force field. Comparing to experiment the HF geometry leads to errors of about 0.02 Å in Si-Si distances, 0.01 Å in Si-H distances, and 0.5° in bond angles (see Table 1).

We use the Potential Derived Charges (PDQ) as the partial atomic charges.¹⁰ PDQ are derived by (i) calculating the electron density distribution, $\rho(r)$, from the HF wavefunction, (ii) using $\rho(r)$ to calculate the electrostatic potential on a set of

grid points around the molecule,

$$V^{HF}(R_g) = \int d^3r \frac{\rho(r)}{|R - R_g|_j} \quad (5)$$

and (iii) determining the set of atomic point charges on the various atoms to optimally fit this electrostatic potential,

$$V^Q(R_g) = \sum_i \frac{q_i}{|R_i - R_g|} \approx V^{HF}(R_g) \quad (6)$$

at grid points outside the vdW radii. The PDQ charges (from Gaussian 92) as well as Mulliken populations are shown in Table 2. Based on these calculations we recommend in Table 2 the charges for P(SiH) chains.

II.C The Biased Hessian Method

From *ab initio* HF wavefunctions we calculate⁸ a full Hessian

$$H_{\alpha i, \beta j}^{HF} = \frac{\partial^2 E^{HF}}{\partial R_{\alpha i} \partial R_{\beta j}} \quad (7)$$

where $R_{\alpha i}$ is the α component (x, y, z) of the coordinates of atom i . After mass weighting,

$$\bar{H}_{\alpha i, \beta j}^{HF} = \frac{1}{\sqrt{M_i M_j}} H_{\alpha i, \beta j}^{HF}, \quad (8)$$

the vibrational modes $\{\mathbf{U}_i^{HF}\}$ and vibrational frequencies $\{\nu_i^{HF}\}$ are obtained by solving

$$\bar{\mathbf{H}}^{HF} \mathbf{U}_i^{HF} = \mathbf{U}_i^{HF} \lambda_i^{HF} \quad (9a)$$

where

$$\lambda_i^{HF} = (C_{freq} \nu_i^{HF})^2 \quad (9b)$$

and $C_{freq} = 108.5913$ converts units so that energies are in kcal/mol, distances are in Å, frequencies are in cm^{-1} , and masses are in atomic mass units (C^{12} has mass =

12.0000 amu). This Hessian provides $g(g + 1)/2$ independent pieces of information [666 for Si_4H_{10}], where $g = 3N - 6$ is the number of degrees of freedom. These constraints are sufficient to determine the force field. In contrast, fitting just the frequencies leads to only g conditions [36 for n- Si_4H_{10}]. However, at the HF level the calculated frequencies, ν_i^{HF} , are 10-20% too high. This led to the development of the Hessian Biased method⁶ for FF parameterization in which the force field is fit to the biased Hessian

$$H^{HB} = U^{HF} \lambda^{exp} \tilde{U}^{HF} \quad (10)$$

where \tilde{U} is the transpose and λ^{exp} is the diagonal matrix based on experimental frequencies

$$\lambda_i^{exp} = (C_{freq} \nu_i^{exp})^2. \quad (11)$$

This Hessian has the property that, $H^{HB} U^{HF} = U^{HF} \lambda^{exp}$, that is, the eigenvalues match experiment while the eigenfunctions match HF theory. Thus, H^{HB} has the best available information on the vibrational modes.

In general the optimum geometry at the HF level differs slightly from experiment, raising the question of which structure to use in (10). We use the structures optimized at the Hartree-Fock level of theory. Previously^{6,11} we advocated the use of the experimental structure for determining force constants from the *ab initio* calculations primarily because the internuclear separations (which strongly affect the Hessian) reflect the experimental system. However, in molecules with low frequency torsions, a slight difference in structure can cause a noticeable rotational contamination of the torsional modes. Since we want to use frequency scaling parameters to compare various molecules, it is better to derive the frequencies for all molecules at the *ab initio* minima (rather than at the experimental minimum for molecules where experimental geometries are available and the *ab initio* minimum for those where

experimental geometries are not available). Fortunately, as indicated in Table 1, the differences between the *ab initio* and experimental geometries are small.

II.D The Potential Energy Surface for Torsions

The distribution of conformations in a polymer and the rates of conformational transitions have a strong effect on the properties (moduli, glass temperature); hence, it is critical that the FF lead to the correct relative energies of the minima (e.g., trans versus gauche) and of the barrier heights between them. Thus torsional FF parameters are particularly important for describing amorphous polymers. We use *ab initio* calculations to provide the torsional potential energy surface. With the 6-31G** basis, the torsional potentials calculated from HF wavefunctions are adequate.¹²

The HF calculations lead to a total torsional potential function $E^{HF}(\phi)$ which we want to fit with the FF,

$$\begin{aligned} E^{HF}(\phi) &\cong E^{FF}(\phi) = E_{B,A}^{val}(\phi) + E^Q(\phi) + E^{vdW}(\phi) + E^{tor}(\phi) \\ &= E_{notor}^{FF}(\phi) + E^{tor}(\phi) \end{aligned} \quad . \quad (12)$$

Here $E_{B,A}^{val}$ contains all parts of E^{val} *except* for the torsional term including ϕ . We have already specified how E^Q and E^{vdW} are to be calculated, and the dependence of $E_{B,A}^{val}$ on bonds and angles will be determined in Section D. Thus we *define* the torsional potential as

$$E^{tor}(\phi) \equiv E^{HF}(\phi) - E_{notor}^{FF}(\phi) \quad (13)$$

where

$$E_{notor}^{FF}(\phi) = E_{B,A}^{val}(\phi) + E^Q(\phi) + E^{vdW}(\phi) \quad (14)$$

contains all terms except the torsion, ϕ .

In determining $E^{tor}(\phi)$ from (13), the simplest procedure would be to fix all bonds and angles so that only the torsional angle ϕ changes [thus $E_{B,A}^{val}(\phi)$ would be

constant]. However such rigid rotations about bonds sometimes lead to bad contacts (very short distances between nonbonded atoms). At a bad contact the *ab initio* wavefunctions readjusts the molecular orbitals to minimize repulsion which invalidates the assumption of constant energy in the bond and angle terms. In addition the E^{vdW} derived from fits to experiment may not accurately describe the inner repulsive wall. Consequently (12) is defined by fixing ϕ and optimizing all other degrees of freedom for each conformation to obtain the adiabatic torsional potential. Thus for the HF wavefunction we optimize the other geometric parameters at each ϕ and for $E^{FF}(\phi)$ we do the same. With this procedure $E^{FF}(\phi)$ depends on the FF for bonds and angles, which is determined from fitting H^{HB} (Section II.E). Thus, to determine the nontorsional parts of the FF using HBFF, we use approximate torsional parameters and put zero weights on fitting the torsional modes. Then after determining $E^{tor}(\phi)$ from (13) we redo the HBFF using $E^{tor}(\phi)$ and then use the final bond and angle FF to calculate a new $E^{FF}(\phi)$ and hence a final $E^{tor}(\phi)$. We started with the Dreiding FF and found that one such iteration was generally sufficient.

An alternative to the above procedure is to use the same geometry for both the HF and FF calculations. This could be optimized either for HF or for the FF. The problem is that the HF structure is generally not optimum for the HBFF. Hence fitting to (13) to determine $E^{tor}(\phi)$ would lead to residual forces (due to bond and angle terms in the unoptimized structure). Thus at the top of the barrier, the total forces on the molecule from either HF or HBFF would be nonzero so that it would not be a true maximum.

The HF wavefunction was calculated by fixing the dihedrals of interest (in increments of 15°) and optimizing all other degrees of freedom, leading to the results in Figures 1-3 and Table 3.

For each dihedral, the geometry was optimized using the force field with the dihedral constrained (zero barrier used for this torsion). As indicated in (13) the true torsional energy $E^{tor}(\phi)$ [or $E^{tor}(\phi_1, \phi_2)$, in the case of Si_3H_8] is defined as the difference between $E^{HF}(\phi)$ and $E^{FF}(\phi)$ with the torsion excluded. For SiH_8 we considered the two-dimensional surface where the two torsions (ϕ_1 and ϕ_2) are changed independently. In this case a bicubic spline was fitted to $E^{tor}(\phi_1, \phi_1)$

$$E^{tor}(\phi_1, \phi_2) \approx E^{tor}(\phi_1) + E^{tor}(\phi_2) \quad (15)$$

to generate a denser grid which was in turn fitted to a Fourier series of torsional terms

$$E^{tor}(\phi) = \frac{1}{2} \sum_{m=0}^p K_m [1 + \cos m\phi] = V_0 + \sum_{m=1}^p \frac{1}{2} V_m \cos m\phi, \quad (16)$$

For a single term this becomes

$$E^m(\phi) = \frac{1}{2} K_m (1 + \cos m\phi) \quad (17)$$

where K_m is the barrier.

For a given $J - K$ dihedral there are 3 choices for atom I bonded to J and 3 choices for atom L bonded to K , leading to 9 possible $I - J - K - L$ terms. In POLYGRAF²⁰ the energy for this torsion is written as

$$E_{JK}^{tor} = \frac{1}{9} \sum_{I=1}^3 \sum_{L=1}^3 E_{IJKL}^{tor}(\phi_{IJKL}).$$

Thus each torsional energy $E_{IJKL}^{tor}(\phi)$ is written as if the whole barrier were due to this term, but it is scaled to 1/9 of this value.

Tables 3a-c show $E^{HF}(\phi)$, and $E^{FF}(\phi)$ [or $E^{HF}(\phi_1, \phi_2)$ and $E^{FF}(\phi_1, \phi_2)$ in the case of Si_3H_8]. The fit to the *ab initio* energy surface was Boltzmann weighted so that the errors near the minima are smaller than the errors near the maxima (since

the higher barrier regions will be sampled less in molecular dynamics simulations). We found that a single K_3 term (barrier of 0.94 kcal/mol) for $H - Si - Si - H$ was sufficient for Si_2H_6 . For Si_3H_6 , we assumed the same $H - Si - Si - H$ term and found that for $H - Si - Si - Si$ a single K_3 term (barrier of 0.806 kcal/mol) was sufficient. For $n - Si_4H_{10}$ we assumed the $H - Si - Si - H$ and $H - Si - Si - Si$ terms from Si_2H_6 and Si_3H_8 and added $Si - Si - Si - Si$. Here we found a 3-term potential (with K_1 , K_2 , and K_3) was sufficient. The resultant PES are plotted in Figures 1-3 for HF and HBFF.

II.E Valence Force Field Terms

The bond and angle part of the valence FF is written as

$$E_{B,A}^{val} = E^{bond} + E^{angle} + E^{cross}.$$

We take E^{bond} as a sum over all bond pairs, each of which has the form of a Morse function,⁷

$$E^{Morse}(R) = D_R [\chi^2 - 2\chi] \quad (18a)$$

with

$$\chi = e^{-\alpha(R - R_e)} \quad (18b)$$

and

$$\alpha = \sqrt{\frac{k_R}{2D_R}}. \quad (18c)$$

This includes anharmonicity and allows bond dissociation. Here there are three independent parameters R_e , k_R , and D_R . However D_R is not sensitive to the Hessian or geometry; Hence, we choose D_R based on the experimental bond energy (it was not optimized).

We take E^{angle} as a sum over all six angle terms $I - J - K$ for each atom J , where each angle term is described with the cosine angle form,⁷

$$E^{cosine}(\theta) = \frac{C}{2} [\cos \theta - \cos \theta_e]^2 \quad (19a)$$

with

$$C = \frac{k_\theta}{\sin^2 \theta_e}. \quad (19b)$$

This form leads correctly to $dE/d\theta = 0$ for $\theta = 0, 180^\circ$ and has a barrier of

$$E^{barrier} = \frac{C}{2} [1 + \cos \theta_e]^2. \quad (20)$$

We found that bond-bond cross-terms

$$E_{1BB} = K_{RR} (r_1 - r_1^e) (r_2 - r_2^e) \quad (21)$$

sharing an apex atom (e.g., IJ and JK for the atoms I and K bonded to J) are generally useful when the two are equivalent (e.g., $Si - H/Si - H$ at SiH_3 or SiH_2 groups). However, $Si - Si/Si - H$ at the SiH_3 group does not have much effect on the force field. This is because the splitting between equivalent terms is dominated by off-diagonal interactions whereas analogous couplings for inequivalent bonds can be built into the force field by modifying the diagonal terms. Thus we include bond-bond cross terms only for equivalent bonds.

Bond-angle cross terms (e.g., bond IJ with angle IJK),

$$E_{1BA} = D_{r\theta} (r_1 - r_1^e) (\cos \theta_1 - \cos \theta_1^e) \quad (22)$$

are necessary for a good description of the vibrations. For a given $I - J - K$ there are two such terms, one for r_{IJ} and one for r_{JK} .

In addition we find that one-center angle-angle cross terms (involving bonds defining two angles sharing a common bond) are important,

$$E_{1AA} = F_{\theta\theta} (\cos \theta_1 - \cos \theta_1^e) (\cos \theta_2 - \cos \theta_2^e). \quad (23)$$

The sign and magnitude of these terms are difficult to predict *a priori*. Hence we started with various combinations of sign and magnitude and allowed the optimization to determine both the sign and magnitude of these coupling constants.

For long chain molecules, we found that 2-center angle-angle cross terms are also important,

$$E_{2AA} = G_{\theta\theta} (\cos \theta_1 - \cos \theta_1^e) (\cos \theta_2 - \cos \theta_2^e) f(\phi). \quad (24)$$

Thus for the dihedral $I - J - K - L$, θ_1 corresponds to the IJK angle and θ_2 corresponds to JKL . For disilane such terms determine the splitting between rocking modes of different symmetries. In the case of polyethylene,¹¹ they are essential in reproducing the stiffness in the chain direction. For group IV and III/V solids (e.g., diamond, silicon, GaAs, etc.) they are necessary to describe the mode softening of the transverse acoustic (TA) mode near the zone boundary.¹³ In P(SiH), we find that they are important for predicting the modulus in the chain direction. For semiconductors the factor $f(\phi)$ is taken as $f(\phi) = \frac{1}{3} [1 - \frac{2}{3} \cos(\phi)]$ so that $f(0^\circ) = f(180^\circ) = 1$ and $f(60^\circ) = f(240^\circ) = 0$. This is because only trans coupling is important. For P(SiH) $f(\phi)$ is taken as $f(\phi) = 1 - \cos(\phi)$.

Summarizing we take

$$E_{cross} = \sum E_{1BB} + \sum E_{1BA} + \sum E_{1AA} + \sum E_{2AA}. \quad (25)$$

II.F Scaling of Ab Initio Frequencies

For both Si_3H_8 and $n-Si_4H_{10}$ the set of experimental frequencies is incomplete. In order to estimate of the experimentally undetermined modes, we scale the *ab initio* frequencies for these modes using scale factors (the ratio of the experimental frequency to the *ab initio* frequency) obtained from observed modes. This works well because within a particular class of vibrations the scale factor is nearly

constant, even between different molecules. For example, it is 0.901 ± 0.016 for the SiH bending modes of Si_3H_8 . (A further refinement is to calculate separate average scales for the rocking, wagging, and scissor SiH -bending modes.) Table 4 shows the scale factors derived for each molecule. Because the scales vary little from molecule to molecule, the scaling procedure can be applied even to molecules with no experimental frequencies. Table 5 shows the Si_5H_{12} scaled frequencies (from HF) and those predicted by the MSXX (from $n - Si_4H_{10}$). Here the MSXX vibrations differ from the HF scaled values by 13 cm^{-1} (rms error), about the same as for cases where experiment is available.

Torsions do not follow the same scaling trend as bending and stretching modes. However we base all torsional parameters on the HF torsion curves (Section III.C) rather than on scaled torsional vibrations.

II.G Optimization of Parameters

We used the program FFOPT¹⁴ developed by Yamasaki, Dasgupta, and Goddard to optimize the valence HBFF parameters. This uses Singular Value Decomposition (SVD) and emphasizes changes in parameters that most affect the properties of interest (and to eliminates parameter redundancies).

III. Polysilane Oligomers

III.A SiH_4

The vibrational frequencies for silane are shown in Table 6 and the silane force field is shown in Table 7a. HBFF exactly reproduces the geometry and the experimental frequencies.¹⁵ The MSXX (from $n - Si_4H_{10}$) leads to slightly low (about 1%) frequencies for silane, and the inaccuracy in applying the MSXX to disilane and trisilane is much smaller. (Table 6 also shows the accuracy of the silane HBFF for predicting the frequencies of deuterated silane.¹⁵) This indicates

the robustness of the MSXX.

The MSXX FF parameters from the P(SiH) oligomers are shown in Table 7a (the calculated oligomer geometries are in Table 1). The MSXX FF leads to excellent geometries and frequencies.

III.B Si_2H_6

Disilane is the largest oligomer of P(SiH) having a complete set of experimental vibrational assignments.¹⁶ In addition, all the isotopic shifts, except for the torsional mode, are available for fully deuterated disilane. Table 8 shows predicted frequencies, where we find an RMS difference of 4.8 cm^{-1} between HBFF and experiment.¹⁶ The HBFF accurately reproduces the geometry as shown in Table 1. The validity of the force field is shown by its accurate prediction of the Si_2D_6 experimental frequencies¹⁷ as shown in Table 8.

Included in the complete set of frequencies for disilane is the torsional frequency (determined indirectly from a two photon process). However we do not use this in our fit. As discussed above the torsional potential is fitted to the entire torsional potential surface. Disilane is the only P(SiH) oligomer for which we can compare the torsional frequency for the single bond rotational potential to experimental data. Figure 1 and Table 3a show the accurate match of the *ab initio* and HBFF torsional potentials over the entire dihedral angle range. This accuracy comes at the modest cost of an error of 8.2 cm^{-1} in the torsional frequency.

III.C Si_3H_8

Silylpropane is the smallest model compound containing the $[-SiH_2-]$ repeating unit of P(SiH). Some experimental data (13 of 27 modes)¹⁸ are available on the vibrational frequencies of Si_3H_8 , but a complete set of experimental frequencies for the isolated molecule in the gas phase is not available. Consequently,

for each class we considered only the experimentally known vibrations to obtain the accurate scale factor for that class, which was then applied to all *ab initio* frequencies to predict the complete set of “experimental” frequencies. Using scales from within the same molecule leads to very small standard deviations of the scales and thus is likely to yield accurate scaling of the experimentally unassigned modes. The average error between the HBFF frequencies and the experimentally available frequencies¹⁸ is 7.7 cm^{-1} (6.0 cm^{-1} including the scaled HF frequencies). Table 9 also shows the frequencies for two deuterated species to compare with future experimental results. We find that fitting the force field to experiment requires the use of different valence terms for the SiH_2 hydrogens and the SiH_3 hydrogens (we use the $H - \text{Si} - \text{Si} - H$ torsional potential transferred from disilane). Using the MSXX FF from $n - \text{Si}_4\text{H}_{10}$ to calculate the modes of Si_3H_8 leads to good accuracy, especially for the geometry (Table 1). This justifies the transferability of the HBFF between molecules and indicates that the HBFF description of P(SiH) or the other P(SiH) oligomers should be accurate.

The torsional modes were not obtained from HBFF. In the Si_3H_8 force field we include the disilane H-Si-Si-H torsional potential and fit a Fourier series of torsions to the combinations of rotations of the two H-Si-Si-Si dihedrals. Figure 2 and Table 3b show the accuracy of the HBFF torsional potential energy surface.

III.D $n - \text{Si}_4\text{H}_{10}$

$n - \text{Si}_4\text{H}_{10}$ is the smallest oligomer which includes all the valence terms necessary to model larger oligomers and P(SiH). Again only a partial assignment from experimental spectra¹⁸ is available for n-silylbutane. We follow the same procedure used for scaling of the silylpropane frequencies. Table 10 shows the HF frequencies, the experimental assigned frequencies and the scales used for modes not observed. Table 10 also shows the narrow range for similar scales. The HBFF procedure re-

produces the experimental frequencies and scaled HF frequencies to 6.2 cm^{-1} rms error. The geometry is accurately reproduced as shown in Table 1.

For $n-Si_4H_{10}$ we also develop the MSXX-R FF which does not distinguish between the SiH_3 and SiH_2 . We find that MSXX-R is only slightly worse than the MSXX, as shown in Table 10. We use the valence terms describing the central silicons of MSXX to describe the larger oligomers and the polysilane crystals. The n-silylbutane HBFF not only includes all the terms to simulate the smaller oligomers, it also includes all the terms necessary to model the larger oligomers and P(SiH) and thus can be used to predict the properties of P(SiH) of arbitrary chain length.

The torsional mode was not scaled, but was calculated by fitting a Fourier series to the rotations of the molecule about the Si-Si-Si-Si dihedral. The H-Si-Si-Si and H-Si-Si-H torsional potentials were transferred from silylpropane and disilane, respectively and not varied. Figure 3 and Table 3c show the HBFF and the *ab initio* torsional potential.

III.E $n-Si_5H_{12}$

The $n-Si_5H_{12}$ molecule has not been observed experimentally. We calculate HF/6-31G** and MP2/6-31G** vibrational frequencies to validate the MSXX force field (from Si_4H_{10}). Scales from the smaller oligomers are applied to the $n-Si_5H_{12}$ HF vibrational frequencies to obtain scaled HF frequencies which can be compared to frequencies calculated using the MSXX. Table 5 shows the MSXX frequencies and the scaled HF frequencies. The RMS difference is less than 12 cm^{-1} with most modes differing less than 2%. Either method provides an acceptable prediction of experimental frequencies; however scaled *ab initio* calculations require substantially greater computational time. MP2 *ab initio* calculations take substantially more time than scaled HF calculations but still overestimate experiment by 3-8% (Table

5), with the exception of the low energy skeletal modes. Since scaled HF and MSXX predictions are generally within a percent of experimental frequencies, we conclude that MSXX is the most cost-effective approach to predicting frequencies in good agreement with experiment. Table 11 compares the geometries for $n-Si_5H_{12}$ from HF and from the MSXX. The differences are small, with the largest error (1.1°) for the $Si - Si - Si$ central angle.

IV. Polysilane

We base the FF for polysilane polymers on the parameters for the central atoms of the HBFF for $n - Si_4H_{10}$ in Table 7a. We refer to this as the MSXX FF (see Table 7b). The charges for polysilane polymer were based on the PDQ atomic charges for the central SiH_2 group of $n - Si_5H_{12}$ (See Table 2).

Particularly important for calculations on P(SiH) polymers are the Si-Si-Si bends denoted as accordion modes in Tables 5, 9, and 10. This mode is prominent on the Raman spectra for long alkanes and extrapolating the frequency of this mode to infinite alkanes leads to an excellent prediction of the Young's modulus (see reference 11 for discussion).

The MSXX FF was used to calculate the properties of the crystal built with the all trans conformation of P(SiH). This is analogous to polyethylene (PE) except that structures with both one and two chains per cell were considered. Table 12 shows the structure and mechanical properties of the crystal at 0, 77 and 300K. The bulk modulus at 0K is 13.10 GPa. The Young's moduli calculated are 11.94, 110.57, and 18.64 GPa at 0K which compare to 9.0, 337.0, and 9.4 for PE. PE is much stiffer along the chain direction than P(SiH) while being softer perpendicular to the chains at low temperatures and being similar in stiffness to P(SiH) perpendicular to the chains at temperatures above 300K. Because of the anharmonicity of vdW and

electrostatic interactions between chains, the Young's moduli perpendicular to the chain direction decrease dramatically with temperature (by $\approx 65\%$ for 0 to 300K). The decrease in the Young's moduli of polyethylene is much smaller ($\approx 35\%$ for 0 to 300K). The elastic constants of P(SiH) behave similarly to those of polyethylene. Thus C_{22} , the elastic constant along the chain direction, decreases by only 15% from 0 to 300K. In PE the decrease is 5.9%. C_{11} and C_{33} for deformations perpendicular to the chain direction show a decrease of 65% while in PE the decrease is $\approx 40\%$. The relative decrease in the deformation properties with temperature is large relative to polyethylene (see Table 12) both along the chain direction and perpendicular to it indicating that both the valence and non-bond interactions are more anharmonic for P(SiH) than for PE.

The properties at 77K and 300K were calculated by averaging the crystal structures from the last 20 ps of a 30 ps Gibbs molecular dynamics calculation (Nosè plus Rahman-Parrinello¹⁹) at several temperatures to calculate the thermal expansion tensor. Using the thermal expansion tensor we calculated the lattice parameters at the desired temperatures and calculated the properties of the crystal at that desired temperature. (After reminimizing the atomic positions for the new lattice constants.)

The cohesive energy of the crystal is calculated to be 3.816 kcal/mol-SiH₂ (Table 13). This compares with 1.8701 kcal/mol-CH₂ for polyethylene calculated by Karasawa et al.¹¹ also using the biased Hessian approach. Their result compared favorably to experiment where the cohesive energy is measured to be 1.84 kcal/mol-CH₂. The larger elastic constants of PSi compared to PE perpendicular to the chain direction indicate the relatively stronger non-bond interactions and thus a larger cohesive energy.

Tables 14 and 15 show the vibrational frequencies for the crystal and for the

infinite single chain, respectively. Calculations by Cui et al.⁵ on single unpacked chains (ignoring vdW and Coulomb) are within 5-30 cm⁻¹ of our results. Our results show that the inclusion of coulombic and vdW forces in the MSXX FF strongly affects interactions between neighboring chains, as shown by the changes in the predicted vibrational frequencies between the packed and unpacked P(SiH). Our single chain frequencies are in better agreement with many of the experimental frequencies (Table 15) than our packed P(SiH) frequencies. This may be because the samples are not very crystalline (including silicon-like clusters and metastable gauche configurations), leading to an inefficiently packed local structure better approximated by a single chain.

Figure 4 shows the phonon dispersion curves for the all-trans polysilane crystal (there are no experimental numbers). The low energy bands depend strongly upon the van der Waals and coulombic interactions as well as the torsional force constant. In the case of PE (Karasawa et al.¹¹) the MSXX led to average errors of 7.9 cm⁻¹ for $n-C_4H_{10}$ and 24 cm⁻¹ for the crystal. The MSXX force field reproduces the vibrational frequencies of $n-Si_4H_{10}$ with an error of 6 cm⁻¹ but we expect larger errors for the crystal.

Figure 5a shows stress-strain curves for stresses along the unit cell axes (perpendicular to the chain) In these calculations we used a super cell consisting of 32 primitive cells. Although the Young's modulii perpendicular to the chain direction are larger for P(SiH) than for PE the yield stress is similar. This is the result of the higher anharmonicity of the P(SiH) non-bond interactions which fall off faster than those of PE. In the case of PE, shear perpendicular to the chain direction eventually leads to a transition to a metastable monoclinic phase. Shearing P(SiH) using our force field did not lead to any stable phases. Minimization from any structure arrived at by shearing always led back to the orthorhombic unit cell.

The surface energy is calculated by stretching the crystal perpendicular to the surface until the crystal breaks (Figure 5b). From the curves in Figure 6 we derive surface energies of 63.5 dyn/cm for the (100) surface and 66.9 dyn/cm for the (001) surface (using a conversion factor of 694.8 to convert from kcal/mol- \AA^2 to erg/cm³). This compares with 106.8 dyn/cm (100) and 109.2 dyn/cm (001) for the analogous surfaces of polyethylene. The (100) surface has two SiH₂ groups per unit cell, leading to a surface energy per SiH₂ of 1.698 kcal/mol while the (001) surface has 4 SiH₂ groups per unit cell leading to a surface energy of 1.609 kcal/mol. This compares with 0.938 kcal/mol and 0.720 kcal/mol for the analogous surfaces of polyethylene. We know of no experimental information on such properties for P(SiH). Assuming only nearest-neighbor fiber-fiber interactions, we would expect a surface energy of $\frac{1}{3}$ the cohesive energy of the crystal. This would predict a surface energy of 1.42 kcal/mol for both the (100) and (001) surfaces, which is low by $\approx 15\%$.

Figure 6 shows the predicted heat capacity (C_v), entropy, enthalpy and free energy versus temperature (again, we know of no experimental data).

V. Summary

In this paper we develop the MSXX force field for P(SiH) that should be accurate and useful for a variety of structural, thermodynamic, spectroscopic, mechanical, and surface properties. The method follows the procedure developed by Karasawa et al.¹¹ for PE (modified for incomplete experimental vibrational data). For PE the substantial amount of data on experimental properties validated the accuracy attained with this procedure. For P(SiH) sample quality is poor and this procedure is used to predict the properties of crystalline P(SiH) in advance of experiment.

Spectroscopic force fields (SFF) usually omit the electrostatic (Q) and van der Waals (vdW) nonbond terms since the geometry is considered fixed. For molecular dynamics (MD) calculations the FF must describe how the energy changes with geometry, and hence the MSXX FF includes these intramolecular nonbond terms. They are small for P(SiH) oligomers except for torsional modes, where they make significant contributions. On the other hand, the bulk properties of P(SiH) depend greatly on the intermolecular interactions.

The HBFF⁶ combines experimental vibrational frequencies with the normal mode description of the vibrations from *ab initio* calculations. For P(SiH) oligomer systems it was necessary to extend the HBFF approach to handle systems with incomplete spectroscopic information through scaling.

The validity of the resulting MSXX force field is tested by calculating the properties for *n*-Si₅H₁₂, where we find the modes to be within 2% of the scaled *ab initio* (HF/6-31G**) results (no experimental data are available). MSXX predicts a Si-Si-Si bond angle 1.13 ° larger than HF, which although not a large error, will manifest itself in predicting a slightly larger bond angle for the crystal. Despite the slight difference in the geometry the MSXX predicts the vibrational frequencies accurately.

The MSXX predictions should be useful for predicting the spectra of larger oligomers where assignments are incomplete (particularly for torsional modes and skeletal modes) and for the P(SiH) condensed phase where there are no assignments.

We used the Nosè formalism¹⁹ of canonical molecular dynamics to extract thermodynamic properties of polysilane from the MD simulations. Properties at various temperatures were averaged from dynamics calculations and thermal expansion coefficients were derived for temperatures up to 450K. Other properties were calculated using the unit cell at the desired temperature.

References

1. R. D. Miller and J. Michl, *Chem. Rev.* **89**, 1359 (1989) and references therein.
2. J. R. Damewood Jr. and R. West, *Macromolecules* **18**, 159 (1985).
3. J. M. Zeigler, *Synth. Met.* **28**, C581 (1989).
4. J. W. Mintmire, *Phys. Rev. B* **39**, 13350 (1989).
5. C. X. Cui and M. Kertesz, *Macromolecules* **25**, 1103, (1992).
6. S. Dasgupta, and W.A. Goddard III, *J. Phys. Chem.* **90**, 7207 (1989).
7. S. L. Mayo, B. D. Olafson, and W. A. Goddard III, *J. Phys. Chem.* **92**, 7488 (1990).
8. M. J. Frisch, G. W. Trucks, M. Head-Gordon, P. M. W. Gill, M. W. Wong, J. B. Foresman, B. G. Johnson, H. B. Schlegel, M. A. Robb, E. S. Replogle, R. Gomperts, J. L. Andres, K. Raghavachari, J. S. Binkley, C. Gonzalez, R. L. Martin, D. K. Fox, D. J. Defrees, J. Baker, J. J. P. Stewart, and J. A. Pople, *Gaussian 92 Revision*, Gaussian, Inc. Pittsburgh, PA, (1992).
9. PS-GVB, Murco Ringnalda, Jean-Marc Langlois, Burnham H. Greeley, Thomas V. Russo, Richard P. Muller, Bryan Marten, Youngdo Won, Robert E. Donnelly, Jr., W. Thomas Pollard, Gregory H. Miller, William A. Goddard III, and Richard A. Friesner, *PS-GVB v1.03*, Schroedinger, Inc., 1994. M. N. Ringnalda, Y. Won, and R. A. Friesner, *J. Chem. Phys.* **93**, 3397 (1990). J-M. Langlois, R.P. Muller, T. R. Coley, W. A. Goddard III, M. N. Ringnalda, Y. Won, and R. A. Friesner, *J. Chem. Phys.* **92**, 7488 (1990).
10. L. E. Chirlian and M. M. Franci, *J. Comp. Chem.*, **8**, 894 (1987).
11. N. Karasawa, S. Dasgupta, and W. A. Goddard III, *J. Phys. Chem.* **95**, 2260 (1991).
12. D. Cremer, J. S. Binkley, J. A. Pople, and W. J. Hehre, *J. Am. Chem. Soc.*

96, 6900 (1974).

13. H. L. McMurry, A. W. Solbrig Jr., J. K. Boyter, and C. Noble, *J. Phys. Chem. Solids* **28**, 2359 (1967).
14. T. Yamasaki, S. Dasgupta, and W.A. Goddard, III, *J. Chem. Phys.*, submitted.
15. H. W. Kattenberg and A. Oskam, *J. Mol. Spectry.* **49**, 52 (1974).
16. J. R. Durig and J. S. Church, *J. Chem. Phys.* **73**, 4784 (1980).
17. D. C. McKean, *Spectrochimica Acta* **48A**, 1335 (1992).
18. F. Feher and H. Fisher, *Naturwissenschaften* **51**, 461, (1969).
19. (a) T. Cagin, W. A. Goddard III, and M. L. Ary, *J. Comp. Polymer Physics* **I**, 241 (1991). (b) T. Cagin, N. Karasawa, S. Dasgupta, and W. A. Goddard III, *Mat. Res. Soc. Symp. Proc.* **278**, 61 (1992). (c) S. Nosé, *J. Chem. Phys.* **81**, 511 (1984). (d) M. Parrinello and A. Rahman, *J. Appl. Phys.* **52**, 7182 (1981).
20. POLYGRAF is from Molecular Simulations Inc., Burlington, Massachusetts.

Table 1. Structural parameters. Distances are in Å, angles are in degrees.

Molecule	Feature ^{b,e}	MSXX ^c FF	HF/6-31G**	<i>n</i> - <i>Si</i> ₄ <i>H</i> ₁₀ FF ^d	Experimental ^a
<i>SiH</i> ₃	<i>Si</i> – <i>H</i>	1.476	1.476		
	<i>H</i> – <i>Si</i> – <i>H</i>	111.01	111.01		110.6
<i>SiH</i> ₄	<i>Si</i> – <i>H</i>	1.476	1.476	1.476	1.481
<i>Si</i> ₂ <i>H</i> ₆	<i>Si</i> – <i>Si</i>	2.353	2.353	2.356	2.331
	<i>H</i> – <i>Si</i>	1.479	1.479	1.479	1.492
	<i>H</i> – <i>Si</i> – <i>Si</i>	110.35	110.35	110.50	110.3
<i>Si</i> ₃ <i>H</i> ₈	<i>Si</i> – <i>Si</i> _c	2.358	2.357	2.351	
	<i>H</i> _c – <i>Si</i> _c	1.482	1.482	1.482	
	<i>H</i> _{ip} – <i>Si</i>	1.479	1.478	1.477	
	<i>H</i> _{op} – <i>Si</i>	1.479	1.479	1.478	
	<i>Si</i> – <i>Si</i> _c – <i>Si</i>	112.73	112.56	108.83	
	<i>H</i> _{ip} – <i>Si</i> – <i>Si</i> _c	110.74	110.69	110.84	
	<i>H</i> _{op} – <i>Si</i> – <i>Si</i> _c	110.17	110.16	109.75	
	<i>H</i> _c – <i>Si</i> _c – <i>Si</i>	109.07	109.12	109.98	
	<i>H</i> _{op} – <i>Si</i> – <i>Si</i> _c – <i>Si</i>	59.77	59.77	59.65	
	<i>Si</i> – <i>Si</i> _c	2.358	2.357		
<i>n</i> – <i>Si</i> ₄ <i>H</i> ₁₀	<i>Si</i> _c – <i>Si</i> _c	2.362	2.361		
	<i>H</i> _c – <i>Si</i> _c	1.481	1.482		
	<i>H</i> _{ip} – <i>Si</i>	1.480	1.479		
	<i>H</i> _{op} – <i>Si</i>	1.479	1.479		
	<i>Si</i> – <i>Si</i> _c – <i>Si</i> _c	113.06	112.73		
	<i>H</i> _{ip} – <i>Si</i> – <i>Si</i> _c	110.86	110.73		
	<i>H</i> _{op} – <i>Si</i> – <i>Si</i>	110.01	110.08		
	<i>H</i> _c – <i>Si</i> _c – <i>Si</i>	109.22	109.30		
	<i>H</i> _{op} – <i>Si</i> – <i>Si</i> _c – <i>Si</i> _c	59.76	59.79		
	<i>H</i> _c – <i>Si</i> _c – <i>Si</i> _c – <i>Si</i>	58.32	58.48		

^a References 15 and 16.^b *Si*_c and *H*_c denote atoms of *SiH*₂ groups. These are used in the P(SiH) FF.^c Separate FF for each molecule, parameters in Table 6a.^d Using the MSXX FF of *n*-*Si*₄*H*₁₀ to calculate the structure of the other molecules.^e *ip* and *op* denote in-plane and out-of-plane hydrogens, respectively.

Table 2. Atomic charges (electron units) from HF calculations on linear (all trans) chains. Based on these results we recommend the following: (i) $Q_{Si} = 0.30$, $Q_H = -0.15$ for SiH_2 of P(SiH). (ii) $Q_{Si} = 0.44$, $Q_H = -0.14$ for terminal SiH_3 groups, and (iii) $Q_{Si} = 0.23$ and $Q_H = -0.125$ for SiH_2 next to a terminal group.

Atom ^a	Si_2H_6		Si_3H_8		Si_4H_{10}		Si_5H_{12}	
	PDQ	Mulliken	PDQ	Mulliken	PDQ	Mulliken	PDQ	Mulliken
Si (SiH_2)'							0.2971	0.2878
H (SiH_2)'							-0.1485	-0.1508
Si (SiH_2)			0.1550	0.2287	0.2211	0.2565	0.2287	0.2617
H (SiH_2)			-0.1042	-0.1491	-0.1274	-0.1501	-0.1260	-0.1495
Si (SiH_3)	0.3936	0.4752	0.4714	0.5096	0.4829	0.5175	0.4494	0.5138
H (SiH_3)-ip	-0.1312	-0.1584	-0.1369	-0.1567	-0.1458	-0.1569	-0.1370	-0.1570
H (SiH_3)-op			-0.1424	-0.159	-0.1518	-0.1584	-0.1446	-0.1584

^a Primes signify central SiH_2 . *ip* and *op* denote in-plane and out-of-plane hydrogens, respectively.

Table 3a. The torsional potential (kcal/mol) for Si_2H_6 . All bonds and angles were optimized at each ϕ . E_{FF}^{tor} is described with a single 3-fold term (17) with a barrier $K_3 = 0.94$ kcal/mol (see Table 7a).

ϕ	HF	MSXX
60.000	0.00000	0.00000
45.000	0.13500	0.14490
30.000	0.47000	0.49150
15.000	0.82300	0.83280
0.0000	0.97400	0.97290

Table 3b. The torsional potential (kcal/mol) of Si_3H_8 for various values of the two dihedral angles, ϕ_1 and ϕ_2 . Same conventions as Table 3a. $E_{tor}^{FF}(\phi)$ is described using the $H - Si - Si - H$ torsion from Table 3a plus a single 3-fold $H - Si - Si - Si$ torsion with barrier of $K_3 = 0.806$ kcal/mol (see Table 7a).

ϕ_1	ϕ_2	MSXX Torsional Energies						HF Torsional Energies			
		180	165	150	135	120	180	165	150	135	120
180	0	0.1205	0.4241	0.7504	0.8995	0	0.1150	0.3389	0.6884	0.8161	
165	0.1205	0.2478	0.5568	0.8839	1.0278	0.1150	0.2058	0.4897	0.8111	0.9728	
150	0.4241	0.5568	0.8734	1.2069	1.3511	0.3389	0.4897	0.8082	1.1716	1.3585	
135	0.7504	0.8839	1.2069	1.5505	1.7011	0.6884	0.8111	1.1716	1.5656	1.7533	
120	0.8995	1.0278	1.3511	1.7011	1.8601	0.8161	0.9728	1.3586	1.7533	1.9196	
105	0.7504	0.8839	1.2069	1.5505	1.7011	0.6884	0.8111	1.1716	1.5656	1.7533	
90	0.4241	0.5568	0.8734	1.2069	1.3511	0.3389	0.4897	0.8082	1.1716	1.3585	
75	0.1205	0.2478	0.5568	0.8839	1.0278	0.1150	0.2058	0.4897	0.8111	0.9727	
60	0.0000	0.1205	0.4241	0.7504	0.8995	0.0000	0.1150	0.3389	0.6884	0.8161	
45	0.1205	0.2478	0.5568	0.8839	1.0278	0.1150	0.2058	0.4897	0.8111	0.9727	
30	0.4241	0.5568	0.8734	1.2069	1.3511	0.3389	0.4897	0.8082	1.1716	1.3585	
15	0.7504	0.8839	1.2069	1.5505	1.7011	0.6884	0.8111	1.1716	1.5656	1.7533	
0	0.8995	1.0278	1.3511	1.7011	1.8601	0.8161	0.9728	1.3586	1.7533	1.9196	

Table 3c. The torsional potential (kcal/mol) for central torsion angle of $n\text{-Si}_4\text{H}_{10}$. For each ϕ all other structural parameters were optimized (at either the HF or FF level). Same conventions as Table 3a. The $E_{tor}(\phi)$ was described with the $H\text{-Si-Si-H}$ and $H\text{-Si-Si-Si}$ terms from Tables 3a and 3b plus a three term Si-Si-Si-Si potential (see Table 7a). The last column is the Si-Si-Si-Si torsional potential (after eliminating the other nonbond and valence torsions).

ϕ	HF	MSXX	E_{tor}
0	1.5631	1.5628	0.7189
15	1.3380	1.3302	0.6682
30	0.8461	0.8345	0.5271
45	0.3893	0.3891	0.3455
60	0.1539	0.1542	0.1891
75	0.1639	0.1504	0.0734
90	0.3238	0.3189	-0.0324
105	0.5261	0.5376	-0.1005
120	0.6735	0.6458	-0.0657
135	0.5359	0.5478	-0.0787
150	0.3190	0.3110	-0.0247
165	0.0986	0.0883	0.0018
180	0.0000	0.0000	0.0000

Table 4. Scale factors (ratio of experimental value to HF value) for estimating experimental frequency from HF vibrational frequencies. Standard deviations are in parentheses.

Mode	SiH_4	Si_2H_6	Si_3H_8	$n-Si_4H_{10}$
Si-H Stretch	0.9255 (0.0035)	0.9113 (0.0215)	0.9163 (0.0015)	0.9140 (0.001)
Si-H Bend	0.9125 (0.0191)	0.8972 (0.0126)	0.9009 (0.0162)	0.9081 (0.0203)
Si-Si Stretch	-	0.9100	0.9370	0.9177
	-	-	(0.0226)	(0.0055)
Si-Si-Si Bend	-	-	1.025	-
	-	-	-	-

Table 5. Predicted vibrational frequencies (cm⁻¹) for $n - Si_5H_{12}$.

Mode	Sym	Character	MSXX	Scaled	HF	MP2
1	B_2	Torsion (Si-Si)	24	23	23	52
2	A_2	Torsion (Si-Si)	26	26	26	43
3	A_1	Si-Si-Si bend	47	45	49	56
4	A_2	Torsion (SiH ₃)	93	89	89	111
5	B_2	Torsion (SiH ₃)	95	90	90	112
6	B_1	Si-Si-Si bend	104	105	115	112
7	A_1	Si-Si-Si bend	138	137	131	124
8	B_2	SiH ₂ rock	303	301	331	300
9	A_2	SiH ₂ rock	322	321	353	329
10	A_1	Si-Si Stretch	366	366	399	383
11	B_2	twist-rock	379	376	414	391
12	B_1	Si-Si stretch	392	397	433	414
13	A_1	Si-Si stretch	446	441	482	463
14	A_2	Si-Si stretch	457	464	506	483
15	B_1	twist	464	461	508	487
16	B_1	SiH ₃ rock	505	491	542	510
17	A_1	SiH ₃ rock	515	526	581	550
18	B_2	SiH ₂ rock	568	567	624	596
19	A_2	twist	646	647	711	674
20	B_1	wag	665	655	721	678
21	B_2	twist	705	703	773	736
22	A_2	wag	732	733	806	768
23	A_1	twist	740	742	816	770
24	B_1	wag	797	799	879	830
25	B_1	SiH ₃ s-def	892	890	982	931
26	A_1	SiH ₃ s-def	892	895	988	938
27	A_1	SiH ₂ scissor	926	927	1019	972
28	B_1	SiH ₂ scissor	929	929	1022	973
29	A_1	SiH ₂ scissor	933	931	1024	978
30	A_2	SiH ₃ def	939	937	1034	993
31	B_2	SiH ₃ def	939	938	1034	993
32	B_1	SiH ₃ def	941	941	1038	997
33	A_1	SiH ₃ def	941	944	1041	999
34	B_2	SiH ₂ stretch	2112	2117	2315	2285
35	A_2	SiH ₂ stretch	2113	2119	2318	2287
36	B_1	SiH ₂ stretch	2122	2120	2319	2290
37	A_1	SiH ₂ stretch	2122	2121	2320	2294
38	B_2	SiH ₂ stretch	2123	2125	2325	2299
39	A_1	SiH ₂ stretch	2124	2128	2328	2304
40	B_1	SiH ₃ stretch	2142	2141	2343	2305
41	A_1	SiH ₃ stretch	2142	2142	2343	2306
42	B_1	SiH ₃ stretch	2142	2142	2343	2319
43	A_1	SiH ₃ stretch	2142	2143	2344	2319
44	A_2	SiH ₃ stretch	2144	2144	2345	2319
45	B_2	SiH ₃ stretch	2144	2146	2348	2320
Error			4.0	0	116.7	92.8

Table 6. Vibrational frequencies (cm^{-1}) for SiH_4 .

Mode	Sym	Char	HBFF	Exper ^a	HF ^b	MP2 ^b	MSXX	Scale	Exper ^a	MCXX
									$\text{Si}D_4$	$\text{Si}D_4$
1	T2		914.0	914.0	1017.1	973.7	883.1	0.899	674	669.9
2	E		975.0	975.0	1053.4	1017.6	970.7	0.926	685	689.5
3	A1		2187.0	2187.0	2370.0	2339.3	2151.6	0.923	1563	1546.4
4	T2		2191.0	2191.0	2360.6	2349.9	2154.2	0.928	1598	1585.8
rms error			0.0	140.6	116.0	25.5			10.7	

^a Reference 15.^b 6-31G** basis.

Table 7a. Parameters for the MSXX FF of various polysilane oligomers.

Valence Terms	SiH_4	Si_2H_6	$Si_3H_8^a$	$n - Si_4H_{10}^a$	$n - Si_5H_{12}$
Bonds see equation (17)					
Si-H	K_R 396.3	399.8	399.4 (381.8)	395.8 (383.1)	377.7 (385.7)
	R_e 1.476	1.471	1.468 (1.477)	1.468 (1.476)	1.479 (1.474)
	D_R^b 92.6	92.6	92.6	92.6	92.6
Si-Si	K_R 276.7	276.7	256.7	278.8 (261.1)	267.9 (253.5)
	R_e 2.369		2.344	2.330 (2.328)	2.321 (2.363)
	D_R^b 73.7	73.7	73.7	73.7	73.7
Angles see equations (18), (20), and (21)					
H-Si-H	K_θ 68.35	55.96	50.91 (64.90)	56.39 (56.05)	50.4 (59.2)
	θ_e 110.4	113.1	117.2 (109.46)	113.6 (113.4)	118.1 (111.6)
	$D_{R\theta}$ -1.90	-10.16	-9.17 (-5.91)	-11.2 (-1.46)	2.49 (-12.0)
	$K_{RR'}$ 4.30	2.39	4.05 (4.20)	3.34 (4.46)	4.43 (3.51)
Si-Si-H	K_θ 42.25		39.30 (43.02)	45.0 (33.3, 41.6)	35.4 (43.1, 42.2)
	θ_e 115.14	115.14	120.78 (110.62)	117.2 (118.5, 115.8)	123.3 (114.4, 114.0)
	$D_{R\theta} (SiSi)$ $D_{R'\theta} (SiH)$	16.14	-8.57 (-2.69)	-5.34 (-6.41, -4.16)	-6.05 (-5.67, 5.74)
Si-Si-Si	K_θ -10.67		-9.23 (-7.02)	-10.54 (-10.64, -2.68)	-2.04 (-7.47, -13.94)
	θ_e 42.53	42.53	35.4	35.4	26.1 (75.9)
	$D_{R'\theta}$ K_{rr}	122.55	126.6	126.0 (114.6)	126.0 (114.6)
		-6.19	-15.6 (-18.7)	-22.9, -11.1, (-18.6)	
		15.21	0.635	0.515 (0.518)	
Torsions see equations (17) and (23)					
Si-Si-Si-Si	K_1^1		5.86	4.60	
	K_2^1		3.54	6.32	
	K_3^1		0.46	-1.02	
	$F_{\theta\theta}^3$		-9.28	-13.2	
H-Si-Si-Si	K_3^2	0.806	0.806 (0.806)	0.806 (0.806)	
	$F_{\theta\theta'}^3$	-2.33	-7.93 (-9.36)	-7.35 (-9.95)	
H-Si-Si-H	K_3^3	0.940	0.940 (0.940)	0.940 (0.940)	
	$F_{\theta\theta}$	-14.749	-15.062	-13.401 (-13.401)	-15.468 (-15.288)
1 Center angle-angle see equation (24)					
Si Si-H-H	$G_{\theta\theta}$	-0.178	0.086 (-1.203)	-0.67 (-0.46, -0.51)	-0.55 (-0.57)
Si Si-Si-H	$G_{\theta\theta'}$	-0.673	-1.51	-1.621 (-1.583)	-1.32
Si H-Si-H	$G_{\theta\theta'}$	-0.333	-1.413 (0.311)	-1.108 (-1.184, -2.204)	-1.56
Si H-Si-Si	$G_{\theta\theta}$	-1.259	-3.900	-0.349	-4.775
Si H-H-H	$G_{\theta\theta}$	5.717	-0.233	-0.349	0.328

^aValues in parenthesis refer to terms involving the central hydrogens. ^bNot optimized. ^cCentral and terminal groups described using the same parameters.

Table 7b. The MSXX FF for polysilane polymers. The subscript on the Si indicates the number of H atoms attached. All quantities are in (kcal/mol), Å, radian units except for θ_e which is in degrees.

Bonds	R_e	K_r	D_r		
H-Si ₄	1.476	396.3	92.6		
H-Si ₃	1.478	395.8	92.6		
H-Si ₂	1.476	383.1	92.6		
Si ₃ -Si ₃	2.369	276.7	73.7		
Si ₃ -Si ₂	2.330	278.8	73.7		
Si ₂ -Si ₂	2.328	261.1	73.7		
Angles	θ_e	K_θ	K_{rr}	$D_{R_1\theta}$	$D_{R_2\theta}$
H-Si ₄ -H	110.4	68.35	4.30	-1.90	-1.90
H-Si ₃ -H	113.6	56.39	3.34	-11.20	-11.20
H-Si ₂ -H	113.4	56.05	4.46	-1.46	-1.46
Si ₃ -Si ₃ -H	115.14	42.25	-	16.14	-10.67
Si ₂ -Si ₃ -H	117.2	45.0	-	-5.34	-10.54
Si ₃ -Si ₂ -H	118.5	33.3	-	-6.41	-10.64
Si ₂ -Si ₂ -H	115.8	41.6	-	-4.16	-2.68
Si ₃ -Si ₂ -Si ₃	122.55	42.53	15.21	-6.19	-6.19
Si ₂ -Si ₂ -Si ₃	126.6	35.4	0.635	-15.6	-18.7
Si ₂ -Si ₂ -Si ₂					
Torsions	K_0	K_1	K_2	K_3	$F_{\theta\theta}$
H-Si-Si-H	0.940			0.940	-13.4
H-Si-Si-Si	0.806			0.806	-9.36
Si-Si-Si-Si	2.785	5.86	3.54	0.46	-9.28
1-Center Angle Angle	$G_{\theta\theta}$				
Si ₄ H-H-H	5.717				
Si ₃ H-H-H	-0.349				
Si ₃ Si-H-H	-1.108				
Si ₂ Si-H-H	-4.775				
Si ₂ Si-Si-H	-1.6				

Table 7c. Van der Waals parameters (reference 7) used for all MSXX force fields, $E_{vdw} = D_v (\rho^{-12} - 2\rho^{-6})$ where $\rho = R/R_v$. The off-diagonal parameters D_v and R_v (Si \cdots H) are obtained from the diagonal parameters by using the geometric mean.

vdW parameters	<i>Si</i>	<i>H</i>
R_v (Å)	4.270	3.195
D_v (kcal/mol)	0.310	0.0152

Table 8. Vibrational frequencies (cm⁻¹) for Si₂H₆.

Mode	Sym	Char	HF ^a	Scale ^g	MP2	Exper ^b	HBFF	MSXX	HBFF ^f	Exper ^d
							Si ₂ H ₆	Cui et al. ^c	Si ₂ D ₆	Si ₂ D ₆
1	A_{1u}	torsion	134.3	0.931	143.6	125.0	133.2	133.3	94.2	
2	E_u	SiH ₃ rock	416.6	0.910	385.7	379.3	400	377.9	271.3	277.0
3	A_{1g}	Si-Si Str	464.0	0.936	458.9	434.2	435.2	418	418.9	407.5
4	E_g	SiH ₃ rock	697.1	0.897	666.8	625.2	625.2	644	630.9	475.4
5	A_{2u}	SiH ₃ def	947.9	0.890	900.5	843.5	844.9	856	870.1	474.7
6	A_{1g}	SiH ₃ def	1031.5	0.881	980.1	909.0	907.0	922	872.9	624.9
7	E_u	SiH ₃ def	1043.1	0.891	984.7	929.3	931.5	964	939.9	683.1
8	E_g	SiH ₃ def	1027.5	0.914	1001.3	939.6	937.1	952	942.4	668.6
9	A_{2u}	SiH ₃ Str	2337.1	0.880	2309.7	2145.3	2152.4	2145	2137.5	662.0
10	A_{1g}	SiH ₃ Str	2352.7	0.915	2319.5	2152.0	2154.9	2160	2139.7	1549.3
11	E_g	SiH ₃ Str	2337.3	0.922	2323.3	2155.6	2166.2	2154	2137.4	1547.5
12	E_u	SiH ₃ Str	2346.7	0.928	2331.7	2178.6	2168.2	2164	2139.0	1569.0
	rms ^e		126.6		101.5	4.8	16.5	14	19.5	1585.0

^a 6-31G** basis^b Reference 16.^c Reference 5.^d Reference 17.^e Excluding the torsional frequency, a_{1u} , which was not fit.^f Using the HBFF for Si₂H₆.^g $\nu_{\text{exper}}/\nu_{HF}$.

Table 9. Vibrational frequencies (cm^{-1}) for Si_3H_8 .

Mode	Sym	Char	HF ^e	Scale	MP2 ^e	Exper ^a	HBFF	Cui FF et al. ⁵	MSXX	HBFF Si_3D_8	HBFF $\text{Si}_3\text{D}_2\text{H}_6$
1	A2	torsion	77.3	107.6	[72]	89.1	88.7	63.4	89.1		
2	B2	torsion	99.2	108.0	[92]	94.7	95.2	69.9	94.3		
3	A1	$\text{Si}-\text{Si}-\text{Si}$ bend ^c	109.3	1.025	120.0	112 ^b	113.4	109.9	103.9	112.6	
4	B2	$\text{Si}-\text{SiH}_2$ rock	353.0	291.9	[317]	321.4	337	324.6	232.3	253.7	
5	A1	$\text{Si}-\text{Si}$ twist	411.3	0.953	395.8	392 ^b	394.1	375.9	303.1	387.9	
6	A2	$\text{Si}-\text{Si}$ twist	464.1	430.9	(420)	422.8	476	421.2	344.1	357.5	
7	B1	$\text{Si}-\text{Si}$ wag	485.3	0.921	458.5	447 ^b	447.9	445	447.2	354.2	389.9
8	B1	SiH_3 rock	625.0	0.904	596.4	565 ^b	545.6	446	470.7	400.5	460.6
9	A1	SiH_3 rock	657.4	0.888	624.5	584 ^b	600.0	582	539.0	430.7	544.9
10	B2	SiH_2 twist	777.8	0.905	730.1	704 ^b	703.5	606	603.0	465.1	577.4
11	A2	SiH_2 wag	810.7	0.883	751.9	716 ^b	714.7	740	748.9	567.5	612.9
12	B1	SiH_3 s-def	983.0	0.891	931.8	876 ^b	883.6	881	859.2	658.5	883.6
13	B1	SiH_3 s-def	989.9	0.939.2	(895)	887.2	897	862.3	657.9	672.1	
14	A1	SiH_2 scissor	1025.9	0.903	973.5	926 ^b	929.1	940	927.2	674.3	887.2
15	A1	SiH_3 d-def	1032.3	991.9	(933)	935.9	935.9	954	939.5	670.5	935.6
16	A2	SiH_3 d-def	1036.2	993.6	(937)	936.2	936.2	959	939.9	670.9	936.1
17	B2	SiH_3 d-def	1034.6	995.6	(935)	937.7	937.7	959	940.9	671.8	937.6
18	B1	SiH_3 d-def	1044.8	1001.4	(944)	940.1	940.1	965	943.1	672.7	939.8
19	A1	SiH_2 str	2321.3	2302.3	(2128)	2127.8	2145	2127.3	1537.4		
20	B2	SiH_3 str	2320.0	0.918	2305.9	2130 ^b	2130.3	2137	2128.3	1524.6	
21	A1	SiH_3 str	2338.3	2315.4	(2143)	2145.5	2149	2144.5	2144.5	1549.6	2145.5
22	A2	SiH_3 str	2339.7	2317.7	(2144)	2145.8	2156	2144.3	1527.7	2145.8	
23	B1	SiH_3 str	2345.0	0.916	2318.9	2148 ^b	2146.2	2158	2145.3	1550.1	2146.1
24	B2	SiH_3 str	2344.4	2319.7	(2149)	2146.6	2159	2145.3	1529.1	2146.6	
25	A1	SiH_3 str	2343.5	2340.7	(2148)	2149.2	2163	2146.6	1551.5	2149.1	
26	B1	SiH_3 str	2350.1	0.915	2352.7	2150 ^b	2149.6	2164	2147.1	1551.9	
27	A1	SiH_3 str	122.5	102.9				6.0 ^d (7.7)	17	12.65	
											rms

^a The values in parenthesis and brackets are not available from experiment and were scaled from HF. The values in parentheses used scaling from corresponding modes of Si_3H_6 , the values in brackets (torsions) used the scale for Si_2H_6 .

^b Reference 18.

^c Accordion mode.

^d Excluding the two torsional frequencies fit using the full PES.

^e 6-31G** basis.

Table 10. Vibrational frequencies (cm^{-1}) for n-butylsilane, $n\text{-Si}_4\text{H}_{10}$. Exper includes the best estimate of experiment using scaled HF results. The MSXX force field distinguishes between the SiH_2 and SiH_3 centers. The MSXX-R FF does not distinguish.

Mode	Sym	Char	MSXX-R	MSXX	Exper	Cui <i>et al.</i> ^f	HF ^e	Scale	MP2
1	Au	Torsion (Si-Si)	23.6	32.1	24.8 ^a	24.8	47.5		
2	Bu	Si-Si-Si bend	73.1	73.8	73.2 ^a	73.2	77.2		
3	Au	Torsion (SiH_3)	97.6	92.5	80.3 ^b	86.3	110.0		
4	Bg	Torsion (SiH ₃)	102.7	97.8	88.0 ^b	94.6	115.5		
5	Ag	Si-Si-Si bend ^g	141.7	131.5	139 ^c	130	126.2	1.047	
6	Au	SiH ₂ rock	307.6	307.8	306.4 ^b	320	310.9		
7	Bg	twist-rock	355.5	350.2	349.4 ^b	368	384.3		
8	Ag	Si-Si stretch	357.1	358.7	361 ^c	357	362.0		
9	Bu	Si-Si stretch	420.5	422.9	422 ^c	418	442.8		
10	Ag	Si-Si twist-rock	458.0	465.7	465 ^c	474	468.8		
11	Bu	Si-Si stretch	462.6	470.7	465 ^c	459	484.6		
12	Bu	wag	492.4	493.1	478 ^c	498	525.8	0.909	495.3
13	Ag	SiH ₃ rock	527.5	527.8	542 ^c	556	566.3		
14	Bg	SiH ₂ rock	581.6	577.8	577.0 ^b	587	636.5	608.9	
15	Au	twist	668.7	651.1	657 ^c	693	739.4	0.889	705.7
16	Bu	wag	718.9	709.4	692 ^c	694	754.7	0.917	709.7
17	Bg	twist	721.0	743.8	744 ^c	753	798.7	0.932	761.5
18	Ag	wag	782.5	782.1	784.1 ^b	780	862.5	815.6	
19	Bu	SiH ₃ s-def	865.6	871.4	874 ^c	883	981.1	0.891	931.4
20	Ag	SiH ₃ s-def	868.4	874.1	869 ^c	891	988.9	0.879	939.4
21	Ag	SiH ₂ scissor	924.1	924.9	917 ^c	941	1024.0	0.896	975.1
22	Bu	SiH ₂ scissor	924.4	927.3	933 ^c	943	1021.8	0.913	975.8
23	Bg	SiH ₃ d-def	940.5	939.8	937.6 ^b	956	1034.1	993.5	
24	Au	SiH ₃ d-def	941.2	940.5	938.0 ^b	957	1034.7	993.7	
25	Bu	SiH ₃ d-def	941.7	941.5	941.7 ^b	963	1040.6	997.1	
26	Ag	SiH ₃ d-def	942.4	942.2	943.4 ^b	961	1038.7	998.6	
27	Bg	SiH ₂ str	2123.7	2120.5	2119.5 ^b	2142	2316.8	2286.4	
28	Au	SiH ₂ str	2125.2	2121.0	2125.7 ^b	2148	2317.6	2287.5	
29	Bu	SiH ₂ str	2125.8	2121.6	2120.6 ^b	2136	2318.0	2295.2	
30	Ag	SiH ₂ str	2126.4	2123.5	2120 ^c	2139	2315.0	0.913	2301.6
31	Bg	SiH ₃ str	2139.3	2141.7	2143 ^c	2159	2341.8	0.915	2303.8
32	Ag	SiH ₃ str	2139.5	2141.9	2144 ^c	2158	2345.0	0.914	2306.8
33	Bu	SiH ₃ str	2139.5	2143.4	2143.6 ^b	2152	2343.2	2318.3	
34	Ag	SiH ₃ str	2139.7	2144.8	2142.9 ^b	2158	2342.4	2320.4	
35	Bu	SiH ₃ str	2140.9	2143.6	2144.1 ^b	2161	2343.8	2319.6	
36	Ag	SiH ₃ str	2148.2	2151.5	2148.5 ^b	2160	2348.5	2319.0	
			7.3 (7.1)	6.2 (6.0)	0.0	16 ^d	119.4	95.3	
		rms							

^a *Ab initio* frequencies. ^b *Ab initio* frequencies scaled by $n\text{-Si}_4\text{H}_{10}$ frequencies. ^c Reference 16. ^d Excluding the torsional frequencies (not fitted). ^e 6-31G** basis. ^f Reference 5. ^g The accordion mode.

Table 11. Predicted structure of $n-Si_5H_{12}$. Distances are in Å, angles are in degrees.

	MSXX	HF ^a	Δ
$Si_c - Si_{cc}$	2.365	2.361	0.004
$Si_c - Si$	2.355	2.357	0.002
$H_c - Si_c$	1.480	1.482	0.002
$H_{cc} - Si_{cc}$	1.479	1.482	0.003
$H_{ip} - Si$	1.478	1.479	0.001
$H_{op} - Si$	1.478	1.479	0.001
$Si - Si_c - Si_{cc}$	112.1	112.69	0.59
$Si_c - Si_{cc} - Si_c$	114.16	113.03	1.13
$H_{ip} - Si - Si_c$	110.06	110.63	0.57
$H_{op} - Si - Si_c$	110.04	110.14	0.10
$H_{cc} - Si_{cc} - H_{cc}$	106.63	107.25	0.62
$H_c - Si_c - Si_{cc}$	110.06	108.93	1.13
$H_{op} - Si - Si_c - Si_{cc}$	59.95	59.81	0.14

^a 6-31G** basis.

Table 12. Properties of P(SiH) at 0K, 77K, and 300K from Gibbs dynamics for a $2 \times 4 \times 4$ supercell (containing 384 atoms).

Property	0K	77K	300K
unitcell (\AA) ^a			
a	8.422	8.526	8.833
b	3.966	3.9769	3.955
c	4.685	4.733	4.929
Bulk Modulus (GPa)			
B	13.095	10.412	4.594
Young's Moduli (GPa)			
Y_x	11.94	9.586	4.720
Y_y	110.57	107.64	98.384
Y_z	18.64	14.750	5.789
Elastic Constants (GPa)			
C_{11}	15.60	12.424	5.937
C_{22}	121.30	116.501	102.85
C_{33}	22.97	18.172	7.088
C_{12}	12.73	10.335	5.045
C_{13}	8.17	6.486	2.765
C_{23}	9.24	7.374	3.369
C_{44}	16.23	13.995	8.322
C_{55}	7.34	5.936	2.876
C_{66}	19.30	16.299	8.906

^a Structure was constrained to remain orthorhombic during the dynamics.

Table 13. Predicted cohesive energy (kcal/mol SiH_2) for polysilane crystal. The cohesive energy at 0K of 3.82 kcal/mol SiH_2 compares with 1.87 kcal/mol CH_2 for polyethylene crystal.

	Total Energy	Zero-point Energy ^a	Lattice Enthalpy
	At minimum		at 0K
Isolated Chain	3.224	8.568	11.792
Crystal (2 chain)	-1.055	9.031	7.976
Cohesive Energy (2 chain)	4.279	-0.463	3.816
Crystal (1 chain)	-1.231	9.053	7.822
Cohesive Energy (1 chain)	4.455	-0.485	3.970

^a Using 5 x 5 x 5 points in the Brillouin zone.

Table 14. Vibrational frequencies (cm^{-1}) for polysilane crystal P(SiH) with two chains per unit cell. Only the values for $k = 0$ (Γ point) are shown. The chain direction is [010].

Mode	Description	Polarization Direction		
		[010]	[100]	[001]
1	interchain	63.6	63.6	63.6
2	interchain	95.7	95.7	96.3
3	interchain	98.1	98.1	98.1
4	skeletal torsion	152.2	152.2	152.2
5	skeletal torsion	160.9	160.9	160.9
6	SiH ₂ rock	320.9	320.9	343.8
7	SiH ₂ rock	357.7	348.9	348.9
8	Si-Si-Si bend	398.7	398.7	398.7
9	Si-Si-Si bend	403.2	403.2	403.2
10	Si-Si stretch	509.5	509.5	509.5
11	Si-Si stretch	532.3	532.3	532.3
12	SiH ₂ rock	573.5	573.5	573.5
13	SiH ₂ twist	573.5	573.5	573.5
14	SiH ₂ rock	583.7	583.7	583.7
15	SiH ₂ twist	648.5	649.0	648.5
16	SiH ₂ wag	702.1	742.5	702.1
17	SiH ₂ wag	771.7	771.7	771.7
18	SiH ₂ twist	840.6	840.6	840.6
19	SiH ₂ wag	871.5	871.5	871.5
20	SiH ₂ twist	927.5	927.5	927.5
21	SiH ₂ scissor	948.2	948.2	953.8
22	SiH ₂ scissor	950.6	950.6	950.6
23	SiH ₂ wag	954.5	940.1	940.1
24	SiH ₂ scissor	954.7	954.7	954.7
25	SiH ₂ scissor	964.7	964.7	964.7
26	SiH stretch	2150.2	2150.2	2150.2
27	SiH stretch	2151.8	2151.6	2151.6
28	SiH stretch	2152.2	2151.8	2153.9
29	SiH stretch	2153.1	2153.1	2153.1
30	SiH stretch	2154.5	2154.5	2160.1
31	SiH stretch	2155.3	2155.3	2155.3
32	SiH stretch	2161.3	2161.3	2161.3
33	SiH stretch	2164.3	2159.0	2159.0

Table 15. Vibrational frequencies (cm^{-1}) of P(SiH). The first two columns are for a single infinite chain, while last two columns are for the crystal, with 1 chain/unit cell.

Mode	Sym	Description	Isolated Chain		Crystal	
			Cui <i>et al.</i> ^a	MSXX	MSXX	Exper
1	Au	SiH ₂ rock	311	307.7	367.9	
2	Ag	Si-Si-Si bend	413	396.8	407.2	
3	Ag	Si-Si stretch	469	493.1	526.7	480
4	Au	SiH ₂ twist	549	556.8	613.0	
5	Bg	SiH ₂ rock	532	562.5	585.1	
6	Bu	SiH ₂ wag	604	685.0	692.9	
7	Bg	SiH ₂ twist	769	795.2	842.4	
8	Ag	SiH ₂ wag	808	852.1	929.8	
9	Ag	Scissor	943	936.4	949.4	909
10	Bu	Scissor	953	935.6	974.7	905
11	Bg	SiH stretch	2140	2128.3	2146.6	2155
12	Bu	SiH stretch	2139	2128.5	2151.0	2100
13	Au	SiH stretch	2158	2132.6	2153.6	2100
14	Ag	SiH stretch	2150	2130.3	2156.5	2115

^a Reference 5.

Table 16. Packing of P(SiH) and Polyethylene. R is the C-H (1.096Å) or Si-H (1.48Å) bond distance and \bar{R} is the C-C (1.553Å) or Si-Si (2.35Å) bond distance for PE and P(SiH), respectively.

Lattice constant	P(SiH)	PE
unitcell ^a		
a	8.422	7.121
b (chain)	3.966	2.546
c	4.685	4.851
a/R	5.69	6.50
b/ \bar{R}	1.69	1.64
c/R	3.17	4.43

Figure Captions

Figure 1. Torsional potential (kcal/mol) of Si_2H_6 from HF calculations and from the MSXX FF. All bonds and angles are optimized for each ϕ . The total $E^{HF}(\phi)$ and $E^{FF}(\phi)$ is plotted.

Figure 2. Torsional potential (kcal/mol) of Si_3H_8 from (a) HF calculations and (b) the MSXX FF. Each is plotted versus the two dihedral angles $\phi_1 = H - Si - Si_2 - Si_3$ and $\phi_2 = Si - Si_2 - Si_3 - H$ (abscissa and respective ordinate). All other bonds and angles are optimized for each ϕ_1 and ϕ_2

Figure 3. Torsional potential (kcal/mol) for the central $Si - Si$ bond of $H_3Si - SiH_2 - SiH_2 - SiH_3$ from HF and HBFF. All other bonds and angles are optimized for each ϕ .

Figures 4a-b. The calculated phonon modes (cm^{-1}) of crystalline $P(SiH)$ for the [010] and [001] directions (the chain direction is [010]). Only the modes below 1000 cm^{-1} are shown.

Figure 5. (a) The calculated stress-strain curves for crystalline $P(SiH)$ in directions perpendicular to the chain axis. (b) The strain energy (kcal/mol) as a function of strain.

Figure 6. The thermochemical properties as a function of temperature (using a 5 by 5 by 5 set of phonons in the Brillouin zone). (a) The heat capacity (C_v). (b) The Helmholtz free energy. (c) The internal energy. (d) The entropy.

Figure 1

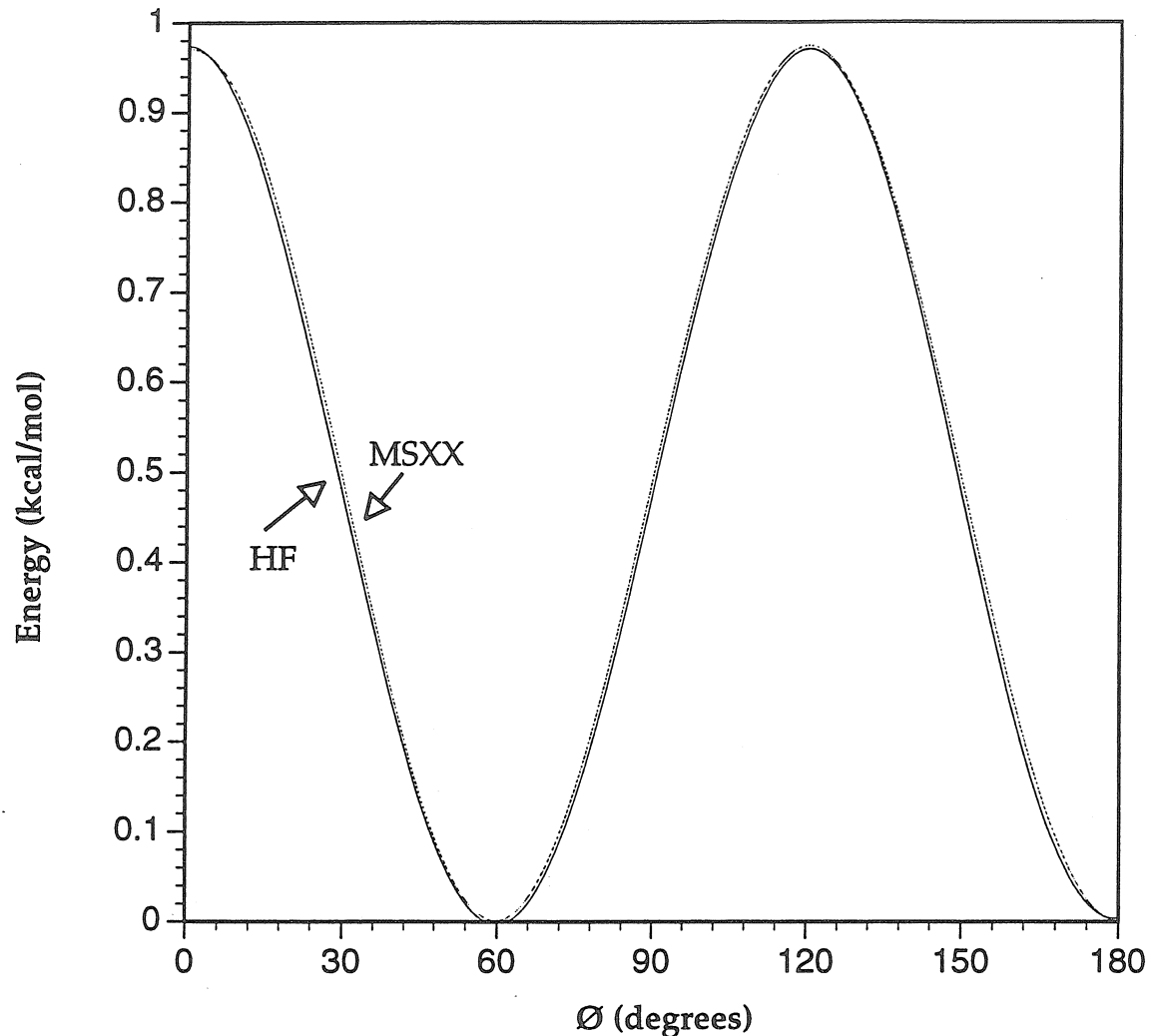


Figure 2a

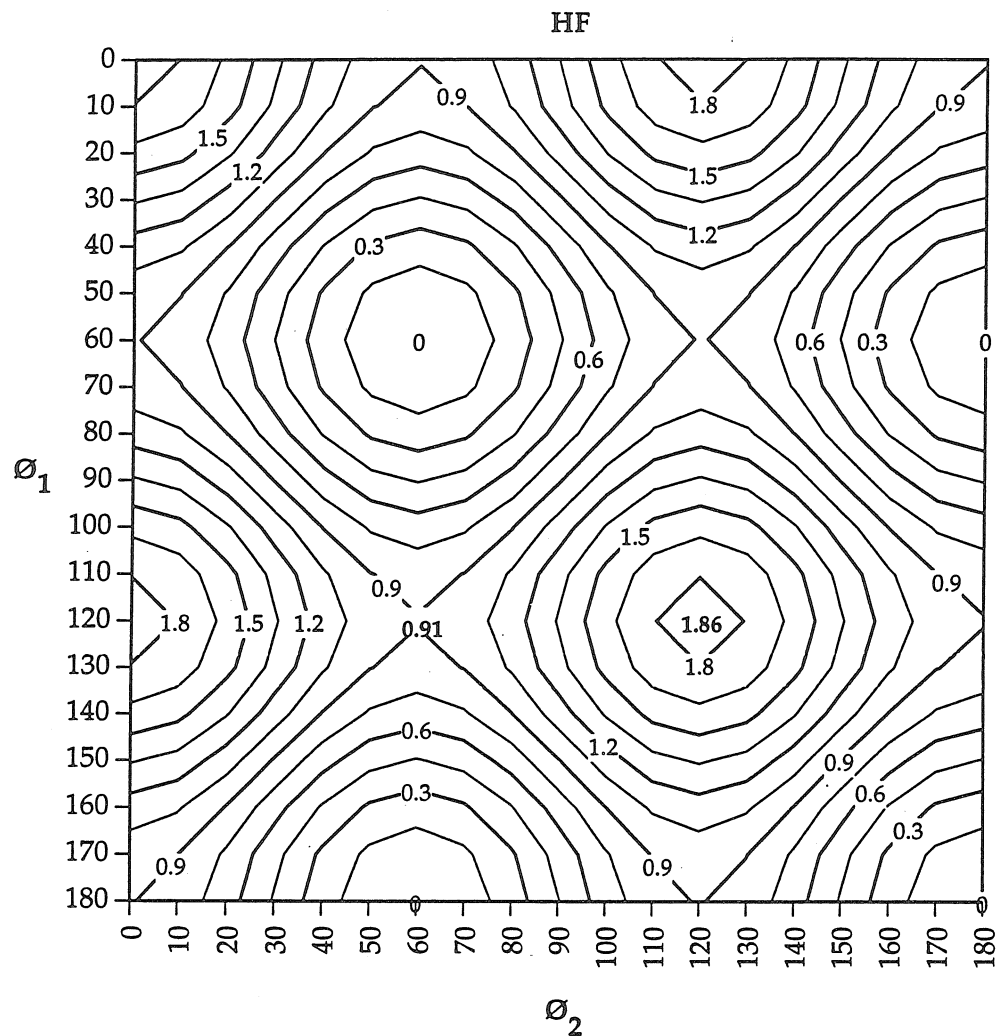


Figure 2b

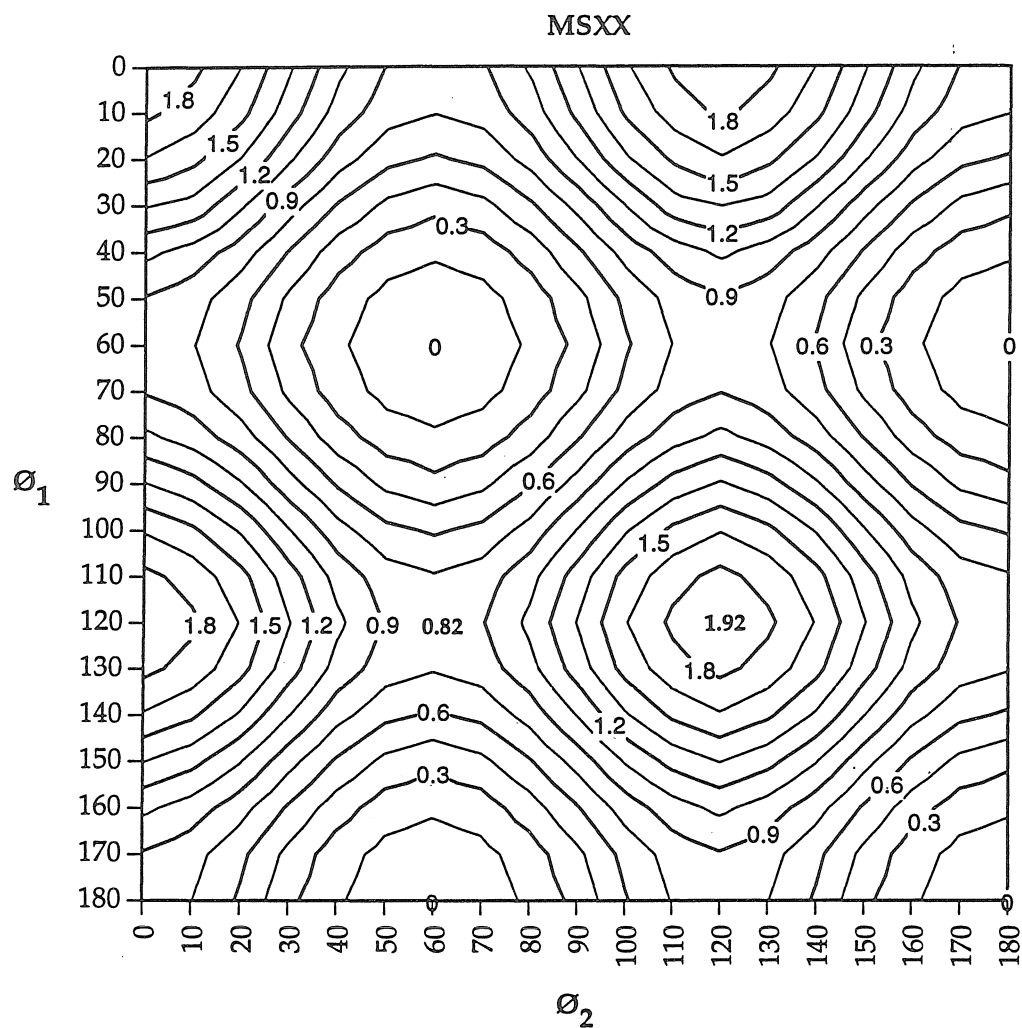


Figure 3

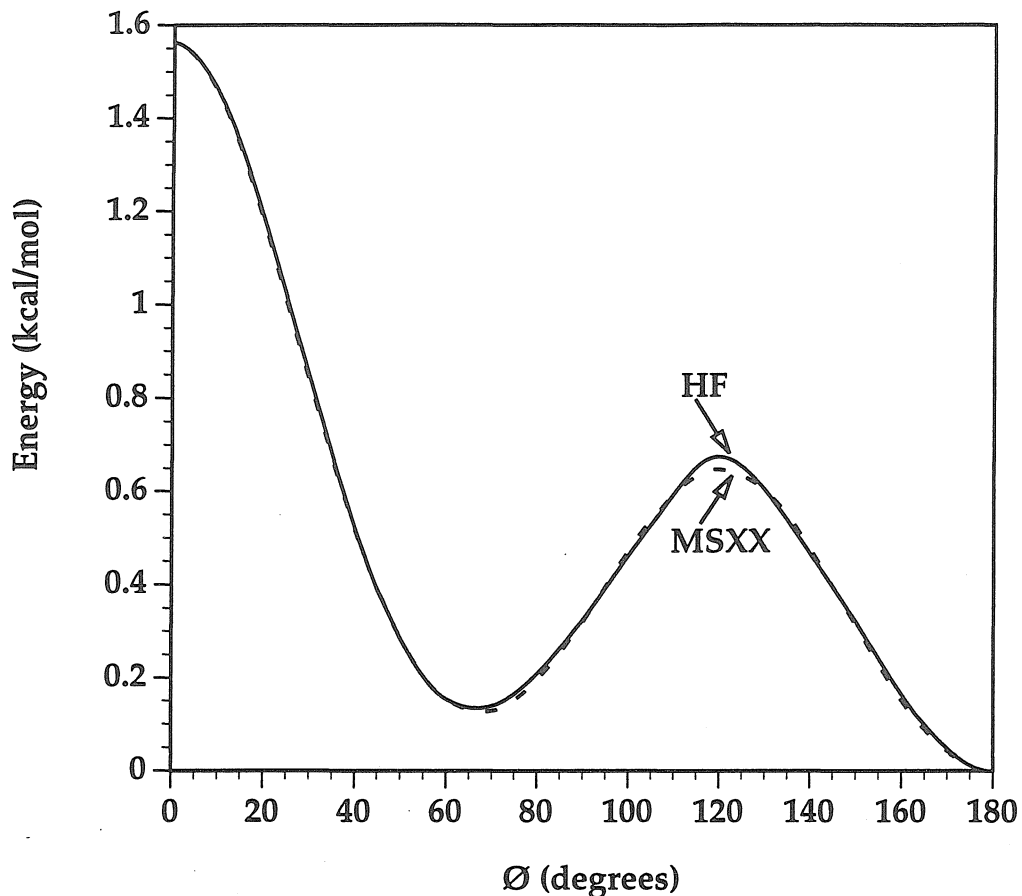


Figure 4a

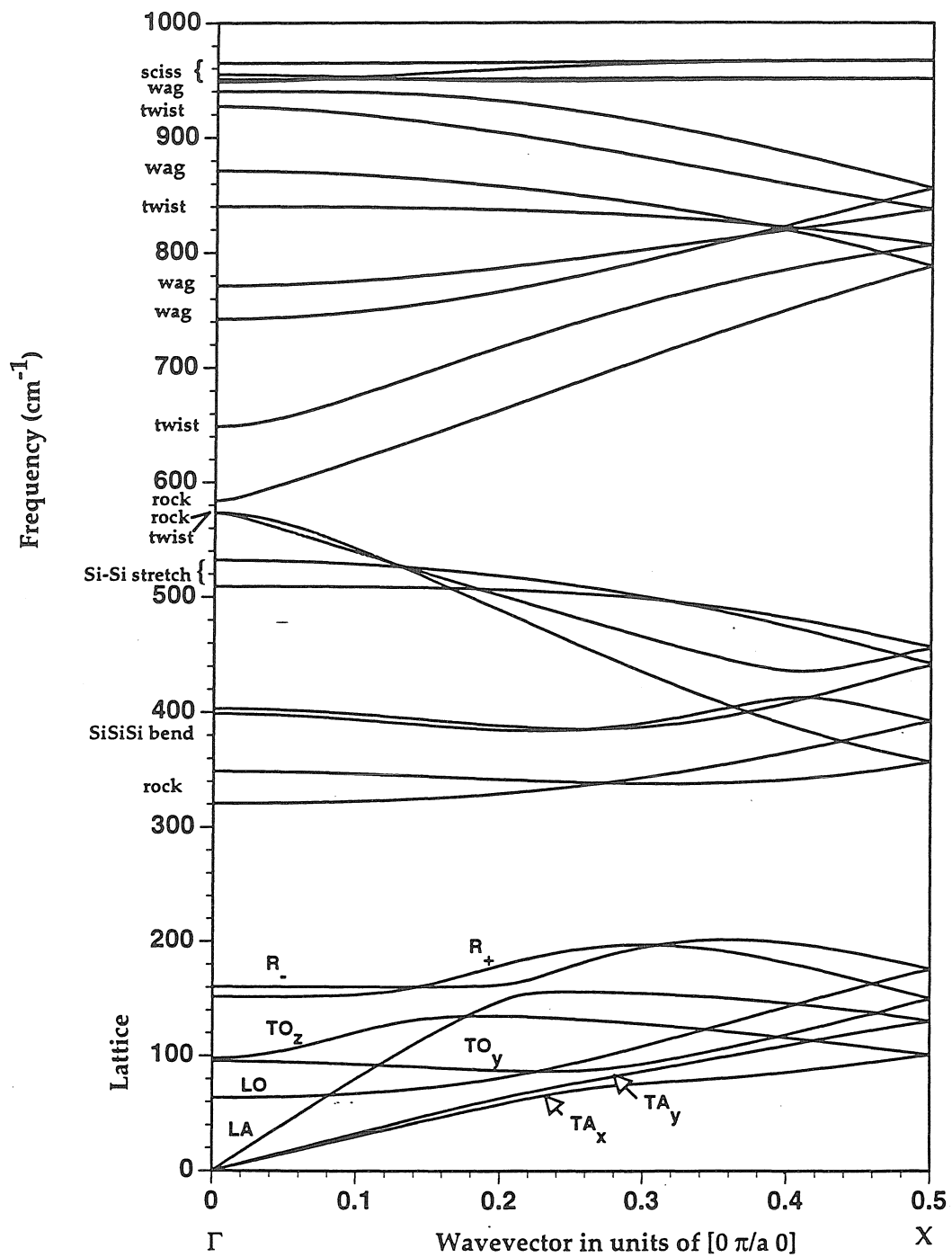


Figure 4b

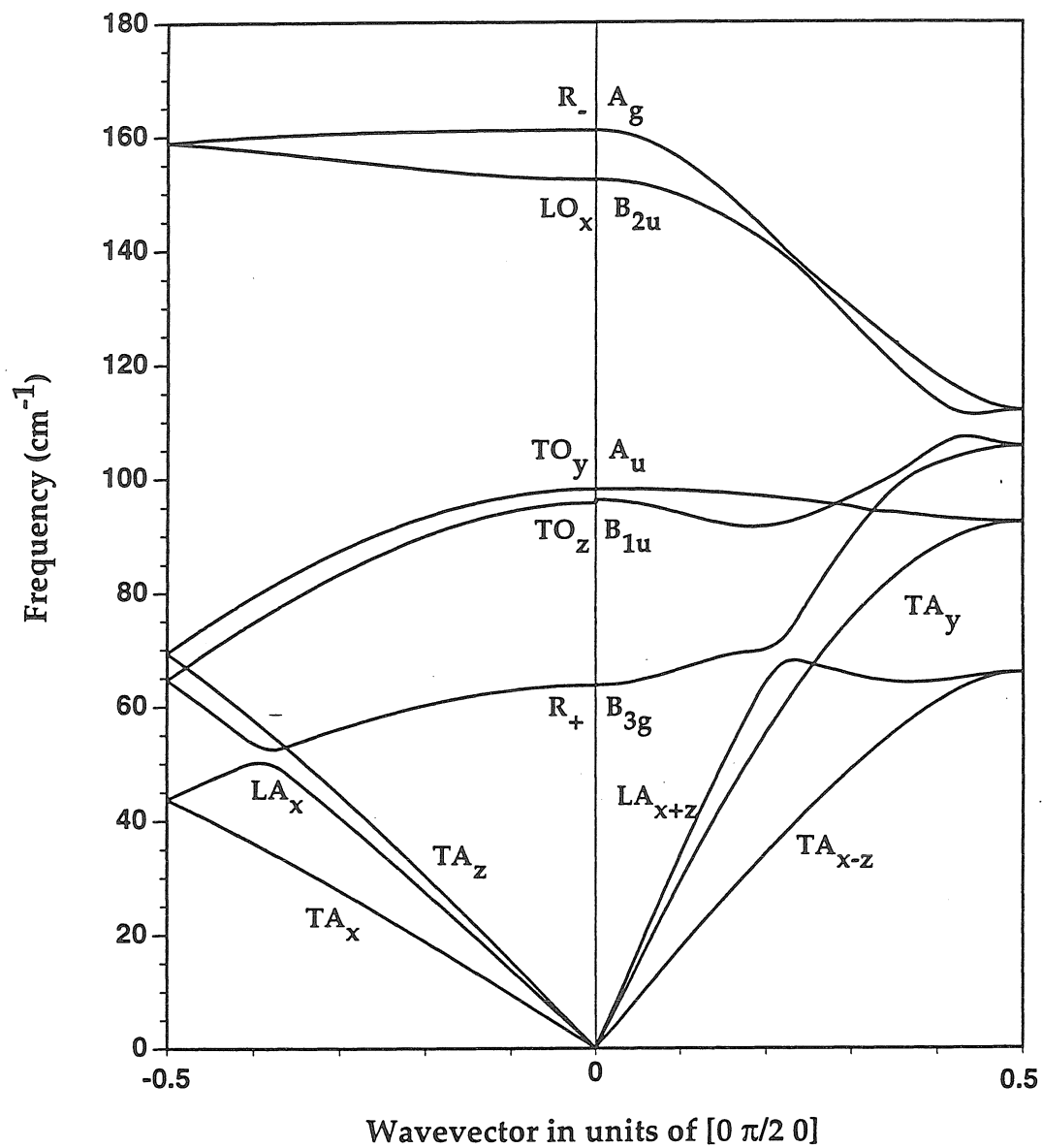


Figure 5a

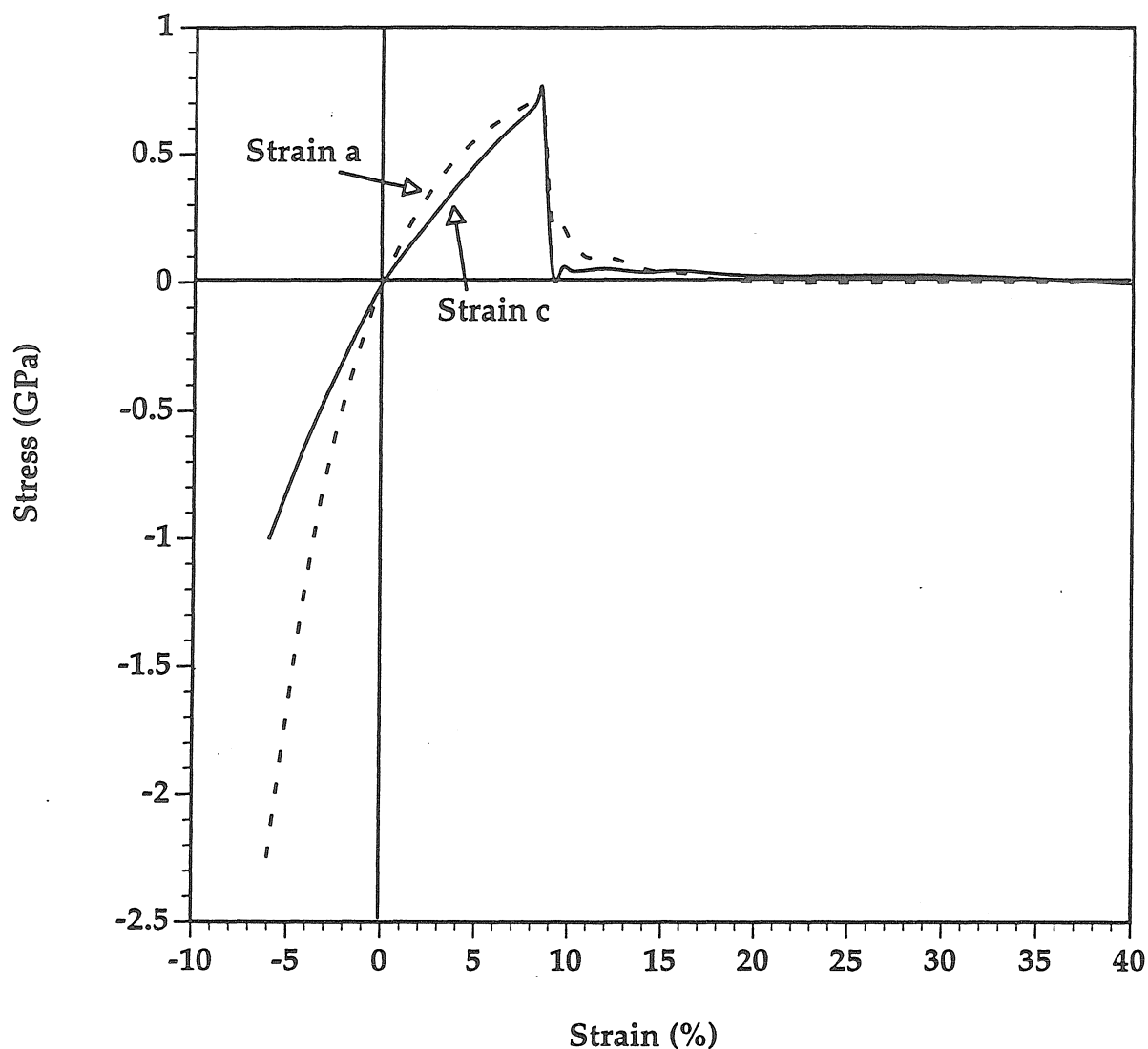


Figure 5b

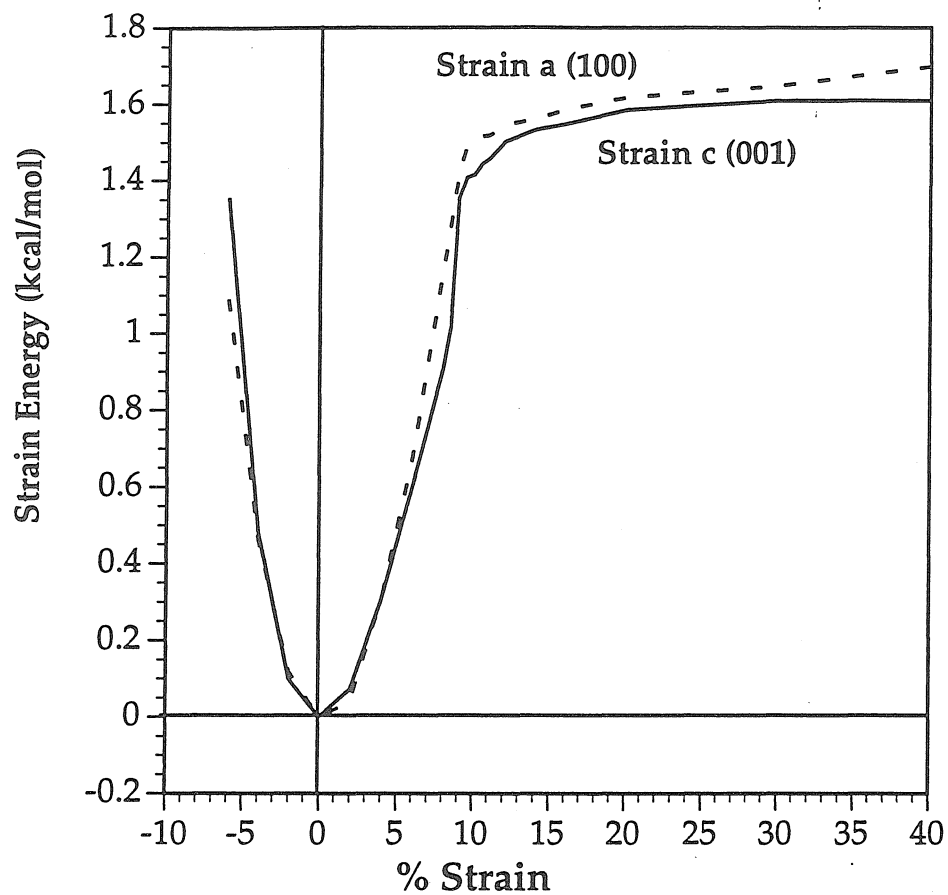


Figure 6a

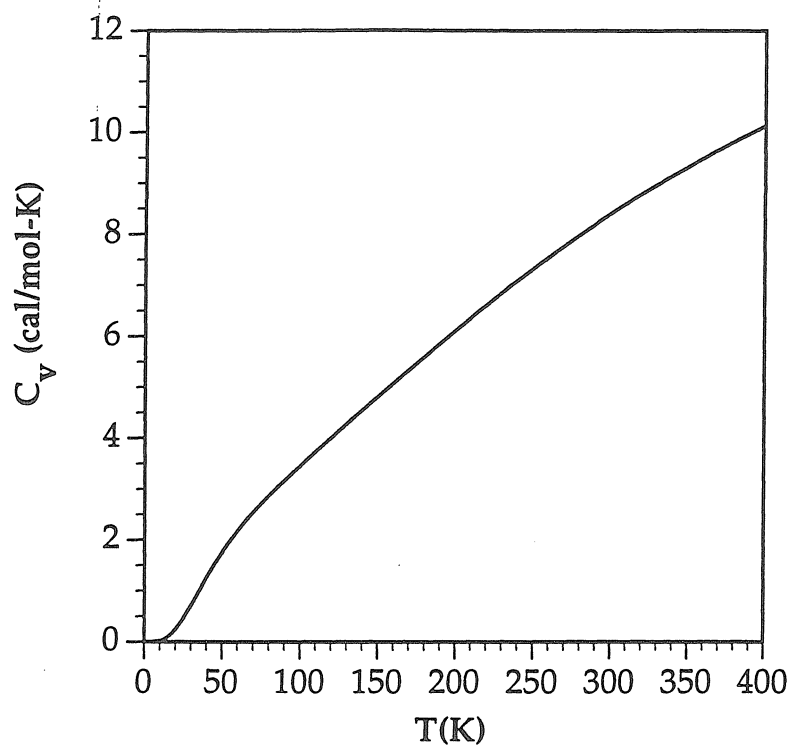


Figure 6b

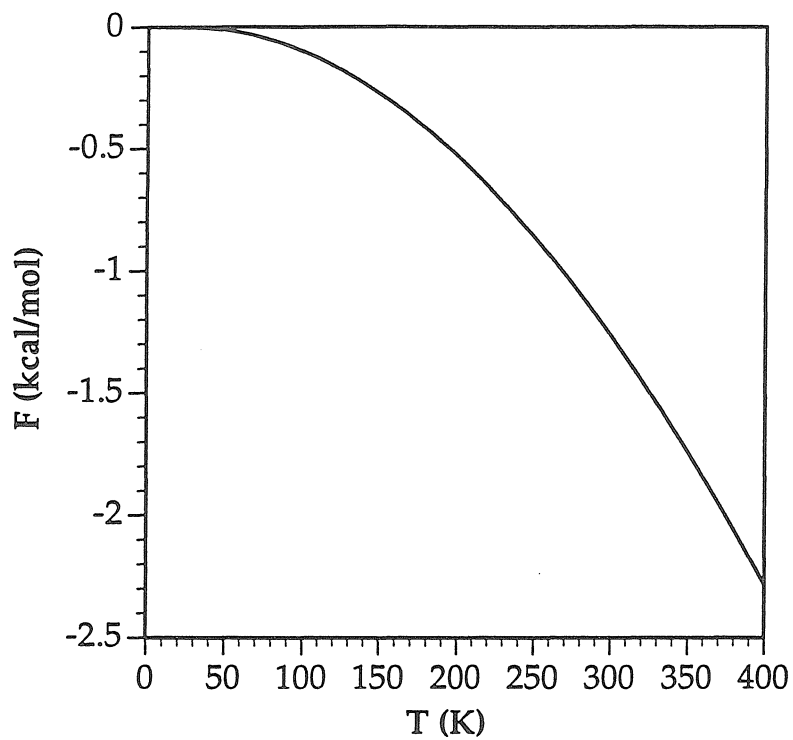


Figure 6c

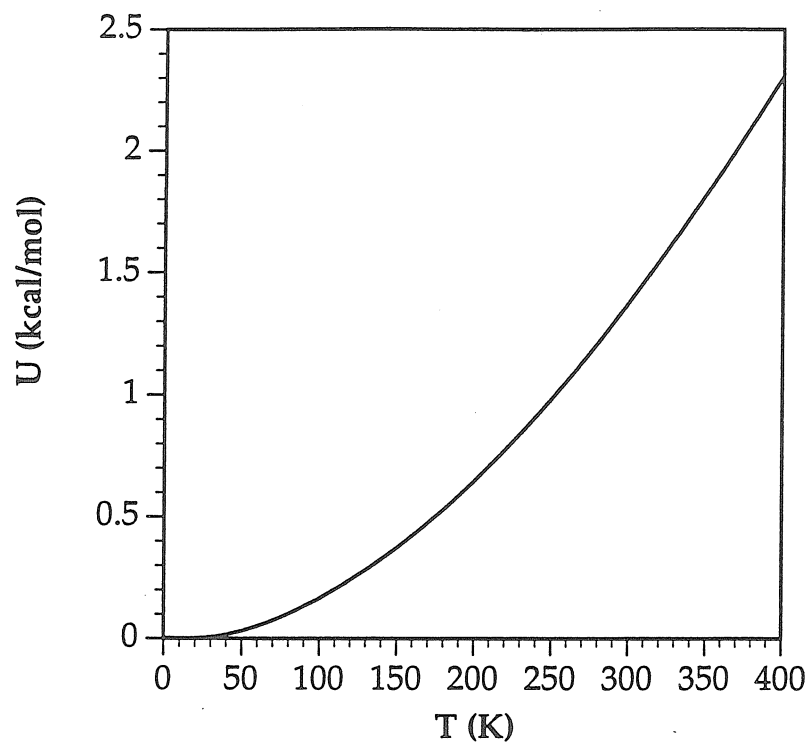
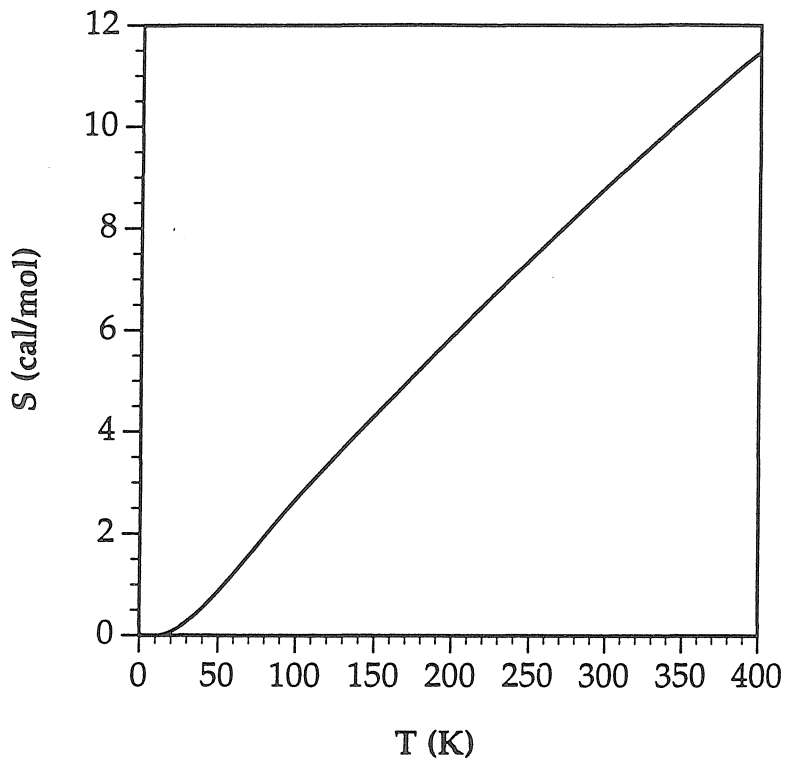


Figure 6d



Chapter 5

Force Fields for Semiconductors and Their Superlattices

Abstract

We develop the MSXX force field (FF) for molecular dynamics (MD) simulations of the group IV diamond materials, and group II/VI and III/V zinc-blende semiconductors. This was developed to fit the structure, elastic constants, and the phonons of the crystal. The MSXX force field for zinc-blende materials contains *only* 6 adjustable force constants, 2 geometric parameters and an atomic partial charge, yet it accurately describes the experimental crystal structure, elastic constants, and phonon dispersion curves, and is suitable for predictions of the strained structures at heterojunctions and for MD. The MSXX FF is used to calculate the interface phonons of various superlattices and the Ge/Si ordered alloy where we find excellent agreement with experiment.

1.0 Introduction

Ab initio quantum mechanics can provide an accurate description of the structures, mechanical properties, and electrical properties of semiconductor materials. Unfortunately, despite recent advances in first principles methods for large systems¹ and for periodic systems,² such simulations are impractical for many important applications to semiconductor materials. Consequently, we have developed a consistent set of valence force fields that should be useful for molecular dynamics simulations of semiconductors. This MSXX (FF) is derived using empirical data on lattice constants, elastic constants, and phonon states. Herein we report the MSXX FF for the nine III/V systems with III= Al, Ga, In and V = P, As, Sb, the five II/VI systems with II = Zn, Cd, Hg, and for VI = S, Se, Te, and the group IV systems, diamond, silicon and germanium.

A prime motivation in developing the MSXX FF is to describe the strain effects and vibrational modes at heterojunction interfaces and superlattices. We illustrate the approach by predicting the vibrational interface states in several superlattices. These results show that the MSXX FF provides an accurate description of the strains and interface phonons.

The form of the MSXX FF is described in Section 2 and the optimization of the parameters is described in Section 3. Comparison to experimental phonon dispersion data is made in Section 4. The calculations of the superlattice phonon dispersion curves are given in Section 5.

2.0 The MSXX Force Field

Chapter 1 describes the general form of the force field. Here we describe the MSXX force field as specifically applied to semiconductor materials. The general form of the force field is taken as³

$$E = E^{val} + E^Q + E^{vdw} \quad (1)$$

where

$$E^Q = C_{coul} \sum_{i>j} \frac{q_i q_j}{R_{ij}} \quad (2)$$

represents the Coulombic interactions between partial charges on the various atoms ($C_{coul} = 332.0637$ ensures that E is in kcal/mol where R in Å),

$$E^{vdw} = \sum_{i>j} E_{ij}^{vdw}(R_{ij}) \quad (3)$$

represents the long-range attraction (London dispersion) and short-range repulsion (Pauli orthogonalization of nonbonded electrons) and

$$E^{val} = E^{bond} + E^{angle} + E^{cross} + E^{torsion} \quad (4)$$

represents all terms involving bonds between atoms and coupling behavior of these bonds. This type of FF has been used to describe polymers (polyethylene,⁴ polyvinylidene fluoride,⁵ polysilane,⁶ nylon⁷), Si_3N_4 ceramics,⁸ and many other systems. It is denoted as MSXX to indicate that it is for materials simulations and that it includes both 1 center and 2 center cross terms.

2.1 Bond Terms

We take E^{bond} as a sum over all bond pairs where each has the form of a Morse function,³

$$E^{Morse}(R) = D_R [\chi^2 - 2\chi] \quad (5)$$

with

$$\chi = e^{-\alpha(R - R_e)} \quad (6)$$

and

$$\alpha = \sqrt{\frac{k_R}{2D_R}}. \quad (7)$$

This includes anharmonicity and allows a proper description of bond dissociation. We choose the Morse form (5) over the more common harmonic description

$$E^{harm}(R) = \frac{1}{2}k_R(R - R_e)^2 \quad (8)$$

in order to better describe anharmonic effects, e.g. thermal expansion. Equation (5) contains three independent parameters R_e , k_R , and D_R . The structure, elastic constant, and phonons are sensitive to R_e and k_R but not to D_R . Consequently we choose D_R based on the experimental atomization energies.⁹

2.2 Angle Terms

We take E^{angle} as a sum over all angles $I-J-K$ for each atom J here each angle term is described with the cosine angle form,³

$$E^{cosine}(\theta) = \frac{C}{2} [\cos\theta - \cos\theta_e]^2 \quad (9)$$

where the force constant is

$$k_\theta = C \sin^2 \theta_e = \left(\frac{\partial^2 E}{\partial \theta^2} \right)_{\theta_e} .$$

This form leads correctly to $dE/d\theta = 0$ at $\theta = 0$ and 180° with a barrier (at 180°) of

$$E^{barrier} = \frac{C}{2} [1 + \cos\theta_e]^2 . \quad (10)$$

One might restrict θ_e to be $\theta_e = 109.471^\circ$, the tetrahedral value, since this is the optimum geometry in these crystals. However we have optimized both θ_e and k_θ .

2.3 Cross Terms

We find, generally, that bond-bond cross-terms

$$E_{RR} = K_{RR}(r_1 - r_{1e})(r_2 - r_{2e}) \quad (11)$$

sharing an apex atom (e.g. IJ and JK) are required to describe the coupling of *equivalent* bonds.⁴ Since bonds sharing a common apex are identical for the zinc-blende structures, we include such terms.

For two bonds $I - J$ and $J - K$ sharing a common atom, there are two bond-angle cross terms of the form³

$$E_{r\theta} = D_{r\theta} (r_1 - r_{1e}) (\cos\theta - \cos\theta_e) \quad (12)$$

$$k_{r\theta} = D_{r\theta} \sin \theta_e.$$

We find these to be necessary for III-V systems.

If three (or more) bonds share a common atom (say $I - J$, $K - J$, $L - J$), we find that the one center angle-angle cross terms (e.g coupling of the IJK and KJL angles)³

$$E_{\theta\theta 1} = F_{\theta\theta} (\cos \theta_1 - \cos \theta_1^e) (\cos \theta_2 - \cos \theta_2^e) \quad (13)$$

$$k_{\theta\theta 1} = F_{\theta\theta} \sin \theta_1^e \sin \theta_2^e$$

are *not* necessary to describe the structure, elastic constants, and phonon spectra of III/V semiconductors.

On the other hand we do find two-center angle-angle coupling to be important. Thus for three sequential bonds $I - J$, $J - K$, and $K - L$, the coupling of the IJK angle (θ_1) with the JKL angle (θ_2)^{3,10}

$$E_{\theta\theta 2} = G_{\theta\theta} (\cos \theta_1 - \cos \theta_1^e) (\cos \theta_2 - \cos \theta_2^e)$$

is important when the IJ and KL bonds are trans (dihedral angle, $\phi = 180^\circ$) but not when they are gauche ($\phi = 60^\circ, 300^\circ$). Consequently we define this coupling term as

$$E_{\theta\theta 2} = G_{\theta\theta} f(\phi) (\cos \theta_1 - \cos \theta_1^e) (\cos \theta_2 - \cos \theta_2^e) \quad (14)$$

where

$$f(\phi) = \frac{1}{3} - \frac{2}{3} \cos \phi$$

and

$$k_{\theta\theta 2} = G_{\theta\theta} \sin \theta_1^e \sin \theta_2^e$$

which leads to $f(180^\circ) = +1$ and $f(60^\circ) = f(300^\circ) = 0$. McMurry¹⁰ first introduced such a coupling term to describe the TA mode softening for k approaching the Brillouin zone boundary in Si. Such terms are generally required to describe the vibrations of long chain molecules (such as polysilane⁶ and polyethylene⁴) that

feature a trans zig-zag chain. Similarly they are needed to describe the stiffness along the $<110>$ chain directions of the diamond and zinc-blende materials.

Summarizing the cross terms are taken as

$$E_{cross} = \sum E_{RR1} + \sum E_{R\theta 1} + \sum E_{\theta\theta 2}. \quad (15)$$

2.4 Torsion Terms

Generally one would include terms of the form³

$$E^{torsion}(\phi) = \frac{1}{2}V^{tor}(1 + \cos 3\phi) \quad (16)$$

for describing the torsional barrier in a tetrahedral system. Such barriers describe the observed preference for staggered dihedral angles and lead to chair-like six membered rings rather than the boat conformation. Thus such interactions would prefer the sphalerite (cubic) or zinc-blende structure over wurzite (where 1/4 of the bonds have eclipsed ligands). However, we find that the structure, elastic constants, and phonon dispersion are not sensitive to V^{tor} and hence do not include it here. We do find electrostatic effects lead to a slight (0.1 kcal/mol) disfavoring of the Wurzite structure with respect to zinc-blende (see below).

2.5 Electrostatics

A valence force field without electrostatic terms leads to degenerate LO and TO modes at the Γ point, thus the group IV materials have degenerate optical Γ points. The observed splitting in these levels for the compound semiconductors results from the macroscopic electric field arising from the macroscopic displacement of charge in the LO mode as $\vec{k} \rightarrow 0$. To describe this splitting requires the electrostatic term in (2). Indeed, fitting the LO-TO splitting leads to unique charges in the range expected from the electronegativity differences of the III/V atoms. [We use the Accuracy Bonded Convergence Acceleration (ABC)A¹¹ procedure to sum the Coulombic interactions.]

2.6 Van der Waals

The energetics of small displacements in a tetrahedral crystal do not require explicit van der Waals interactions. However we intend to use these potentials for materials with surfaces, dislocations, vacancies, etc. where there may be other atoms or molecules. Consequently we want to include the van der Waals interactions required to describe interactions with nonbonded molecules. To do this we use the parameters from the Universal Force Field,¹² which includes vdw parameters for all elements up through Lr (element 103).

3.0 Force Field Optimization

We optimized the MSXX force field by minimizing the error between the calculated and experimental properties (lattice parameter, elastic constants, and phonon special points) of the crystal with respect to variations in the force field parameters.

3.1 The Error Function and Weights

The error function is¹³

$$S_{err} = W_{force} \sum_{i=1}^{3N-6} (\delta E'_i)^2 + W_{freq} \sum_{i=1}^{3N-6} (\delta \nu_i)^2 + W_{stress} \sum_{i=1}^6 (\delta \Sigma_i)^2 + W_{elas} \sum_{i <= j = 1}^6 (\delta C_{ij})^2 \quad (16)$$

where δ denotes the difference between the calculated quantities from the force field and from experiment. Here N is the number of atoms, E'_i is the gradient of the energy (the force), ν_i are the frequencies of the phonons (Γ and X point only), Σ_i are the stresses, and C_{ij} are the elastic constants (only C_{11}, C_{12}, C_{44} are unique for cubic crystals). We use the HB-SVD method^{13,14} to minimize the error, S_{err} . HB-SVD also handles redundancy in force field parameters so that the parameters are changed only when they significantly improve the fit.

We choose the weights to ensure that the forces on the atoms and the stresses on the crystal are zero. These weights were selected with three primary goals:

1. We want to reproduce the crystal geometry and fit the experimental phonon frequencies and elastic constants as closely as possible. There is generally a trade off between these two errors. We choose the weights such that neither is too large, but with more emphasis on the phonon frequencies. The reason is that the low frequency properties associated with the elastic constants have less bearing on the localized strains surrounding defects and surfaces.
2. We want to ensure the intuitive nature of the valence force field by having physically meaningful values for the force constants. This led us to include only the significant cross terms, as discussed above.
3. We want the resulting force constants to show regular behavior as we move across and down the periodic table. This is so that reliable predictions can be made for mixed systems such as heterojunctions. The weights chosen for (1) and (2) lead to this regular behavior.

3.2 Phonon Dispersion

After fitting the force field, we used it to predict the complete phonon dispersion curves along the $<100>$ and $<111>$ directions. Expanding the energy about equilibrium leads to

$$E(R_i) = E(R_i^e) + \sum_i E'_i \delta R_i + \frac{1}{2} \sum_{i,j} E''_{ij} \delta R_i \delta R_j \quad (17)$$

with

$$R_i = R_i^e + \delta R_i.$$

The force at equilibrium is zero

$$F_i = -E'_i = -\frac{\partial E}{\partial R_i} = 0 \quad (18)$$

and

$$E''_{ij} = \frac{\partial^2 E}{\partial R_i \partial R_j} = H_{ij} \quad (19)$$

is the Hessian.

The equations of motion become

$$M_I \frac{\partial^2 [\delta R_{\alpha I}(t)]}{\partial t^2} = - \sum_{\beta J} H_{\alpha I, \beta J} [\delta R_{\beta J}(t)]$$

where the subscripts I and J run from 1 to the number of atoms N , and the subscripts α and β run through the x, y, z components of the atomic coordinates.

The time periodic eigenstates have the form

$$\delta R_{\alpha I}(t) = (\delta R_{\alpha I}^0) e^{i(\vec{k}\vec{r} - \omega t - \phi)},$$

where

$$\omega^2 M_I (\delta R_{\alpha I}^0) = \sum_{\beta J} H_{\alpha I, \beta J} (\delta R_{\beta J}^0) e^{i\vec{k}(\vec{r}_{\beta J} - \vec{r}_{\alpha I})}. \quad (20)$$

Taking \vec{k} in $<100>$ and $<111>$ directions and solving the equation (20) gives the corresponding frequencies.

3.3 Charge Equilibration

For tetrahedral crystals, the splitting of the LO and TO modes at the Γ point is quite sensitive to the charge difference between the cation and anion. This arises from the macroscopic dipole for the LO mode near $\vec{k} = 0$. (With no charge difference these modes are degenerate.) We develop a electronegativity scale based on the splitting of the Γ points. The resulting charges represent the electronegativity difference in the elements. Thus $q_{VI} = 0.88, 0.80, 0.76$ for ZnS, ZnSe, ZnTe indicates that the electronegativities are in the sequence $S = Se > Te$. The $q_{II} = 0.76, 0.86, 0.74$ for ZnTe, CdTe, and HeTe indicate that the electronegativities are in the sequence $Hg > Zn > Cd$. This is in rough agreement with the Pauling values as optimized by Allred¹⁵: 2.58, 2.55, 2.3 for S, Se, Te and 1.65, 1.69, 2.00 for Zn, Cd, Hg.

For the more interesting cases of interfaces and defects, we expect charge readjustments but there is not sufficient experimental data to determine the modified charges. Thus we have used the charge equilibration (QEeq) procedures of

Rappé and Goddard¹² but with the readjusted atomic electronegativities to fit the MSXX FF.

In QEq¹⁶ the energy of an atom A is assumed to be

$$E_A(Q_A) = E_{0A} + \chi_A Q_A + \frac{1}{2} I_{AA} Q_A^2 \quad (21)$$

where

$$\chi_A = \frac{1}{2} (IP + EA) \quad (22)$$

is called the electronegativity and

$$\frac{1}{2} J_{AA} = IP - EA \quad (23)$$

is called the hardness (or idempotency). Then in a molecule or crystal the total energy is taken to have the form

$$E = \sum_A E_A(Q_A) + \sum_{A=B} Q_A Q_B J_{AB}(R_{AB}) \quad (24)$$

where $J_{AB}(R_{AB})$ is the Coulomb potential between spherical charge distributions on A and B with radii R_A and R_B , respectively. For crystals the second term in (42) must be evaluated using the Ewald procedure. The QEq Ewald program was rewritten by Karasawa and Goddard¹⁷ to calculate the ionic charges for periodic systems.

For group II the standard QEq parameters^{9,16} lead to the results in Table 1. The discrepancy with the MSXX values are probably due to the special nature of the group II atoms where the ground state s^2 is used to define χ_A and J_{AA} but, the crystal involves sp^3 hybridization. Consequently we have readjusted the χ_a for group II to agree with MSXX. The results are shown in Table 1. With this readjustment of QEq parameters we can now predict charges at interfaces, impurities, etc.

4.0 Results

4.1 Group IV Materials

The experimental phonon frequencies and elastic constants of the group IV materials are listed in Table 2 and were selected from reference 18 which provides all the elastic constants and special phonon points needed for fitting the FF for all the materials. We choose to fit to the phonon frequencies to the neutron scattering experiment for each case when available. For elastic constants we choose to fit to values that were in best agreement with other experimental techniques (this means we fit to data that was not extreme relative to other experiments). This was done to minimize the possibility of fitting to a piece of experimental data having a large error.

The optimized parameters for the MSXX force fields are listed in Table 3, and the van der Waals parameters (not optimized) are listed in Table 4. The parameters change monotonically going from C, to Si, to Ge. Thus K_r , K_θ , and $K_{\theta\theta 2}$ decrease moving down the periodic table (since the bonds get weaker). The cross terms (except the 2 center angle-angle term) do not demonstrate this behavior. We can also see that the charges decrease as the bonds gets weaker.

The predicted phonon dispersion curves are compared with experiment in Figures 1-3. We plot the FF phonon dispersion curves in the $\langle 100 \rangle$, $\langle 110 \rangle$ and $\langle 111 \rangle$ directions and the neutron scattering data in these directions. Since the data used to fit the curves was the elastic constants and the special points at Γ and X the $\langle 100 \rangle$ direction demonstrates the accuracy of the fitting procedure for fitting to the entire branch while the $\langle 110 \rangle$ and $\langle 111 \rangle$ directions demonstrate the ability of the model to predict values which are not included within the fit. The discrepancy between the neutron scattering data and the theory is remarkably small.

Overall the deviation from experiment is quite small. The ability of MSXX FF to reproduce phonon dispersion with such few parameters adds credibility to the fundamental appropriateness of the description underlying this model. This

suggests that this force field may be useful in predicting the strains and mechanical properties of these systems.

4.2 Group III/V Materials

The experimental phonon frequencies and elastic constants of the group III/V materials are listed in Table 5 and were selected from reference 18 which provides all the elastic constants and special phonon points needed for fitting the FF for all the materials except AlP for which the X points are unavailable.

The optimized parameters for the MSXX force fields are listed in Table 6, and the van der Waals parameters (not optimized) are listed in Table 7. The parameters change monotonically going from AlP to AlAs to AlSb, from GaP to GaAs to GaSb and from InP to InAs and InSb. Thus K_r and K_θ decrease moving down the periodic table (since the bonds get weaker). The cross terms do not demonstrate this behavior. We can also see that the charges decrease as the bonds gets weaker.

The predicted phonon dispersion curves are compared with experiment in Figures 4-12. The best data is for GaAs. We plot the FF phonon dispersion curves in the $\langle 100 \rangle$, $\langle 110 \rangle$ and $\langle 111 \rangle$ directions and the neutron scattering data in these directions. The discrepancy between the neutron scattering data and the theory is small. The largest differences occur along the TA branches in the $\langle 110 \rangle$ direction (which is also the branch for which the neutron data has large error bars).

To extend the MSXX FF to the prediction of polarization properties, we will add a covalent shell description to the valence force field (as was done for PVDF⁵). We could also improve the fits of MSXX by using additional points from the phonon dispersion curve in the set of constraints. However, the current fit is acceptable for all systems.

4.3 Group II/VI Materials

The experimental phonon frequencies and elastic constants of the group II/VI materials are listed in Table 8 and were selected from reference 18. The optimized parameters for the MSXX force fields are listed in Table 9, and the van der Waals parameters (not optimized) are listed in Table 10. The predicted phonon dispersion

curves are compared with experiment in Figures 13-17. Again, as in the case of the group III/V materials the largest errors occur along the TA branches in the $\langle 110 \rangle$ direction.

5.0 Superlattices

Phonon dispersion curves for superlattices have long been an active research area. Since Colvard et al. first observed the folded acoustic phonons,¹⁹ much progress has been made both in theory and experiment. Theoretical work has included the elastic model and Fourier transform analysis which have been proposed to explain the folding of the acoustic branch, and the degeneracy at the Brillouin zone center and boundary.²⁰ The alternating linear chain model has been employed to explain the confined modes.²⁰ And a theory treating the dielectric modulation has been used to explain the interface modes.²⁰ All these models deal only with the dispersion curves along the axis direction. Complicated, non-intuitive, numerical models such as the Valence Overlap Shell model, etc., have been necessary for the full 3-D description of the superlattice phonons. Our approach offers an advantage in that it is much simpler and physically intuitive. Another complicated issue is the effect of strain on the superlattice phonons which is discussed by Jusserand and Cardona.²⁰ The acoustic phonon folding, zone edge and zone center splittings are observed experimentally as are the confined optical modes and interface modes.

A general scheme to model the superlattice phonons is to utilize the models for bulk materials and adapt them to the superlattice. As pointed out in,²⁰ 3 problems should be addressed: (1) The choice of proper lattice dynamical models for the bulk constituents. (2) The transferability of the bulk model parameters to the superlattice case, which is reasonable and straight-forward for local quantities or very short range interactions, but which becomes more difficult for long range forces. (3) Numerical difficulties arising from the size of the secular equations in the case of thick layer superlattices.

In this section we extend the molecular mechanics FF to calculate the phonon

dispersion curves for the superlattices. In the force fields, the local quantities such as bond lengths and angles, bond stretching and angle bending force constants, are all directly transferred, the long range van der Waals forces are also directly transferred. We used the electronegativity of the atoms to calculate the charge on the atoms to determine the Coulomb forces. However, some of the interface local parameters are unique to the interface and we use an averaging method to interpolate the interface potential. We justify the scheme in the following section on detailed calculations and with comparisons to experiment in section 5.3.

The MSXX model is a 3-D model, capable of dealing with all crystallographic directions and interfaces, and with difficult problems as strain, etc. It is also readily modified to simulate surface roughness. The parameters involved are few and so the calculation is relatively fast.

5.1 Calculation Details: Transfer and Extension of the Force Field

We have developed MSXX force fields for the bulk materials elsewhere,²¹ as described in sections 3 and 4 and showed that our force field reproduces the whole range of the dispersion curves well. We directly transfer the force fields to the superlattice after adding interface interactions interpolated from the bulk FF. There are two types of superlattices: one type is $(AB)_{n1}(AC)_{n2}$, and the other is $(AB)_{n1}(CD)_{n2}$. The first type has a common atom on the interface, while the second one doesn't. Here we only deal with the first type. The second type is very similar, and will be investigated in future work. For the first type, the superlattice consists of layers of AB and AC, e.g. $(HgTe)_{n1}(CdTe)_{n2}$. From the bulk FF we have the parameters involving only AB and AC. For the atoms on the interface, the force fields are different from both of the bulk materials as new three and four body (and higher) interactions are involved. We derive the new interactions using a simple averaging technique.

For the Angle B-A-C; We take the angle to be the geometric mean, i.e:

$$\theta_{BAC} = \sqrt{\theta_{BAB} * \theta_{CAC}}.$$

We also do this for the angle bending force constant:

$$K_{\theta,BAC} = \sqrt{K_{\theta,BAB} * K_{\theta,CAC}}.$$

The other terms needed to describe the interface are the cross terms and these become more slightly more complicated. For the B-A-C angle we need two bond-cross-angle terms which we obtain from the related parameters in the original bulk material. However, the original bond-cross-angle terms are symmetric for angle B-A-B and C-A-C, so the obvious way to extend it to the B-A-C is to use them directly:

$$K_{r\theta,BAC} = K_{r\theta,BAB}$$

$$K_{r\theta,CAB} = K_{r\theta,CAC}$$

and for the bond-bond cross-term, we can also take the geometric mean:

$$K_{rr,BAC} = \sqrt{K_{rr,BAB} * K_{rr,CAC}}.$$

In developing the MSXX FF for the II/VI and III/V systems we did not use torsion terms and likewise we don't include them here. However, we did use the two-center angle-cross-angle terms, for the superlattices we obtain from the two-center angle-cross-angle terms in the chain B-A-C-A and C-A-B-A of the component materials taking the geometric mean of the two-center angle-cross-angle terms B-A-B-A and C-A-C-A :

$$K_{angang,BACA} = \sqrt{K_{angang,BABA} * K_{angang,CACA}}$$

$$K_{angang,CABA} = \sqrt{K_{angang,BABA} * K_{angang,CACA}}.$$

With these interpolations we get all the force field parameters we need, (Table 11 shows the additional terms needed for the ZnSe/ZnTe superlattice, as an example).

5.2 Superlattice Dispersion Curve Calculation

The superlattice dispersion is calculated in the same way we calculated the bulk phonon dispersion curves.²¹ We build a unit cell and apply periodic boundary conditions. However, there are several concerns about building the cell. (1) The number of atoms in the cell should be as small as possible to reduce the expense of the calculation. In the superlattice $(AB)_{n_1}(AC)_{n_2}$, if $n_1 + n_2 = even$, the space group is $P4m2(D_{2d^5})$, and if $n_1 + n_2 = odd$, the space group is $I4m2(D_{2d^9})$. Both lattices are $4m2(D_{2d})$. In the $n_1 + n_2 = even$ case it is easy to build a unit cell which contains the smallest number of atoms. And in the $n_1 + n_2 = odd$ case, we have to double the cell size so that the cell can repeat itself. This increases the computer time required to compute the vibrations. (2) The II-VI superlattices are usually strained. In the commensurate case the lattice constant in-plane is constrained by the substrate or buffer layer. In the free standing case, the lattice constant in-plane can be different from that of substrate, and the stress is released. When we build the lattice unit cell, we can fix the in-plane lattice constant to be that of substrate or buffer to simulate the commensurate case; or we can optimize all the lattice parameters to simulate the free standing case. (3) The charge on the atoms may be different from the bulk materials. For example, we expect the charge on the interface atom to be intermediate between the two component materials. We assigned the charge by doing Ewald charge equilibration: First, we used the fitted Mulliken eletronegativities of the atoms that reproduce the charges of the bulk material, and then use those eletronegativities to calculate the charges on the atoms of the superlattice unit cell. Indeed, we see that the interface atom has a charge which is intermediate to the charges of the like atoms in the two component materials, and the charge transition is entirely confined to the interface layer and the two monolayers adjacent to it. 4) Usually the unit cell is under stress; Both the short range and long range interactions will contribute stress to the unit cell. So we fix the in-plane lattice constant to the substrate lattice constant and do charge equilibration and energy minimization of the cell iteratively until convergence. We

then obtain the cell size and the right charge. We also obtain the in-plane stress. Usually 3 or 4 iterations will suffice. It is also possible to free the in-plane lattice constant and iterate to get the cell without strain for free standing superlattices.

5.3 Results

Our model is first compared to the available experimental data. Unfortunately, the experimental phonon frequencies are scant and incomplete. The available data for ZnS/ZnSe are from Cui,²² for ZnSe/ZnTe from Cui,²³ Shen,²⁴ Ozaki,²⁵ and Wu,²⁶ and for CdTe/ZnTe from Menendez.²⁷ In the simulation, we calculated the layers of the composite material and constructed the corresponding unit cell. It is required that the number of layers of the composite be an integer. For the commensurate case we require the in-plane lattice constant to be clamped by the buffer layer or substrate layer; while for the free-standing case we allow the lattice completely relax, optimizing the unit cell without constraints. Another assumption we made is that the superlattices have perfect interfaces. We show that the interface phonons are insensitive to surface roughness and then only consider perfect interfaces. The results are summarized in Tables 12-14. Both the commensurate(stressed) and free-standing (relaxed) cases are shown. The stressed cases should be compared to the experiment. For ZnS/ZnSe (Table 12) it is not clear whether the sample is commensurate or free-standing. We find basically the prediction of our model is in agreement with experiment. However, there are also 3 discrepancies. (1) For the ZnS/ZnSe LA mode we have to use a $(ZnS)_{12}(ZnSe)_{12}$ unit cell to reasonably reproduce the experimental results, instead of $(ZnS)_{10}(ZnSe)_{10}$ unit cell which has the layer thickness reported in the experiment. This could possibly be explained by an error in the thickness measurement in the experiment. (2) The prediction of a few of the interface modes deviates from experiment. In the first sample of CdTe/ZnTe, Menendez²⁷ assigned the Raman scattering peaks at 155.92 cm^{-1} and 199.69 cm^{-1} as interface modes, and in the second sample of CdTe/ZnTe, Menendez²⁷ attributed the Raman scattering peaks at 153.4 cm^{-1} and 192.1 cm^{-1} to interface modes. However, our simulations clearly show that there is no interface

modes around those frequencies, instead we found interface modes at 176 cm^{-1} and 179 cm^{-1} , and they are independent of the slab thickness. This may not be explained by the roughness of the interface of the experimental sample, because the surface roughness should not affect the optical phonons drastically. On the other hand it could be explained by an error in the experimental assignment. (3) For the 184 cm^{-1} LO frequency in sample (1) of CdTe/ZnTe, Menendez²⁷ assigned it to be LO modes in the CdTe. We didn't find any LO modes of CdTe around that frequency, instead we found that there is a ZnTe confined LO mode at 185.3 cm^{-1} so we assign this mode to the experimental peak at 184 cm^{-1} as a confined LO mode in ZnTe. Other than that our model agrees well with experiment.

The above comparison of our model and experiment shows that the model is accurate and therefore useful for making predictions, which we make in the form of phonon dispersion curves for the superlattices. The dispersion curves $(AB)_{n1}(AC)_{n2}$ for the ZnS/ZnSe, ZnSe/ZnTe, CdTe/ZnTe and HgTe/CdTe superlattices are shown for $n_1 = 1, n_2 = 1$ in Figures 18-21, for $n_1 = 2, n_2 = 2$ in Figures 22-25, for $n_1 = 4, n_2 = 4$ in Figures 26-29, for $n_1 = 10, n_2 = 2$ in Figures 30-33. Dispersion curves along both parallel and perpendicular to the interface are shown.

5.4 Acoustic Phonon Folding and Splitting

Here we compare the superlattice dispersion curves with those of the bulk materials. For illustrative purposes we used the simplest case $(ZnSe)_1(ZnTe)_1$ and compare it to the bulk ZnSe and ZnTe in figure 34. From the figure we notice that the dispersion curve of the superlattice is constructed by folding the composite dispersion curves and then mixing the corresponding branches, e.g. the TA and LA modes of the superlattice of $(ZnSe)_1(ZnTe)_1$ is a mixture of the folded TA(LA) modes of ZnSe and ZnTe. If we compare the dispersion of $(ZnSe)_1(ZnTe)_1$ to that of $(ZnSe)_2(ZnTe)_2$, we immediately observe that the dispersion curves of $(ZnSe)_2(ZnTe)_2$ are just the folded dispersion curves of $(ZnSe)_1(ZnTe)_1$. The bulk materials' TA modes flatten near the zone boundary, and when they are folded,

they remain essentially flat at the new BZ boundary. When the acoustic branches are folded, the once degenerate branches split. The splitting increases as the energy of the branch increases.

Also shown in Figure 18-33 are the in-plane dispersion curves. The TA modes are split, as expected, and one of the TA modes is degenerate with the LA mode at the zone boundary. This is because for the in-plane wave vector, the motion of the LA modes is in-plane, while for TA modes, the motion of one of the branches is in-plane and the other is perpendicular to the plane. At zone boundary, the in-plane part of the higher energy TA mode takes on LA mode character.

5.5 Optical Confined Modes

We also observe the folding of the optical modes of the bulk composite dispersion curves. When the number n_1 and n_2 are small, the optical dispersion curves remain curved. However, as the number of atomic layers in the superlattice increases, the optical modes flatten, and the “folding” becomes harder and harder to see, and it becomes more appropriate to treat them as confined modes. In our simulation we distinguish the TO and LO modes by their multiplicity: TO modes are doubly degenerate and LO modes are non-degenerate. The in-plane optical dispersion curves are also shown in the Figure 18-33. However, in this case the double degeneracy of the TO modes is lifted and the resulting branch becomes a mixture of the TO and LO modes of the bulk component materials. However, a clear identification is difficult.

Notice at the reciprocal cell zone center, the phonon frequencies are different for branches, in different directions. That is the Γ points have split depending on the direction of the wavevector (thus the polarization direction). This polarization dependency is entirely due to the charge of the atoms. If the ionic charge is removed, all the corresponding branches are continuous along different directions. With an ionic charge a finite jump will occur as \vec{K} passes through Γ for some of the optical modes. This behavior also exists in other anisotropic materials such as hcp crystals, and it is called “Angular dispersion.” It doesn’t exist in materials with the fcc lattice

because of the cubic symmetry.

5.6 Interface Phonons

Interface modes in semiconductor superlattices have been reported by several studies. In our simulations, we can directly distinguish the interface modes from the non-interface modes by analyzing the displacement vectors of the atoms, making assignments much easier. We list the interface modes in various superlattices in Table 15. For comparison, the typical motion of the folded TA and LA modes, the confined TO and LO modes, and the interface modes of $(ZnSe)_4(ZnTe)_4$ are shown in Figure 35.

Analysis of the normal mode character of the interface modes listed in Table 15 indicates that all the interface modes are TO modes of the superlattice, being confined to the interface, and being doubly degenerate. The motion of the atoms is in-plane, and only the atoms on the interface and immediately adjacent to it move. The frequency is characteristic of the interface, almost independent of the layer thickness except in the $(AB)_1(AC)_1$ case, where the slab is very thin and there is no clear difference between interface atoms and inner layer atoms. To verify this assumption we constructed several other superlattices with different slab thicknesses, and found the assumption that interface modes are independent of layer thickness to be true. The result is shown in Table 15. This means that the interface phonon can be employed to characterize the interface properties for crystal growth.

Another important issue is that interface phonons are insensitive to surface roughness. Since surface phonons are essentially TO modes, they come from folding of the bulk material optical branches, and surface roughness just means that the length of the reciprocal lattice perpendicular to the interface is different at different parts of the superlattice, the lattice parameter being just the average of the entire interface. However, the TO phonons are almost independent of the reciprocal length, and so the effect of the interface roughness is minimal. In order to test this, we constructed a supercell of $(ZnSe)_4(ZnTe)_4$ and made the interface roughness vary from 30% to 50%, and we found the interface modes varied in the small range

of 192.6 to 194.6 cm⁻¹.

5.7 Elastic Constants of the Superlattice

The elastic constants of the superlattice are shown in Table 16 along with the bulk materials. The superlattice has lower symmetry and the elastic constant matrix has the relation $C_{11} = C_{22}$, $C_{31} = C_{32}$, $C_{44} = C_{55}$. We have 6 unique ($C_{11}, C_{12}, C_{33}, C_{13}, C_{44}, C_{66}$) non-vanishing components. We find that the elastic constants are usually between those of the component materials. Currently, no measurement of elastic constants for superlattice has been reported.

6.0 Discussion

A number of approaches have been proposed to describing the interatomic interactions of semiconductor crystals. This includes the bond charge models of Martin²⁸ and Weber²⁹ and the quasiparticle valence bond force field of Messmer.³⁰ These models require a greater number of parameters (for example Messmer's FF requires 10 parameters for Si while MSXX requires only 7 parameters) and lead to fairly complicated equations. These models succeed in modeling the phonon spectra of the diamond lattice and zinc-blende semiconductors, although with some cost in accuracy and simplicity. These models may provide a good model of the polarization effects in these materials. The Kane potential³¹ models such properties through the interaction of his dipoles and quadrupoles with the polarization field.

The MSXX FF is essentially as accurate as the experimental data to which it was fitted. Although more accurate and more complete experimental data is becoming available there is still significant uncertainty in the experimental values for some properties of some of these materials. These uncertainties often arise from some of the indirect methods required to measure the phonon spectra.

Force fields capable of describing the strain fields, geometric structures, and vibrational properties of distorted systems must be capable of reproducing the interatomic potential energy surface for moderate strains and also the couplings of interatomic interactions. It is possible to reproduce the phonon spectra of a zinc-

blende crystal to relatively high accuracy using harmonic potentials. However, harmonic potentials are inappropriate for describing the breaking of a bond. Thus even though the phonon dispersion curve is reproduced, the strain fields may not be sufficient for accurate modeling of highly distorted structures. For this reason we use Morse potentials to approximate the anharmonic effects of strained bonds as bonds are broken. This should lead to a good description of thermal expansion. Furthermore, the use of Morse potentials for bonds should allow phonon-phonon couplings to be described in the harmonic description of the interatomic interactions.

The MSXX FF includes the coupling of coplanar angles that share a common side, but not a common apex. This term (also used by Kane³¹) was first implemented by McMurry¹⁰ to describe the flattening of the TA modes on approaching the X and Γ points along the $<100>$ and $<111>$ directions. Formally a fifth neighbor interaction, it allows for through bond coupling of the accordion chains along $<110>$. Furthermore, Kane³¹ observed that the introduction of an impurity in the diamond lattice polarizes the charge distribution with high directionality along the $<110>$ chains. Again, the form of the coplanar-two-center-angle-angle coupling leads to an effective model and an intuitive picture of this effect through the coupling of adjacent bond angles along the $<110>$ direction. This effect emphasizes the necessity for such terms. Because this coupling depends on the large delocalization of bond charge along $<100>$ chains associated with through bond coupling, we expect the coupling to fall quickly as the bond angles become non-coplanar. For the perfect crystals this is irrelevant, but for strain fields that break the crystal symmetry and structures sampled with molecular dynamics at higher temperatures, the damping of the coplanar angle-angle coupling is necessary. Although the coupling between the two coplanar angles of the trans dihedral is critical to the description of the TA mode, we find that the dihedral angle torsion force constant itself is unnecessary for our fits. It might play a role in distinguishing between the sphalerite and wurzite forms of the crystal, and if so it would be important for describing of the stacking fault energy.

7.0 Conclusion

The simple MSXX valence force field with just a few parameters leads to accurate structural, mechanical, and vibrational properties of the zinc-blende semiconductors. The systematic behavior of the force constants allows one to interpolate force constants for tertiary interactions, as illustrated for the II/VI superlattices. The MSXX FF describes anharmonic interactions in bonds and should be useful for describing the thermal expansion, temperature dependence of the phonons, and phonon-phonon interactions.

References

1. R. Friesner, J. Chem. Phys. **85**, 1462, (1986); R. Friesner, J. Chem. Phys. **86**, 3522, (1987); M. Ringnalda, Y. Won and R. Friesner, J. Chem. Phys. **92**, 1163, (1990).
2. C. Pisani, R. Dovesi and C. Roetti, Hartree-Fock *ab initio* Treatment of Crystalline Systems, Lecture Notes in Chemistry **48**, 1 (Springer-Verlag, Berlin, 1988).
3. S. L. Mayo, B. D. Olafson and W. A. Goddard III, J. Phys. Chem. **92**, 7488 (1990).
4. N. Karasawa, S. Dasgupta, and W. A. Goddard III, J. Phys. Chem. **95**, 3358 (1991).
5. N. Karasawa and W. A. Goddard III, Macromolecules **25**, 7268, (1992).
6. C. B. Musgrave, S. Dasgupta, and W. A. Goddard III, The Hessian Biased Force Field for Polysilanes, To be submitted to Macromolecules.
7. S. Dasgupta, W. B. Hammond, and W. A. Goddard III, A New Hydrogen-Bond Potential for Peptides: Crystal Structure and Properties of Nylon.
8. J. A. Wendel and W. A. Goddard III, J. Chem. Phys. **97**, 5048 (1992).
9. NBS Technical Note 270-3, selected values of chemical thermodynamic properties U. S. Department of Commerce, National Bureau of Standards.
10. H. L. McMurry, A. W. Solbrig Jr., J. K. Boyter and C. Noble, J. Phys Chem. Solids **28** 2359 (1967).
11. N. Karasawa and W. A. Goddard III, J. Phys. Chem. **93**, 7320 (1989).
12. A. K. Rappé, C. J. Casewit, K. S. Colwell, W. A. Goddard III, and W. M. Skiff, J. Am. Chem. Soc. **114**, 10024 (1992).
13. S. Dasgupta and W. A. Goddard III, J. Chem. Phys. **90**, 7207 (1989).
14. T. Yamasaki, S. Dasgupta, and W. A. Goddard III, Hessian Biased Force Fields: II. The Singular Value Decomposition (SVD) Based Least Squares Method for Optimization and Analysis of Force Field Parameters, submitted

to J. Chem. Phys.

15. Allred and Provin, Pauling electronegativities.
16. A. K. Rappé and W. A. Goddard III, J. Phys. Chem. **95**, 3358 (1991).
17. N. Karasawa and W. A. Goddard III, unpublished. See N. Karasawa Thesis, Applied Physics 1991.
18. K. H. Hellwege, *Landolt-Bornstein Numerical Data and Functional Relationships in Science and Technology* Springer-Verlag (1982).
19. C. Colvard, R. Merlin, M. V. Klein, A. C. Gossard, Phys. Rev. Lett., **43**, 298 (1980).
20. M. Cardona and G. Guntherodt, Light Scattering in Solids, V : Superlattices and Other Microstructures, Springer-Verlag, 49 (1989).
21. J. Hu, C. B. Musgrave, W. A. Goddard III, to be published.
22. J. Cui, H. Wang, F. Gan and A. Li, J. Crys. Grwth., **111** 811 (1991).
23. J. Cui, H. Wang, F. Gan, J. Appl. Phys **72**, 1521 (1992).
24. A. Shen, J. Cui, H. Wang and Z. Wang Superlattices and Microstructures, **12**, (1992).
25. H. Ozaki, D. Suzuki, K. Imai, and K. Kumazaki, Phys. Stat. Sol (a) **133**, 523 (1992).
26. Y. H. Wu, H. Yang, A. Ishida, and H. Fujiyasu, Appl. Phys. Lett., **54**, 239 (1989).
27. J. Menendez, A. Pinczuk, J. P. Valladares, R. D. Feldman and R. F. Austin, Appl. Phys. Lett., **50**, 1101 (1987).
28. R. M. Martin, Phys. Rev. B **1**, 4005 (1970).
29. W. Weber, Phys. Rev. Lett. **33**, 371 (1974).
30. H. X. Wang and R. P. Messmer, Phys. Rev. B **41** (1990).
31. E. O. Kane, Phys. Rev. B **31**, 7865 (1985).

Table 1. Ewald charge equilibration parameters and the comparison of the charges resulted from phonon gap fitting and charge equilibration.

Atom	Zn	Cd	Hg	S	Se	Te
(a) Modified QEeq Parameters						
Electroneg (eV)	0.900	0.376	0.850	6.928	6.428	5.816
Hardness (eV)	4.285	3.957	4.160	4.486	4.131	3.526
(b) Predicted CHARMM						
Material	ZnS	ZnSe	ZnTe	CdTe	HgTe	
Calculated Cation q	0.90	0.79	0.77	0.86	0.74	
Fitted Cation q	0.88	0.80	0.76	0.86	0.74	

Table 2. Experimental lattice constants, phonon frequencies, elastic constants, used in determining the MSXX FF (from reference 8, see discussion in Section 4.1). Comparison with theoretical predictions.

Quantity	Diamond	Silicon	Germanium
Lattice Parameters (Å)			
Experiment	3.5610	5.4310	5.6507
MSXX	3.5610	5.4310	5.6507
Elastic Constants (GPa)			
C_{11} exper	1076.0	167.5	129.0
MSXX	1083.5	170.7	138.2
C_{12} exper	125.0	65.0	48.0
MSXX	125.1	64.2	47.1
C_{44} exper	576.0	80.1	67.0
MSXX	573.4	78.6	64.5
rms C_{ij} deviation	2.61	3.38	0.51
Phonons (cm⁻¹)			
TA(X) exper	803.6	150.4	80.1
MSXX	808.8	150.6	80.2
LA-LO(X) exper	1078.1	415.0	240.5
MSXX	1069.4	412.7	238.7
TO(X) exper	1194.8	463.7	275.5
MSXX	1161.8	463.8	275.4
Γ_{15} exper	1333.9	518.1	298.9
MSXX	1341.7	518.7	300.4
rms phonon deviation	0.40	2.69	0.94

Table 3. MSXX force field parameters for the group IV materials.

Quantity	Diamond	Silicon	Germanium
(a) Bond			
k_R [kcal/(molÅ ²)]	576.55	193.75	180.04
R_e (Å)	1.522	2.380	2.465
D_R^a (kcal/mol)	110.0	73.7	73.7
(c) Angle			
k_θ [kcal/(mol rad ²)]	118.60	33.61	21.76
θ (degree)	109.41	105.05	109.47
$k_{r\theta}$ [kcal/(molÅ rad)]	-59.56	-14.76	-14.86
k_{rr} [kcal/(molÅ ²)]	8.05	3.39	0.56
(e) Two Center Angle-Angle Cross Term			
$G_{\theta\theta}$ [kcal/(mol rad ²)]	-27.54	-25.14	-23.35

Table 4. van der Waals parameters (from reference 23). See equations (4) and (5).

Atom	C	Si	Ge
R^{vdw} (Å)	3.883	4.270	4.270
D^{vdw} (kcal/mol)	0.0844	0.3100	0.3100

Table 5. Lattice Constant, elastic constants, and phonon frequency from experiment and from the MSXX force field. Numbers in square braces were *not* used in the fit (they were extrapolations from trends in other materials and are included for comparison).

	AlP	AlAs	AlSb	GaP	GaAs	GaSb	InP	InAs	InSb
(a) Lattice Constants (Å)									
a	5.467	5.6611	6.1355	5.4506	5.6419	6.0940	5.8687	6.0584	6.4788
(b) Elastic Constants (GPa)									
c_{11} exp	132.0	125.0	87.69	141.20	118.1	88.39	102.0	83.29	66.69
MSXX	128.3	124.0	86.46	142.16	122.9	93.50	106.6	85.11	68.56
c_{12} exp	63.00	53.40	43.41	62.53	53.20	40.33	57.6	45.26	36.45
MSXX	67.42	57.01	41.63	61.13	51.89	36.63	57.4	42.71	35.12
c_{44} exp	46.00	54.20	40.76	70.47	59.40	43.16	46.0	39.59	30.30
MSXX	65.71	57.70	39.39	69.44	57.57	40.52	44.9	37.07	29.04
rms C_{ij}	11.86	2.65	1.47	1.15	3.06	3.95	2.73	2.32	1.51
(c) Phonon Frequencies (cm⁻¹)									
TA(X) exp	[51.91]	108.9	70.00	106.7	81.7	56.6	68.33	53.0	37.3
MSXX	147.60	109.2	70.30	106.7	81.9	56.7	68.9	53.0	37.5
LA(X) exp	[47.67]	221.8	155.00	249.0	225.0	166.3	193.33	160.0	143.3
MSXX	356.60	216.6	152.90	249.0	221.9	163.3	182.8	160.6	141.3
TO(X) exp	[436.10]	334.0	296.00	353.5	256.3	212.0	323.33	216.0	179.3
MSXX	437.20	333.9	296.30	353.9	256.7	213.1	323.5	217.0	179.9
LO(X) exp	[371.54]	402.5	341.00	366.2	240.0	211.7	331.67	203.0	158.3
MSXX	395.50	400.8	346.60	365.8	236.8	209.3	326.6	201.7	156.4
TO(Γ) exp	439.40	360.9	323.40	366.2	271.0	232.3	304.00	217.3	184.7
MSXX	439.30	363.5	320.80	365.5	272.2	231.7	307.8	215.6	185.0
LO(Γ) exp	501.00	404.1	344.40	404.1	293.0	235.0	346.00	238.6	196.7
MSXX	500.80	406.4	341.80	403.5	294.0	[240.5]	349.3	237.1	196.9
rms ν_i	0.16	2.64	2.87	0.44	1.94	1.81	5.17	1.17	1.16

Table 6. Optimized parameters for the MSXX force field.

	AlP	AlAs	AlSb	GaP	GaAs	GaSb	InP	InAs	InSb
(a) Charge (e)									
Cation (e)	0.83	0.78	0.60	0.72	0.64	0.46	0.83	0.72	0.61
(b) Bond									
k_R	143.36	101.67	94.996	107.51	99.10	85.68	93.77	78.26	75.82
R_e	2.480	2.630	2.779	2.559	2.631	2.805	2.772	2.865	2.998
D_R ^a	48.25	44.53	40.80	40.60	38.88	34.73	38.64	36.11	32.04
(c) Angle at III									
k_θ	32.15	36.882	28.97	50.09	34.69	36.85	32.29	34.91	21.15
θ_e	124.96	114.87	114.80	110.46	107.16	109.09	114.13	112.15	112.27
$K_{r\theta}$	-17.57	-15.84	-10.02	-21.58	-15.24	-11.79	-21.09	-18.54	-6.49
K_{RR}	7.10	3.33	2.71	4.19	4.70	4.071	2.55	3.25	1.61
(d) Angle at V									
K_θ	29.61	41.53	25.10	33.87	43.30	35.57	47.19	33.71	30.19
θ_e	125.05	119.79	118.23	113.14	112.20	99.55	112.26	107.93	108.84
$K_{r\theta}$	-26.28	-14.74	-10.67	-19.22	-17.76	-10.35	-20.03	-13.42	-17.17
K_{rr}	7.25	16.67	8.84	9.47	6.27	1.96	10.48	4.11	2.76
(e) Cross Term									
$K_{\theta\theta 2}$	-15.08	-17.44	-17.45	-18.99	-18.37	-18.77	-14.95	-14.89	-16.37

^a D_R is based on atomization data at 298.15K from reference 21.

Table 7. Van der Waals parameters from the universal force field (reference 5).

	Al	Ga	In	P	As	Sb
Rv (Å)	4.499	4.383	4.465	4.147	4.230	4.420
Dv Pkcal/mol)	0.505	0.415	0.599	0.305	0.309	0.449

Table 8. Experimental lattice constants, phonon frequencies, elastic constants, used in determining the MSXX FF (from reference 8, see discussion in Section 4.1). Comparison with theoretical predictions.

Quantity	ZnS	ZnSe	ZnTe	CdTe	HgTe
Lattice Parameters (Å)					
Experiment	5.410	5.6687	6.1037	6.481	6.461
MSXX	5.410	5.6687	6.1037	6.481	6.461
Elastic Constants (GPa)					
C_{11} exper	104.62	86.00	71.30	53.30	59.71
MSXX	107.37	90.49	72.17	49.33	53.71
C_{12} exper	65.33	51.10	40.70	36.50	41.54
MSXX	62.18	47.91	40.83	31.85	32.89
C_{44} exper	46.50	40.20	31.20	20.44	22.59
MSXX	43.85	38.14	31.08	18.42	18.25
rms C_{ij} deviation	2.61	3.38	0.51	3.37	2.70
Phonons (cm⁻¹)					
TA(X) exper	89.67	70.00	54.0	35.0	15.86
MSXX	89.68	70.40	54.10	34.90	15.86
LA(X) exper	211.33	194.00	143.0	97.0	85.00
MSXX	210.60	189.20	141.10	125.00	84.80
TO(X) exper	315.67	219.00	173.7	148.00	133.93
MSXX	315.60	219.60	173.7	147.80	133.80
LO(X) exper	330.00	213.00	183.7		85.00
MSXX	329.50	208.20	182.40	125.30	84.80
TO(Γ) exper	276.67	213.00	176.7	140.50	118.00
MSXX	277.20	214.40	177.50	138.80	118.60
LO(Γ) exper	348.00	253.00	206.7	167.0	138.00
MSXX	348.60	255.50	207.50	168.30	138.50
rms phonon deviation	0.40	2.69	0.94	0.80	0.72

Table 9. MSXX force field parameters for the II-VI zinc blende materials.

Quantity	ZnS	ZnSe	ZnTe	CdTe	HgTe
(a) Charge (e)					
Cation	0.88	0.80	0.76	0.86	0.74
(b) Bond					
k_R [kcal/(molÅ ²)]	100.51	71.72	68.51	62.32	55.44
R_e (Å)	2.519	2.686	2.809	2.971	3.005
D_R^a (kcal/mol)	36.78	31.13	26.59	23.97	21.35
(c) Angle, Group II Atom at Apex					
k_θ [kcal/(mol rad ²)]	34.33	29.85	17.02	17.98	20.13
θ (degree)	119.23	113.60	116.35	128.08	116.03
$k_{r\theta}$ [kcal/(molÅ rad)]	-24.01	-16.51	-17.92	-14.22	-2 0.51
k_{rr} [kcal/(molÅ ²)]	13.01	7.61	9.11	6.11	8.43
$k_{r\theta}$ [kcal/(molÅ rad)]	-23.21	-15.40	-9.63	-11.34	-7 .39
k_{rr} [kcal/(molÅ ²)]	4.63	8.07	6.46	3.70	0.45
(e) Two Center Angle-Angle Cross Term					
$G_{\theta\theta}$ [kcal/(mol rad ²)]	-10.20	-10.47	-11.40	-9.12	-1 1.11

^a D_R is based on atomization energies at 298.15K from reference 30.

Table 10. van der Waals parameters (from reference 23). See equations (4) and (5).

Atom	Zn	Cd	Hg	S	Se	Te
R^{vdw} (Å)	2.763	2.848	2.705	4.035	4.205	4.470
D^{vdw} (kcal/mol)	0.124	0.228	0.385	0.274	0.291	0.398

Table 11. Additional force field terms for the ZnSe/ZnTe superlattice.

(a) Angle Se-Zn-Te

$$k_\theta = 22.54 \text{ kcal/mol}$$

$$\theta_e = 114.97 \text{ degree}$$

$$k_{r\theta} = -17.92 \text{ kcal/(mol\AA)} \text{ for } R = Se - Zn$$

$$k_{r\theta} = -16.51 \text{ kcal/(mol\AA)} \text{ for } R = Zn - Te$$

$$k_{rr} = 8.33 \text{ kcal/(mol\AA}^2)$$

(b) Two-Center Angle-Angle

$$G_{\theta\theta, Zn-Se-Zn-Te} = G_{\theta\theta, Zn-Te-Zn-Se} = -10.93 \text{ kcal/mol}$$

Table 12. Comparison of the ZnS/ZnSe,²² superlattice predictions and the available experimental data.

Table 13. Comparison of the ZnS/ZnTe,^{22,23} superlattice predictions and the available experimental data.

Table 14. Comparison of the CdTe/ZnTe²⁷ superlattice predictions and the available experimental data.

$(CdTe)_3(ZnTe)_5$				
LO modes in Sublattice	CdTe	CdTe	ZnTe	ZnTe
experiment	172.88	184	203.87	205.5
stressed	175.7	185.3	205.5	207.1
(relaxed)	173.7	182.5	202.3	204.5
Sample: $d_{CdTe} = 21\text{\AA}$, $d_{ZnTe} = 27\text{\AA}$, $N = 21$, buffer $0.9\mu\text{ Cd}_{0.1}Zn_{0.9}Te$,				
substrate GaAs <100>				
$(CdTe)_7(ZnTe)_{11}$				
LO modes in CdTe Layer	LO_2	LO_4	LO_6	LO_8
experiment	180	175.84	171	165.86
(stressed)	179.54	176.92	172.74	167.16
relaxed	177.41	174.78	170.60	165.03
Sample $d_{CdTe} = 51\text{\AA}$, $d_{ZnTe} = 61\text{\AA}$, $N = 15$, buffer $0.9\mu\text{ Cd}_{0.1}Zn_{0.9}Te$,				
substrate GaAs <100>				

Table 15. Interface modes for several II/VI superlattices.

superlattice	IF mode cm^{-1}	IF mode cm^{-1}
$(ZnS)_2(ZnSe)_2$	223.0	
$(ZnS)_4(ZnSe)_4$	225.9	
$(ZnS)_{10}(ZnSe)_2$	226.1	
$(ZnS)_{10}(ZnSe)_{10}$	225.9	
$(ZnS)_{12}(ZnSe)_{12}$	225.9	
$(ZnSe)_2(ZnTe)_2$	191.6	195.1
$(ZnSe)_4(ZnTe)_4$	192.6	193.6
$(ZnSe)_{10}(ZnTe)_2$	194.4	197.7
$(ZnSe)_{10}(ZnTe)_{10}$	193.8	195.3
$(ZnSe)_{18}(ZnTe)_{20}$	192.2	193.5
$(CdTe)_2(ZnTe)_2$	170.2	
$(CdTe)_4(ZnTe)_4$	169.1	
$(CdTe)_3(ZnTe)_5$	170.3	
$(CdTe)_7(ZnTe)_{11}$	170.1	
$(CdTe)_{10}(ZnTe)_2$	170.7	
$(HgTe)_2(CdTe)_2$	137.6	151.6
$(HgTe)_4(CdTe)_4$	135.1	152.6
$(HgTe)_8(CdTe)_8$	135.3	152.3
$(HgTe)_{10}(CdTe)_2$	138.8	151.8

All interface modes are of TO character.

Table 16. Elastic constants of the bulk materials, force field fitted results and the predicted results for superlattice.

Name	C_{11}	MSXX	C_{12}	MSXX	C_{44}	MSXX
ZnS	104.50	107.37	65.30	62.18	46.00	43.85
ZnSe	85.90	90.49	50.60	47.91	40.60	38.14
ZnTe	71.30	72.17	40.70	40.83	31.20	31.08
CdTe	53.30	49.33	36.50	31.85	20.44	18.42
HgTe	50.80	53.71	35.80	32.89	20.50	18.25
Name	C_{11}	C_{12}	C_{33}	C_{13}	C_{44}	C_{66}
$(\text{ZnS})_1(\text{ZnSe})_1$	117.13	34.44	98.82	54.11	41.01	22.01
$(\text{ZnS})_2(\text{ZnSe})_2$	118.39	35.22	98.43	54.84	40.46	22.05
$(\text{ZnSe})_4(\text{ZnTe})_4$	118.90	35.58	97.95	55.05	40.01	22.12
$(\text{ZnS})_{10}(\text{ZnSe})_2$	125.97	41.01	104.99	61.20	41.51	22.24
$(\text{ZnSe})_1(\text{ZnTe})_1$	95.49	28.07	81.86	44.62	33.82	17.75
$(\text{ZnSe})_2(\text{ZnTe})_2$	95.66	28.51	82.15	44.70	33.76	18.04
$(\text{ZnSe})_4(\text{ZnTe})_4$	95.67	28.57	81.88	44.66	33.90	18.23
$(\text{ZnSe})_{10}(\text{ZnTe})_2$	103.00	29.65	87.74	46.47	36.72	20.25
$(\text{CdTe})_1(\text{ZnTe})_1$	70.43	24.54	62.19	36.66	23.59	11.22
$(\text{CdTe})_2(\text{ZnTe})_2$	70.78	24.65	62.58	36.88	23.31	11.57
$(\text{CdTe})_4(\text{ZnTe})_4$	70.87	24.69	62.81	36.96	23.11	11.71
$(\text{CdTe})_{10}(\text{ZnTe})_2$	62.37	23.12	54.28	33.64	19.94	9.62
$(\text{HgTe})_1(\text{CdTe})_1$	60.16	23.28	52.06	32.37	18.16	9.39
$(\text{HgTe})_2(\text{CdTe})_2$	60.30	23.50	51.78	32.39	18.21	9.49
$(\text{HgTe})_4(\text{CdTe})_4$	60.25	23.62	51.70	32.41	18.22	9.52
$(\text{HgTe})_{10}(\text{CdTe})_2$	61.21	24.65	53.16	32.81	18.21	10.11

Experimental lattice constant and elastic constant taken from reference.¹⁸

Table 17. Cell geometries of the superlattices.

Name	a	
ZnS	5.41	
ZnSe	5.6687	
ZnTe	6.1037	
CdTe	6.481	
HgTe	6.461	
Name	$a_{//}$	d_{SL}
(ZnS) ₁ (ZnSe) ₁	5.5324	5.5457
(ZnS) ₂ (ZnSe) ₂	5.5308	11.0631
(ZnSe) ₄ (ZnTe) ₄	5.5321	22.0902
(ZnS) ₁₀ (ZnSe) ₂	5.4321	32.5660
(ZnSe) ₁ (ZnTe) ₁	5.8748	5.9100
(ZnSe) ₂ (ZnTe) ₂	5.8687	11.8163
(ZnSe) ₄ (ZnTe) ₄	5.8673	23.6193
(ZnSe) ₁₀ (ZnTe) ₂	5.7389	34.5737
(CdTe) ₁ (ZnTe) ₁	6.2413	6.3539
(CdTe) ₂ (ZnTe) ₂	6.2421	12.6978
(CdTe) ₄ (ZnTe) ₄	6.2408	25.4010
(CdTe) ₁₀ 6(ZnTe) ₂	6.3880	38.7556
(HgTe) ₁ (CdTe) ₁	6.4531	6.4760
(HgTe) ₂ (CdTe) ₂	6.4615	12.9465
(HgTe) ₄ (CdTe) ₄	6.4641	25.8917
(HgTe) ₁₀ (CdTe) ₂	6.4591	38.7802

Experimental lattice constant and elastic constant taken from reference.¹⁸

Figure Captions

Figure 1. Phonon dispersion curve for diamond.

Figure 2. Phonon dispersion curve for silicon.

Figure 3. Phonon dispersion curve for germanium.

Figure 4. Phonon dispersion curve for AlP.

Figure 5. Phonon dispersion curve for AlAs.

Figure 6. Phonon dispersion curve for AlSb.

Figure 7. Phonon dispersion curve for GaP.

Figure 8. Phonon dispersion curve for GaAs.

Figure 9. Phonon dispersion curve for GaSb.

Figure 10. Phonon dispersion curve for InP.

Figure 11. Phonon dispersion curve for InAs.

Figure 12. Phonon dispersion curve for InSb.

Figure 13. Phonon dispersion curve for ZnS.

Figure 14. Phonon dispersion curve for ZnSe.

Figure 15. Phonon dispersion curve for ZnTe.

Figure 16. Phonon dispersion curve for CdTe.

Figure 17. Phonon dispersion curve for HgSe.

Figure 18. Phonon dispersion curve for HgTe.

Figures 19-22. Superlattice phonons of ZnS/ZnSe, ZnSe/ZnTe, CdTe/ZnTe, and HgTe/CdTe grown in the [111] direction.

Figures 23-38. Phonons of ZnS/ZnSe, ZnSe/ZnTe, CdTe/ZnTe, and HgTe/CdTe for superlattices with layer thicknesses of 1, 2, 4 and 10 grown in the [100] direction.

Figures 39. Comparison of folded phonons with phonons of component materials for ZnSe/ZnTe.

Figure 1. Phonon Dispersion Curve for Diamond

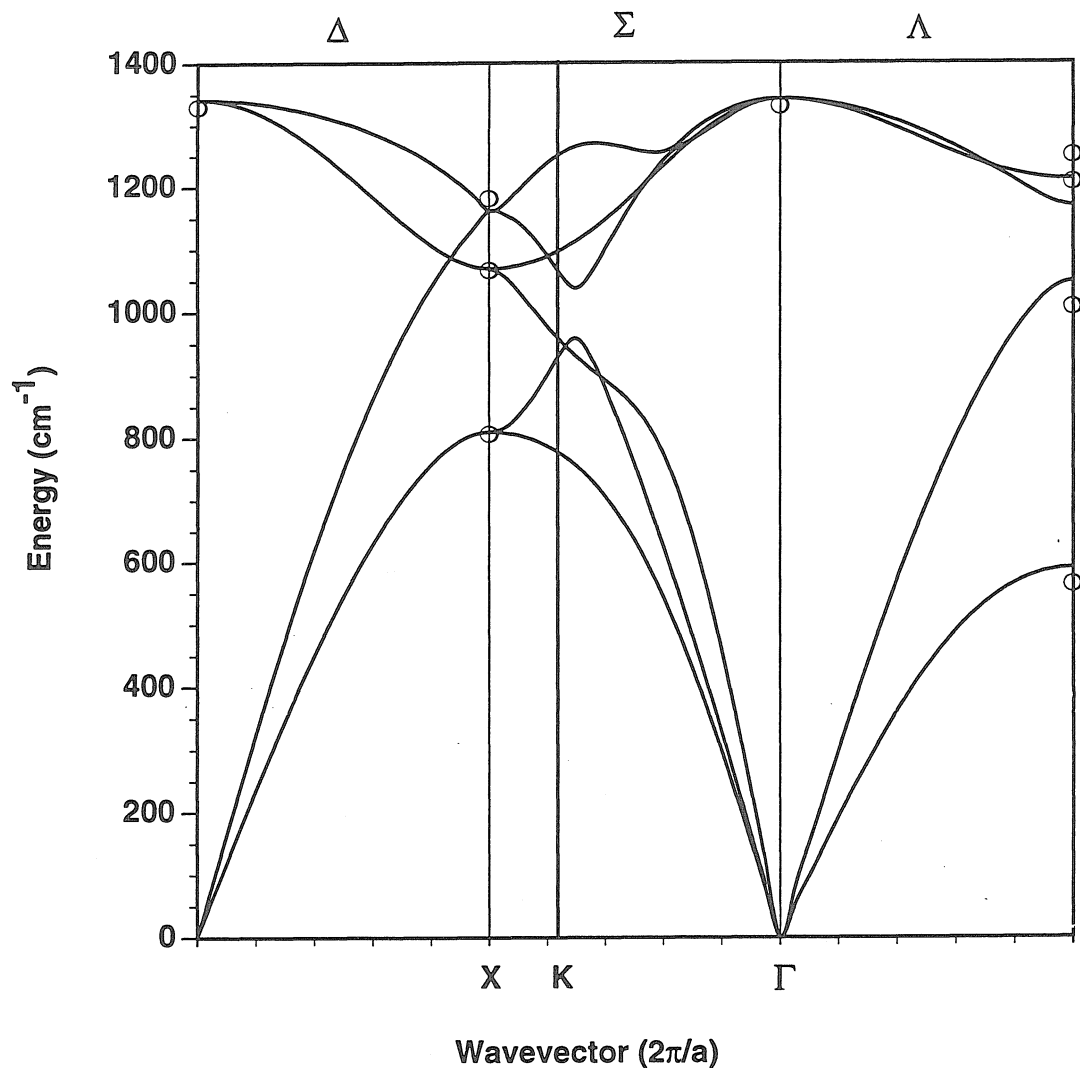


Figure 2 Phonon Dispersion Curve for Si

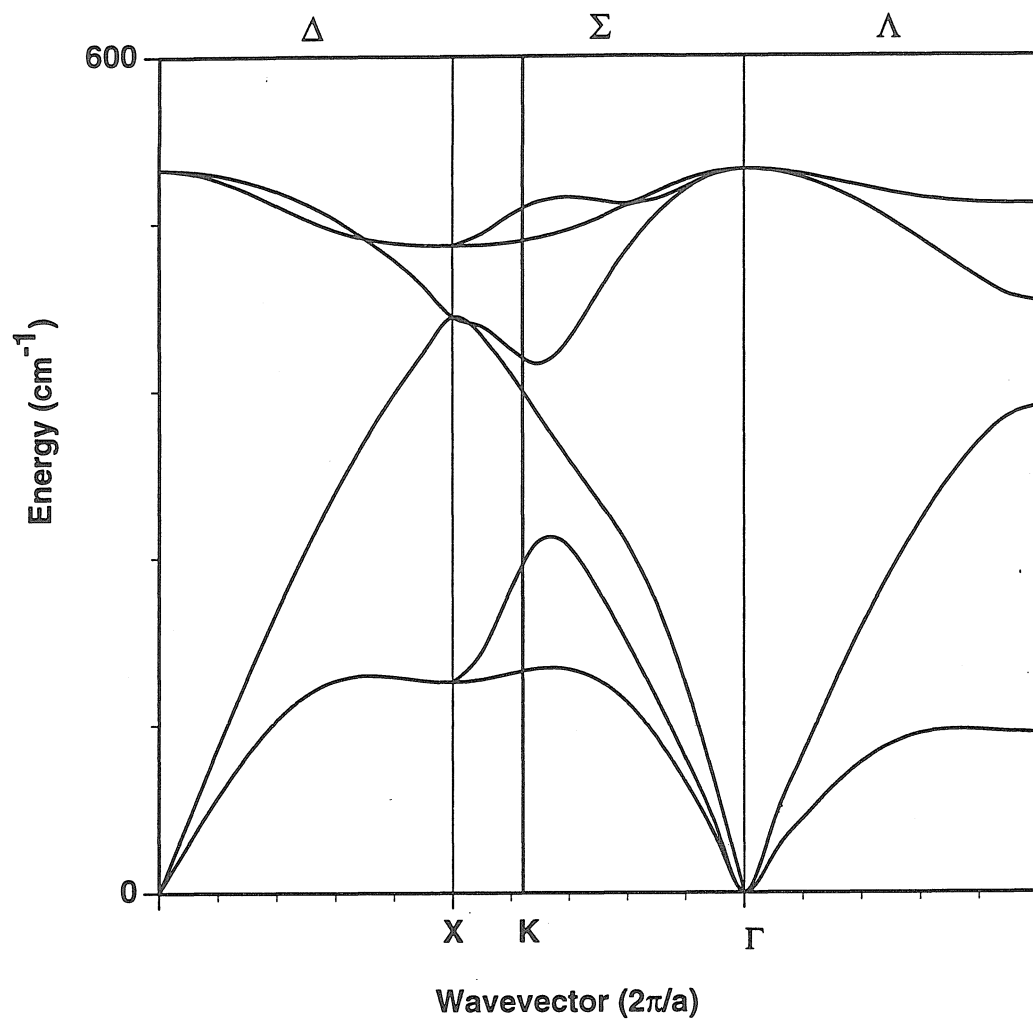


Figure 3. Phonon Dispersion Curve for Ge

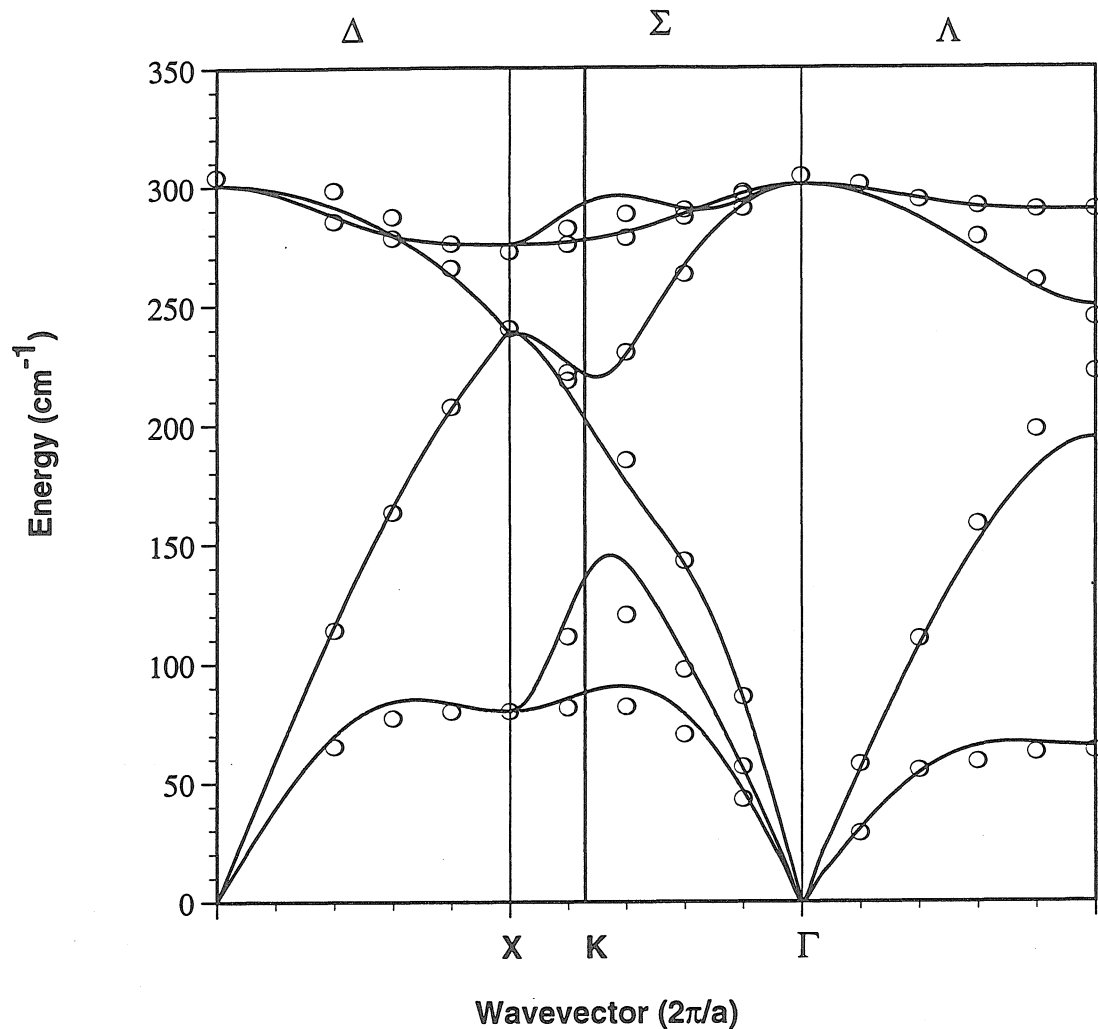


Figure 4. Phonon Dispersion Curves for AlP

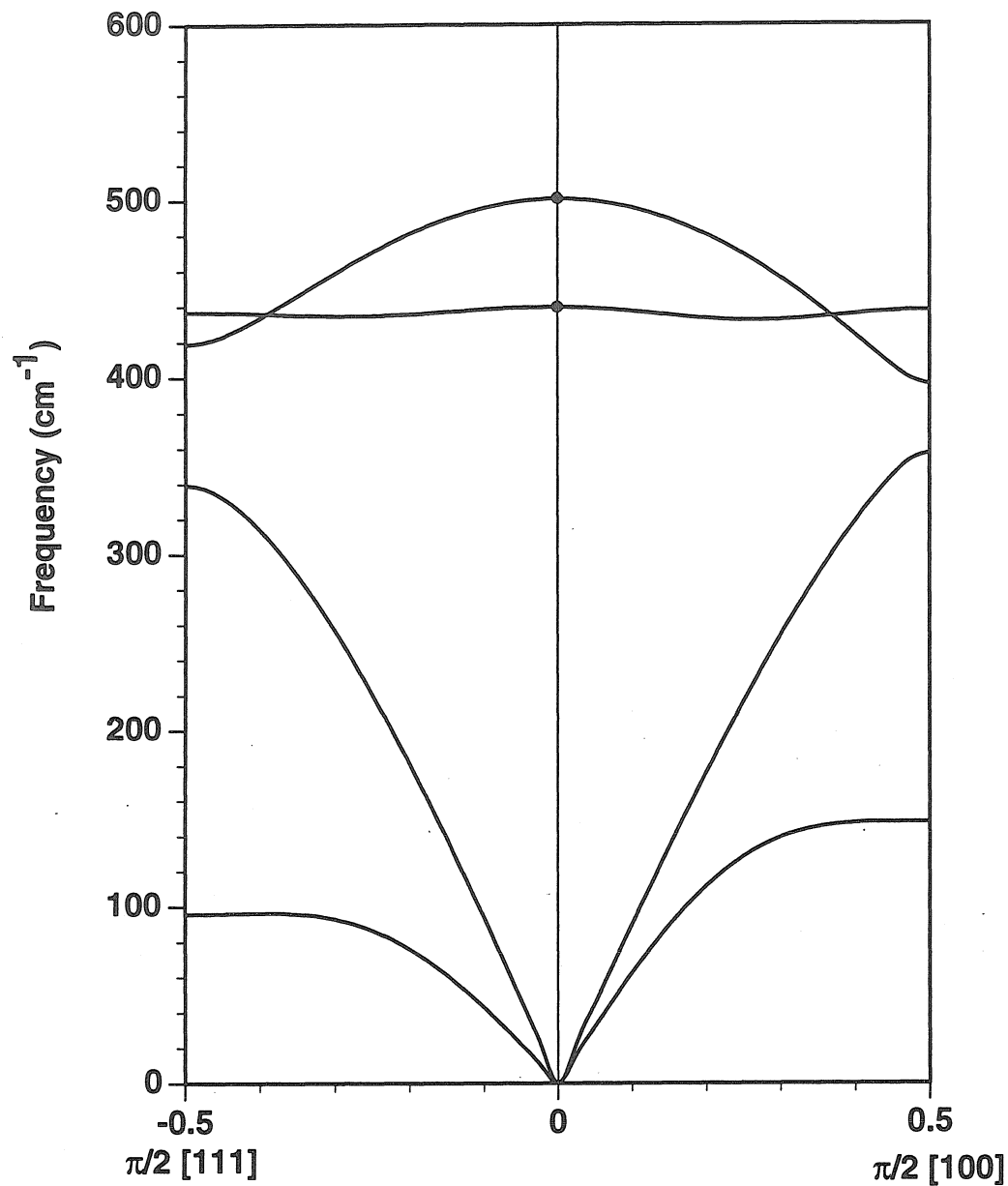


Figure 5. Phonon Dispersion Curves for AlAs

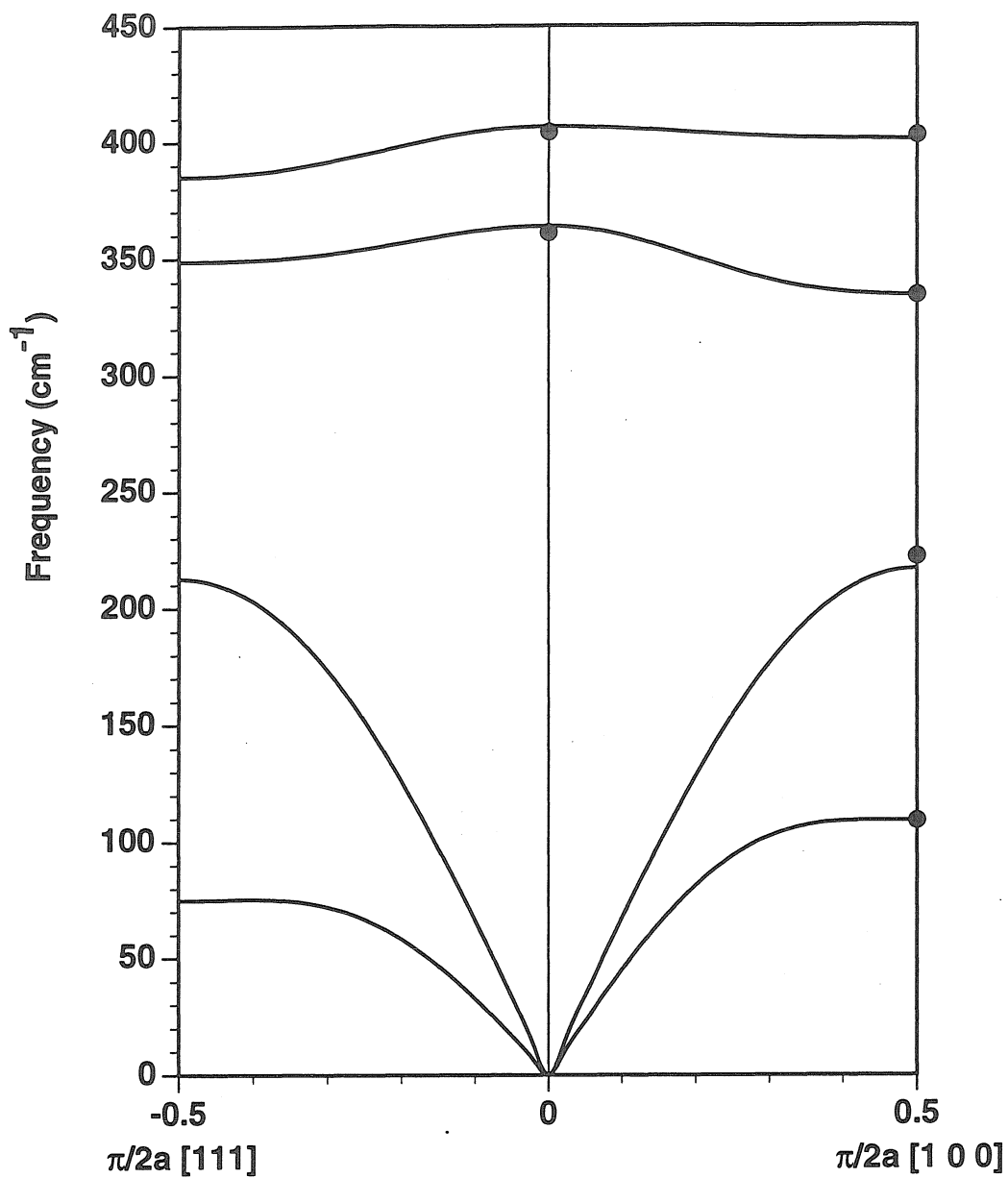


Figure 6. Phonon Dispersion Curves for AlSb

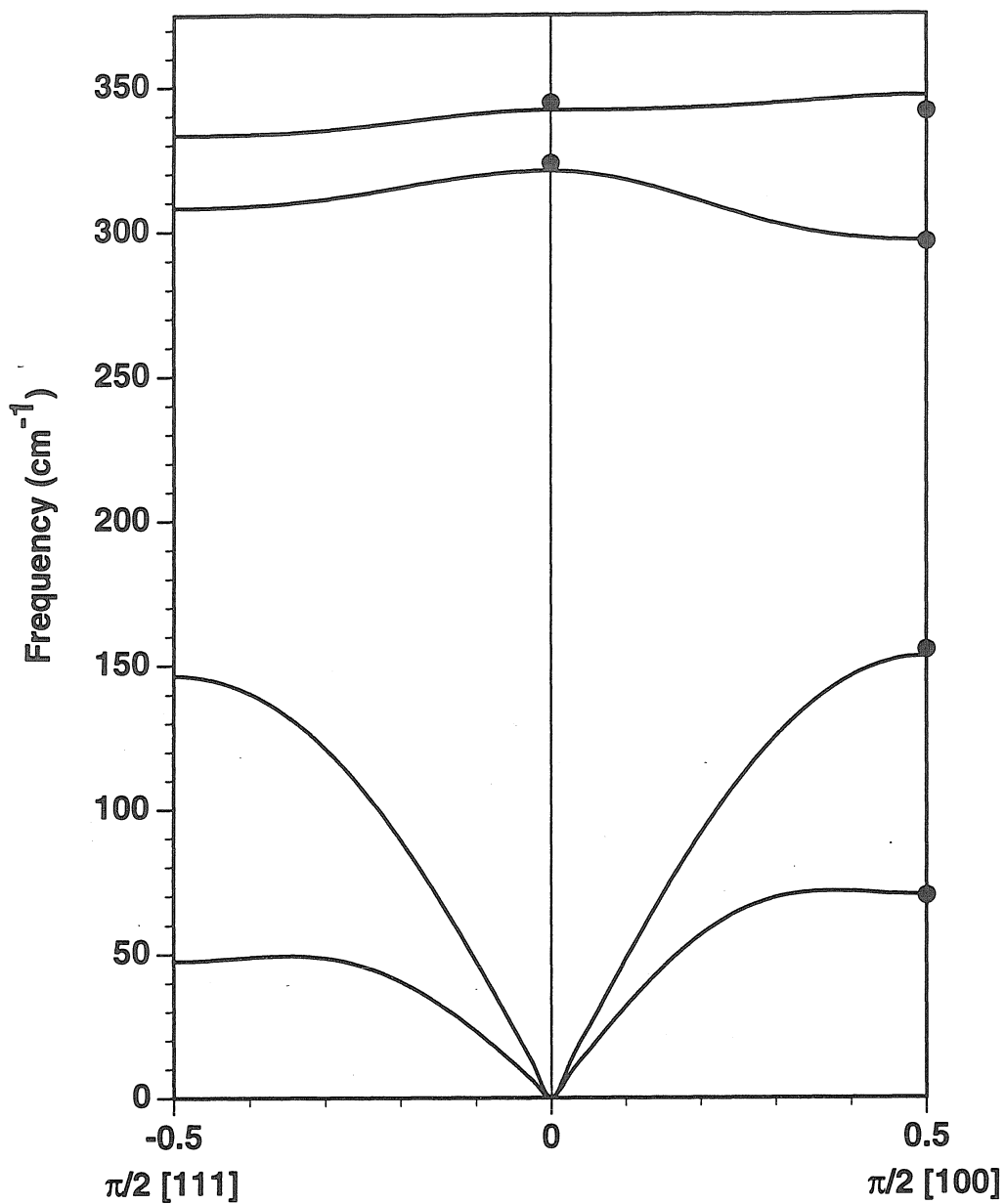


Figure 7. Phonon Dispersion Curves for GaP

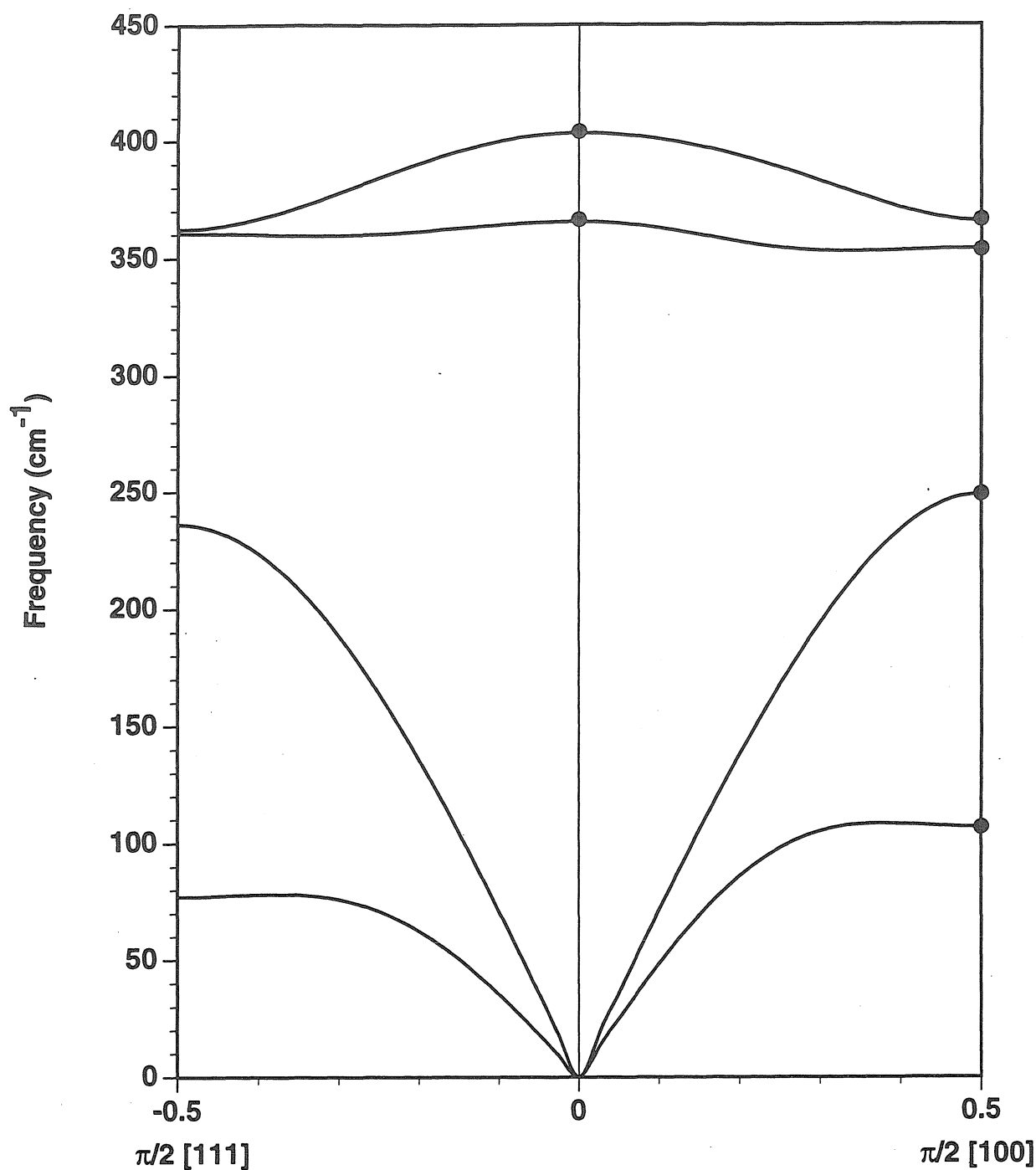


Figure 8. Phonon Dispersion Curves for GaAs

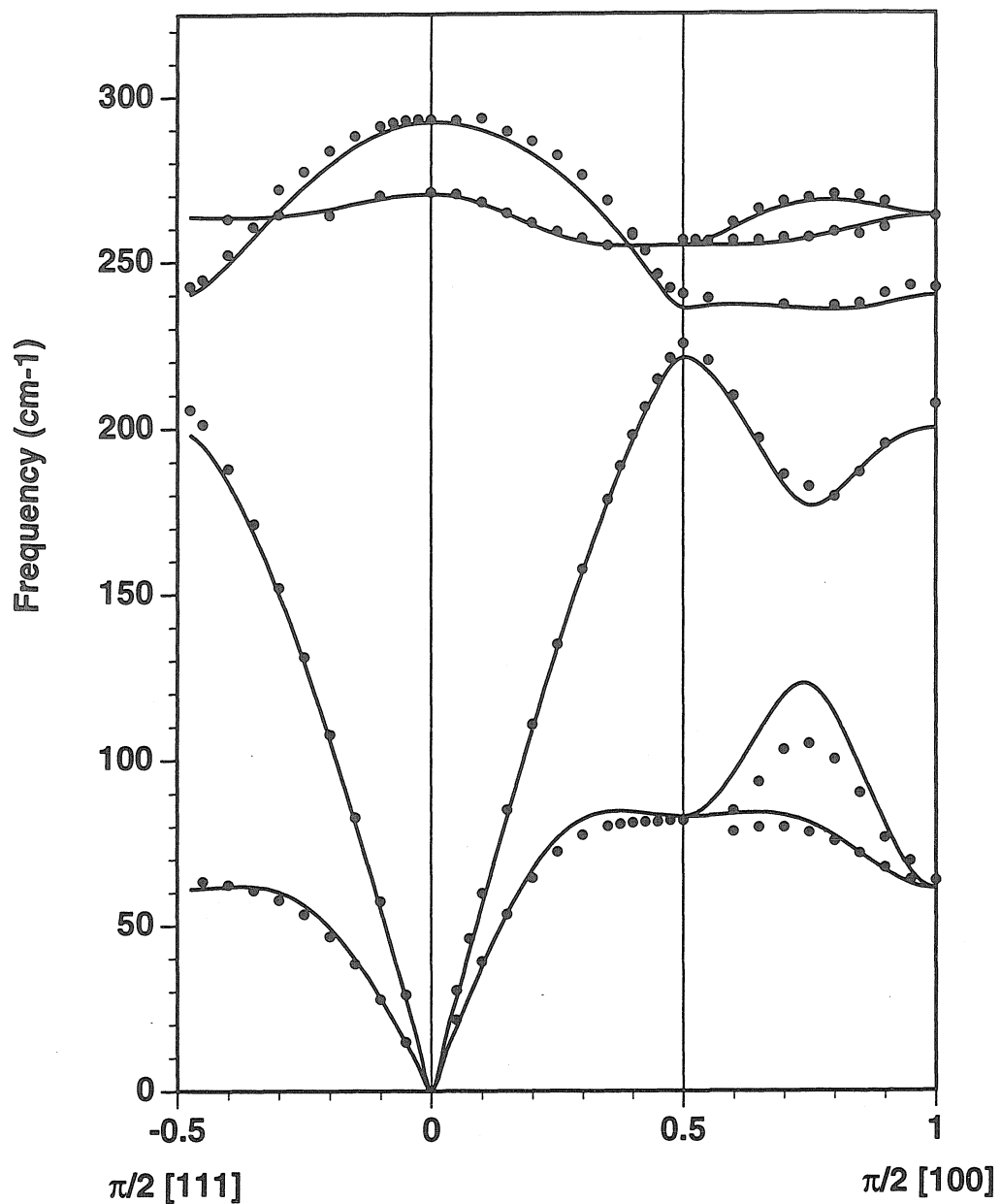


Figure 9. Phonon Dispersion Curves for GaSb

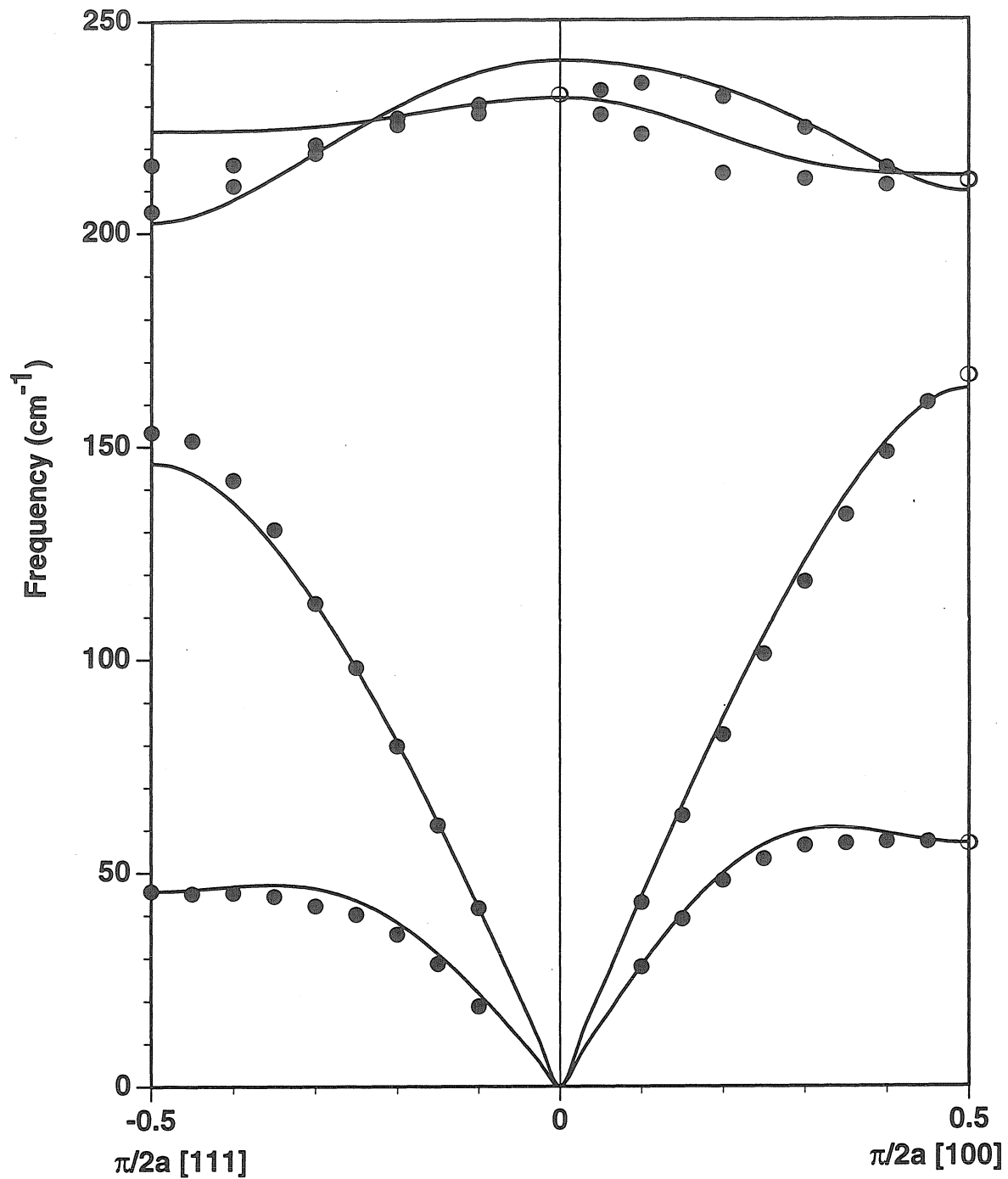


Figure 10. Phonon Dispersion Curves for InP

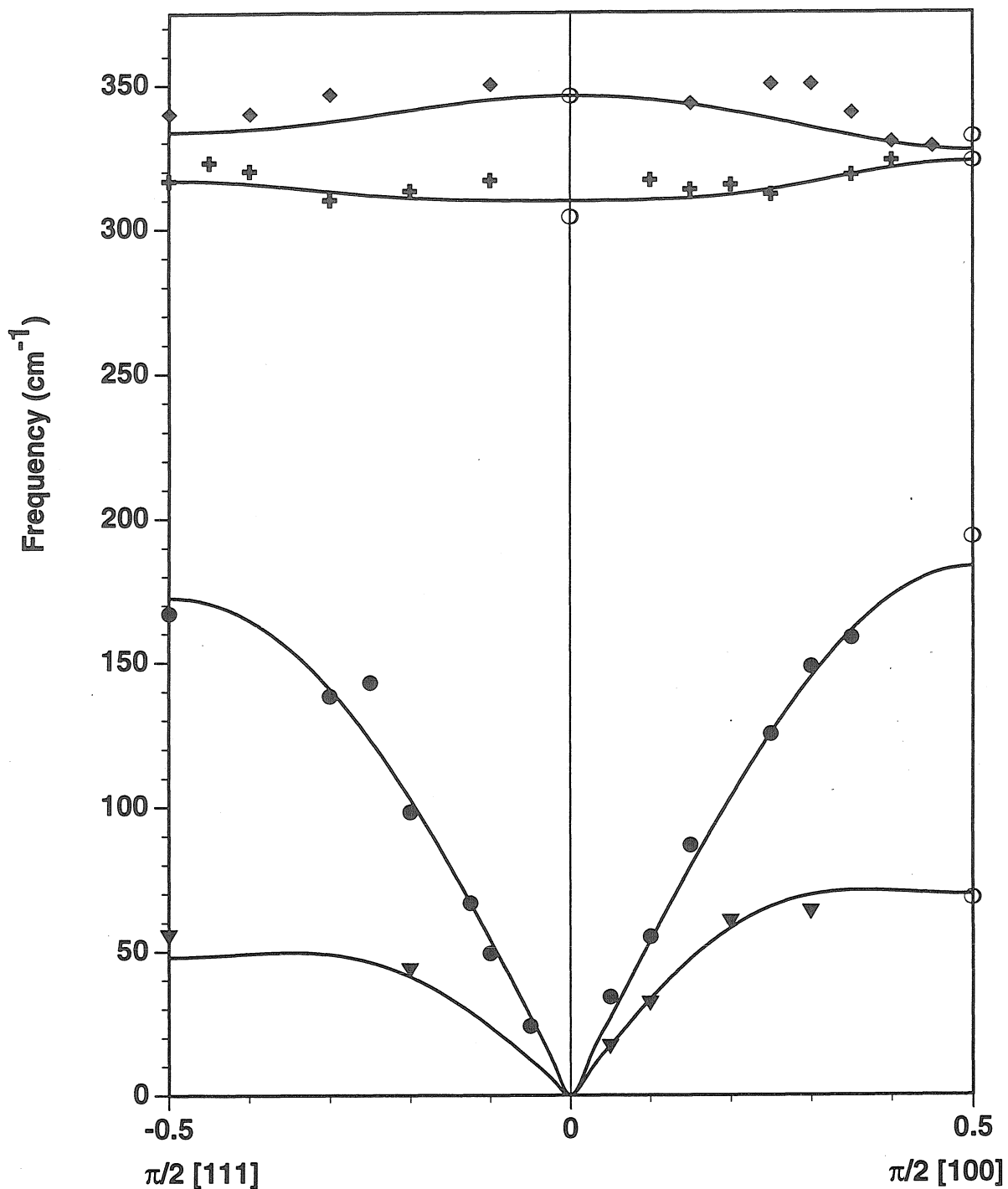


Figure 11. Phonon Dispersion Curves for InAs

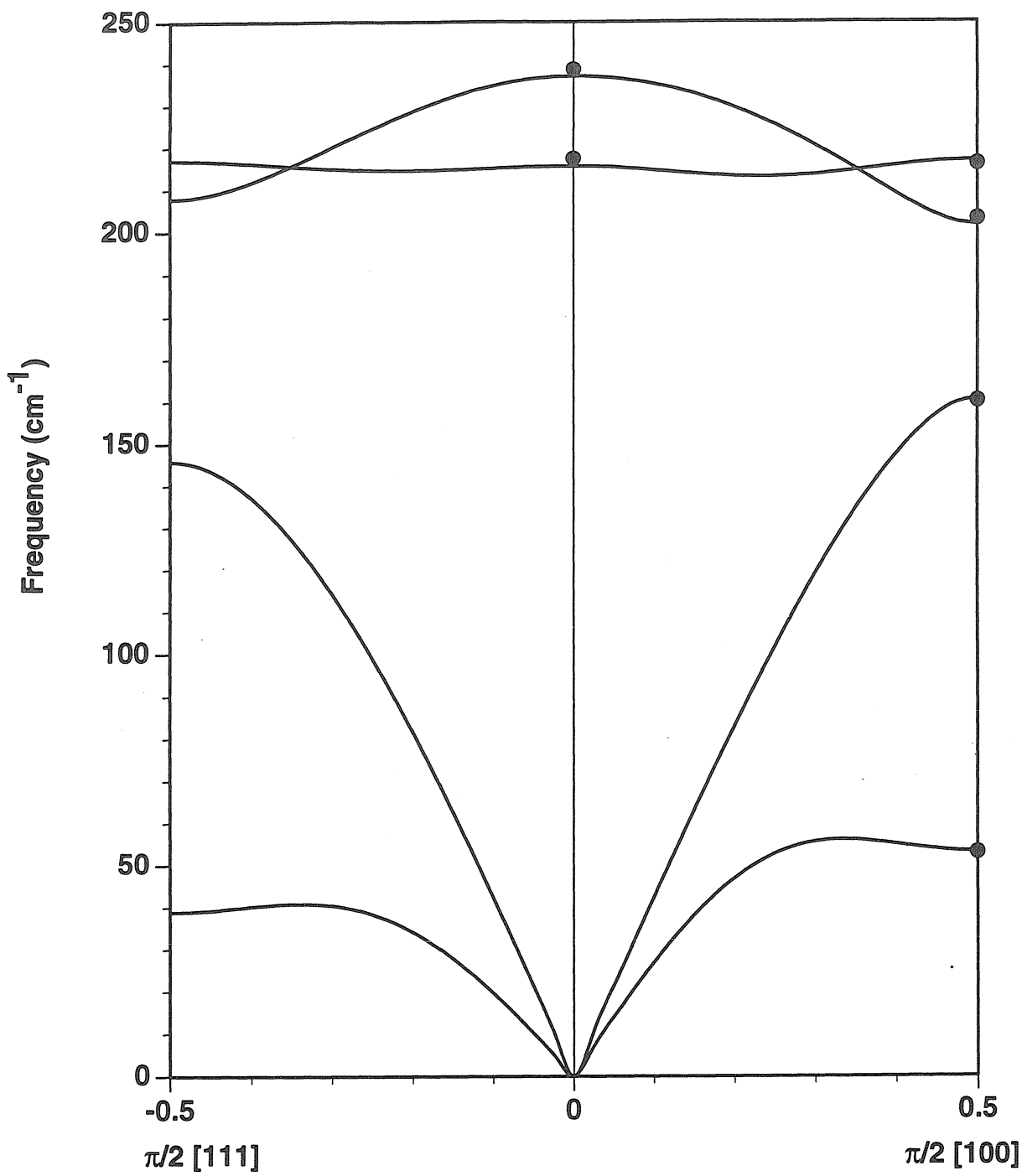


Figure 12. Phonon Dispersion Curves for InSb

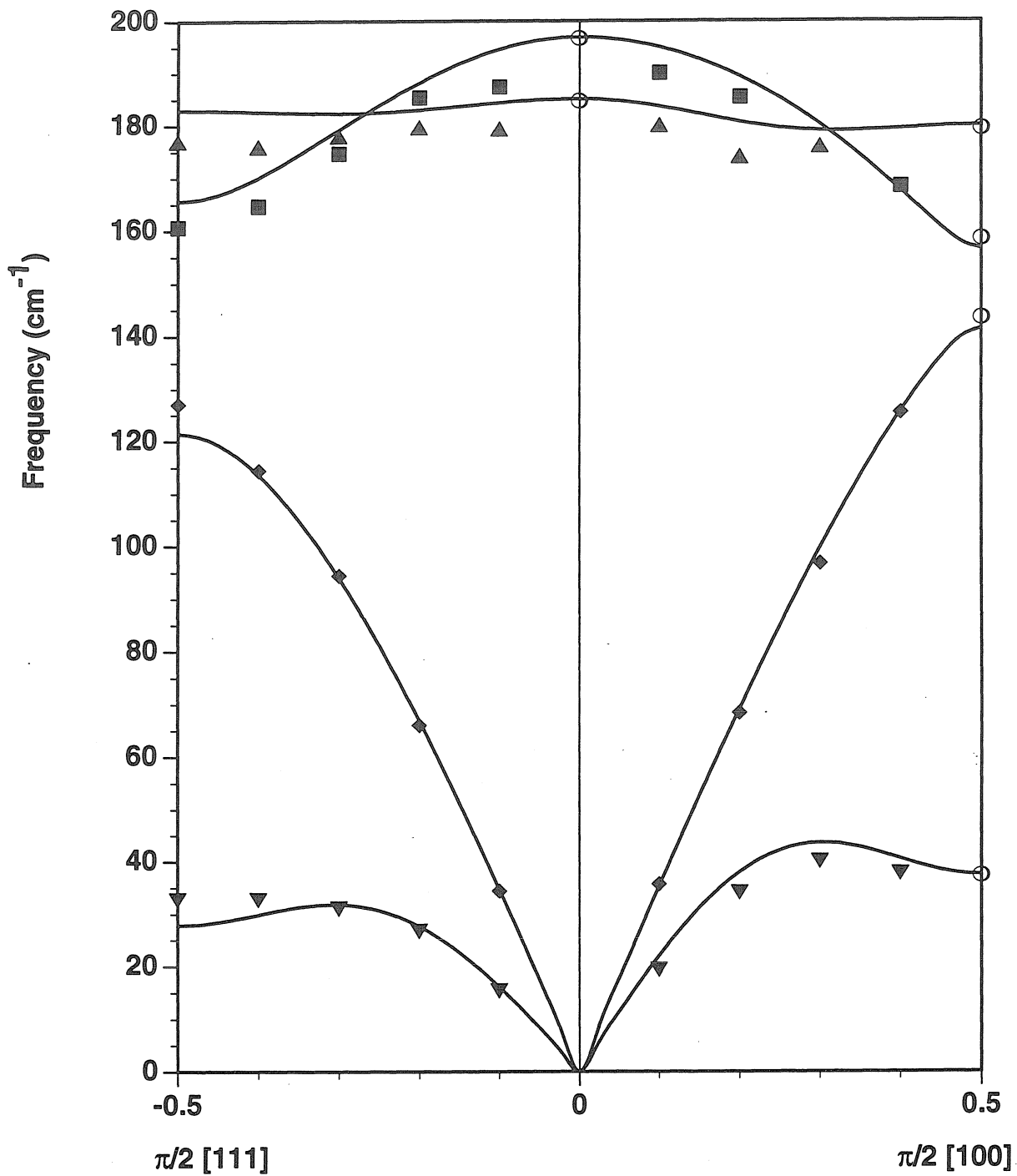


Figure 13. Phonon Dispersion Curve for ZnS

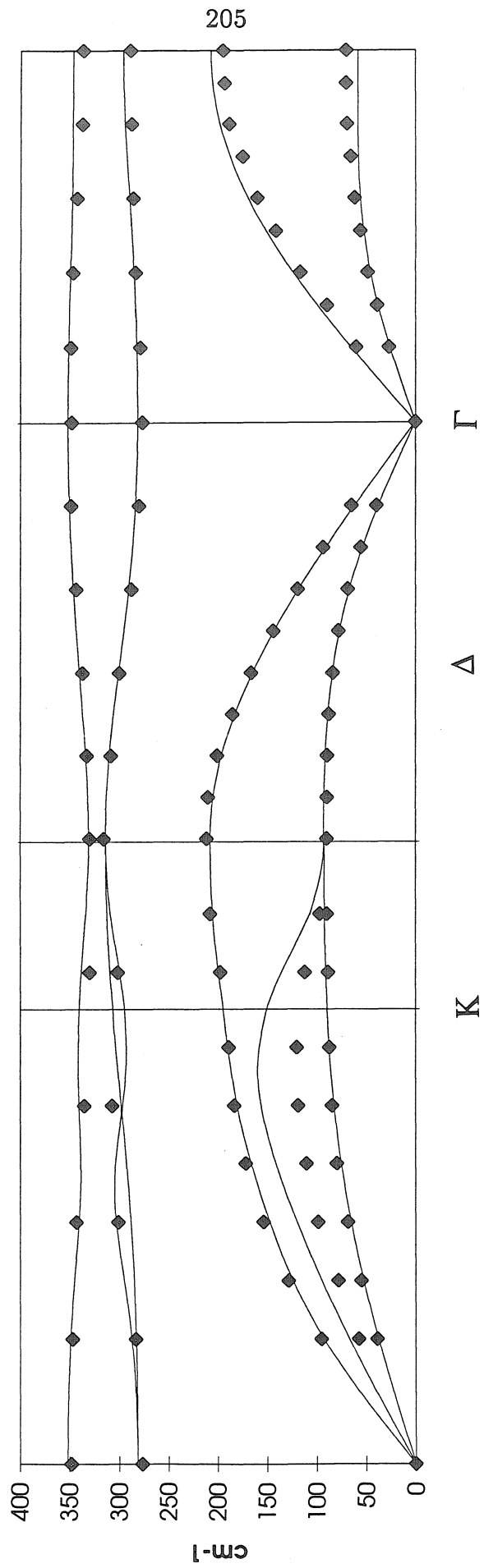


Figure 14. Phonon Dispersion Curve for ZnSe

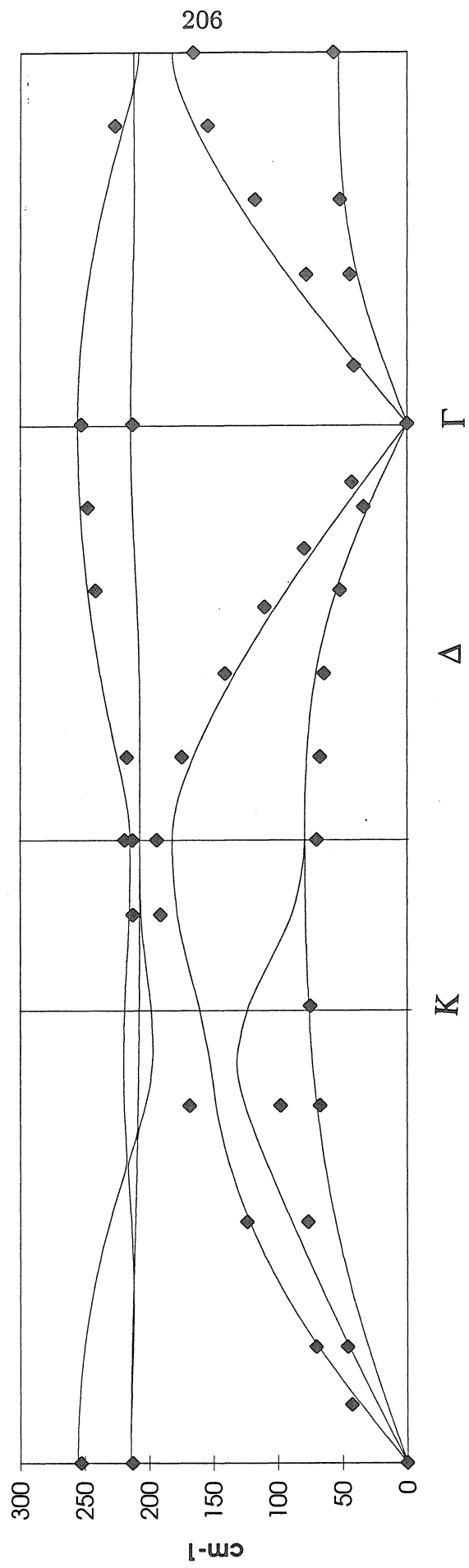


Figure 15. Phonon Dispersion Curve for ZnTe

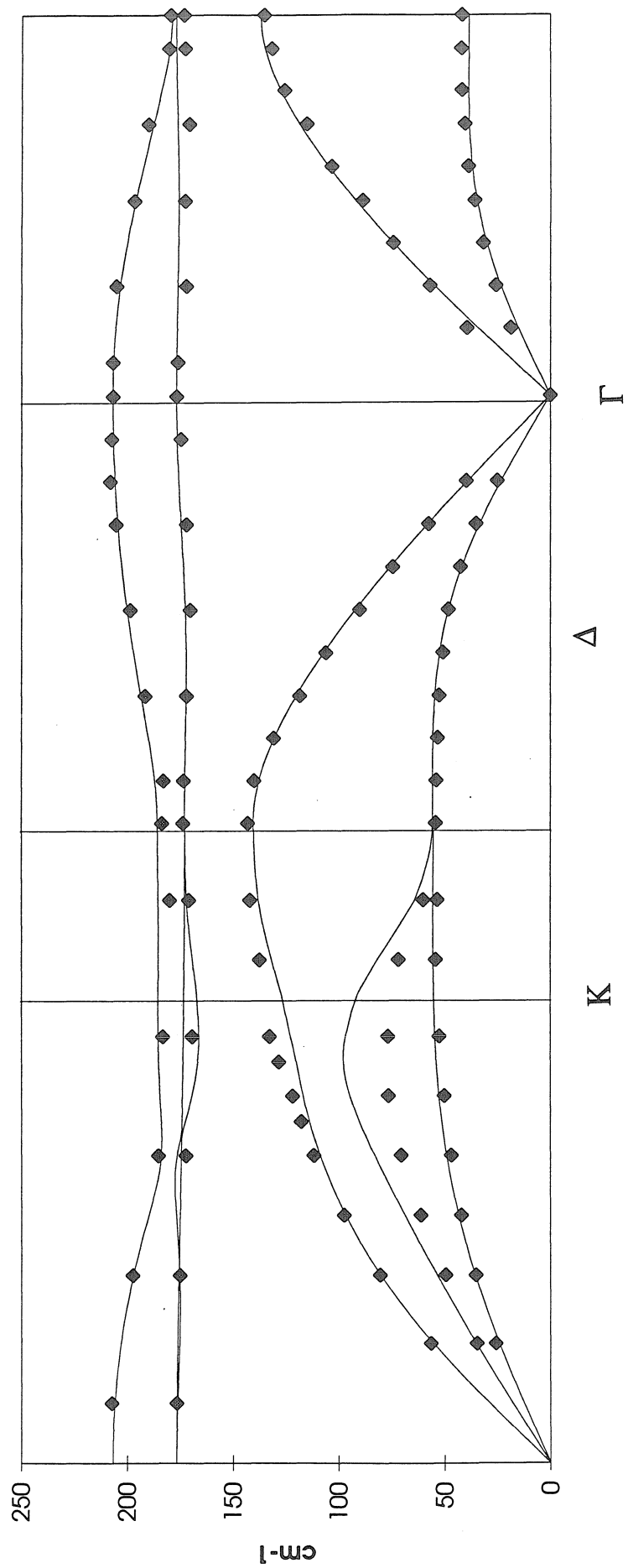


Figure 16. Phonon Dispersion Curve for CdTe

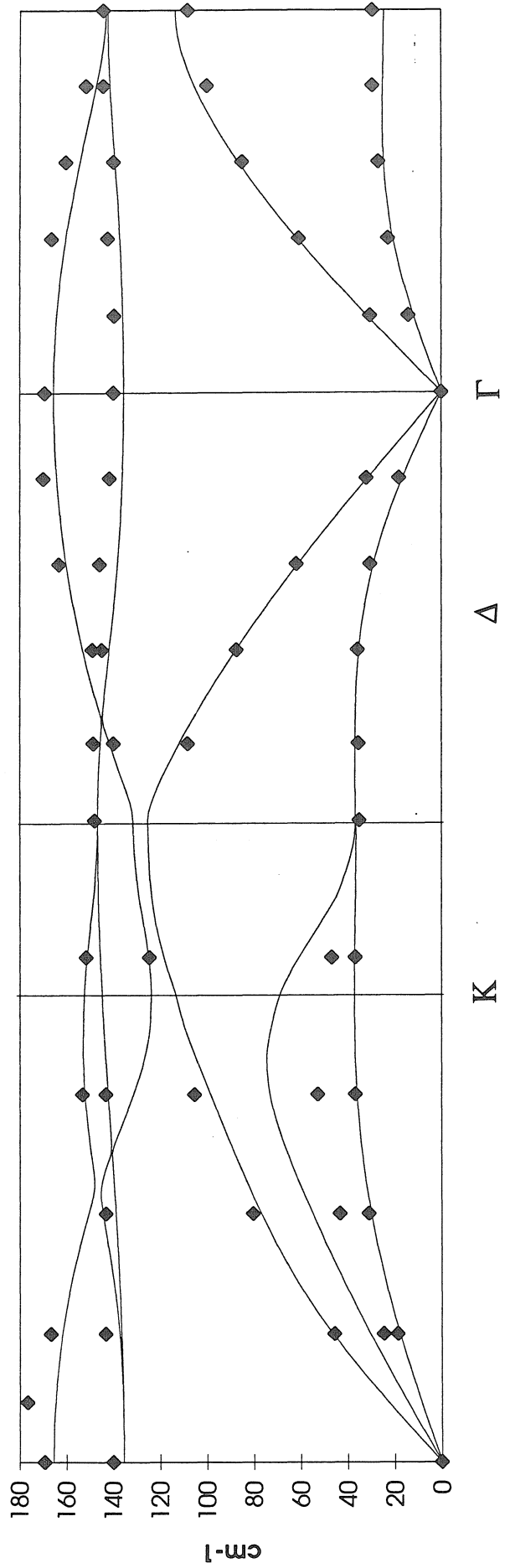


Figure 17 Phonon Dispersion Curve for HgSe

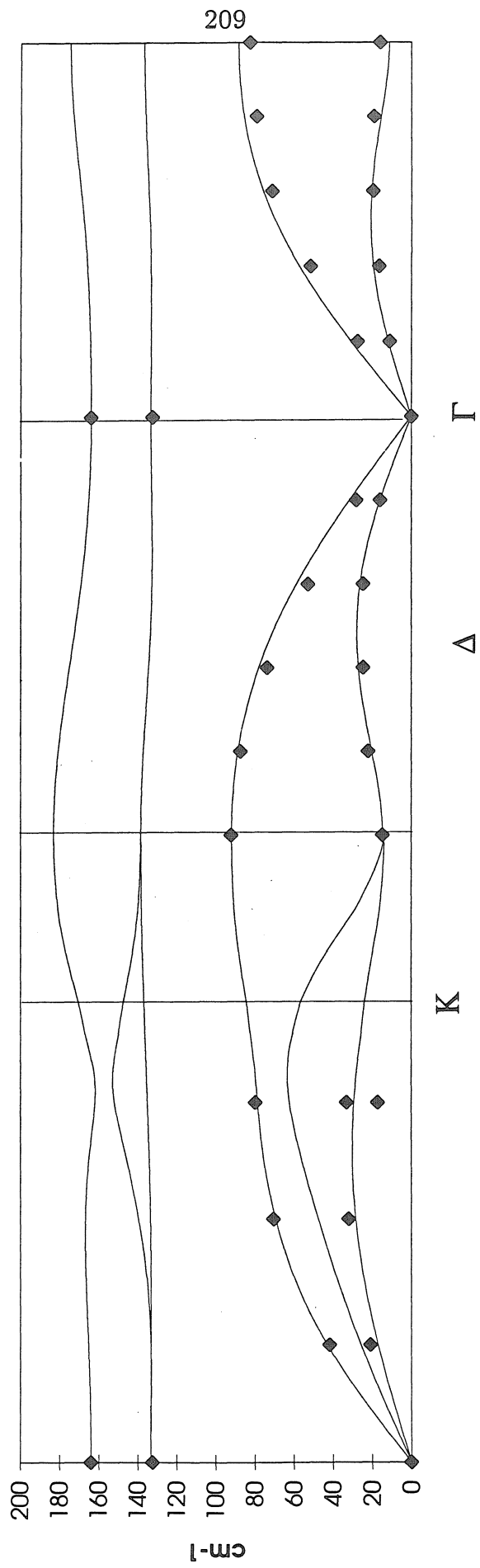


Figure 18 Phonon Dispersion Curve for HgTe

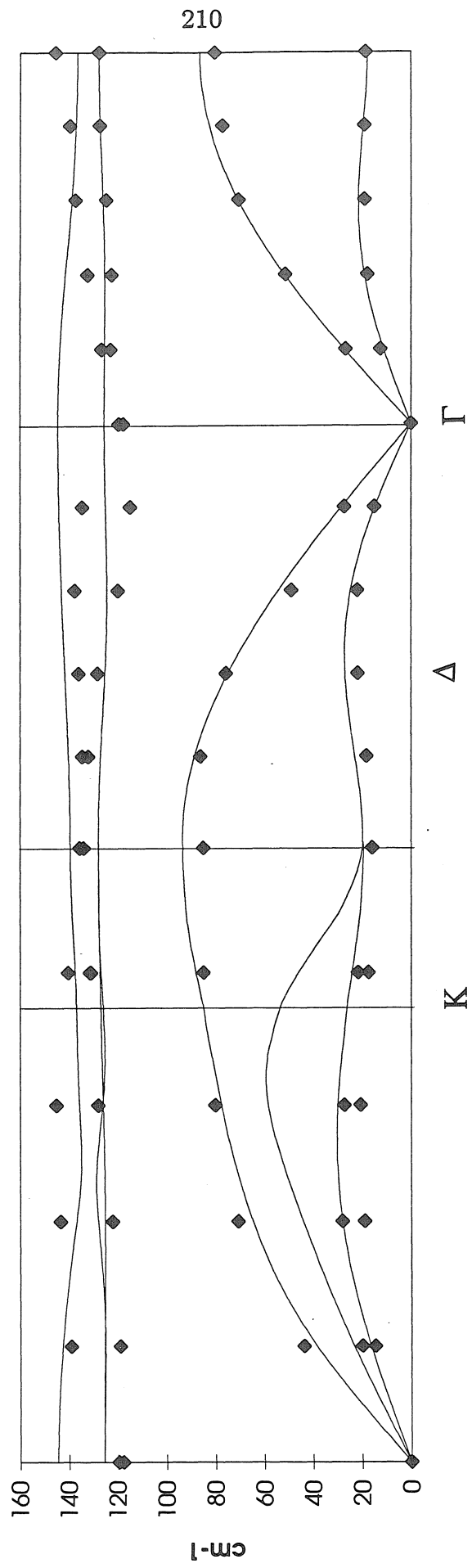


Figure 19

ZnS1/ZnSe1 superlattice (grown on $<111>$ surface) phonon

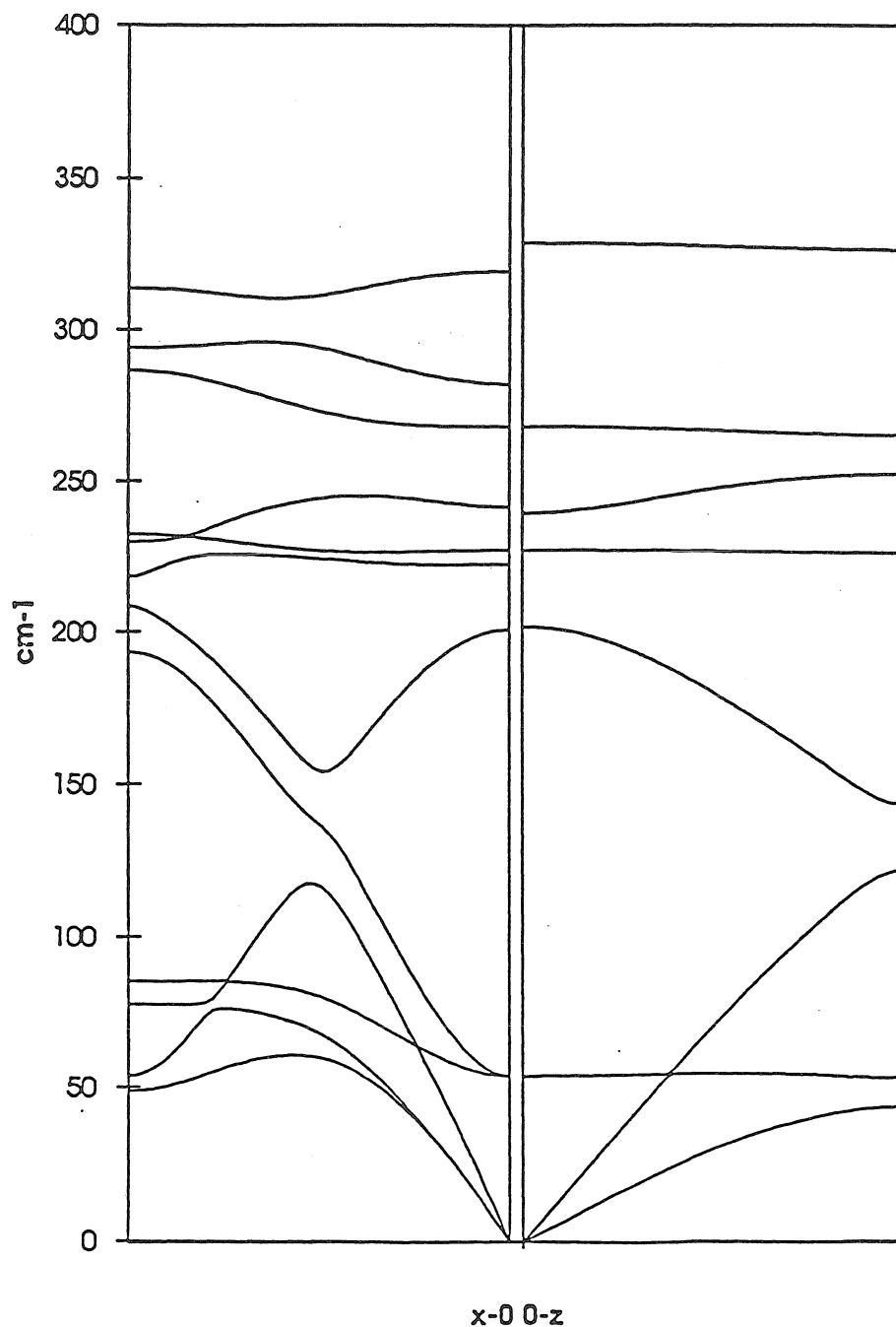


Figure 20

ZnSe1/ZnTe1 superlattice (grown on $<111>$ surface) phonon

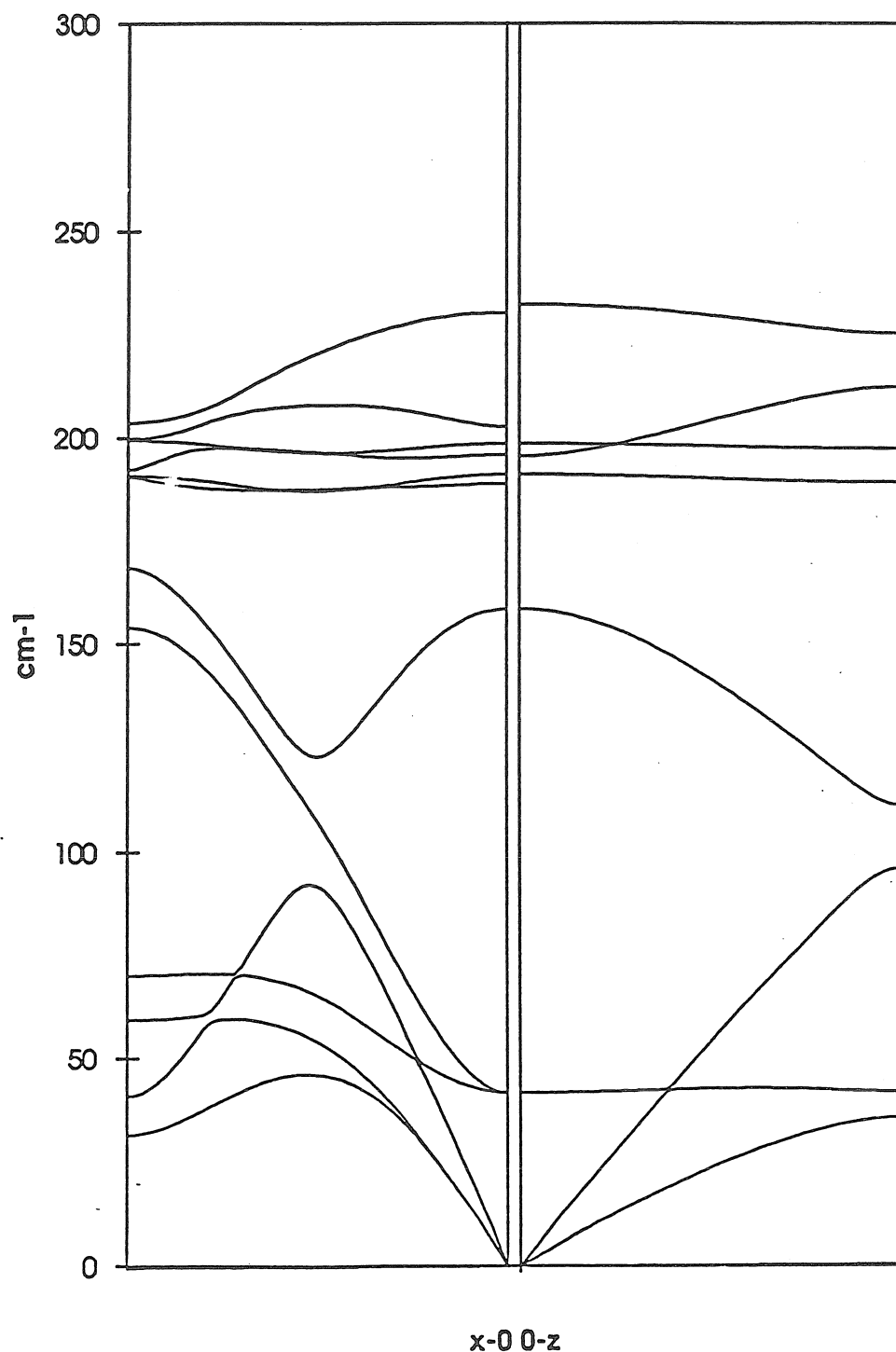


Figure 21

CaTe1/ZnTe1 superlattice (grown on $<111>$ surface) phonon

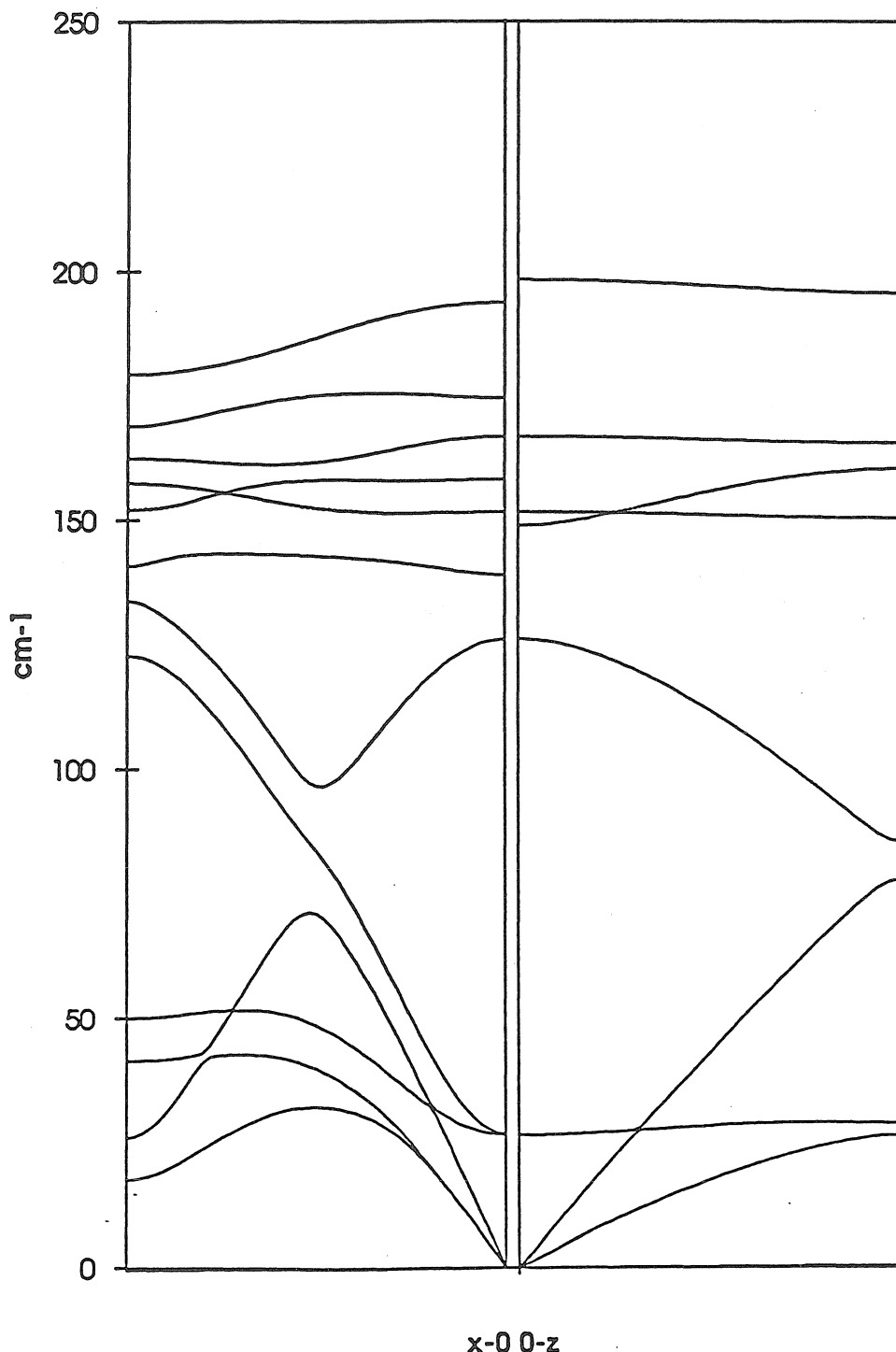


Figure 22

HgTe1/CdTe1 superlattice (grown on $<111>$ surface) phonon

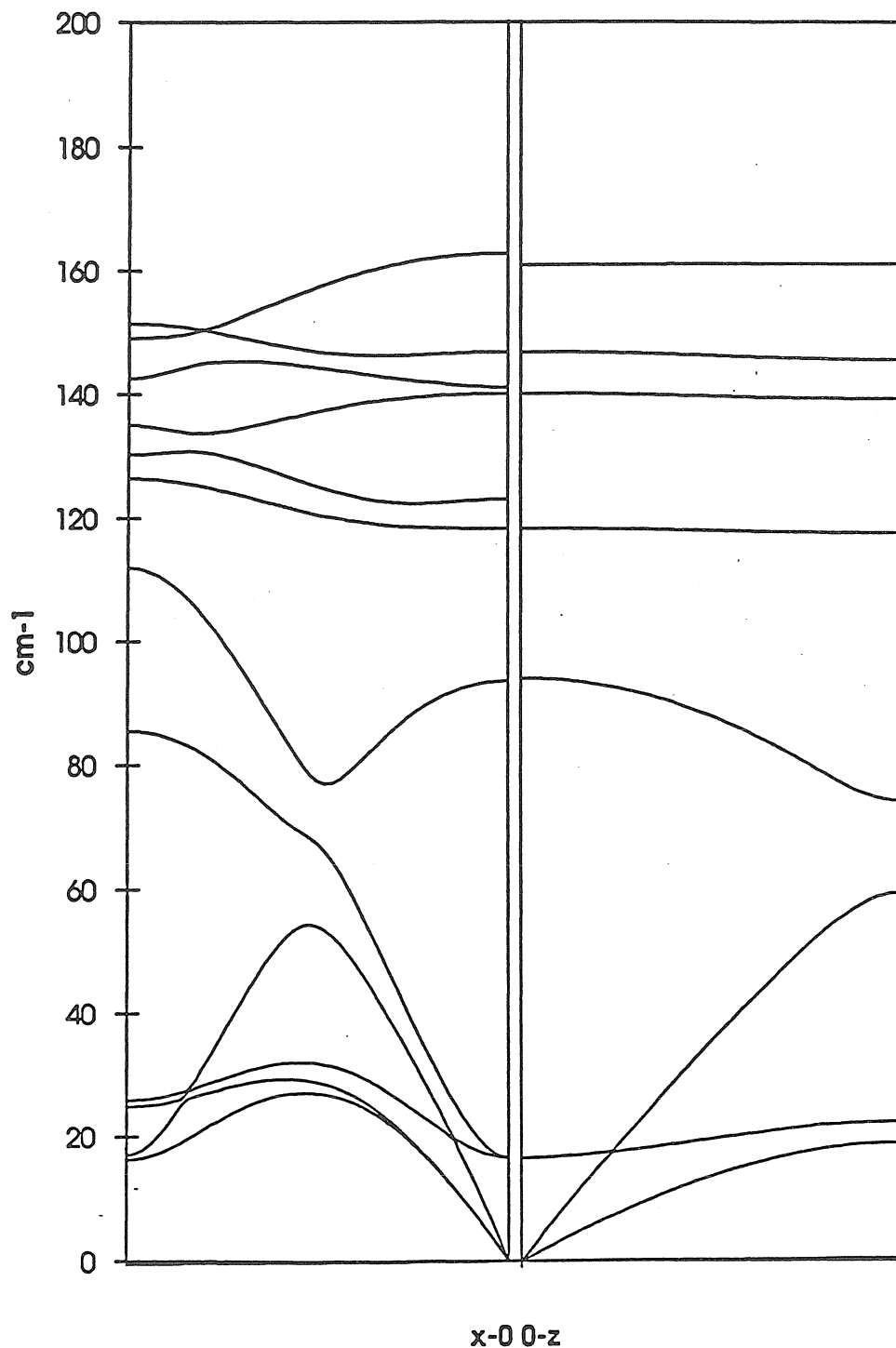


Figure 23

ZnS1/ZnSe1 superlattice phonon

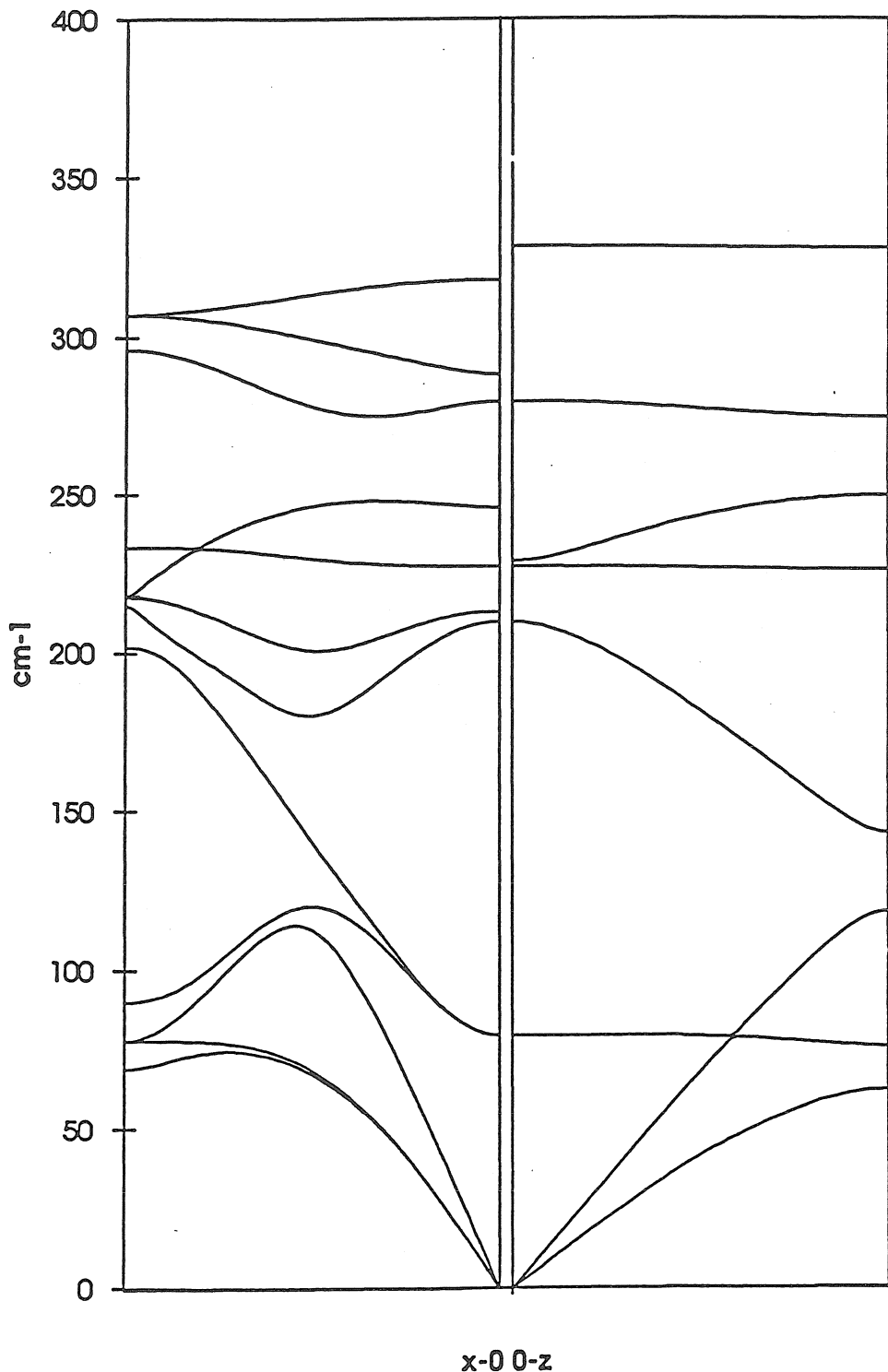


Figure 24

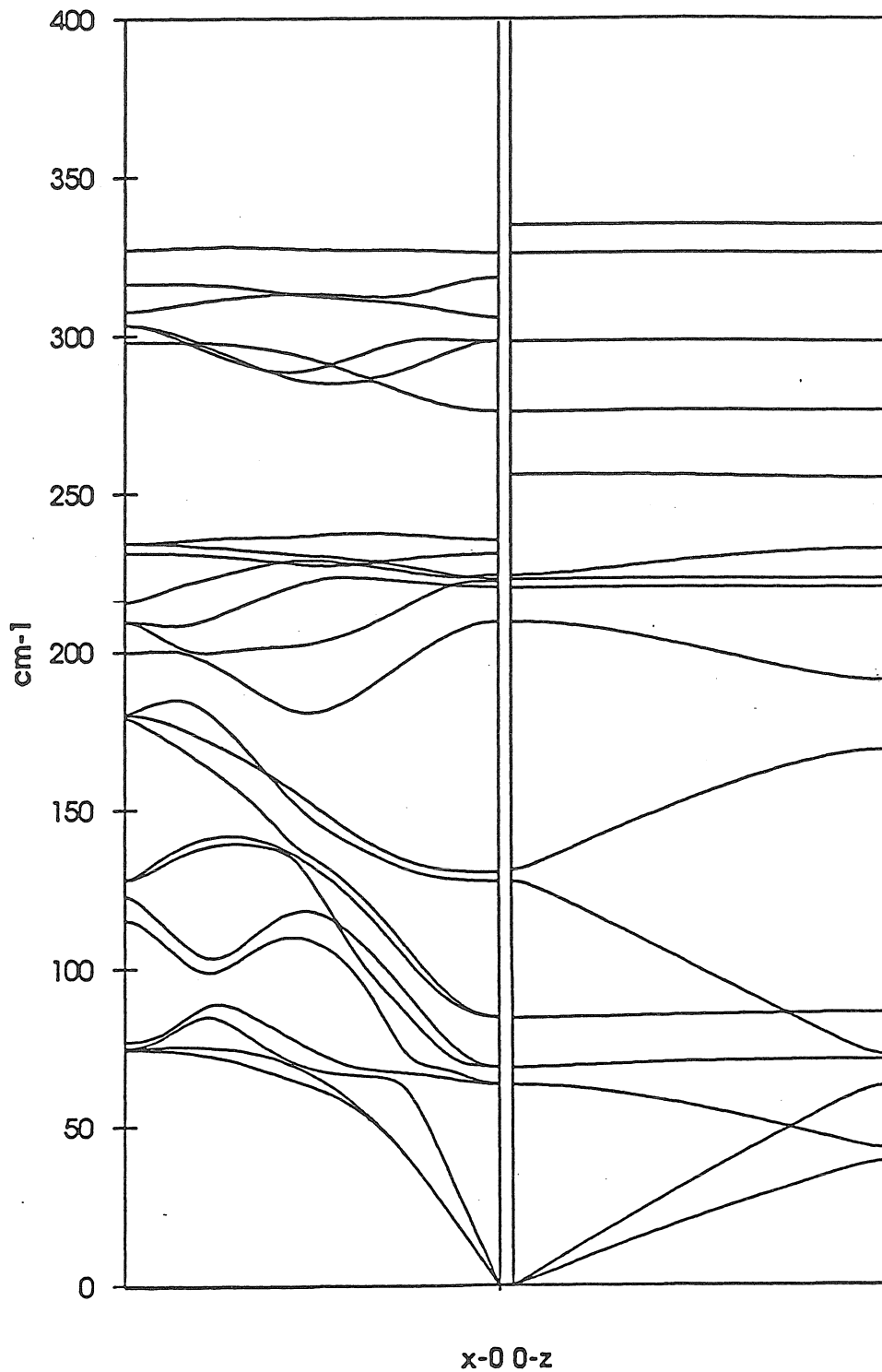
ZnS₂/ZnSe₂ superlattice phonon

Figure 25

ZnS4/ZnSe4 superlattice phonon

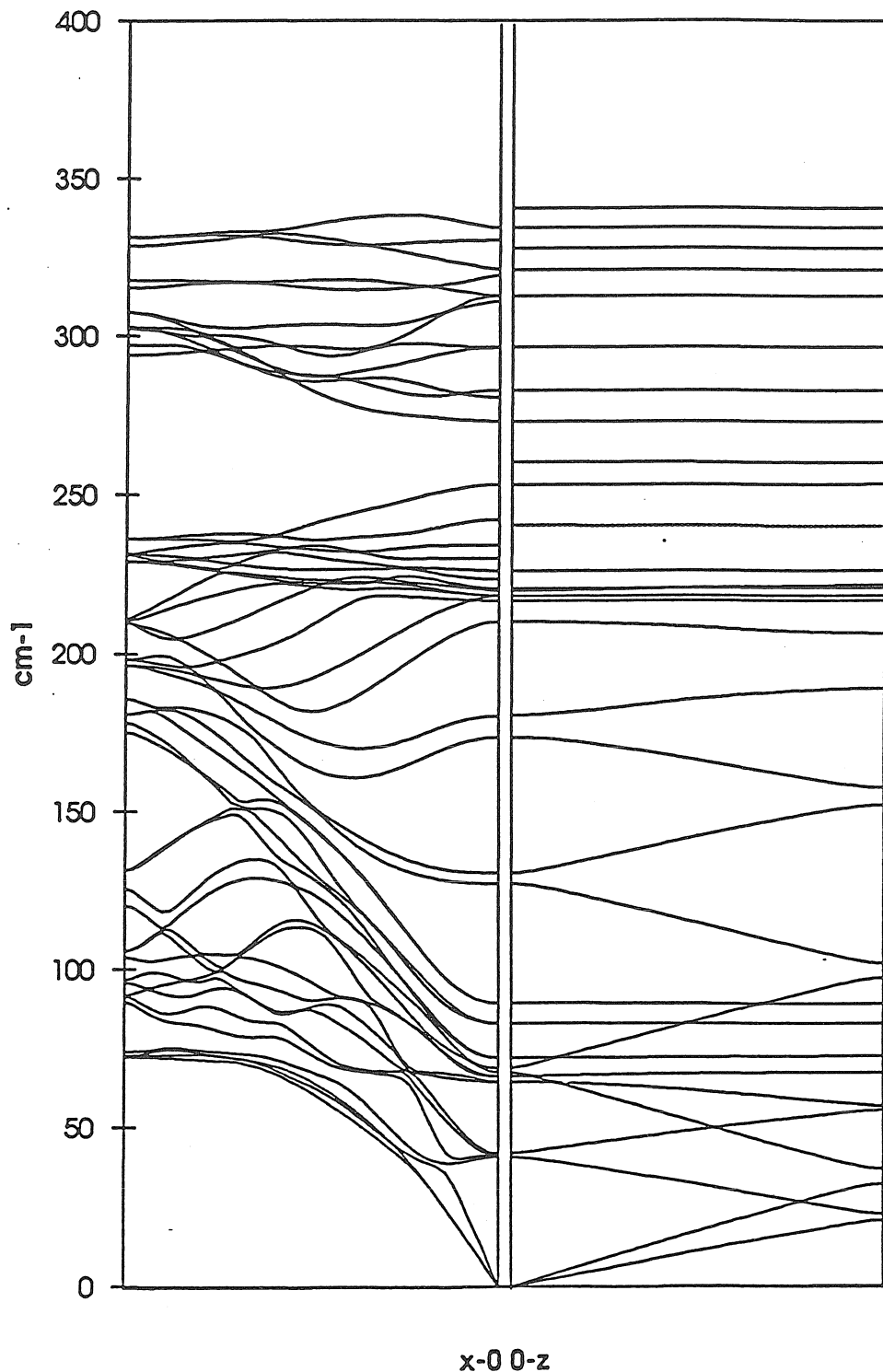


Figure 26

ZnS10/ZnSe2 superlattice phonon

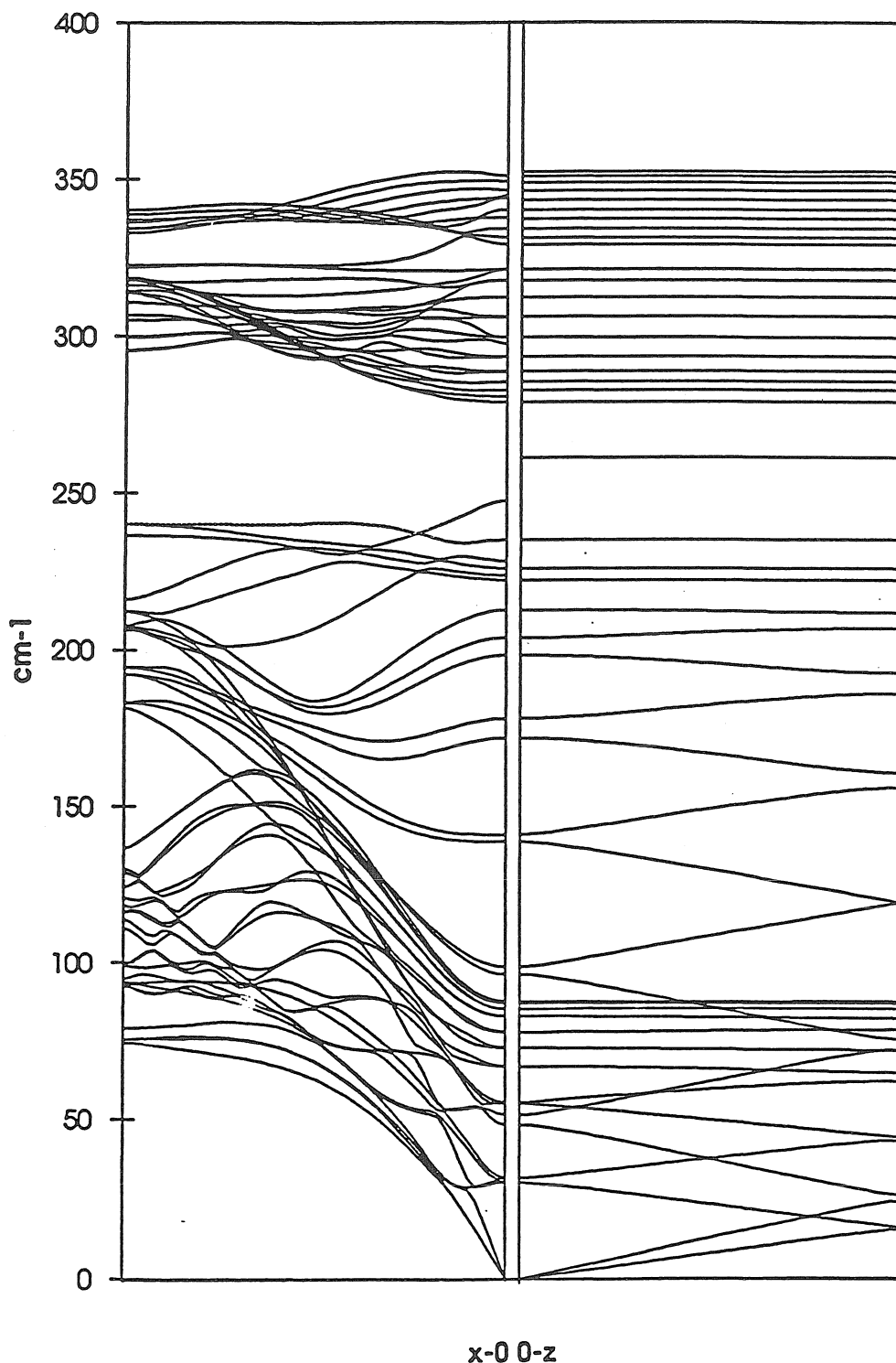


Figure 27

ZnSe1/ZnTe1 superlattice phonon

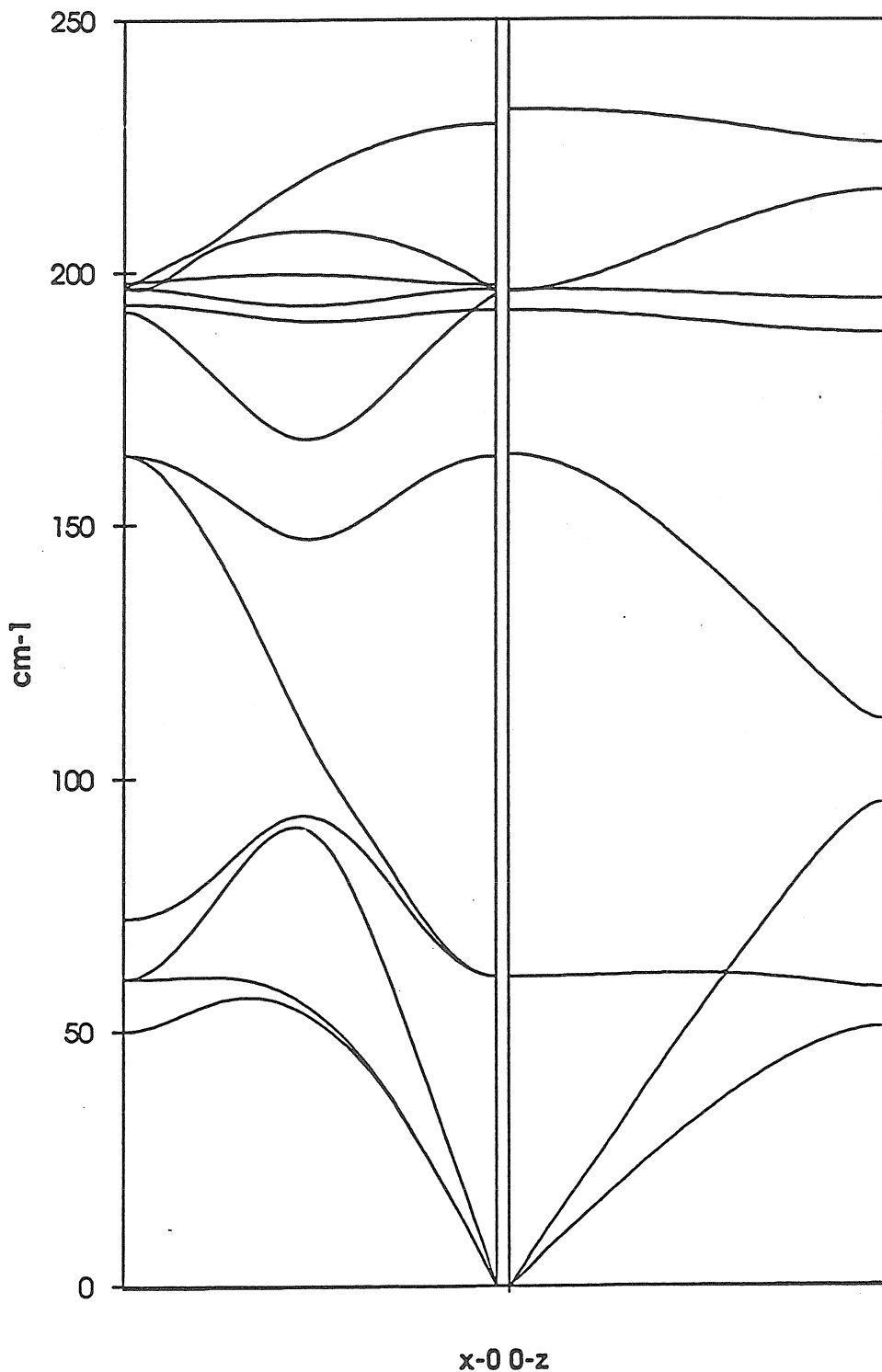


Figure 28

ZnSe2/ZnTe2 superlattice phonon

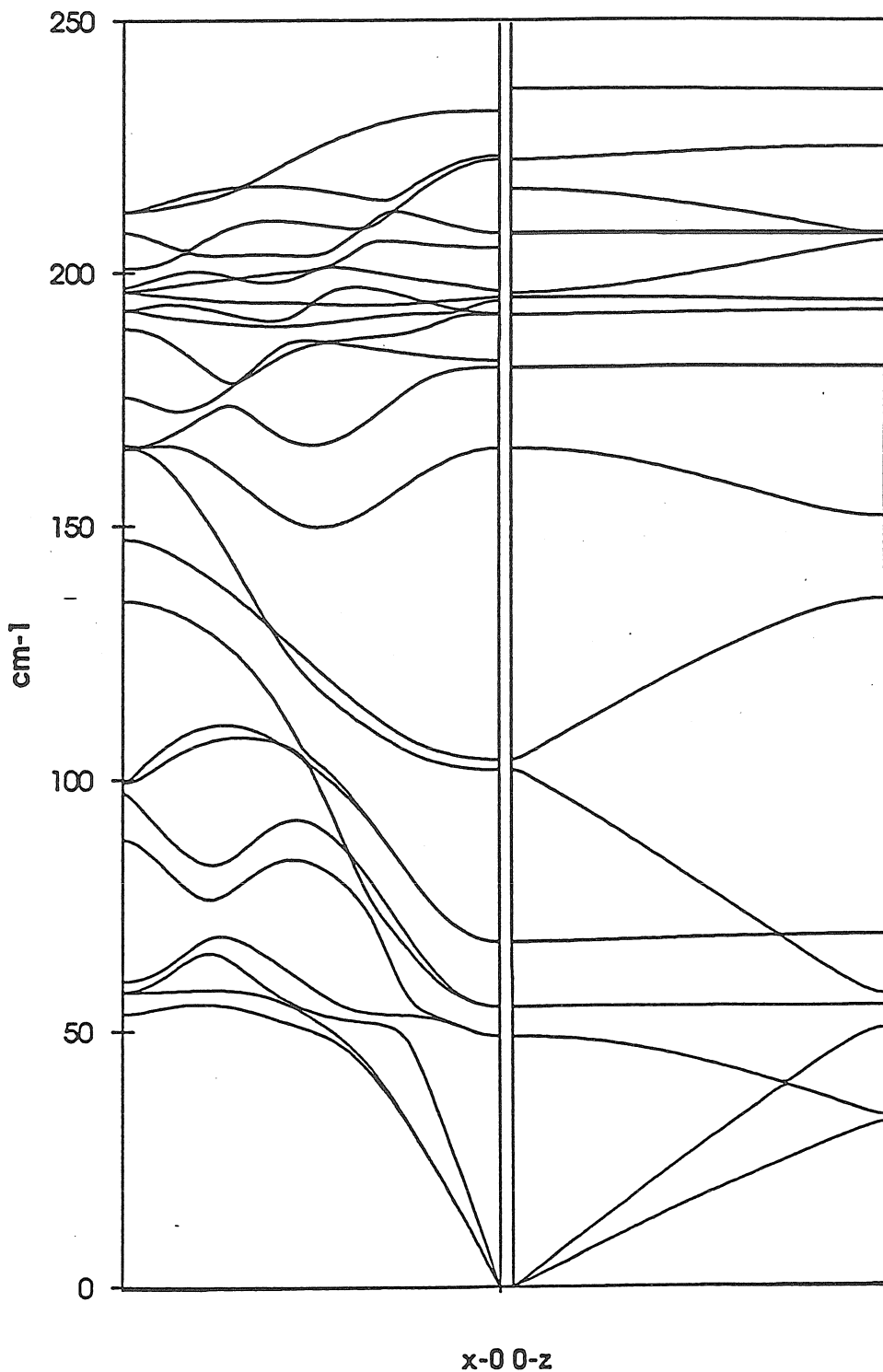


Figure 29

ZnSe4/ZnTe4 superlattice phonon

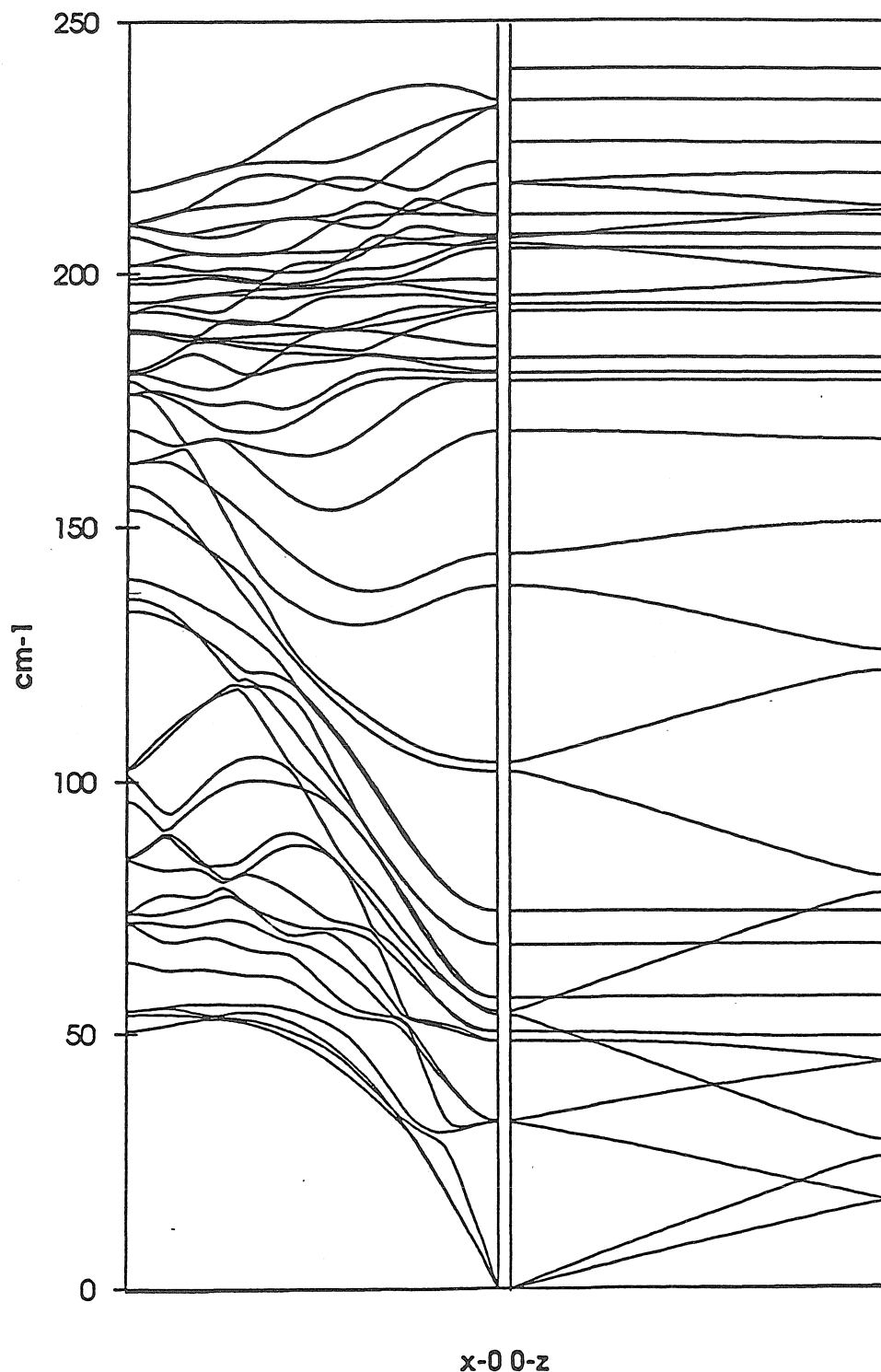


Figure 30

ZnSe10/ZnTe2 superlattice phonon

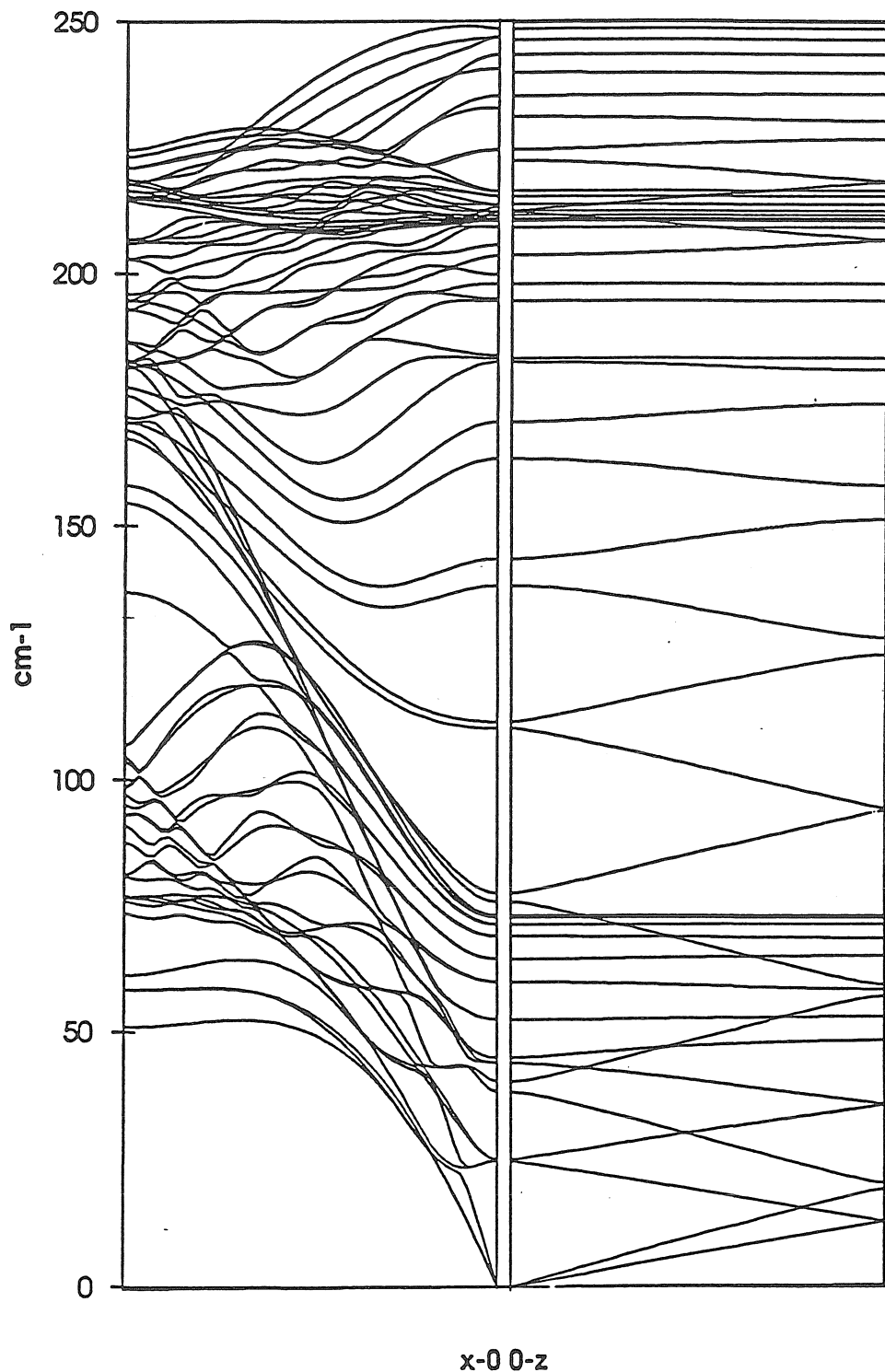


Figure 31

CdTe1/ZnTe1 superlattice phonon

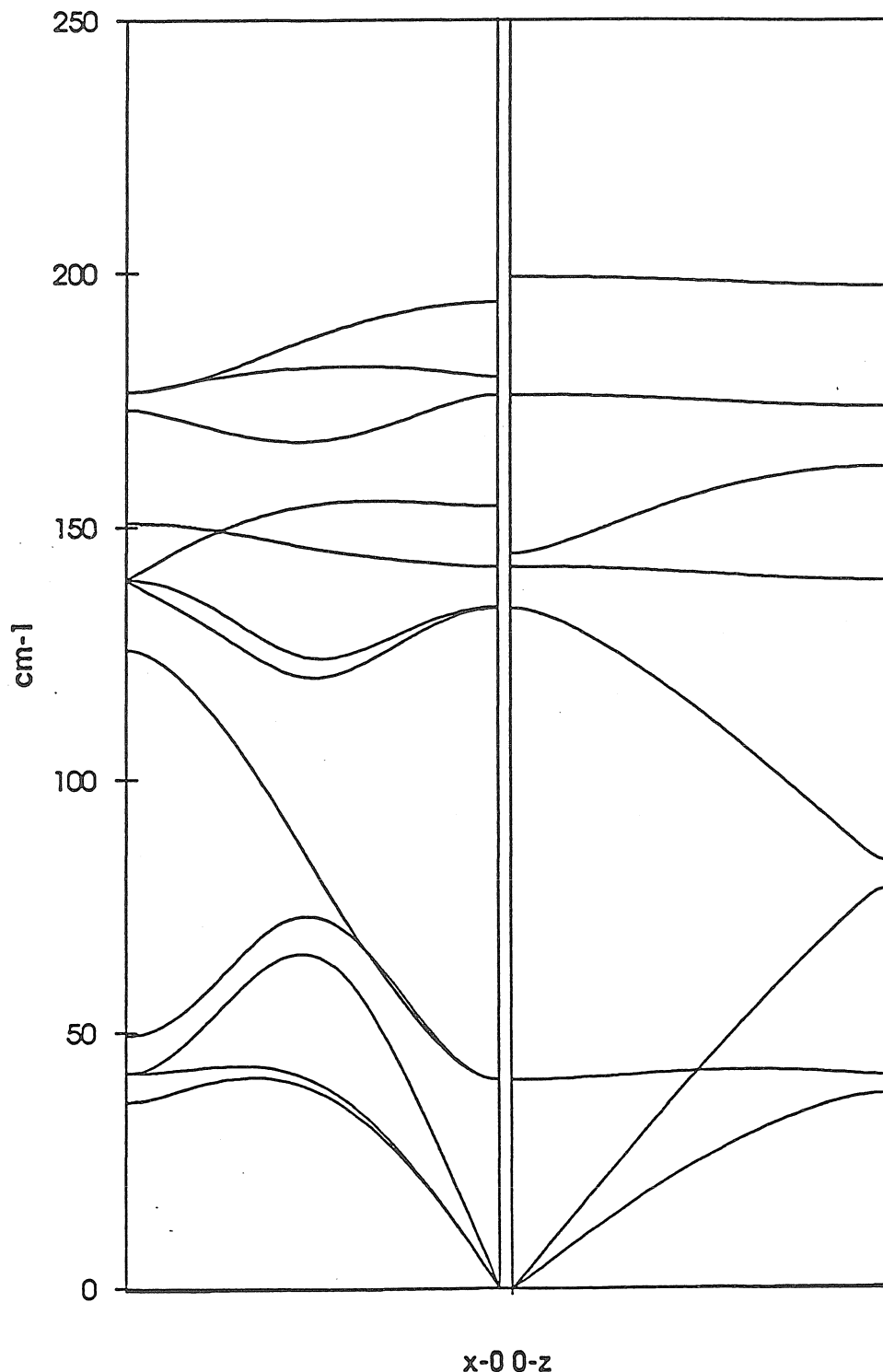


Figure 32

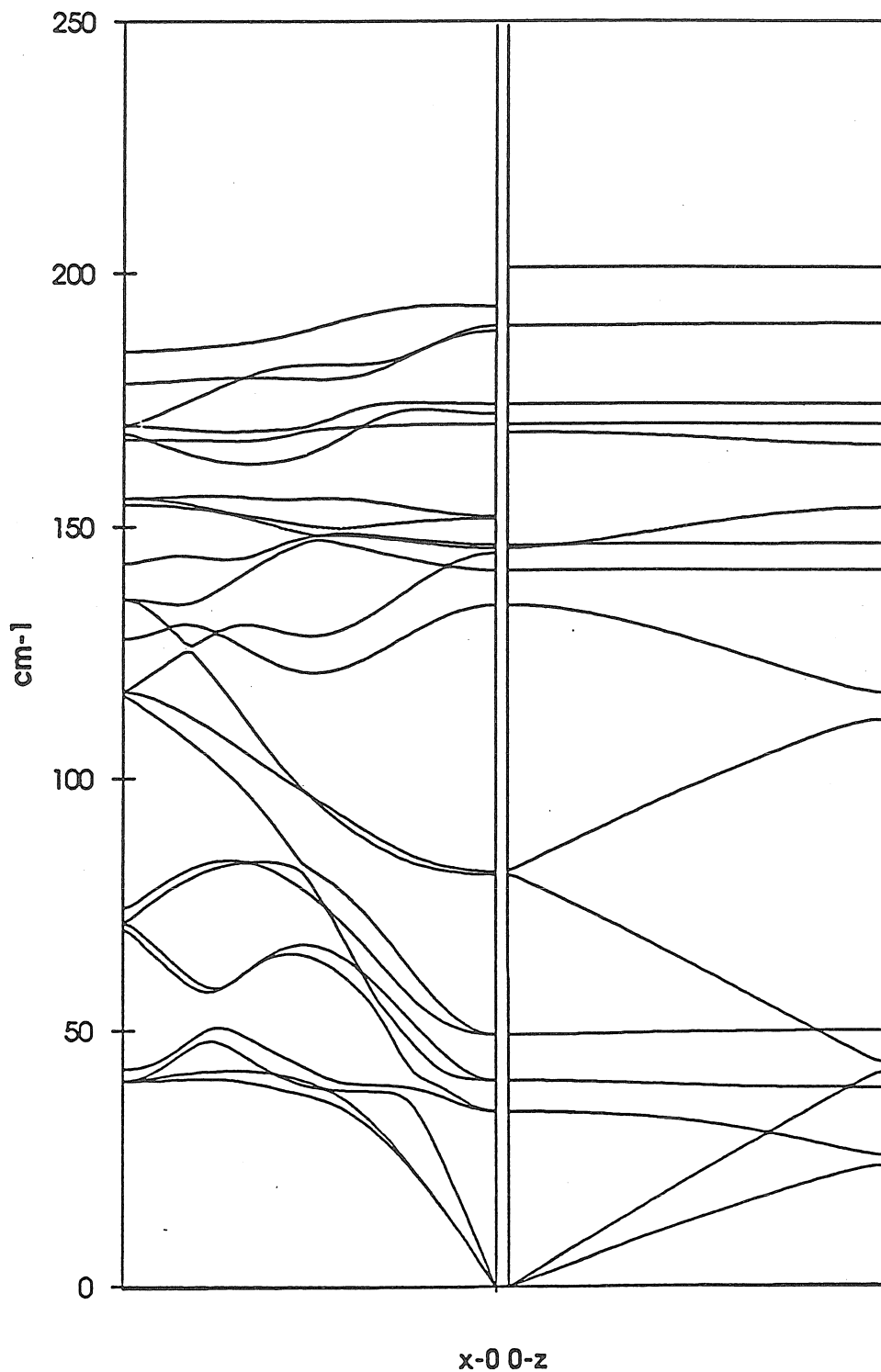
CdTe₂/ZnTe₂ superlattice phonon

Figure 33

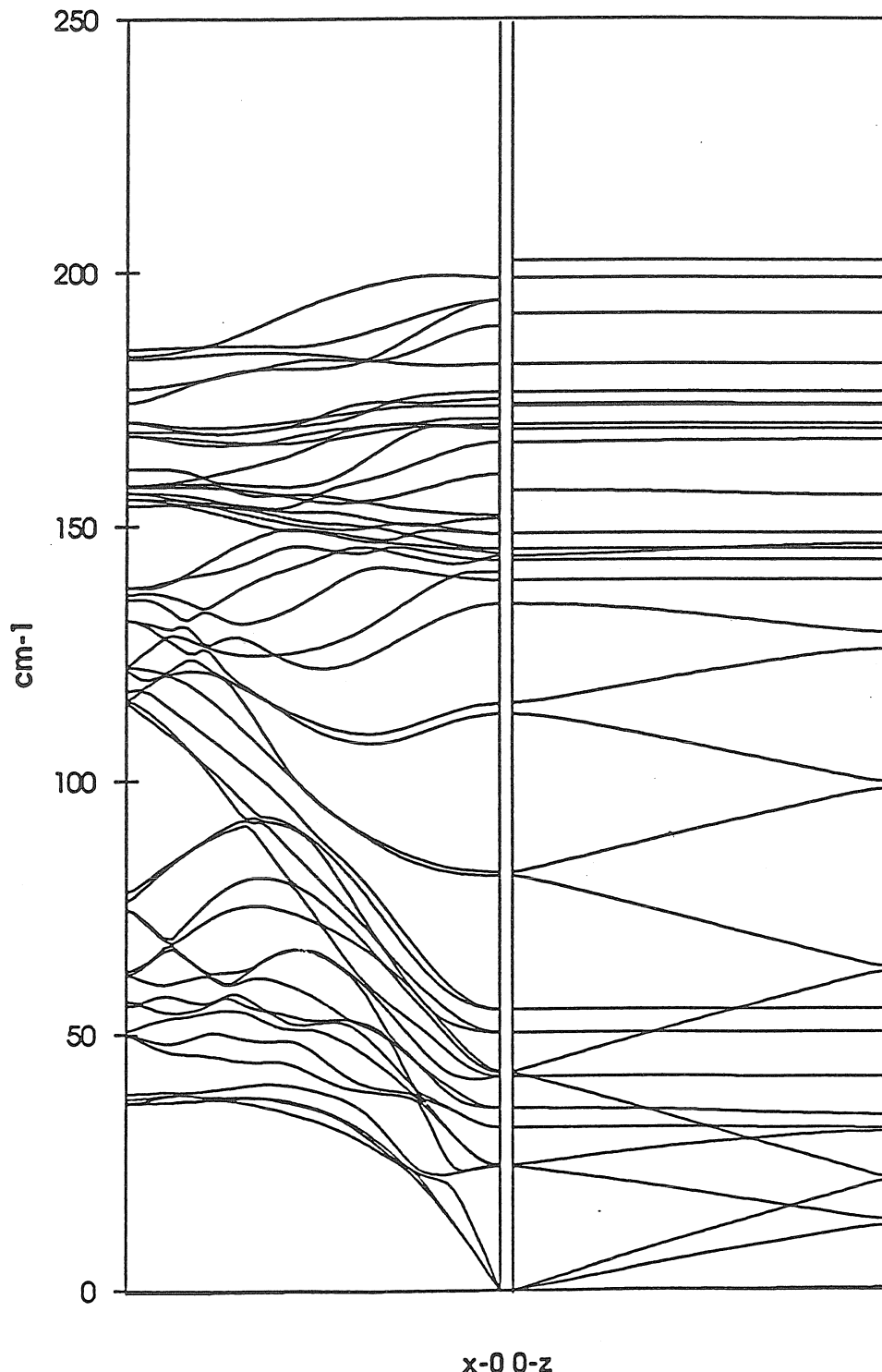
CdTe₄/ZnTe₄ superlattice phonon

Figure 34

CdTe10/ZnTe2 superlattice phonon

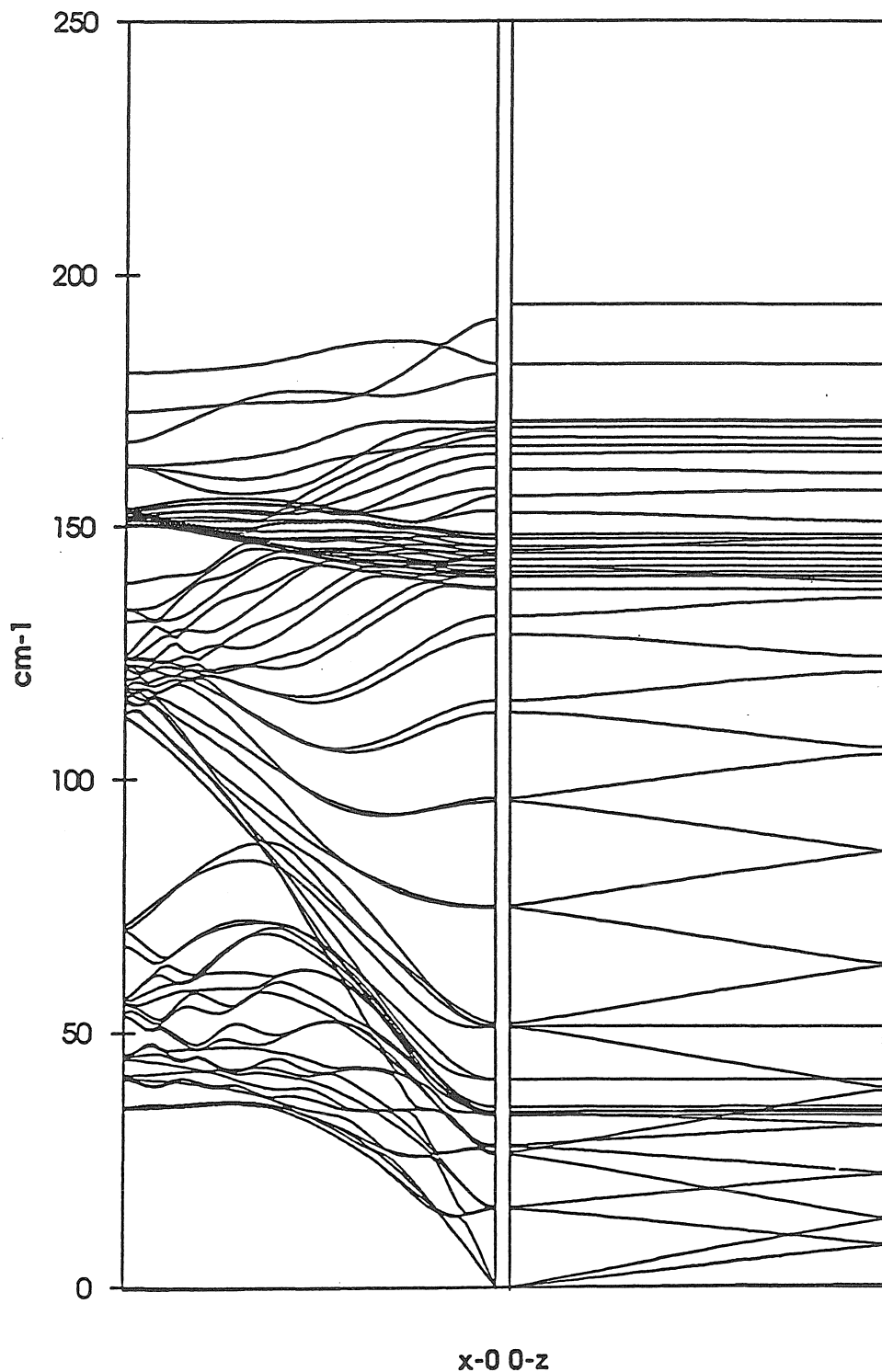


Figure 35

HgTe1/CdTe1 superlattice phonon

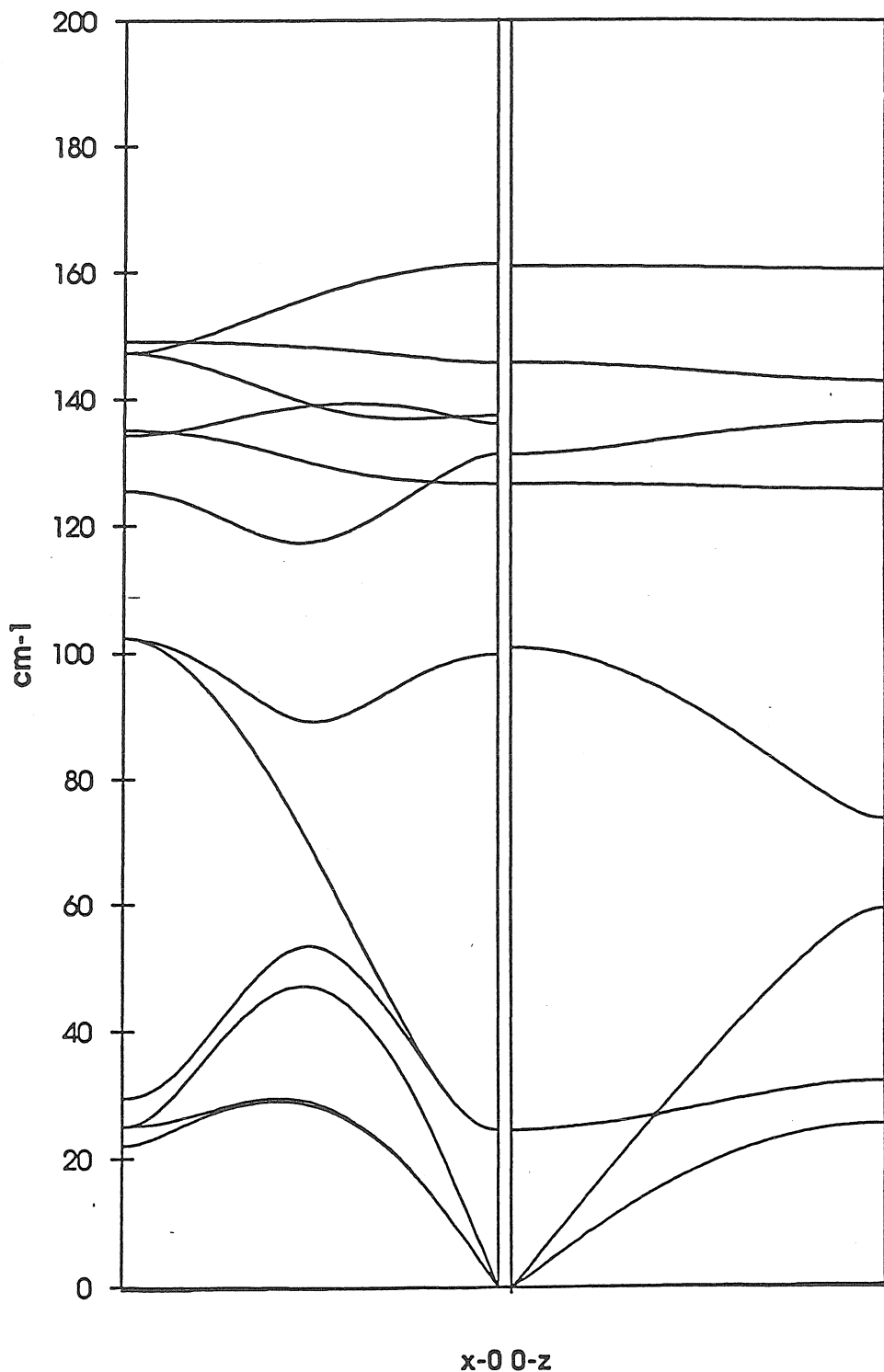


Figure 36

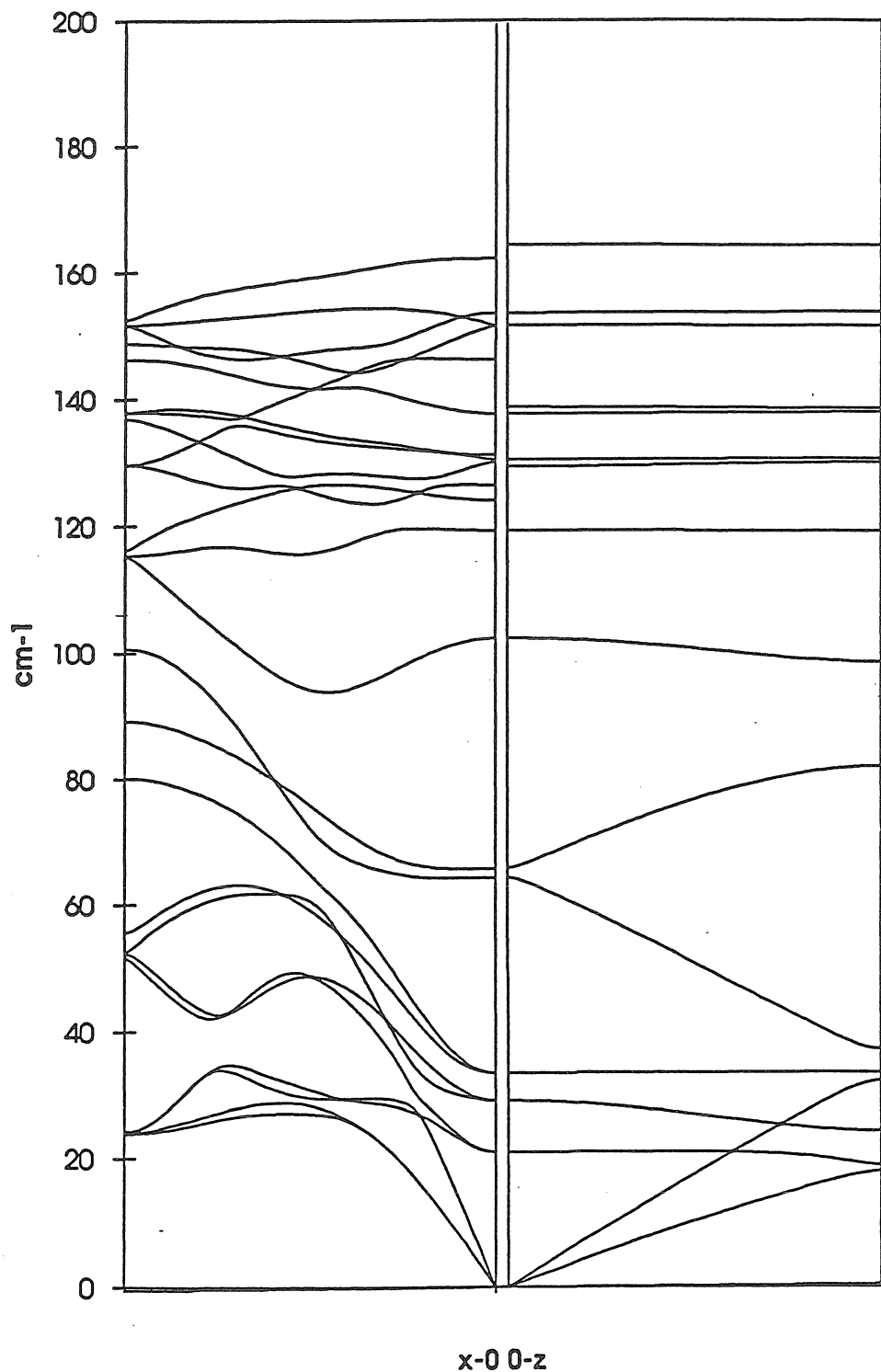
HgTe₂/CdTe₂ superlattice phonon

Figure 37

HgTe4/CdTe4 superlattice phonon

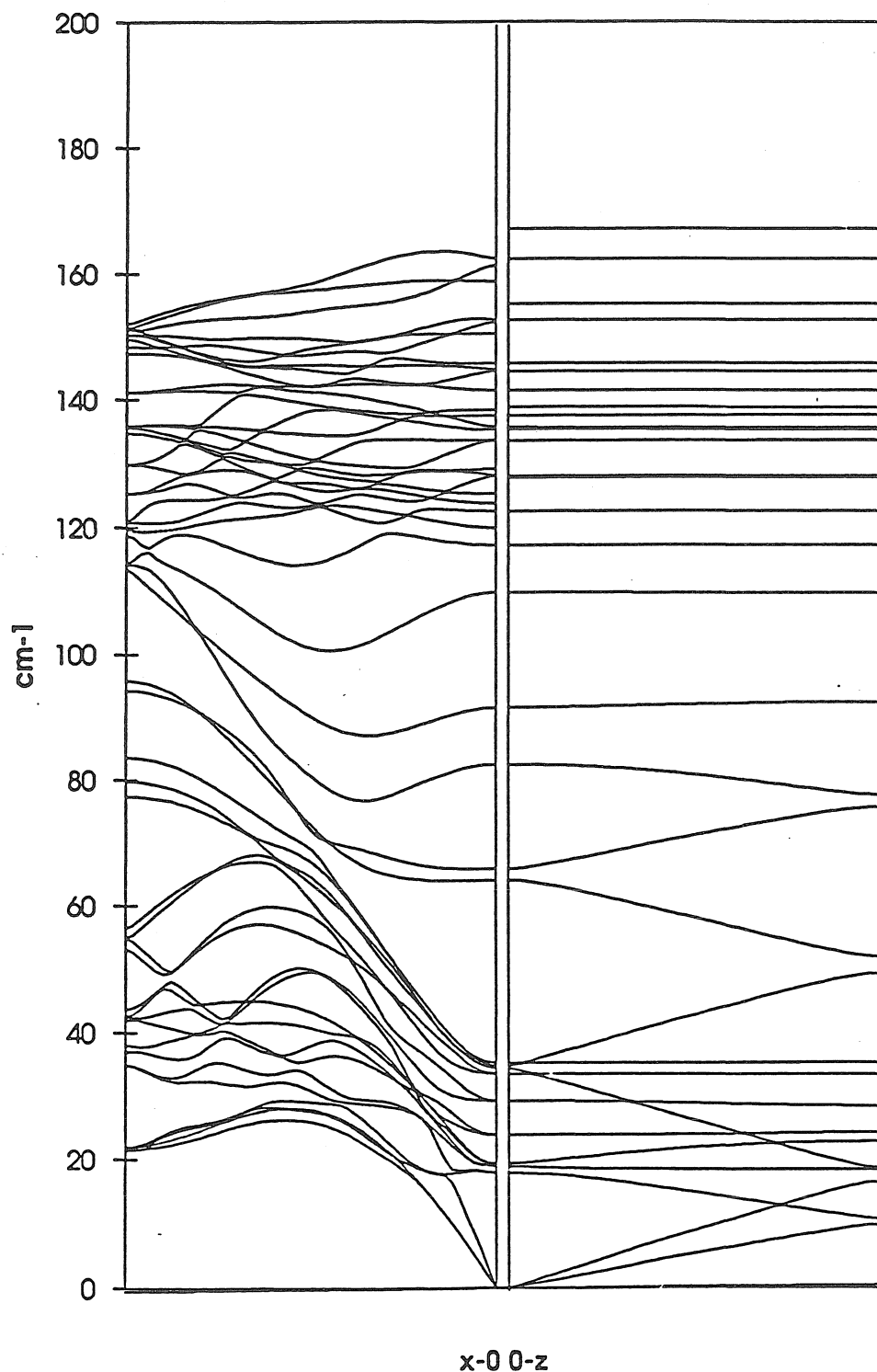
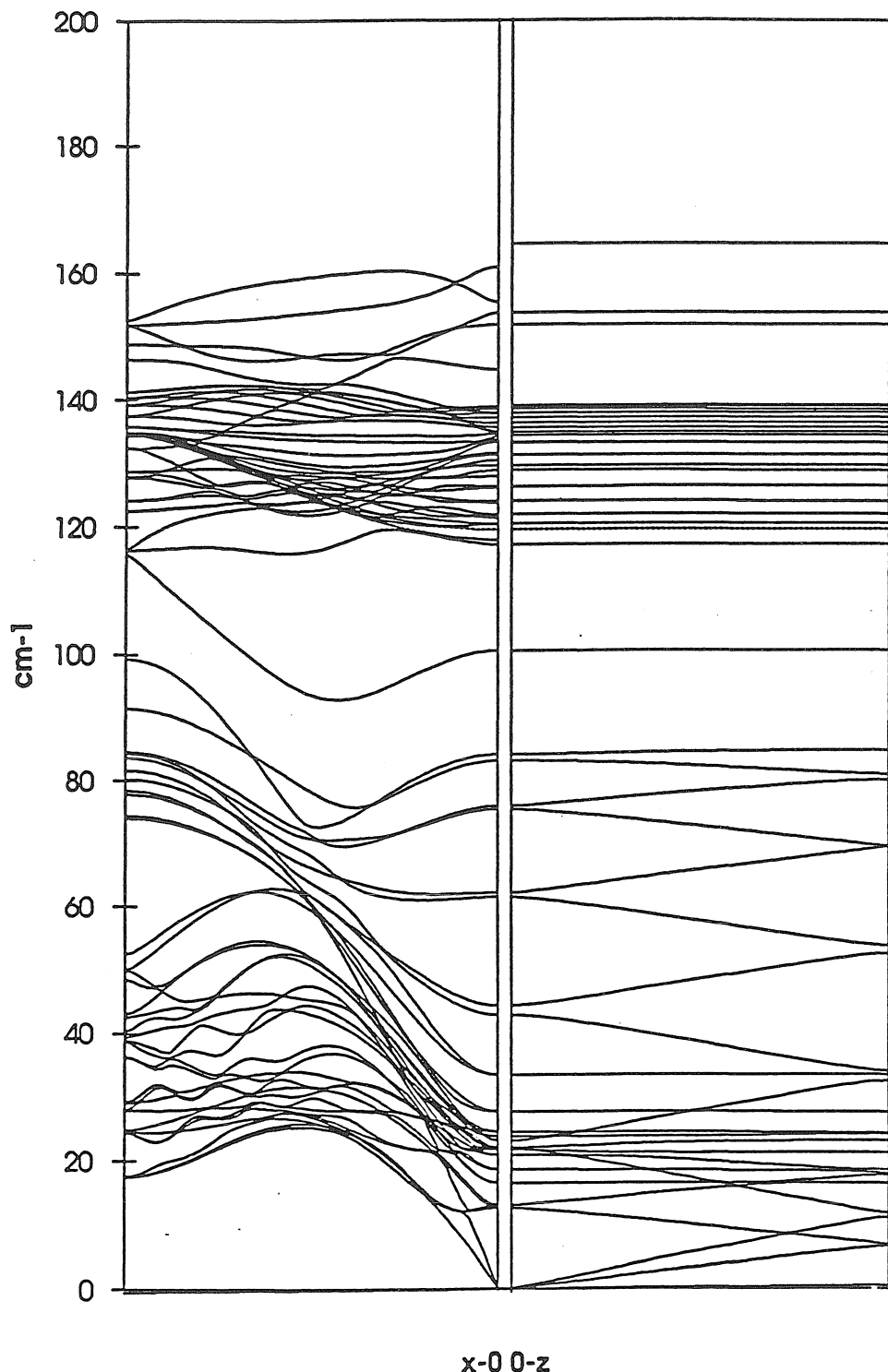


Figure 38

HgTe10/CdTe2 superlattice phonon



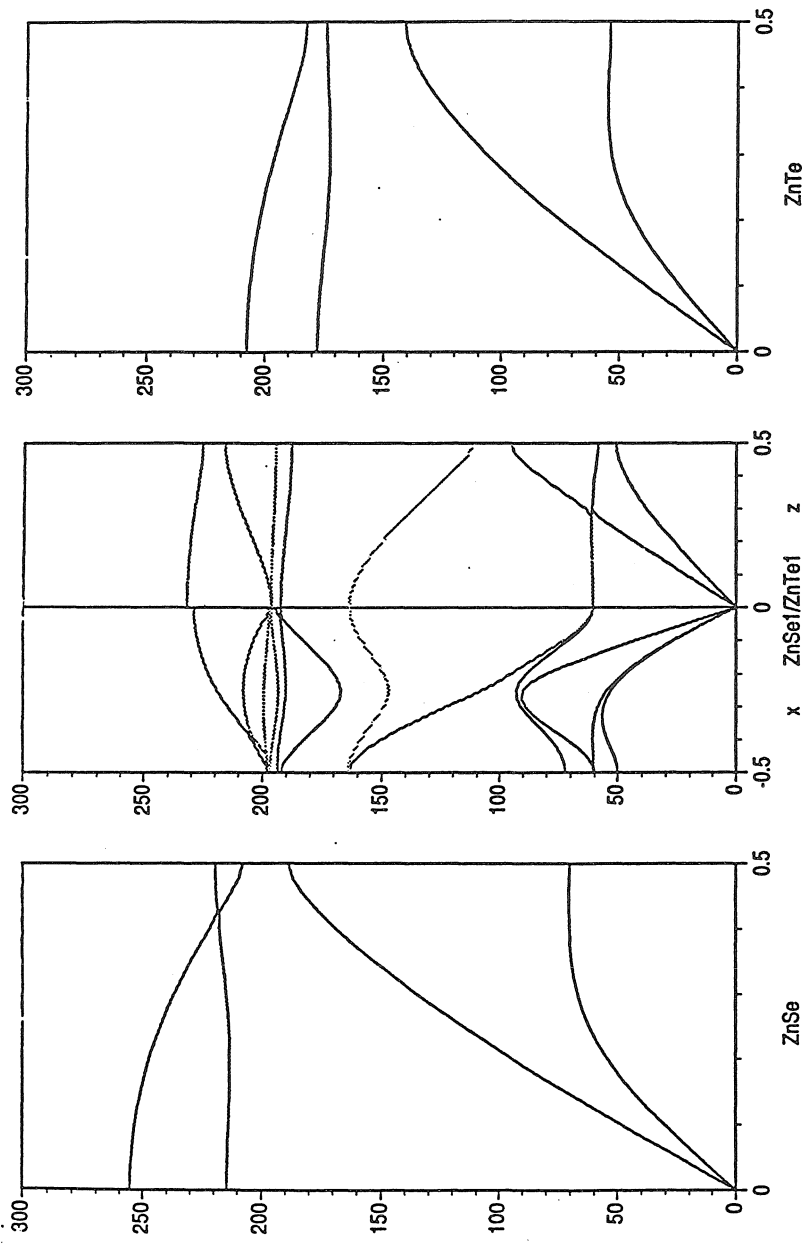


Figure 39

Chapter 6
Silicon (111) Surface Reconstructions

Abstract

We use the biased Hessian method in conjunction with *ab initio* generalized valence bond (GVB) calculations on Si clusters to derive the MSXX force field (FF) for silicon (111) surfaces. This FF is tested by calculating the atomic geometries and relative energies of the $(2n+1) \times (2n+1)$ DAS models of the Si (111) reconstruction. We find that the (5×5) and (7×7) surfaces are most stable.

1.0 Introduction

Since Schlier and Farnsworth¹ first observed the 7th order spots in the LEED pattern in 1959, numerous models of the Si (111)-7 \times 7 surface reconstruction have been proposed based on the results of various experiments and theoretical calculations.²⁻⁵ Strong evidence from STM experiments have led to wide acceptance of the Dimer Adatom Surface (DAS) model Takayangi^{7,8} which involves dimers, adsorbed atoms, and a stacking fault. However the large number of atoms in the surface unit cell has impeded detailed *ab initio* theoretical study. Indeed with approximately 100 atoms in just the first two layers of the 7 \times 7 unit cells, it has been difficult to unambiguously determine the structure from LEED and RHEED experiments. Angle resolved X-ray photoemission spectroscopy (ARXPS), X-ray diffraction, ion scattering, transmission electron diffraction, and scanning tunneling microscopy each give clues to the atomic structure. However, no one technique has conclusively determined the atomic arrangement of the Si (111)-7 \times 7 surface.

McRae⁹ suggested a model containing a stacking fault in one of the two sub-cells which was supported by Bennet's¹⁰ medium energy ion scattering results. Himpel³ and McRae⁹ each described how 12 atom rings around corner holes, two 8 atom rings around shallow holes on the sub-cell borders, and dimers along the sub-cell borders resulted from removing the broken bonds across the stacking fault boundary. These features are all observed by STM.⁵ Harrison² first proposed an adatom model. However, it was STM that first gave strong evidence that each unit cell contained 12 adatoms and led Bennig¹¹ to propose such a model. Takayangi^{7,8} combined the stacking fault-dimer idea with the adatom model to arrive at the DAS model. The calculated intensities of over one hundred atomic arrangements were compared to the TED pattern to refine the atom positions until the projected surface geometry was well described.

Figure 1 shows the projected geometry of the DAS model, where the detailed atom positions are from the MSXX force field described below. The unit cell consists of two triangular sub-cells. The surface double layer of one sub-cell has the wurtzite stacking and the other sub-cell the sphalerite stacking. The broken bonds needed to create the stacking fault are removed by dimers that form at the sub-cell boundaries. The cell corner contains a large hole with a twelve atom ring and one atom in the

center with a dangling bond. Holes with eight atom rings separate dimers except at the cell corners. Twelve adatoms occupy the T_4 sites, removing a net of 24 dangling bonds. Three rest atoms in each sub-cell remain each with a dangling bond. Twelve dangling bonds from the adatoms, six from the rest atoms and one in the cell corner account for the 19 dangling bonds per unit cell in the Si (111)- 7×7 DAS model. This structure eliminates 30 dangling bonds of the 49 dangling bonds for the unreconstructed Si (111) surface, accounting for most of the stability of this reconstruction. The essential features of the DAS model are observed by STM. The small and large holes are easily seen as depressions in the STM micrographs. The twelve adatom dangling bonds produce tunneling current at a different tunneling voltage than the dangling bonds of the six rest atoms which are seen as twelve bright spots at one voltage and six at another voltage, respectively.⁵

There remain, however, many questions. The 7×7 structure does not result uniquely from the DAS reconstruction scheme. Thus one can form a family of $(2n + 1) \times (2n + 1)$ DAS surfaces: 3×3 , 5×5 , 7×7 , 9×9 , etc. Of these, the 7×7 reconstruction is observed for the most part, although small amounts of the 5×5 surface reconstruction has been found to co-exist with the 7×7 surface in some temperature ranges. To fully understand Si surface reconstruction, we need a more quantitative description of the relative stabilities of such structures.

Due to the small surface normal momentum required to make the diffraction experiment surface sensitive, TED like LEED provides little information about the vertical positions of the atoms. However, unlike LEED, dynamical effects are much less important for TED giving it an advantage for determining structure. Clearly the surface normal positions must be determined in order to obtain quantitative understanding of Si reconstruction. Other experimental techniques or theoretical calculations more sensitive to the surface normal positions can be used to refine the vertical atomic positions of the DAS model.

Several investigators have proposed refined atomic positions for the DAS model.¹²⁻¹⁷ A key configuration is the adatom in the T_4 site. This leads to a trigonal bipyramidal with a sub-surface atom directly below the adatom. The distance between these two atoms, $R_{13}(T_4)$, is referred to as the 1-3 or nonbond distance. Proposed values of $R_{13}(T_4)$ have ranged from 2.45 to 3.1 Å, indicating the uncer-

tainty remaining in the structure characterization. From *ab initio* calculations on clusters, we obtain $R_{13}(T_4) = 2.52$ to 2.56\AA (depending on the site) which we believe is accurate to 0.05\AA . The Si-Si bond length of the dimer has also been subject to considerable uncertainty. We find values of 2.46 to 2.50\AA depending upon the site. This is stretched by 0.11 to 0.15\AA from the bulk value.

The large unit cell has made impractical the use of *ab initio* methods to study the surface. However, *ab initio* calculations can be performed on clusters of moderate size that model specific configurations of the surface. Messmer¹⁸ used the GVB *ab initio* method to calculate the geometries of various clusters to estimate the atomic geometry of the Si (111)- 7×7 surface. Using GVB calculations with the interstitial electron model,¹⁹ he also developed a silicon FF which was applied to study the Si (111)- 7×7 surface.²⁰ Other methods include the density functional theory^{21,22} (LDA) and semi-empirical methods such as modified intermediate neglect of differential overlap (MINDO)²³ and tight binding energy minimization.^{13,24}

Khor et al. calculated the energies of several of the DAS $(2n + 1) \times (2n + 1)$ reconstructions using LDA and found the experimentally observed 7×7 surface to be slightly higher in energy than the 5×5 surface.¹⁴ The 5×5 surface was observed experimentally (in small areas) after low temperature anneals of the cleaved Si (111)- 2×1 surface.²⁵ The predicted energy difference 0.008 eV/ 1×1 cell. is probably less than the uncertainty in the method, so that these calculation do not show conclusively which surface is lowest. Chadi¹³ used a semi-empirical tight binding based energy minimization method to calculate the structure and found the DAS 7×7 model to be energetically more stable than 5×5 by 0.008 eV/ 1×1 cell and more stable than the Si (111) c- 2×8 dimer chain model by 0.223 eV/ 1×1 cell.

We have used the Biased Hessian force field method^{26,27} to combine the second derivatives (Hessian) from *ab initio* calculations with the experimental geometry and spectroscopic data to generate an accurate force field (MSXX). This force field is then used to calculate the atomic structures and energies of the 3×3 , 5×5 , 7×7 and 9×9 Si (111) DAS models, the Si (111) c- 2×8 structure, two Si (111)- 2×2 structures, two Si (111)- $\sqrt{3} \times \sqrt{3}$ surfaces and the perfect Si (111) surface.

2.0 Method

2.1 The MSXX Force Field

The force field of a molecule or surface can be described by the following expression:

$$E = E_b + E_a + E_t + E_\psi + E_x + E_{vdW} + E_Q, \quad (1)$$

which includes bond stretch (E_b), angle bend (E_a), dihedral angle torsion (E_t), umbrella inversion (E_ψ), cross (E_x), van der Waals (E_{vdW}), and electrostatic (E_Q) terms.

2.1.1 Bonds

Bond stretching is described by the Morse potential,

$$E_{IJ} = D_b \left[e^{-\alpha_b(R-R_b)} - 1 \right]^2, \quad (2)$$

where R is the length of bond IJ, R_b and D_b are the position and depth of the well, and $k_b = 2D_b\alpha_b^2$ is the force constant.

2.1.2 Angles

Angle bending is described by the harmonic cosine expression,

$$E_a = \frac{1}{2} C [\cos \theta - \cos \theta_a]^2, \quad (3)$$

where θ is the angle between bonds IJ and JK, θ_a is the equilibrium angle, and $k_\theta = C \sin^2 \theta_a$ is the diagonal force constant.

2.1.3 Torsions

The dependence of the energy on the dihedral angle between bonds IJ, JK, and KL is described by the three fold potential,

$$E_t = \frac{1}{2} V_3 (1 + \cos 3\phi), \quad (4)$$

where ϕ is the torsional angle, and V_3 is the barrier.

2.1.4 Inversions

Given an atom I bonded to exactly three other atoms J, K, and L, we can include an inversion to describe the energy associated with the umbrella motion. We use the harmonic expression

$$E_i = \frac{1}{2} K_\psi [\cos^2 \psi - \cos^2 \psi_e], \quad (5)$$

where ψ is the angle between the IL bond and the IJK plane. Here the barrier to planarization is

$$V_{bar}^{inv} = \frac{1}{2} K_\psi (1 - \cos^2 \psi).$$

2.1.5 Cross Terms

Bond-angle and bond-bond cross terms are given by the following expression,

$$E_{ax} = D_1(\cos \theta - \cos \theta_a)(R_1 - R_{b1}) + D_2(\cos \theta - \cos \theta_a)(R_2 - R_{b2}) + K_{rr}(R_1 - R_{b1})(R_2 - R_{b2}) \quad (6)$$

associated with each angle term (6), where R_1 and R_2 are the lengths of the IJ and JK bonds, $k_{r\theta} = -D \sin \theta_a$ is the angle-stretch force constant, and k_{rr} is the stretch-stretch force constant.

One-center angle-angle cross terms are of the form,

$$E_{1aa} = G(\cos \theta_{IJK} - \cos \theta_{aIJK})(\cos \theta_{IJL} - \cos \theta_{aIJL}), \quad (7)$$

where $k_{1\theta\theta} = G \sin \theta_{aIJK} \sin \theta_{aIJL}$ is the force constant for two angle terms (IJK and IJL) sharing a common central bond (IJ) and a common central atom (J).

Two-center angle-angle terms are described by,

$$E_{2aa} = f(\phi)F(\cos \theta_{IJK} - \cos \theta_{aIJK})(\cos \theta_{JKL} - \cos \theta_{aJKL}) \quad (8)$$

where $k_{2\theta\theta} = f(\phi)F \sin \theta_{aIJK} \sin \theta_{aJKL}$ is the force constant for angle terms (IJK and JKL) in which the central atoms (J and K) are bonded to each other. This interaction is important when IJ and KL are trans (dihedral angle, $\phi = 180^\circ$), but not when they are gauche ($\phi = 60^\circ, 300^\circ$). Consequently we define this coupling term as

$$f(\phi) = \frac{1}{3} - \frac{2}{3} \cos \phi. \quad (9)$$

These cross terms are considered collectively as

$$E_x = E_{ax} + E_{1aa} + E_{2aa}. \quad (10)$$

2.1.6 Charges

The electrostatic nonbond interaction (E_Q) is described using the Coulomb expression

$$E_Q = \frac{Q_I Q_J}{\epsilon_0 \epsilon R_{IJ}} \quad (11)$$

where Q_I is the charge (electron units) on center I , $\epsilon = 1$, and $1/\epsilon_0 = 332.0637$ converts units to give E in kcal/mol when R_{IJ} is the distance in Å.

The charges used for each molecule were calculated from the Hartree-Fock wave function by using the Mulliken populations.

2.1.7 van der Waals

The van der Waals part of the nonbond interaction (3) for atoms I and J is described using the exponential-6 potential

$$E_{vdwIJ} = D_v \left[\left(\frac{6}{\zeta - 6} \right) e^{\zeta(1-\rho)} - \left(\frac{\zeta}{\zeta - 6} \right) \rho^{-6} \right], \quad (12)$$

where $\rho = R_{IJ}/R_v$.

2.2 The Biased Hessian Method

The energy expression of a molecule can be expanded as:

$$E(X_1 \dots Z_N) = E_0 + \sum_{i=1}^{3N} \left(\frac{\partial E}{\partial R_i} \right)_0 (\delta R_i) + \frac{1}{2} \sum_{i, j=1}^{3N} \left(\frac{\partial^2 E}{\partial R_i \partial R_j} \right)_0 (\delta R_i)(\delta R_j) + \dots \quad (13)$$

where the force on the i^{th} component is:

$$F_i = -\frac{\partial E}{\partial R_i}, \quad (14)$$

and

$$H_{ij} = \frac{\partial^2 E}{\partial R_i \partial R_j} \quad (15)$$

is the Hessian. To calculate the vibrational frequencies we mass weight H_{ij} to form $\mathcal{H}_{ij} = H_{ij}(M_i M_j)^{-1/2}$ and diagonalize

$$\mathcal{H}\mathbf{U} = \mathbf{U}\lambda, \quad (16)$$

where

$$\lambda_i = (C_{vib}\nu_i)^2$$

gives the vibrational frequencies (with energies in kcal/mol, distances in Å, and masses in AMU, $C_{vib} = 108.5918$ gives ν_i in cm^{-1} and the columns of \mathbf{U} give the vibrational eigenfunctions. To extract a force field we could require that the force field reproduce this Hessian and the experimental geometry. However, the Hartree-Fock wave function predicts frequencies that are 10% to 20% too large and thus force constants derived from the theoretical Hessian would be too large. The biased Hessian^{26,33} alternative combines the normal mode description (\mathbf{U} matrix) from Hartree-Fock with the experimental frequencies to form a biased Hessian. That is, using

$$\mathcal{H}^{HF}\mathbf{U}^{HF} = \mathbf{U}^{HF}\lambda^{HF}, \quad (17)$$

we construct

$$\mathcal{H}^{BH} = \mathbf{U}^{HF}\lambda^{exp}\tilde{\mathbf{U}}^{HF} \quad (18a)$$

(where \sim indicates transpose), which leads to

$$\mathcal{H}^{BH}\mathbf{U}^{HF} = \mathbf{U}^{HF}\lambda^{exp}. \quad (18b)$$

We then fit the FF parameters to \mathcal{H}^{BH} . The $(3N - 6)(3N - 5)/2$ independent elements of \mathcal{H}^{BH} provide constraints on the force field parameters. Requiring the force field to also reproduce the experimental geometry leads to $3N - 6$ additional constraints on

$$\left(\frac{\partial E^{FF}}{\partial R_i} \right)_{EQ} = 0. \quad (19)$$

The MSXX force field is obtained by simultaneously minimizing the error in fitting (20) and (21).

2.3 Electronic Structure Calculations

Hartree-Fock calculations were performed using GAUSSIAN 86²⁸ to determine the theoretical second derivatives. We used the experimental structure where available. For others we used the HF optimized geometry. We used the 6-311G** basis (valence triple zeta on both Si and H with d polarization functions on Si and p polarization functions on H).

2.4 Scaling Theoretical Force Fields

The MSXX force field for the Si (111)-7 \times 7 surface is obtained from combining the force fields of Si_4H_9 (Figure 2), Si_5H_7 (Figure 3), and bulk silicon. First the Biased Hessian method was used to calculate the force fields for SiH_3 , SiH_4 and Si_2H_6 .

Because no experimental frequencies or geometries were available for Si_4H_9 , we used the following approach. We calculated *theoretical* force fields for SiH_3 , SiH_4 , and Si_2H_6 in the same manner as the BH force fields except that we fit to the Hartree-Fock frequencies. Comparing the force constants for the theoretical force fields and the experimentally biased force fields for each of the three molecules led to scaling rules for each type of term in the force field. This works well for bonds, angles, and cross terms but not for inversion and torsion. We then calculated the Hessian for Si_4H_9 at the Hartree-Fock optimized geometry and fit the force field to the Hartree-Fock frequencies and geometry. The various terms in this force field were then scaled using the scaling rules obtained from SiH_3 , SiH_4 , and Si_2H_6 . (It is sufficient to use only the scaling rules for disilane.) The energy versus distance curves for Si_4H_9 from the Hartree-Fock wave function from the MSXX FF are compared in Figure 4.

In order to calculate the force field for the Si_5H_7 , we must add additional force constants to the Si_4H_9 force field. These terms are calculated from bulk Si calculations.

Zur *et al.*²⁹ reported a five parameter force field for bulk silicon obtained from fitting the vibrational modes of Si_5H_{12} calculated using the GVB-configuration interaction (GVB-CI) wave function. We use this FF as a starting point and optimize the parameters to fit the phonons and the elastic constants. Using this FF (Table 1) we reproduce the phonon dispersion frequencies and elastic constants found by Zur *et al.* However, the MSXX FF also includes van der Waals interactions (which tend to stiffen the lattice), and hence we reoptimized the bulk force field (to calculate accurate elastic constants, and phonons). We started with the Zur force field optimized with van der Waals interactions and added two center angle angle and torsion terms. The parameters were optimized to fit the elastic constants and phonons (Table 2).

In agreement with McMurry³⁰ we find that the two center angle angle force constant (with couplings only between planar angles)^{ref} is necessary to describe the very flat transverse acoustic mode along the delta direction, Figure 5. The resulting bulk silicon force field is similar to that of Turbino.³¹ We use the same terms except the addition of the van der Waals interaction.

The torsion term (7) has little effect on the phonons and elastic constants. Instead we calculate V_3 from the difference in energy between the wurtzite and sphalerite forms of silicon obtained from first principles local density calculations by Cohen *et al.*³² The energy difference between these two forms is due to one of every four torsions being in the eclipsed rather than the staggered position. There are two torsions per atom and one quarter of these are responsible for the energy difference between the two phases. Thus the torsional barrier is one half of the energy difference per atom, or $V_3 = 0.738$ kcal/mol. The van der Waals interactions also affect the energy difference between the two forms of silicon. Thus we find that $V_3 = 0.51$ kcal/mol reproduces the difference 0.016 ev per atom as obtained by Cohen from DFT calculations.³¹ Because the Si (111)-7 \times 7 reconstructed surface contains a stacking fault, V_3 plays a role in determining the energetics of the surface reconstruction.

On adding the bulk force constants to those of Si_4H_9 to complete the force field for Si_5H_7 , we then calculate the energy of the Si_5H_7 cluster as a function of the cap silicon position along the C_3 axis. The MSXX FF accurately reproduces this curve, including the equilibrium 1-3 distance (Figure 6). This requires an equilibrium angle for the $Si_3 - Si_2 - Si_3$ (see Figure 3) angle terms of 115° (HF calculations on Si_4H_9 lead to 122°). The HF equilibrium 1-3 distance of 2.906 Å was fit to within 0.02 Å.

With the MSXX force field for Si_5H_7 , we optimized the geometries of the (3 \times 3), (5 \times 5), (7 \times 7), and (9 \times 9) DAS Si (111) reconstructed surfaces, the centered (2 \times 8), and three (2 \times 3) surfaces, and the relaxed perfectly terminated Si (111) surface.

2.5 Optimization

All calculations were carried out using POLYGRAF,³³ an interactive molecular simulations package for molecular mechanics and molecular dynamics of crystals.

The atomic coordinates were optimized (using conjugate gradient techniques) until the RMS force became less than 0.01 (kcal/mol)/Å. At the optimized structure, all stress components are less than 0.005 GPa. We modelled the surface using 6 layers of silicon (three double layers). The bottom four layers having undergone no reconstruction. The sixth layer of silicon atoms has its bonding saturated with hydrogen atoms. The surface unit cell is constrained to an integral multiple of the lateral size of the bulk unit cell.

3.0 Results

3.1 SiH₄

Table 3 compares the MSXX frequencies with experiment. Table 4 shows the MSXX force field, the theoretical force field, and the scales. The MSXX FF leads to forces less than 0.005 kcal/molÅ at the experimental geometry.

3.2 Si₂H₆

Table 5 lists the MSXX force constants and Table 6 compares the frequencies from the MSXX and theoretical force fields for *Si*₂H₆.

3.3 SiH₃

The MSXX force field for silyl radical in Table 7 leads to the frequencies and geometry in Table 8. Table 7 also gives the scaling factor for this force field (the ratio of the force constants fitting the experimental frequencies to the force constants fitted the HF frequencies). The stretch stretch cross terms do not scale the same as found for silane and disilane. The inversion force constant scales differently than the other valence terms.

3.4 Si₄H₉ and Si₅H₇

Table 9 shows the force constants for Si₄H₉ from fitting to the HF frequencies. To obtain the MSXX we used the scaled force constants from *Si*₂H₆ plus (i) the inversion term was fitted to the HF energy curve for inversion and (ii) we adjusted the equilibrium *Si*₃*Si*₂*Si*₃ angle to fit the geometry. The MSXX force field at the experimental geometry leads to an rms force of less than 0.08 kcal/molÅ.

For *Si*₅H₇ we used the MSXX force field for *Si*₄H₉ plus additional terms from the bulk force field (Table 10). We find that we can obtain the HF optimized

geometry for this cluster and the HF energy curve for the Si_2 position along the C_3 axis by adjusting the equilibrium $Si_3 - Si_2 - Si_3$ bond angle.

3.5 DAS Structures

3.5.1 The $R_{13}(T_4)$ Distance

The adatom geometry for the Si (111)-7×7 reconstructed surface is of most interest. In the DAS model the 12 adatoms sit directly above second layer atoms in T_4 sites. The repulsive interaction between the adatom and the third layer atom tends to push the adatom outwards. On the other hand, the four coordinated silicon of the second and third layer atoms prefer tetrahedral bond angles and the triply coordinated adatom prefers angles near 113°. This tends to limit the $R_{13}(T_4)$ distance. Ichmiya¹⁷ found a back bond distance of 2.56 Å using RHEED. Tong *et al.*¹⁵ used dynamical LEED and reported a back bond distance that ranged from 2.49 Å to 2.56 Å (depending on whether the adatom was on the faulted half, unfaulted half, near a corner or near the center). Tromp and van Loenen¹² found that the back bond distance must be approximately 2.6 Å using medium energy ion scattering. Robinson¹⁶ used XRD experiments to estimate a back bond distance of 2.64 Å. Qian and Chadi¹³ used a tight binding energy minimization calculation to determine the atomic structure. They reported a back bond distance of 3.1 Å. Messmer^{18,20} reported a 1-3 distance of 2.52 Å based on GVB calculations and 2.45 Å from calculations on the surface using a silicon potential based on the interstitial electron model. We find $R_{13}(T_4) = 2.52$ Å to 2.56 Å, depending on the location of the adatom within the unit cell.

3.5.2 The $R_{34}(T_4)$ Distance

Tong finds $R_{34}(T_4)$, the bond length between the sub-surface eclipsed atom in the T_4 site and the atom directly below it, to be 2.13 Å or 2.18 Å (with uncertainties of 0.1 Å), depending on whether the bond is in the faulted or the unfaulted side of the unit cell respectively. We find $R_{34}(T_4) = 2.25$ Å.

3.5.3 The Dimer Distance

In addition to the adatom structures the dimer distances are also important. Tong¹⁵ finds a dimer distance of 2.45 Å using dynamical LEED. Khor and Das Sarma¹⁴ using an empirical potential and Robinson¹⁶ using X-ray diffraction find

the dimer distance to be 2.49Å. We find a dimer distance of 2.46Å if the dimer is not adjacent to a cell corner, and 2.50Å if it is next to a cell corner. The equilibrium bond distance in silicon is 2.35Å, showing that the dimer is in tension.

3.5.4 Relative Energy of $(2n + 1) \times (2n + 1)$ DAS Structures

Optimizing the structures of each of the (3×3), (5×5), (7×7), and (9×9) DAS models of the Si (111) reconstruction, we find that the (5×5) structure has the lowest energy, with (7×7) slightly higher in energy. We find that the strain energies decreases as the size of the DAS unit cell increases (Table 10). Although the 5×5 unit cell has a higher tensile stress than the 7×7 reconstruction, the lower density of 0.0244 dangling bonds/Å² compared to 0.0263 dangling bonds/Å² for the 7×7 reconstruction accounts for part of the stability of the 5×5 cell over the 7×7 cell. The surface energy 0.8995 kcal/molÅ² due to the dangling bonds for the 5×5 unit cell is 0.0694 kcal/molÅ² less than the surface energy of 0.9689 kcal/molÅ² due to dangling bonds for the 7×7 surface. Here we assign an energy per dangling bond equal to half the energy required to break a bond in bulk silicon (73.7/2 kcal/mol). On the other hand, assigning an energy per dangling bond equal to half the average energy required to break all the bonds in the silicon lattice (54.3/2 kcal/mol) gives a surface energy difference due to the dangling bonds of 0.0511 kcal/molÅ². The 5×5 reconstruction is still slightly lower than the 7×7 by 0.0055 kcal/molÅ². We assign an energy of 73.7/2 kcal/mol per dangling bond. Although the 3×3 DAS structure has the lowest dangling bond density (0.0226/Å²) of the DAS structures, it leads to stresses too large for stability. Several investigators have reported finding the 5×5 DAS structure to be slightly more stable than the 7×7 DAS structure. Table 10 shows the relative energies of the $(2n + 1) \times (2n + 1)$ structures from our results, and those of Khor et al. and Vanderbilt. It is unclear which structure is the lowest energy structure since both are experimentally observed on the same samples and the calculated energy difference is so small that the difference may be within the error of the calculation.

4.0 Discussion

Because the MSXX force field differentiates between three coordinated and four coordinated silicon atoms, it can model both the geometric and elastic proper-

ties of the bulk as well as the energetics of surface atoms with large angle strains. This makes MSXX appropriate for the modeling of the silicon (111) surface because local adatom strains and the strain of the surface unit cell on the bulk both contribute to the energetic stability. Earlier force fields^{34–36} are successful in particular areas, for example in the reconstruction of the (100) surface, modeling the bulk elastic properties, and melting. However, they are inappropriate for the reconstruction of the (111) surface. The empirical potential used by Khor and Das Sarma¹⁴ successfully describes the DAS structures. The MSXX potential has the advantage that it is partitioned into physically significant valence energy terms. Additionally, being derived from theoretical and experimental studies of small clusters, we can get a quantitative test of the concepts. Although the energy difference between the 5×5 and 7×7 DAS surfaces is too close to resolve with our current level of theory, the stability with respect to other $(2n+1)\times(2n+1)$ structures and the unreconstructed surface is successfully demonstrated.

The geometric description given by the MSXX FF is in excellent agreement with the available experimental data on the 7×7 surface. This is evident in the agreement between this study and experiment for $R_{13}(T_4)$, the dimer length, and the overall strain in the system.

5.0 Conclusion

Using the Biased Hessian method, we developed the MSXX FF for silicon and use it to analyze the energetics and structures for the DAS $(2n+1)\times(2n+1)$ reconstructions of the Si (111) surface. For $n = 1$ to 4, we find that the tensile stress increases as the unit cell size decreases. We find the 3×3 and 9×9 structures to be stable relative to the relaxed perfect (111) surface but much less stable than 7×7 surface. We find the 5×5 and 7×7 surfaces to be nearly equal in energy (in agreement with some agreement with some previous findings) with the 5×5 surface slightly more stable.

For the 7×7 surface we find dimer distances of 2.50\AA and 2.46\AA for dimers adjacent to cell corners and dimers between small eight atom ringed holes respectively, in agreement with X-ray diffraction studies. We find $R_{13}(T_4) = 2.52\text{\AA}$ (for the distance between the adatom and the eclipsed atom in the T_4) for the faulted subcell center, 2.54\AA for the site unfaulted subcell center, 2.53\AA in the faulted sub-

cell corner, and 2.56Å in the unfaulted subcell corner. These distances compare well with RHEED and LEED data.

This MSXX FF is appropriate for calculating structures containing a stacking fault since it describes the energy difference between the sphalerite and wurtzite forms of silicon.

The elastic constants, and phonon dispersion curves are accurately calculated by the MSXX FF including the TA mode flattening. Of most importance is the ability of this potential to describe the energetics, geometry and vibrations of surface silicon atoms in both T_4 and H_3 sites.

7.0 References

*To whom correspondence should be addressed.

1. R. E. Schlier and H. E. Farnsworth, *J. Chem. Phys.* **30**, 917 (1959).
2. W. A. Harrison, *Surf. Sci.* **55**, 1 (1976).
3. F. J. Himpsel, *Phys. Rev. B* **27**, 7782 (1983).
4. E. G. McRae, *Surface Sci.* **147**, 663 (1984).
5. R. J. Hamers, R. M. Tromp, and J. E. Demuth, *Phys. Rev. Lett.* **56**, 1972 (1986).
6. D. J. Chadi, R. S. Bauer, R. H. Williams, G. V. Hansson, R. Z. Bachrach, J. C. Mikkelsen Jr., F. Houzay, G. M. Guichar, R. Pinchaux, and Y. Pétroff, *Phys. Rev. Lett.* **44**, 799 (1980).
7. K. Takayanagi, Y. Tanishiro, M. Takahashi, and S. Takahashi, *J. Vac. Sci. Technol. A* **3**, 1502 (1985).
8. K. Takayanagi, Y. Tanishiro, S. Takahashi, and M. Takahashi, *Surf. Sci.* **164**, 367 (1986).
9. E. G. McRae, *Phys. Rev. B* **28**, 2305 (1983).
10. P. A. Bennett, L. C. Feldman, Y. Kuk, E. G. McRae, and J. E. Rowe, *Phys. Rev. B* **28**, 3656 (1983).
11. G. Binnig, H. Rohrer, Ch. Gerber, and E. Weibel, *Phys. Rev. Lett.* **50**, 120 (1983).
12. R. M. Tromp, and E. J. Van Loenen, *Surface Sci.* **155**, 441 (1985).
13. G. X. Qian and D.J. Chadi, *Phys. Rev. B* **35**, 1288 (1987).
14. K. E. Khor and S. Das Sarma, *Phys. Rev. B* **40**, 1319 (1989).
15. H. Huang, S. Y. Tong, W. E. Packard, and M. B. Webb, *Phys. Lett. A* **130**, 166 (1988).
16. I. K. Robinson, *J. Vac. Sci. Technol. A* **6**, 1966 (1988).
17. A. Ichimiya, *Surface Sci.* **192**, L893 (1987).
18. C. H. Patterson and R. P. Messmer, *Chem. Phys. Lett.* **192**, 277 (1992).
19. M. H. McAdon and W. A. Goddard III, *Phys. Rev. Lett.* **55**, 2563 (1985); M. H. McAdon and W. A. Goddard III, *J. Phys. Chem.* **91**, 2607 (1987).
20. H.-X. Wang and R. P. Messmer, *Phys. Rev. B*, **41**, 9241 (1990).
21. D. Vanderbilt, *Phys. Rev. B* **36**, 6209 (1987).

22. D. Vanderbilt, Phys. Rev. Lett. **59**, 1456 (1987).
23. P. Badziag and W. S. Verwoerd, Phys. Rev. B **40**, 1023 (1989).
24. G. X. Qian and D.J, Chadi, J. Vac. Sci. Technol. **16**, 1290 (1979).
25. R.I.G. Uhrberg, E. Landemark, and L. S. O. Johansson, Phys. Rev. B **39**, 13525 (1989).
26. S. Dasgupta and W. A. Goddard III, J. Chem. Phys. **90**, 7207 (1989).
27. T. Yamasaki, S. Dasgupta, and W. A. Goddard, III, J. Chem. Phys., submitted.
28. Gaussian86: M. J. Frisch, J. S. Binkley, H. B. Schlegel, K. Raghavachari, C. F. Melius, R. L. Martin, J. J. P. Stewart, F. W. Bobrowicz, C. M. Rohlfing, L. R. Kahn, D. J. Defrees, R. Seeger, R. A. Whiteside, D. J. Fox, E. M. Fleuder, and J. A. Pople, Carnegie-Mellon Quantum Chemistry publishing Unit, Pittsburgh, PA, 1984.
29. A. Zur, Ph.D. Thesis, California Institute of Technology (198).
30. H. L. McMurry, A. W. Solbrig Jr., J. K. Boyter and C. Noble, J. Phys. Chem. Solids **28**, 2359 (1967).
31. R. Tubino, L. Piseri, and G. Zerbi, J. Chem. Phys. **56**, 1022 (1971).
32. M. T. Yin and M. L. Cohen, Phys. Rev B **26**, 5668 (1982).
33. Polygraf is from Molecular Simulations Inc., Burlington, Massachusetts.
34. F. H. Stillinger and T. A. Weber, Phys. Rev. B **31**, 5262 (1985).
35. B. W. Dodson Phys. Rev. B **35**, 2795 (1987).
36. J. Tersoff, Phys. Rev. Lett. **56**, 632 (1986).

Table 1. Force constants for bulk silicon.

		MSXX
van der Waals	D_v	0.310
	R_v	4.270
Bond Stretch [eq (5)]	R_b	2.381
	k_b	193.0936
	D_b	(73.70)
Angle Bend [eq (6)]	k_θ	31.2682
	θ_a	105.0467
Angle Cross Terms [eq (8)]	$k_{Si_3\theta}$	-14.8184
	k_{rr}	3.6001
Torsion [eq (7)]	V_3	0.5100
2-C A-A [eqs (9) and (11)]	$F_{Si_3:Si_3Si_3:Si_3}$	-25.7242

Table 2a. Elastic constants (in GPa) and the bulk modulus (B) of silicon from the MSXX FF compared with experiment.

Parameter	MSXX	Experiment
C_{11}	170.7	167.5
C_{12}	64.2	65.0
C_{44}	78.6	80.1
B	99.1	99.2

Table 2b. Phonon frequencies (in THz) of silicon from the MSXX FF and experiment.

Phonon	MSXX	Experiment
LA-LO(X_1)	12.38	12.44
TA(X_3)	4.51	4.51
TO(X_4)	13.92	13.90
TO-LO(Γ_{25})	15.56	15.53

Table 3. Vibrational frequencies of SiH_4 .

Modes	Expt.	MSXX	HF	Scale
SiH_3 d-deform.	914	914	1017.1	0.899
SiH_3 d-deform.	975	975	1053.4	0.926
SiH s-str.	2187	2187	2370.0	0.923
SiH d-str.	2191	2191	2360.6	0.928
$ \Delta\nu _{rms}$		0	140.3	

Table 4. SiH_4 FF.

		MSXX	HF	Scale
Bond Stretch [eq (5)]				
Si-H	R_b	1.479	1.478	1.000
	k_b	400.0273	459.1177	0.871
	D_b	(92.60)	(92.60)	1.000
Angle Bend [eq (6)]				
H-Si-H	k_θ	67.5345	79.8951	0.845
	θ_a	110.9769	112.2213	0.989
Angle Cross Terms [eq (9)]				
H-Si-H	$k_{H\theta}$	-10.2182	-11.1244	0.919
	k_{rr}	4.021	6.030	0.667
One-Center Angle-Angle Cross Terms [eqs (9) and (10)]				
$G_{SiH:HH}$		5.3177	7.3658	0.722

Table 5. Si_2H_6 FF.

		MSXX	HF	Scale
Bond Stretch [eq (5)]				
Si-H	R_b	1.4782	1.4781	1.000
	k_b	393.9586	455.8698	0.864
	D_b	(92.60)	(92.60)	1.000
Si-Si	R_b	2.3366	2.3517	0.994
	k_b	286.9195	342.3163	0.838
	D_b	(73.70)	(73.70)	1.000
Angle Bend [eq (6)]				
H-Si-H	k_θ	57.3767	69.2450	0.829
	θ_a	111.9874	112.6561	0.994
Si-Si-H	k_θ	43.3213	53.2658	0.813
	θ_a	114.6627	116.1750	0.987
Torsion [eq (7)]				
H-Si-Si-H	V_3	0.848	1.3542	0.626
Angle Cross Terms [eq (9)]				
H-Si-H	$k_{H\theta}$	-3.5257	-3.6203	0.974
	k_{rr}	3.2252	4.8795	0.661
Si-Si-H	$k_{Si\theta}$	19.8201	26.7122	0.742
	$k_{H\theta}$	-3.7978	-4.6882	0.810
	k_{SiH}	1.3292	1.5511	0.857
One-Center Angle-Angle Cross Terms [eqs (9) and (10)]				
$G_{SiH:HH}$		-0.6003	-0.6424	0.934
$G_{SiSi:HH}$		-0.1914	-0.2321	0.825
$G_{SiH:SiH}$		0.3563	0.4043	0.881
Two-Center Angle-Angle Cross Terms [eqs (9) and (11)]				
$F_{H:SiSi:H}$		-16.4782	-19.9482	0.826

Table 6. Vibrational frequencies of Si_2H_6 .

Modes	Expt.	MSXX	HF	Scale
Torsion	125	127	134.3	0.931
SiH ₃ -rock	379	378	416.6	0.910
Si-Si stretch	432	431	464.0	0.936
SiH ₃ -rock	628	625	697.1	0.897
SiH ₃ s-deform.	844	854	947.9	0.890
SiH ₃ d-deform.	941	946	1031.5	0.881
SiH ₃ s-deform.	920	925	1043.1	0.891
SiH ₃ d-deform.	940	931	1027.5	0.914
SiH ₃ d-str.	2155.00	2166	2337.1	0.880
SiH ₃ s-str.	2154.30	2158	2352.7	0.915
SiH ₃ d-str.	2178.60	2166	2337.3	0.922
SiH ₃ s-str.	2163.00	2161	2346.7	0.928
$ \Delta\nu _{avg}$		6.66		

Table 7. SiH_3 FF.

		MSXX	HF	Scale
Bond Stretch [eq (5)]				
Si-H	R_b	1.4830	1.4830	1.000
	k_b	323.6191	443.7879	0.729
	D_b	(92.60)	(92.60)	1.000
Angle Bend [eq (6)]				
H-Si-H	k_θ	50.9033	52.9548	0.961
	θ_a	110.5997	110.5997	1.000
Angle Cross Terms [eq (9)]				
H-Si-H	$k_{H\theta}$	-13.1042	-15.2668	0.858
	k_{rr}	-0.1102	4.0105	-0.027
One-Center Angle-Angle Cross Terms [eqs (9) and (10)]				
$G_{SiH:HH}$		-9.7116	-12.6668	0.767
Inversion [eq (8)]				
$F_{Si:HHH}$		65.9534	61.5300	1.072

Table 8. Vibrational frequencies frequencies of SiH₃.

Modes	Expt.	MSXX	HF	Scale
SiH ₃ deform.	926	926	871.2	1.063
SiH ₃ deform.	996	996	1016.5	0.9800
SiH str.	1955	1955	2342.4	0.836
SiH str.	1999	1999	2361.0	0.847
$ \Delta\nu _{rms}$		0	266.6	

Table 9a. Si_4H_9 FF.

		MSXX	HF
Bond Stretch [eq (5)]			
Si_2-Si_3	R_b	2.395	2.395
	k_b	215.845	257.5712
	D_b	(73.70)	(73.70)
Si_3-H_i	R_b	1.483	1.483
	k_b	382.387	442.578
	D_b	(92.60)	(92.60)
Si_3-H_o	R_b	1.485	1.484
	k_b	381.585	441.650
	D_b	(92.60)	(92.60)
Angle Bend [eq (6)]			
$H_i-Si_3-H_o$	k_θ	58.256	70.273
	θ_a	110.953	110.953
$H_o-Si_3-H_o$	k_θ	54.843	66.156
	θ_a	111.562	111.562
$Si_2-Si_3-H_i$	k_θ	55.267	67.979
	θ_a	116.838	116.838
$Si_2-Si_3-H_o$	k_θ	49.711	61.146
	θ_a	112.207	112.207
$Si_3-Si_2-Si_3$	k_θ	50.8023	62.488
	θ_a	122.671	124.2864
Torsion [eq (7)]			
$Si_3-Si_2-Si_3-H_i$	V_3	1.020	1.630
$Si_3-Si_2-Si_3-H_o$	V_3	2.126	3.396
Inversion [eq (8)]			
$Si_2:Si_3-Si_3-Si_3$	K_ψ	1.500	0.9700
	ψ_e	81.0000	38.5060
			-

Table 9b. Si_4H_9 FF continued.

		MSXX	HF
Angle Cross Terms [eq (9)]			
$Si_i-Si_3-H_o$	$k_{H_o\theta}$	-2.602	-2.672
	$k_{H_i\theta}$	-2.787	-2.862
	$k_{H_iH_o}$	3.457	5.230
$Si_o-Si_3-H_o$	$k_{H_o\theta}$	-1.899	-1.950
	k_{rr}	3.339	5.052
$Si_2-Si_3-H_o$	$k_{Si_2\theta}$	10.730	14.461
	$k_{H_o\theta}$	-1.914	-2.363
	$k_{Si_2H_o}$	1.958	2.285
$Si_2-Si_3-H_i$	$k_{Si_2\theta}$	0.821	1.106
	$k_{H_i\theta}$	-3.662	-4.522
	$k_{Si_3H_i}$	5.120	5.974
$Si_3-Si_2-Si_3$	$k_{Si_3\theta}$	5.637	7.598
	k_{rr}	0.908	1.060
One-Center Angle-Angle Cross Terms [eqs (9) and (10)]			
$G_{Si_2Si_3:Si_3Si_3}$		0.7610	0.992
$G_{Si_3Si_2:H_iH_o}$		6.388	7.251
$G_{Si_3Si_2:H_oH_o}$		2.645	3.002
$G_{Si_3H_i:H_oH_o}$		-0.756	-0.810
$G_{Si_3H_o:H_iH_o}$		-0.783	-0.838
$G_{Si_3H_o:Si_2H_i}$		-2.476	-3.001
$G_{Si_3H_o:Si_2H_o}$		-2.031	-2.461
$G_{Si_3H_i:Si_2H_o}$		-2.771	-3.001
Two-Center Angle-Angle Cross Terms [eqs (9) and (11)]			
$F_{Si_3:Si_2Si_3:H_i}$		-30.891	-37.398
$F_{Si_3:Si_2Si_3:H_o}$		-16.495	-19.970

Table 10. Relative energies (kcal/mol) of the $(2n+1) \times (2n+1)$ DAS structures and the relaxed (111) surface from this work, Khor and Das Sarma,¹⁴ Vanderbilt²⁴ and Chadi.¹³

Structure	This work	Khor	Chadi
DAS 3×3	-0.310	-0.326	-
DAS 5×5	-0.341	-0.344	-0.395
DAS 7×7	-0.333	-0.335	-0.403
DAS 9×9	-0.328	-0.325	-

Table 11. Additional Surface Force Constants.

Angle Bend [eq (6)]		
Si ₂ -Si ₃ -Si ₃	k_θ	11.0000
Si ₂ -Si ₃ -Si ₂	k_θ	11.0000
	θ_a	109.4712
Angle Cross Terms [eq (8)]		
Si ₂ -Si ₃ -Si ₃	$k_{Si_3\theta}$	-17.0000
Si ₂ -Si ₃ -Si ₂	$k_{Si_3\theta}$	-17.0000
	k_{rr}	0.0000
Torsion [eq (7)]		
Si ₃ -Si ₂ -Si ₃ -Si ₃	V_3	0.5100
Si ₂ -Si ₃ -Si ₃ -Si ₃	V_3	0.5100
Two-Center Angle-Angle Cross Terms [eqs (9) and (11)]		
$F_{Si_3:Si_2Si_3:Si_3}$		-24.3179
$F_{Si_2:Si_3Si_3:Si_3}$		-24.3179

Figure Captions

Figure 1. Top view of the optimized 7×7 DAS model. Blue shaded atoms denote silicon atoms in the corner of the unit cell with a dangling bond. Yellow shaded atoms are surface silicons in H_3 sites and with a dangling bond. Silicon adatoms in T_4 sites have a dangling bond and are shaded red. All other atoms are Si, shaded orange and have four bonds.

Figure 2. The Si_4H_9 cluster.

Figure 3. The Si_5H_7 cluster.

Figure 4. The ab initio and force field energies plotted versus the central Si atom position for Si_4H_9 .

Figure 5. Phonon dispersion curve for Si.

Figure 6. The ab initio and force field energies plotted versus the cap Si atom position for Si_5H_7 .

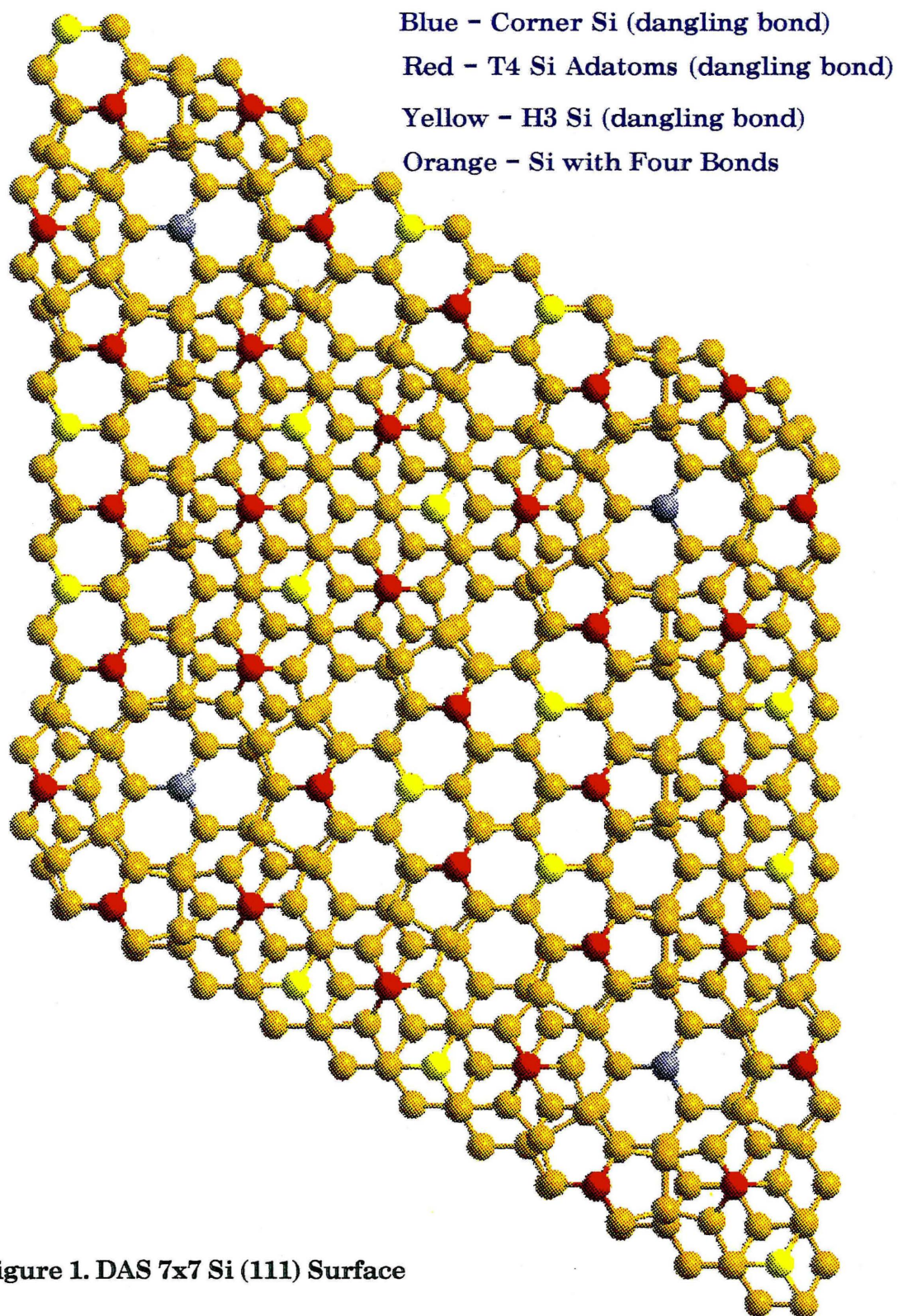


Figure 1. DAS 7x7 Si (111) Surface

Figure 2

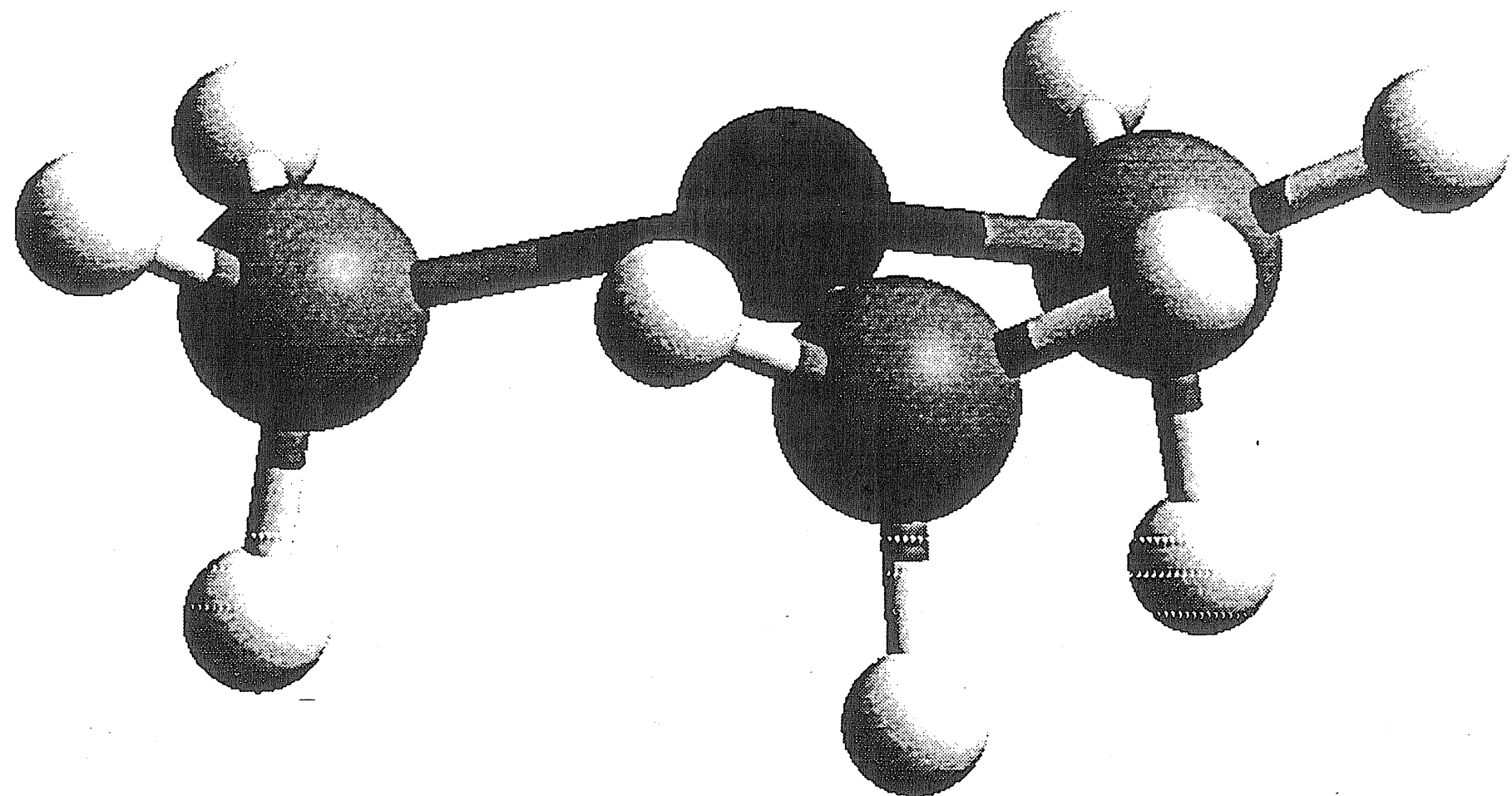


Figure 3

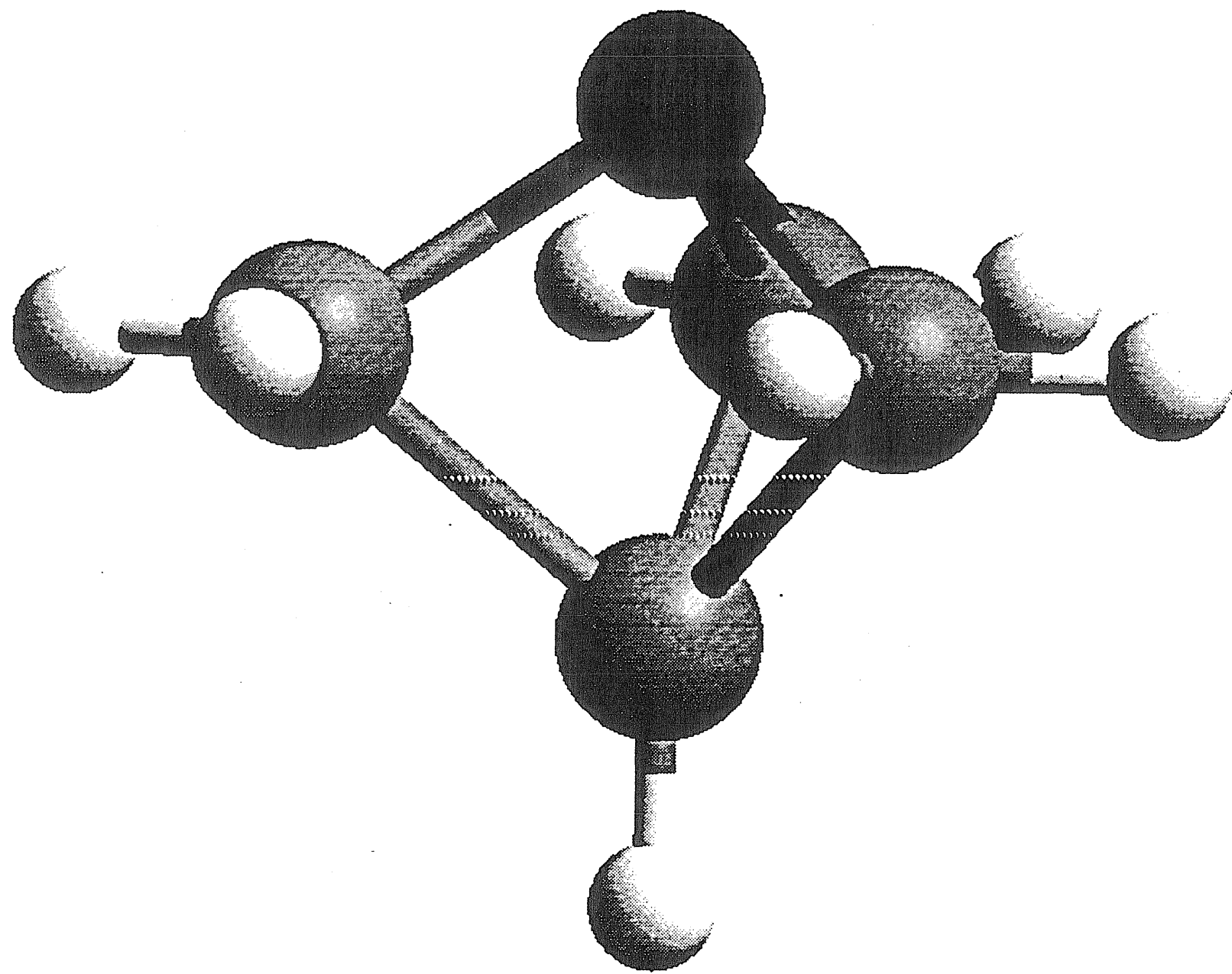


Figure 4 Si4h9 Energy vs. R

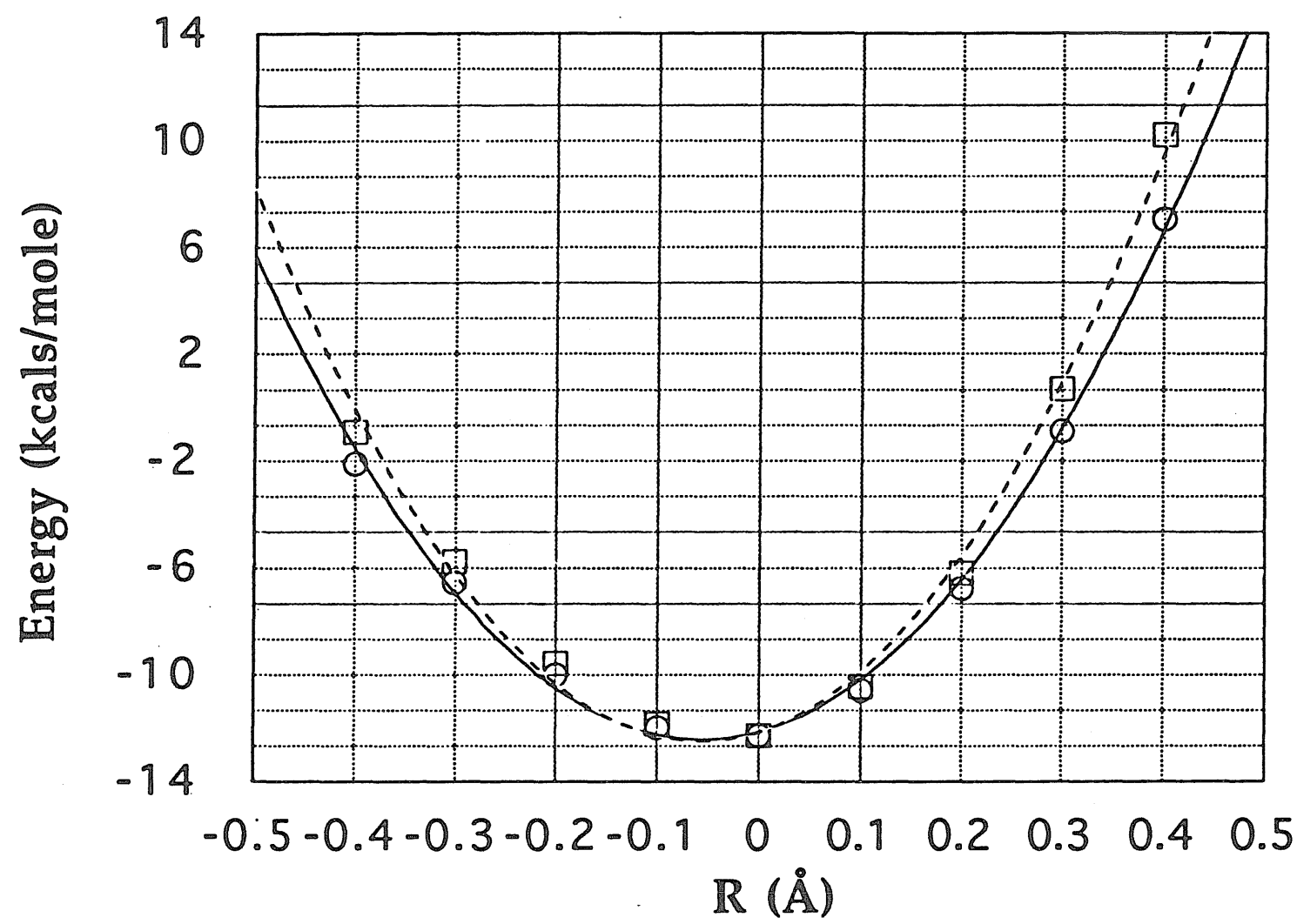


Figure 5. Phonon Dispersion Curve for Si

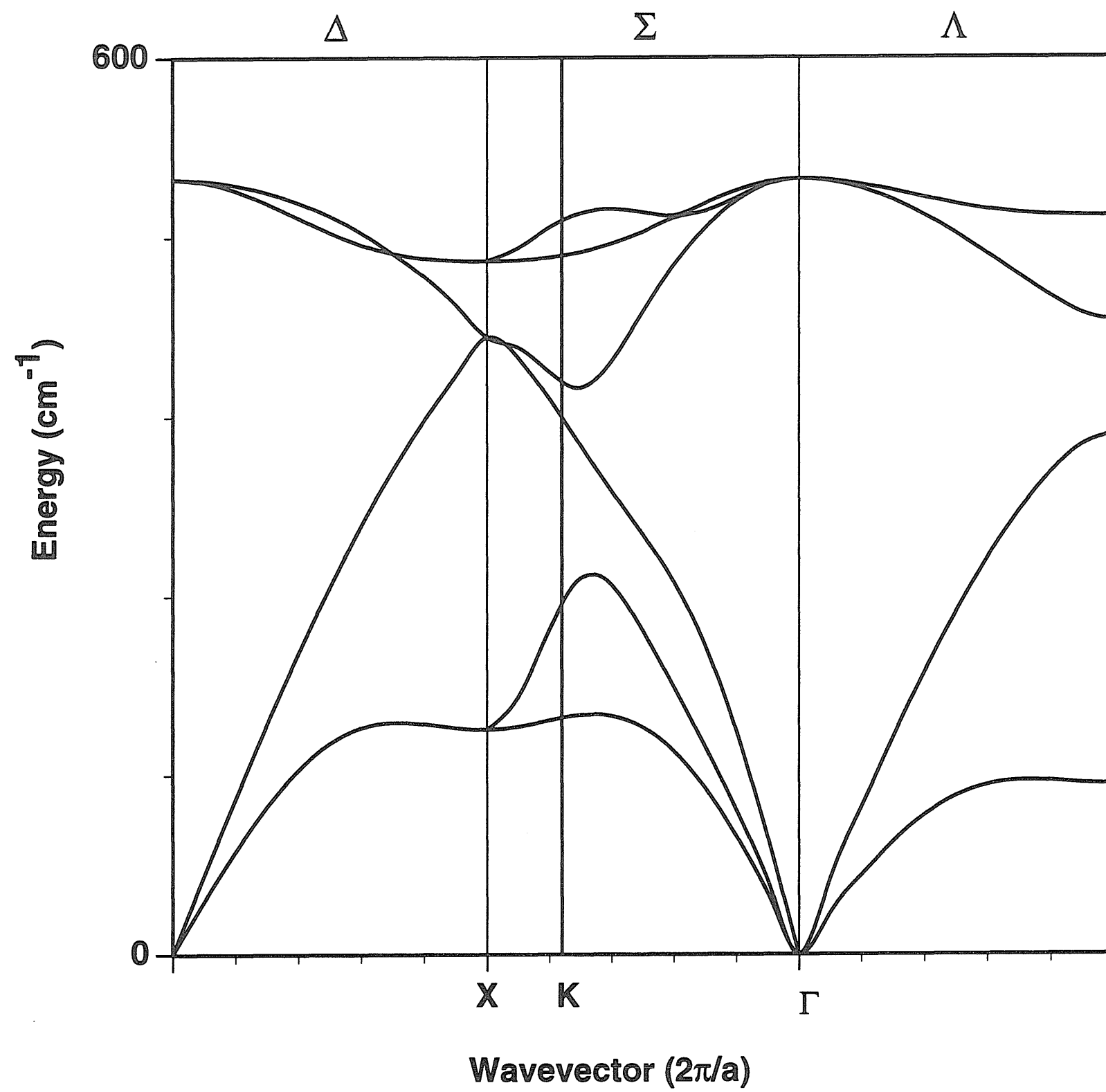
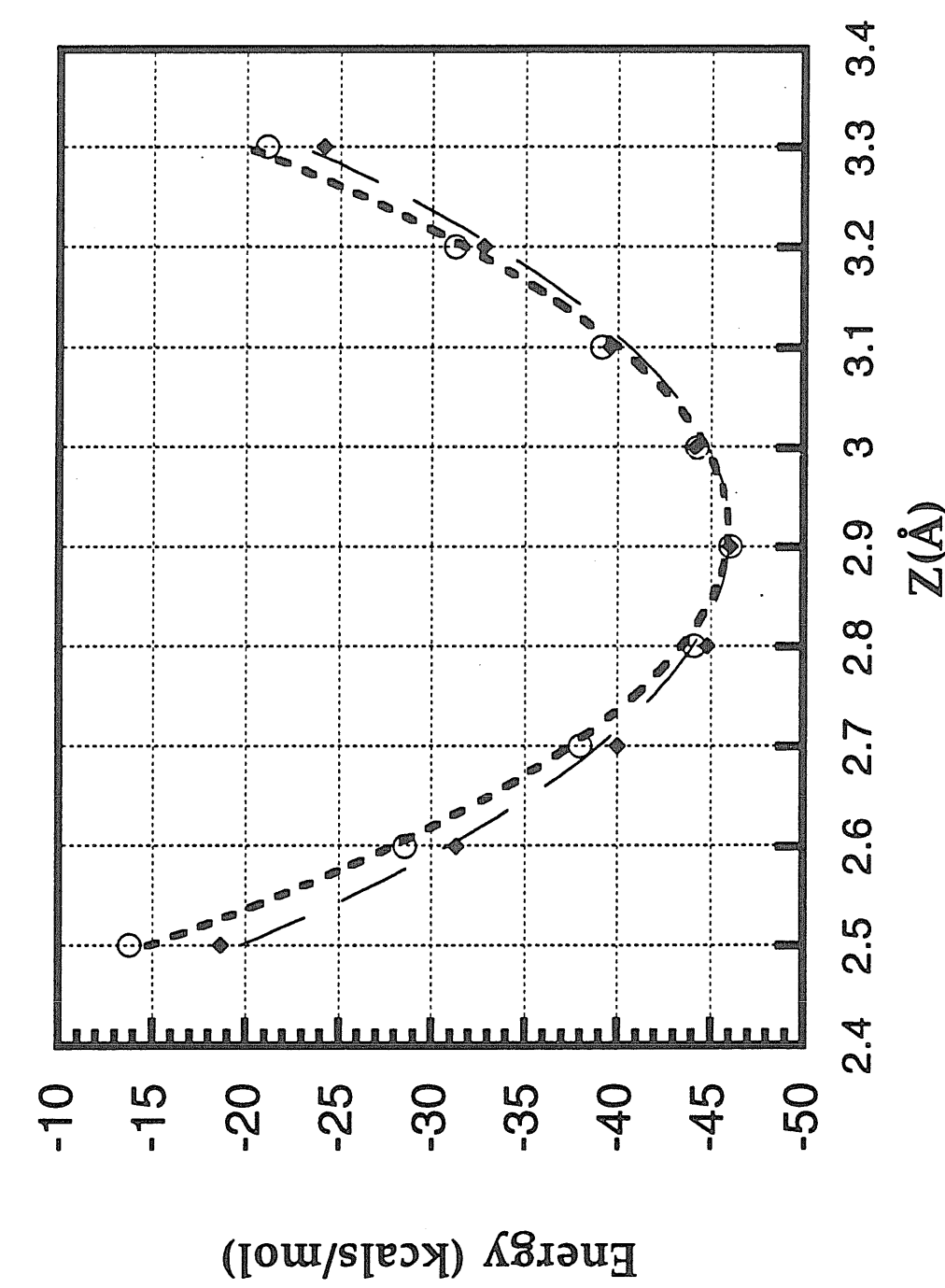


Figure 6. Si_5H_7 Energy vs Z



Chapter 7

The Generalized London Force Field for Hydrocarbon Reactions

Abstract

In this chapter we use the Generalized London Force Field (GLFF) method to derive the potential energy surface (PES) for the exchange reaction: $CH_4 + H \rightarrow CH_3 + H_2$. The GLFF includes the effect of the Pauli Exclusion Principle on the PES of chemical reactions. We find excellent agreement with the PES from *ab initio* quantum chemical reactions (GVB*SD CI).

1.0 Introduction

In chapters 2 and 3 we described the calculation of transition barriers for reactions of diamond surfaces (for CVD growth and nanotechnology). The calculation of the potential energy surface for these reactions to determine the transition state geometry and the activation barrier required a large quantity of CPU time on a Cray supercomputer. This chapter describes a method for calculating the same PES, but at a very small fraction of the computer cost.

Chemical reactions such as



generally lead to a reaction barrier [~ 9.6 kcal/mol for (1)] much less than the bond energy [10% for (1)]. There are clearly subtle interplays of bonding and antibonding factors where the bond is never really broken, but rather as one bond is dissociating the other is forming. Thus the transition state is a resonance between the reactant and product states. The transition state barrier is a direct consequence of the Pauli principle which allows only two electrons per orbital. As the third electron (of the H) approaches the D_2 , it must remain orthogonal to the bond pair on the D_2 (to satisfy Pauli), leading to antibonding character and hence a barrier. Such reaction barriers are adequately described with the modern methods of quantum chemistry, however they generally require intensive calculations, especially if quantitative accuracy is required. Furthermore, the generation of a PES is even more intensive since to generate the surface the wave function must be calculated at a grid of geometries along the reaction path.

In contrast, the FF for a Molecular Dynamics (MD) study would use a bonding interaction (say a Morse function) between each particle. This incorrectly predicts that the H_3 molecule is stable, with a triangular geometry and a bond energy of ~ 100 kcal/mol rather than a barrier of 10 kcal/mol and a linear transition state. This property prevents the simulation of reaction dynamics since the description of the reaction surface is poorly described. For a proper description of the reaction surface, *must include the effects of the Pauli principle*, which are rarely incorporated into MM potentials.

Of course quantum chemistry calculations automatically include the Pauli Principle. However

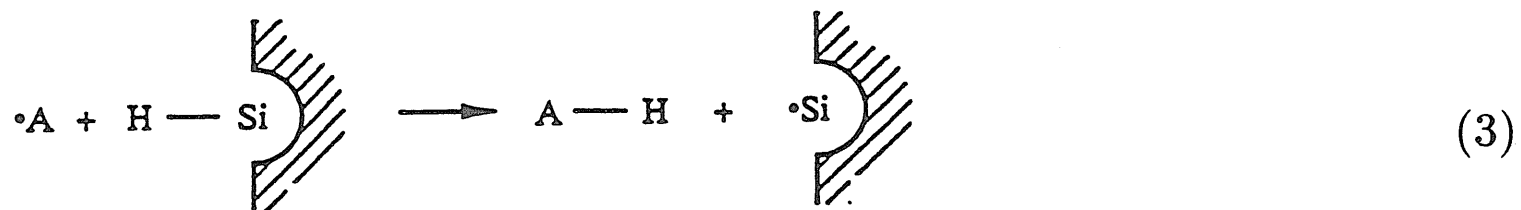
- i. the quantum chemistry (QC) requires a great deal of work for each geometry and we would like a way to fit the QC with a general potential function
- ii. the size of the QC calculation grows rapidly with the size of the system, making it impractical for many cases of interest and we would like to have a way of predicting the interaction energies in the absence of QC.

We have developed a general procedure,¹⁻³ the Generalized London Force Field (GLFF), for accomplishing both objectives. This methodology allows a general procedure for all reactions and permits development of routines for using this procedure with commercial molecular simulation codes such as POLYGRAF.⁴

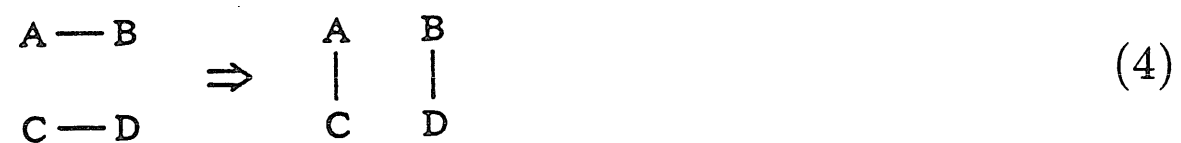
The GLFF methodology is straightforward for any simple (three-electron) radical reaction, e.g.



including surface reactions such as



The same formalism can also be used for simple four electron reactions, such as metathesis



and insertion



(e.g. Ziegler-Natta polymerization).

2.0 The Generalized London Force Field

2.1 Spin Coupling and the London Potential

Consider the bonding in the reactant (Figure 1a), transition state (Figure 1b), and product (Figure 1c) as given in Figure 1.

The consequences of the Pauli principle can be directly expressed in terms of the spin couplings shown schematically in the middle row of Figure 1 and more explicitly in the bottom row.

For the reactant configuration of (1) the Valence Bond (VB) wave function is $\mathcal{A}\{\phi_l\phi_c\phi_r[\alpha(\alpha\beta - \beta\alpha)]\}$ where the electrons on the D_2 always have opposite spins, leading to the singlet or bonding state of D_2 . (Here ϕ_l, ϕ_c, ϕ_r refer to atomic orbitals on the left, center, and right atoms.) However the spin on the H is sometimes the same and sometimes different than the spin on the D atoms. This leads to an $H-D$ interaction that contains both antibonding (or triplet) interactions and bonding (or singlet) interactions. Analysis of the VB wave function shows that the HD interaction is 75% triplet and 25% singlet. The result of these triplet or antibonding terms is that the energy increases as H approaches D_2 .

For the transition state the VB wave function is

$$\mathcal{A}\{\phi_l\phi_c\phi_r[\alpha(\alpha\beta - \beta\alpha) - (\alpha\beta - \beta\alpha)\alpha]\} \quad (6)$$

which describes the resonance of $H-D$ $D\cdot$ with $H \cdot D-D$. Analysis of the wave function shows that the outer orbitals are always triplet coupled whereas the middle atom has interactions with the outer two atoms that are 75% singlet and 25% triplet.

Thus during the reaction the interactions between the H and central D changes from 25% singlet (reactant), to 75% singlet (transition state), to 100% singlet (product) and the other interactions change correspondingly. Thus to include the effect of the Pauli principle, the simplest description is

$$E(R_1, R_2, R_3) = \sum_{i>j} E_{ij}(R_{ij}) \quad (7)$$

where

$$E_{ij}(R_{ij}) = f_{ij}^S E_{ij}^S(R_{ij}) + f_{ij}^T E_{ij}^T(R_{ij}). \quad (8)$$

Here f^S and f^T are the fractions of singlet and triplet character and E^S and E^T describe the bonding and antibonding two-body interactions. Defining the classical and exchange energies as

$$E^{cl} = \frac{1}{2} (E^T + E^S) \quad (9)$$

$$E^x = \frac{1}{2} (E^T - E^S)$$

and the spin coupling fractions as

$$\begin{aligned} f_{ij}^S &= (\cos \frac{1}{2} \gamma_{ij})^2 \\ f_{ij}^T &= (\sin \frac{1}{2} \gamma_{ij})^2 \end{aligned} \quad (10)$$

the energy (7) can be rewritten as

$$E = \sum_{i>j} [E_{ij}^{cl}(R_{ij}) + \cos \gamma_{ij} E_{ij}^x]. \quad (11)$$

The three spin coupling angles in (11), γ_{ij} , are related to each other (by $\pm \frac{2\pi}{3}$) so that there is only one degree of freedom. Requiring that γ be optimum, $\partial E / \partial \gamma = 0$, leads to

$$\tan \gamma_{13} = \frac{\frac{\sqrt{3}}{2} (E_{23}^x - E_{12}^x)}{E_{12}^x + E_{23}^x - 2E_{13}^x}. \quad (12)$$

Since (12) depends only on the exchange energies, $E^x(R_{ij})$, which depend only on the distances, the optimum spin coupling is uniquely determined by the geometry. Thus the full effect of the Pauli principle is included by using (12) with (11), leading to

$$E_L = E_1^{cl} + E_2^{cl} + E_3^{cl} - [(E_1^x)^2 + (E_2^x)^2 + (E_3^x)^2 - E_1^x E_2^x - E_2^x E_3^x - E_2^x E_3^x - E_1^x E_3^x]^{\frac{1}{2}}. \quad (13)$$

This expression was originally derived by London.⁵⁻⁷ Table 1 shows the special cases of the energy for various γ 's.

2.2 Generalization of the London Force Field

Using the exact two body functions for the triplet and singlet states of H_2 in the London expression (1), leads to a potential surface that is qualitatively correct. Thus for H_3 it leads to a barrier of 12.4 kcal/mol rather than 9.6 kcal/mol⁸ and a saddle point geometry of 1.7922 bohr rather than 1.7757 bohr. In addition the barrier is too narrow having too low an energy for particles along the reaction path far from the transition state. Donnelly et al.^{1,2} showed that the problem at

the saddle point involves three body corrections when all three orbitals have high overlap.

By substituting the two-body VB energy expressions with $S_{ab}^2 \neq 0$ into the three-body VB energy expressions, also with $S_{ab}^2 \neq 0$, and retaining terms in overlap squared only, the first order overlap correction to (13) was found to be^{1,2}

$$\Delta_3 = -\frac{1}{2} [(S_{13}^2 + S_{23}^2)E_{12}^x + (S_{12}^2 + S_{23}^2)E_{13}^x + (S_{12}^2 + S_{13}^2)E_{23}^x]. \quad (14)$$

The problem with (11) is that it considers overlaps S_{ij} as addition to the exchange energies. This is not acceptable since we will generally not have overlaps. However S_{ij}^2 is proportional to E_{ij}^x so that S_{ij}^2 in (11) can be replaced with

$$S_{ij}^2 = \delta^\circ E_{ij}^x, \quad (15)$$

where δ° is a scaling constant. Using just this one parameter, the overestimate of the energy barrier is removed. The resulting three-body correction depends only on E^x .

For larger distances the energy for (12) is too attractive because interference between the London dispersion (vdw attraction) terms of different pairs of atoms is ignored. The dynamic correlation effects (responsible for this attraction) between atoms 1 and 2 interfere with the 1-3 and 2-3 dispersions, leading to less attraction. This dispersion correction has the form

$$\Delta_{disp} = -\delta^d \sum_{i>j} E_{ij}^d (S_{ik}^2 + S_{jk}^2) \quad (16)$$

where E_i^d is the (negative) dispersion energy of pair i , and δ^d is a constant. A good estimate of the dispersion energy is found from the difference between the exact energy (experiment or configuration interaction) and the VB or GVB energy.

The Generalized London Force Field (GLFF) has the form

$$E^{GLFF}(R_1, R_2, R_3) = \sum_{i>j} [E_{ij}^{Cl}(R_{ij}) + \cos\gamma_{ij} E_{ij}^x(R_{ij})] + \Delta_3 + \Delta_{disp} \quad (17a)$$

$$= \sum_{i>j} \left\{ [E_{ij}^{Cl}(R_{ij}) + \cos\gamma_{ij} E_{ij}^x] - \sum_{k \neq i,j} (S_{ik}^2 + S_{jk}^2) \left[\frac{1}{2} E_{ij}^x + \delta^d E_{ij}^d \right] \right\} \quad (17b)$$

$$= \sum_{i>j} \left\{ \left[E_{ij}^{Cl}(R_{ij}) + E_{ij}^x \left[\cos\gamma_{ij} - \frac{1}{2} \sum_{k \neq i,j} (S_{ik}^2 + S_{jl}^2) \right] - \delta_d E_{ij}^d \sum_{k \neq i,j} (S_{ik}^2 + S_{jl}^2) \right] \right\} \quad (17c)$$

where δ° is given by (16).

3.0 Ab Initio Calculations

To derive *ab initio* potentials (PES) that include the essential effects important in describing saddle points of chemical reactions, one must employ QC methods that accurately describe bold dissociation. Chemically accurate descriptions of the PES generally require a large computational cost. Our goal is to predict accurate reaction surfaces using a simple method practical for molecular dynamics simulations. We will illustrate the procedure for the reaction



Elsewhere¹¹ we required extensive GVB-CI calculations on (2). These studies involved Generalized Valence Bond (GVB) calculations followed by configuration interaction through single and double excitations from all GVB configurations. This is denoted as GVB*SD CI.

These studies used an extended basis set [Dunning and Huzinaga^{9,10} double-zeta contraction of the 9s5p carbon basis with one additional set of d polarization functions ($\eta^d = 0.75$). We also add diffuse s and p functions ($\eta^s = 0.0474$ and ($\eta^p = 0.0365$). The hydrogens were described using the triple-zeta contraction of the 6s set with one additional set of p polarization functions ($\eta^p = 0.60$)]. The final potential surface is shown in Figures 2.

This method has been applied to the



and

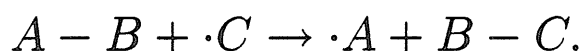


reactions using $H \cdot \cdot H$, $H \cdot \cdot \cdot CH_3$, and $CH_3 \cdot \cdot \cdot CH_3$ two-body interactions from QC. The potential surface for (20) is shown in Figure 3. The barrier from GLFF

is 10.6 kcal/mol, in excellent agreement with the 10.9 kcal/mol from extensive QC calculations on the reaction (17).

4.0 Discussion

The approach outlined above can be used for any three electron (or four electron) exchange reaction,



The first step is to obtain the singlet and triplet states for A-B and for B-C. For best results we should do QC calculations at various distances for A-B and B-C separately. With no additional data on the A-B-C system, the London Equation would predict the full potential surface in Figure 2. This leads to a barrier $\sim 25\%$ too high and transition state bond distances about 3% too long. If there were no additional information, this could be used to simulate the reactions. Better yet we might do a quantum mechanical calculation at a single point near the predicted saddle point and another single point half way to dissociation. This would determine δ^o and δ^d , allowing an accurate description of most geometries. Thus the GLFF allows a little bit of QC information to predict a great deal about the potential surface.

Alternatively with no QC data on the reacting units, we could use data, say, on the barrier height from experiment to estimate the overlap correction constant (δ^o). In addition, if there were no QC data on the A-B bond and antibond, one could get a qualitative estimate by using a Morse curve for the singlet or bond state (which requires only R_e , k_e , and D_e) and we could use an antimorse curve for the triplet or antibond state (no additional data).

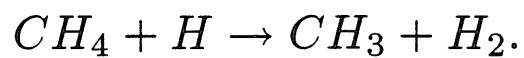
5.0 Application to Hydrocarbon Reactions

We have shown that the Generalized London Potential is effective in modeling $H_2 + H$ and $CH_3 + H$ by comparing the GLFF results to accurate *ab initio* calculations. Because quantum chemistry calculations of potentials of systems with more than several electrons are so impractical most systems have little available data. We developed the GLP with the intention that it could accurately predict the

entire potential energy surface using only two-body potentials plus a limited amount of three-body information. Our results indicate that the GLP is indeed well suited for such predictions. An accurate PES can be derived in a matter of hours or minutes, on a small computer where quantum chemical calculations have taken tens of hours of super computer CPU for PES derivation on similar systems.^{11,12} Actually, the GLP may work best to compliment *ab initio* calculations in reducing the amount of work required to find the saddle point. An expected sequence would be:

1. Calculation of two-body curves.
2. Use of London Potential to predict saddle point.
3. Use of GLP using parameters estimated from similar systems to improve estimate of saddle point.
4. *Ab initio* calculation of several energies near saddle point.
5. Incorporation of new information into GLP to improve estimates of entire potential energy surface and saddle point.
6. Possible refinement of GLP parameters using a small number of additional *ab initio* points.
7. Use of GLP for simulations.

Our overall objective is to perform accurate reaction dynamics with molecular modeling where reaction rates would be accurately modelled and mechanisms could be studied, and extracted from the dynamics trajectories. We are especially interested in applications to surface reconstructions, growth of thin films, polymer and crystalline systems. Important carbon-based examples exist for all of these cases. We first examine the case of hydrogen exchange among hydrocarbons. We first considered the abstraction of one hydrogen from methane by an atomic hydrogen:



Actually, this reaction as written is uphill in energy by several kcal/mol, however this is not true for most hydrogen abstractions from hydrocarbons by a lone hydrogen atom. Thus, we write this equation in this direction, however it is more appropriate to write it in the opposite direction for this system only. With the CH_4 bond angles fixed, we first calculate a first approximation of hydrogen abstraction from a diamond surface. Of course, an improved model would consider

abstraction from isobutane or larger clusters. Allowing the CH_4 bond angles to relax gives this reaction an extra degree of freedom not present in H_3 . This better describes smaller systems and polymers where relaxation is not constrained by the surrounding structure as in a surface reaction. For both the fixed and variable angle cases the two-body interaction potentials are required. We present them next before their use in the GLP.

5.1 Application to the $CH_4 + H \rightarrow CH_3 + H_2$ Reaction

The GLFF is expressed in terms of two body potentials. Thus for



we need to consider the



and



potentials. We carried out calculations on (18) and (19) at the same level of basis set^{9,10} and electron correlation as previously used for *ab initio* studies of (17). The details of the calculations are in section 3.0. The potential curves are shown in Figures 2 and 3. In (18) we considered three values $\theta_{HCH} = 90^\circ, 105^\circ, 120^\circ$. For consistency we used a harmonic fit to predict the choice of θ_{HCN} for each particular R_{CH} .

The constants δ° and δ^d were chosen by fitting to the saddle point and 50 % dissociated energies for the reaction.

5.2 Comparison to *ab initio* calculations

The GVB-CI calculations optimized the structure near the saddle point for reaction (17). As a first step we used the transition state geometries from these calculations to calculate the London and GLFF energies. The results are in Table 2. Here we see the LFF leads to an energy barrier too high by 2.1 kcal/mol or 15%. Using $\delta^d = 0.003$ from the H_3 studies leads to $E_{ACT} = 12.63\text{kcal/mol}$. Adjusting to match the *ab initio* surface leads to $E_{ACT} = 12.9\text{kcal/mol}$. In the remainder of this chapter we use $\delta^d = 0.003$ from H_3 .

To obtain a full potential surface, we first considered the same angle $\theta_{HCH} = 104^\circ$ for all R_{CH} and R_{HH} . This leads to the London and GLFF PES in Figures 2 and 3. We then used the spin coupling at each geometry to determine the optimum θ_{HCH} by minimizing the energy (8) with respect to the angle.

We recalculated the London and GLFF potential surfaces shown in Figures 2 and 3. Very little change occurs in the spin coupling so that additional iterations were not needed.

We conclude that GLFF gives an excellent description of the QC potential surface.

5.3 H_2 and CH_4 Potentials

When all of our information is based on *ab initio* calculations, it is best to use a consistent level of calculation for all potential surfaces. The $CH_4 + H$ calculations of Musgrave et al. on the saddle point of $CH_4 + H^2$ are not to high accuracy, however a similar level calculation is feasible on larger systems. Calculations at a similar level of accuracy were done for H_2 and CH_4 ¹ and are reported in Tables 3 and 4 for H_2 and CH_4 , respectively.

We include the tetrahedral geometries for the fixed-angle, surface-like atom case. For a lone CH_4 , the angle between the H whose bond is being stretched and the other hydrogens relaxes from tetrahedral to planar during the course of the reaction with H . For lone CH_3 , about 7 kcal/mol is required to go from planar to tetrahedral. Calculations of the snap bond energies at various angles are possible which can then be used to do the general relaxed angle case. To simplify matters here, we report the energies at 104° which is about the optimized saddle point geometry.^{3,11}

5.4 Fixed Angle $CH_4 + H$

We consider the first approximation of using CH_4 with the bond angle fixed at tetrahedral and calculate the resulting potential energy surface. We start from spline fits to the H_2 and CH_4 energies of the previous subsection. The London Potential for this system is shown in Figure 2.

The $CH_3 + H_2$ limit is taken as the zero of energy. While the bond energies of CH_4 and H_2 are only several kcal/mol apart, the additional energy to bend CH_3 to tetrahedral makes the energy difference in the channels about 9 kcal/mol.

As expected, the saddle point is closer to the higher energy H_2 channel. The corresponding spin coupling is shown in Figure 1. This shows that the “transition state” as defined by the spin coupling ($\gamma = 0$) is even further into the H_2 valley than the saddle point. The smooth variation of γ along the reaction path is again seen as for H_3 in Figure 4 and for $CH_4 + H$ in Figure 5.

The potential energy surface is improved by assuming that the parameters of the H_3 GLP are about on the order of those for $CH_4 + H$. Given the similar bond energies, this should be a reasonable approximation. The corrections from second order overlap and dispersion for H_3 lead to the new surface of Figure 3. Thus, we have estimated the entire potential energy surface for $CH_4 + H$ using only two-body curves and our knowledge of the London Equation error for H_3 . With more experience in the variation of the GLP parameters across various systems, we can hopefully establish a methodology of creating such surfaces to a reasonable accuracy with little more than two-body input.

5.5 Relaxed Angle $CH_4 + H$

In order to compare the $CH_4 + H$ results of Reference 2 with the GLP results, we need to allow the CH_4 bond angle to relax as the reaction proceeds. The singlet and triplet energies at several angles for each $CH_3 - H$ distance could be calculated in order to obtain the angular dependence. If the angle relaxed to its singlet minimum, it would be planar at far distances, near tetrahedral at the bond distance, and slightly beyond tetrahedral at shorter distances. At the saddle point distance of about 2.6 bohr, the energy of the singlet is a minimum for an angle between 106 and 107°. This is in contrast to the optimized angle of 103.8° of Reference 11. The discrepancy arose because the energy minimum with respect to angle for the triplet is much nearer planar. From the spin coupling γ_i , we know the mix of singlet and triplet character for a given pair of atoms i :

$$E_i = f_i^T E_i^T + f_i^S E_i^S.$$

This is the function to be minimized with respect to bond angle at each geometric configuration.

Even without knowledge of the CH_4 triplet and singlet energies at various angles and distances, we can still estimate the energy at the saddle point. Using

the 104° energies of CH_4 from Subsection A, the saddle point for the relaxed angle $CH_4 + H$ reaction can be found. This was done for the London Potential and the GLP with second order corrections based on the H_3 parameters. Table 5 shows that predicted GLP energy is within 0.3 kcal/mol of the *ab initio* value.

Separate H_2 and CH_4 corrections would improve the saddle point position. The information that went into this prediction includes only two-body H_2 and CH_4 potentials, an estimate of two GLP parameters from H_3 , and an estimate of the CH_4 bond angle at the saddle point. This last piece of information is also derivable independently by knowing the angular dependence of the separate singlet and triplet curves at the saddle point distance. In addition to this saddle point information, we now have an estimate of the potential energy surface over the entire range of geometries. This can be used to add reactive dynamics to molecular modeling simulations.

6.0 Conclusions

We use the Generalized London Force Field (GLFF) method to derive the potential energy surface (PES) for the exchange reaction: $CH_4 + H \rightarrow CH_3 + H_2$. We find that we are able to accurately determine the PES when including dispersion and three body interaction corrections. The GLFF includes the effect of the Pauli Exclusion Principle on the PES of chemical reactions and greatly speeds up the calculation of accurate PES over quantum chemical methods. Our results show excellent agreement with the PES from *ab initio* quantum chemical reactions (GVB*SD CI) where primarily only two-body interactions were included. To describe other PES for other reactions a set of accurate two-body potentials are required. With these potentials it is hoped that a large number of reactions could be described accurately and with vastly reduced computational effort.

References

1. R. E. Donnelly, Ph. D. Thesis, California Institute of Technology, (1992).
2. R. E. Donnelly, C. B. Musgrave, and W. A. Goddard III, to be submitted.
3. C. B. Musgrave, R. E. Donnelly, and W. A. Goddard III, to be submitted.
4. These calculations used POLYGRAF from Molecular Simulations Inc. (Burlington Mass).
5. J. C. Slater, "Quantum Theory of Molecules and Solids" Vol. 1 (McGraw-Hill Book Company, Inc., New York, 1963). Page 53 contains two "typos": add e^{-w} after $\alpha^2(1 + w - \frac{1}{3}w^2)$ on $-\alpha^2(K + S)$ line and replace $\frac{1}{3}w^2$ with $\frac{1}{3}w^3$ on αK line. Also note that Rydberg (not Hartree) energy units are used.
6. F. London, Probleme der Modernen Physik-Sommerfeld Festschrift, (S. Herzel, Leipzig, (1928).
7. Ztschr. f. Elektrochem, 35, 552 (1929).
8. Huber, K. P. and Herzberg, G., Molecular Structure IV: Constants of Diatomic Molecules, Van Nostrand Reinhold Company (New York), 1979.
9. Dunning, T. H., J. Chem. Phys., 53, 2823, (1970).
10. Huzinaga, S. J., Chem. Phys. 42, 1293, (1965).
11. C. B. Musgrave, J. K. Perry, R. C. Merkle, and W. A. Goddard III, Nanotechnology 2, 187 (1991).

Table 1. Special Cases of Energy for Various γ 's.

γ	$E_L + E_c + E_b + E_a$
0	$E_3^T + \frac{1}{4}E_2^T + \frac{3}{4}E_2^S + \frac{1}{4}E_1^T + \frac{3}{4}E_1^S$
$\frac{\pi}{3}$	$E_1^S + \frac{3}{4}E_3^T + \frac{1}{4}E_3^S + \frac{3}{4}E_2^T + \frac{1}{4}E_2^S$
$\frac{2\pi}{3}$	$E_2^T + \frac{1}{4}E_1^T + \frac{3}{4}E_1^S + \frac{1}{4}E_3^T + \frac{3}{4}E_3^S$
π	$E_3^S + \frac{3}{4}E_2^T + \frac{1}{4}E_2^S + \frac{3}{4}E_1^T + \frac{1}{4}E_1^S$
$-\frac{2\pi}{3}$	$E_1^T + \frac{1}{4}E_3^T + \frac{3}{4}E_3^S + \frac{1}{4}E_2^T + \frac{3}{4}E_2^S$
$-\frac{\pi}{3}$	$E_2^S + \frac{3}{4}E_1^T + \frac{1}{4}E_1^S + \frac{3}{4}E_3^T + \frac{1}{4}E_3^S$

Table 2. Geometries and transition barriers for $CH_4 + H \cdot \rightarrow \cdot CH_3 + H_2$ (energies in kcal/mol).

	θ_{HCH}	R_{CH}	R_{HH}	$GVB - CI$	<i>London</i>	<i>GLFF</i>
Reaction	109.47	1.09	∞			
TS	104.0	1.459	0.868	12.91	15.00	12.64
Product	90.0	∞	0.7			

Table 3. Two-Body Potentials for H_2 . Distances are in Å (note that so far we have dealt mainly in bohr), and energies are in Hartrees.

R	E^S	E^T
0.4	-0.96387083	
0.5	-1.09183076	-0.57411048
0.6	-1.14695975	-0.68374487
0.7	-1.16604573	-0.75632627
0.74	-1.16781588	
0.8	-1.16641530	-0.80860353
0.9	-1.15698075	-0.84849745
1.0	-1.14262579	-0.87990173
1.2	-1.10924298	-0.92499045
1.4	-1.07765713	
1.5	-1.06391438	-0.96391211
1.6	-1.05181371	
1.8	-1.03262628	-0.98315379
2.0	-1.01952662	-0.99000541
2.5	-1.00460386	-0.99738858
3.0	-1.00090262	-0.99930581
5.0	-0.99988367	-0.99988112
50.0	-0.99988096	-0.99988096

Table 4. Two-Body Potentials for CH_4 . Distances are in Å, and energies are in Hartrees.

R	Tetrahedral		104°	
	E^S	E^T	E^S	E^T
0.80	-40.25584723	-39.87551304	-40.25047509	-39.86470574
0.90	-40.32346617	-39.94289320	-40.31871254	-39.92518046
1.00	-40.35288348	-39.95152791	-40.34895780	-39.96925500
1.05	-40.35863390	-39.96678868	-40.35518093	-39.98352944
1.09	-40.36023885	-39.97693589	-40.35718587	-39.99279529
1.15	-40.35887945	-39.99059157	-40.35645516	-40.00497786
1.20	-40.35516185	-40.00201942	-40.35328124	-40.01514904
1.25	-40.34974849	-40.01428129	-40.34842353	-40.02631230
1.30	-40.34311129	-40.02727004	-40.34234854	-40.03843393
1.40	-40.32756398	-40.05334920	-40.32792504	-40.06325829
1.50	-40.31062243	-40.07708134	-40.31207546	-40.08607365
2.00	-40.23606332	-40.14743236	-40.24161279	-40.15436516
2.50	-40.19695719	-40.16986183	-40.20385300	-40.17646641
3.00	-40.18315200	-40.17612653	-40.19006031	-40.18274728
4.00	-40.17853794	-40.17815402	-40.18525719	-40.18483343
6.00	-40.17824863	-40.17824772	-40.18493831	-40.18493718
50.00	-40.17824051	-40.17824051	-40.18493026	-40.18493025

Table 5. Saddle Points for $CH_4 + H$. Distances are in atomic units, and saddle point energies are from H_2 channel in kcal/mol.

	R_{1sp}	R_{2sp}	E_{sp}
London	2.6095	1.7435	14.9974
GLP	2.6448	1.6998	12.6379
Reference 39	2.63	1.74	12.91

Figure Captions

Figure 1. The product, transition and reactant states of a H exchange reaction.

Figure 2. $CH_4 + H$ London Potential Contour Plot. The contour values shown are the powers of two times ± 3 kcal/mol and zero. Axes are distances in atomic units. H_2 channel is to the upper left and CH_4 channel is to the bottom right.

Figure 3. $CH_4 + H$ GLP Contour Plot. The contour values shown are the powers of two times ± 3 kcal/mol and zero. Axes are distances in atomic units. H_2 channel is to the upper left and CH_4 channel is to the bottom right.

Figure 4. Contour Plot of γ for $H_2 + H$. Contours are spaced every 10 degrees with negative contours endashed.

Figure 5. Contour Plot of γ for $CH_4 + H$. Contours are spaced every 10 degrees with negative contours endashed.

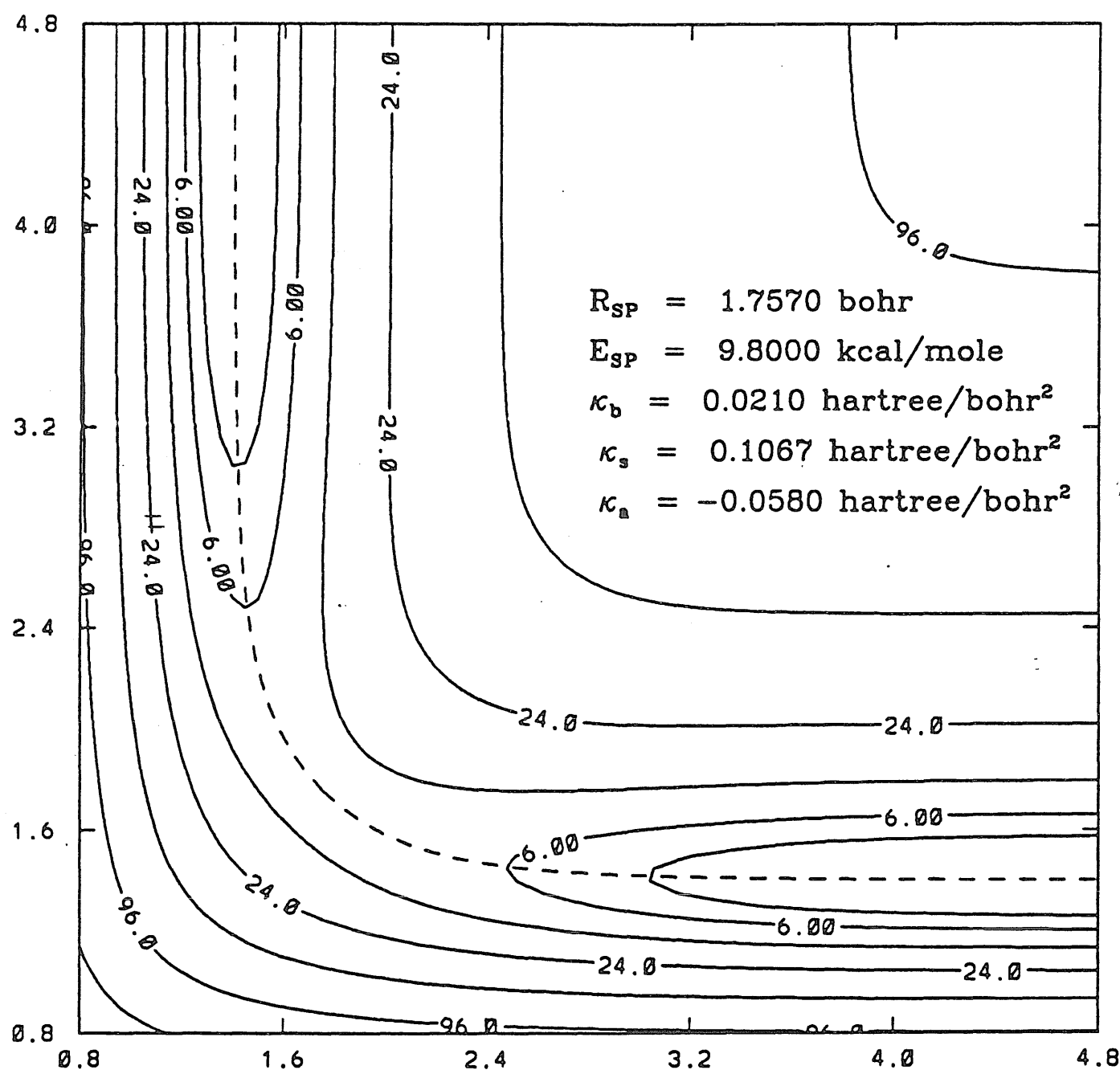


Figure 1. Truhlar and Horowitz (LSTH) Contour Diagram. Reported saddle point properties are actually those of CI calculations of Liu et al.

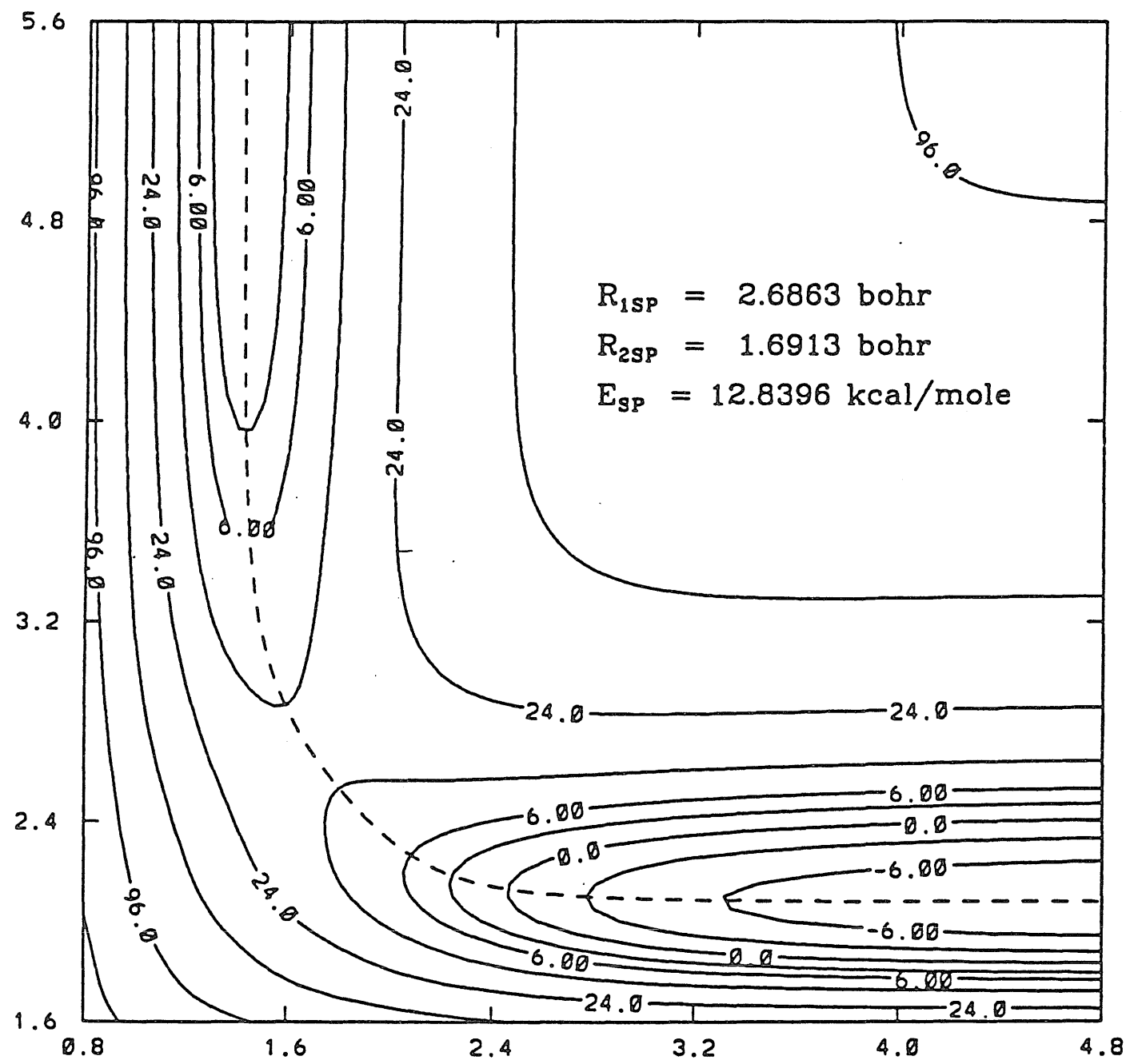


Figure 2 $CH_4 + H$ London Potential Contour Plot. The contour values shown are the powers of two times ± 3 kcal/mole and zero. Axes are distances in atomic units. H_2 channel is to the upper left and CH_4 channel is to the bottom right.

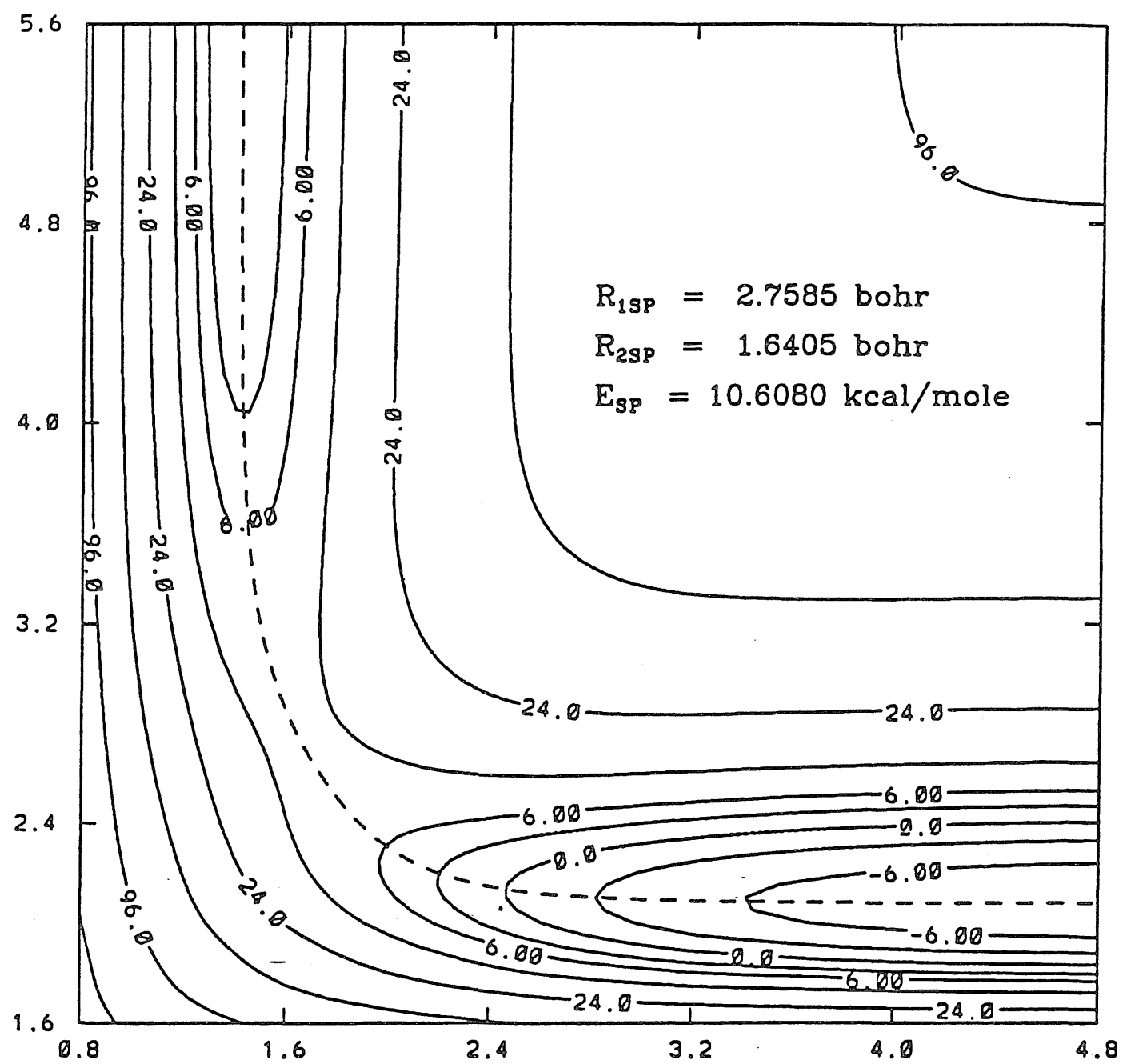


Figure 3 $CH_4 + H$ GLP Contour Plot. The contour values shown are the powers of two times ± 3 kcal/mole and zero. Axes are distances in atomic units. H_2 channel is to the upper left and CH_4 channel is to the bottom right.

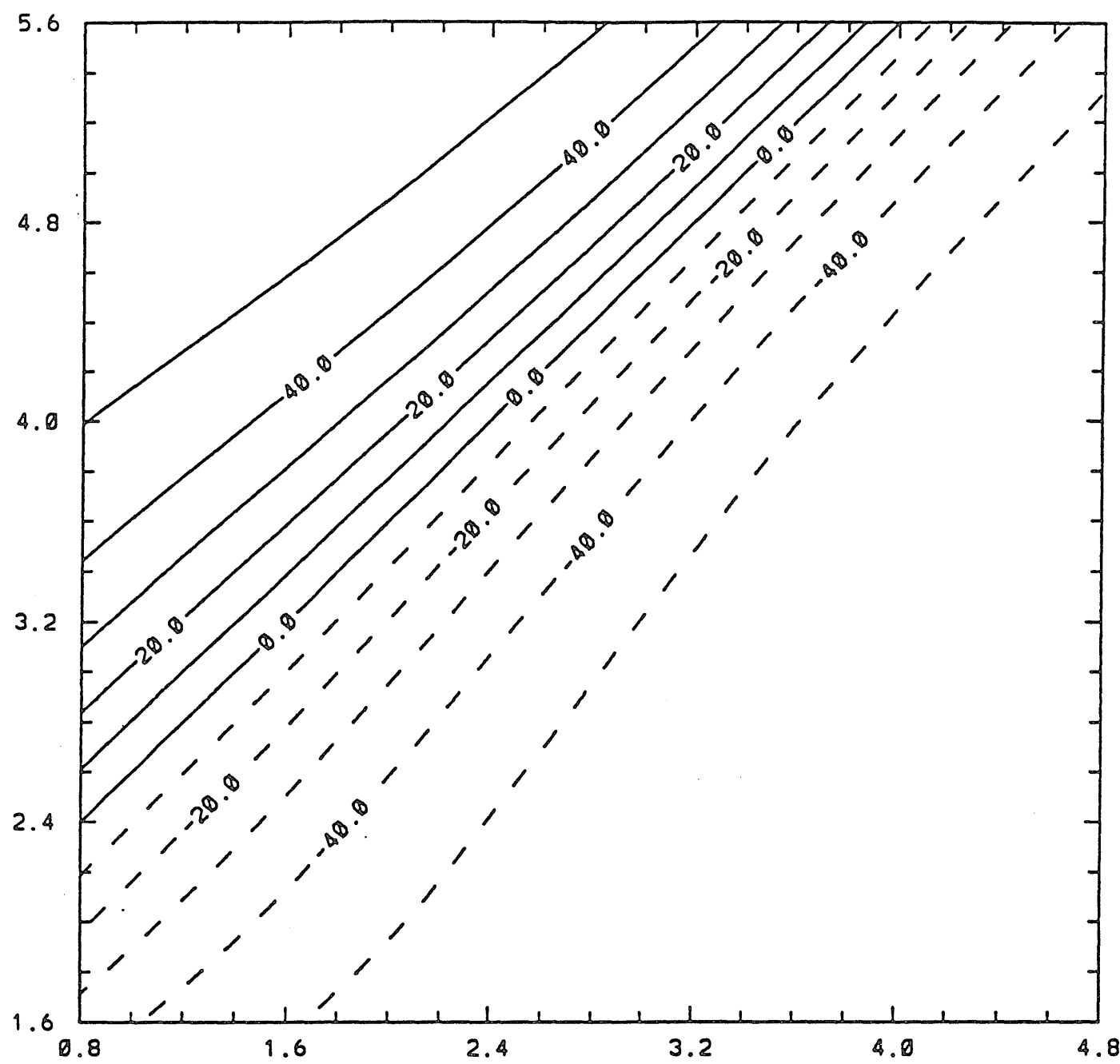


Figure 4 Contour Plot of γ for $CH_4 + H$. Contours are spaced every 10 degrees with negative contours endashed.

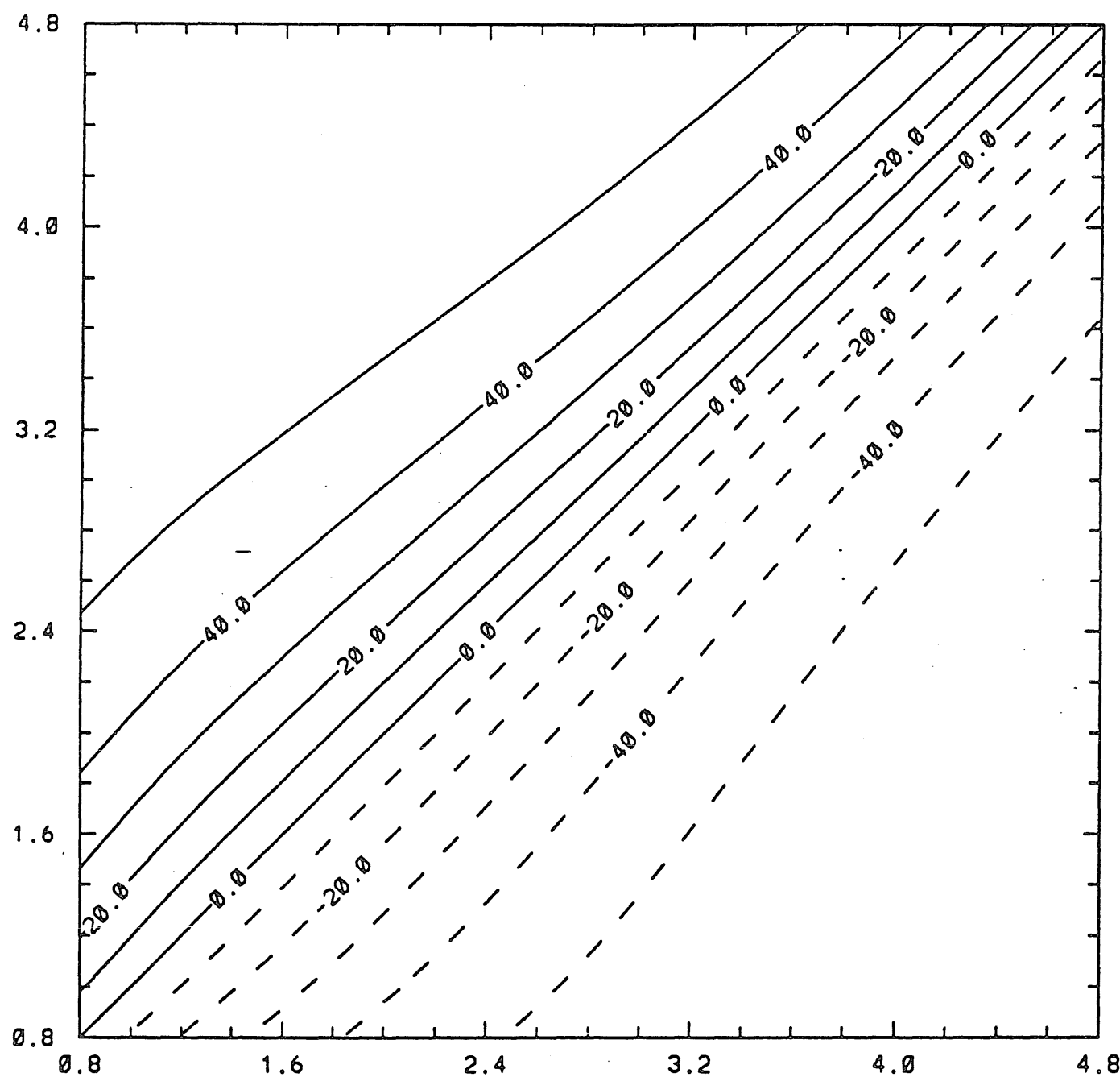


Figure 5. Contour Plot of γ for Linear H_3 . Contours are spaced every 10 degrees with negative contours endashed.